Dominik Gilberg

Continuum Models for bi-disperse Granular Material Flows capturing the Process of size Segregation

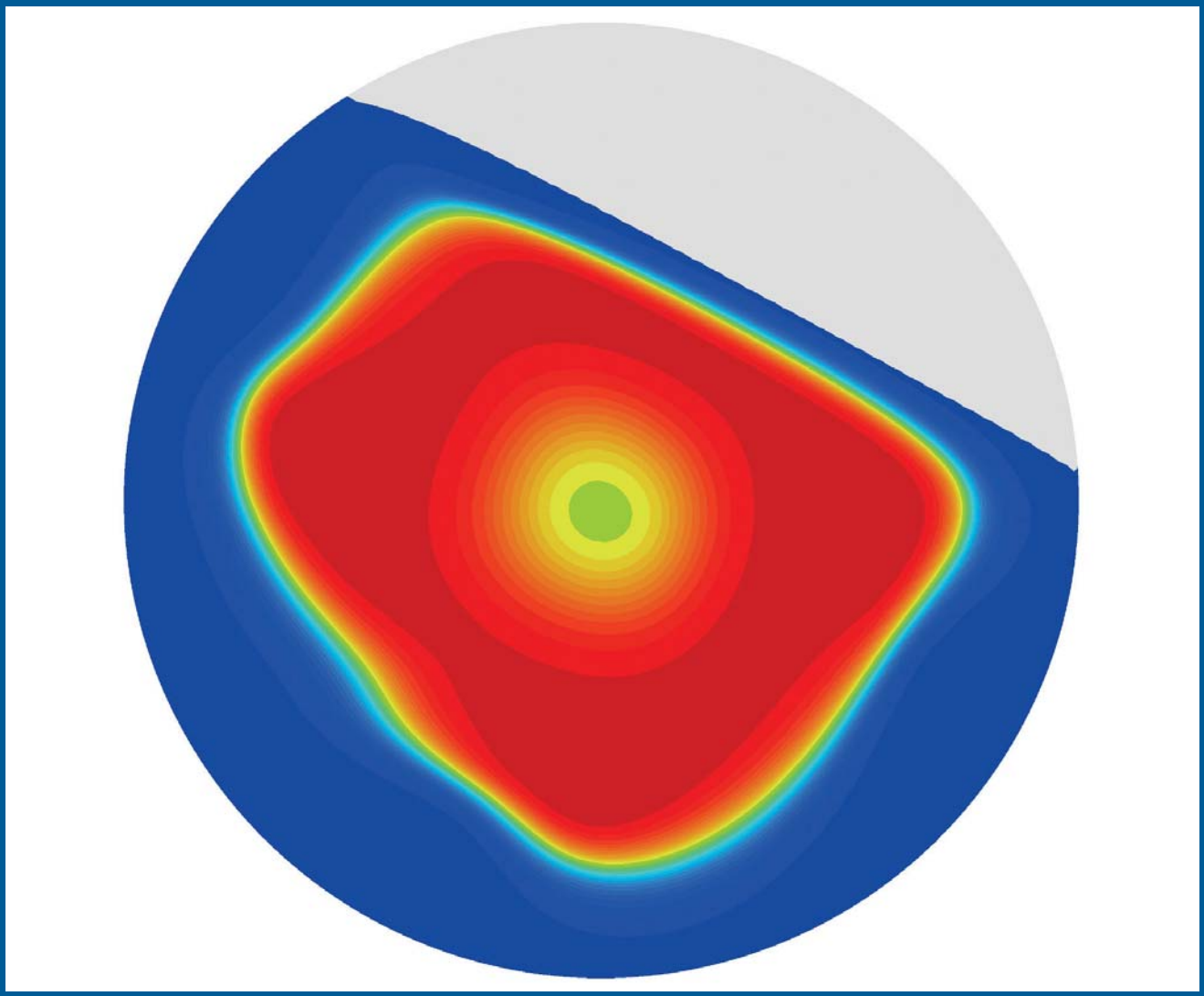

Technische Universität Kaiserslautern

Fraunhofer ITWM

Fraunhofer-Institut für
Techno- und Wirtschaftsmathematik ITWM

Continuum Models for bi-disperse Granular Material Flows capturing the Process of size Segregation

Dominik Gilberg

FRAUNHOFER VERLAG

Kontakt:
Fraunhofer-Institut für Techno- und Wirtschaftsmathematik ITWM
Fraunhofer-Platz 1
67663 Kaiserslautern
Telefon +49 631/31600-0
Fax +49 631/31600-1099
E-Mail info@itwm.fraunhofer.de
URL www.itwm.fraunhofer.de

Bibliografische Information der Deutschen Nationalbibliothek
Die Deutsche Nationalbibliothek verzeichnet diese Publikation in der Deutschen Nationalbibliografie; detaillierte bibliografische Daten sind im Internet über http://dnb.d-nb.de abrufbar.
ISBN (Print): 978-3-8396-1411-2

D 386

Zugl.: Kaiserslautern, TU, Diss., 2018

Titelbild: © Dominik Gilberg

Druck: Mediendienstleistungen des
Fraunhofer-Informationszentrum Raum und Bau IRB, Stuttgart

Für den Druck des Buches wurde chlor- und säurefreies Papier verwendet.

Fraunhofer-Informationszentrum Raum und Bau IRB
Postfach 80 04 69, 70504 Stuttgart
Nobelstraße 12, 70569 Stuttgart
Telefon 07 11 9 70-25 00
Telefax 07 11 9 70-25 08
E-Mail verlag@fraunhofer.de
URL http://verlag.fraunhofer.de

Technische Universität Kaiserslautern

Continuum models for bi-disperse granular material flows capturing the process of size segregation

Dominik Gilberg

Vom Fachbereich Mathematik der Technischen Universität Kaiserslautern zur Verleihung des akademischen Grades Doktor der Naturwissenschaften (Doctor rerum naturalium, Dr. rer. nat.) genehmigte Dissertation

Gutachter:
Prof. Dr. Axel Klar
Technische Universität Kaiserslautern
Prof. Dr. Michael Junk
Universität Konstanz

Datum der Disputation:
30. August 2018

D386

Danksagung

Das Entstehen einer jeden Arbeit wird auch beeinflusst durch die Menschen die einen beruflich und privat umgeben. Auch bei mir haben diese Menschen durch ihr Wirken mit dazu beigetragen das Gelingen dieser Arbeit zu ermöglichen.

Daher möchte ich mich zuerst bei Prof. Dr. Axel Klar und Dr. Konrad Steiner bedanken, welche mir die Möglichkeit zu dieser Promotion gegeben und mich während dieser Zeit betreut haben. Ebenso danke ich Prof. Dr. Michael Junk für seine Bereitschaft als externer Gutachter für diese Arbeit zu fungieren.

Ein weiterer Dank geht an alle Mitarbeiter und Doktoranden der Abteilung SMS. Im Speziellen danke ich Dr. Dariusz Niedziela, bei dem ich jeder Zeit Unterstützung erhalten habe, wenn ich in den Tiefen des CoRheoS-Quellcodes wandelte. Dieser Dank gilt auch Dr. David Neusius, der bereits vor mir mit den Herausforderungen des granularen Modells konfrontiert war.

Für viele hilfreiche fachliche, aber auch private Gespräche zur Mittagszeit bedanke ich mich bei dem harten Kern Doktoranden und ehemaliger Doktoranden, die sich täglich auf den Weg zur Mensa gemacht haben. Im Speziellen bedanke ich mich bei Dr. Sebastian Osterroth, Dr. Tobias Hofmann, Stephan Höcker und Anika Kinscherff für die Korrekturlesung dieser Arbeit.

Nicht zuletzt bedanke ich mich bei meiner Freundin, meiner Familie und meinen Freunden für die Unterstützung und den Beistand während der Promotionszeit.

Abstract

This thesis deals with the topic of segregation in granular materials. The basis for this work is a hydrodynamic model for granular material flows of Navier-Stokes type, which is extended to capture segragation of systems with small and large particles. The extended model is required to capture the dynamic process of segregegation of such systems.

The granular flow equations consist of a set of Navier-Stokes-like equations as well as an equation for the granular temperature. With the help of the granular temperature equation, the model is able to cover dense and dilute regimes. Therefore, the model and its dependencies are extensively described at the beginning of this thesis.

To derive the segregation equation, the framework of mixture theory is used. Special focus is lain on two topics. First, the segregation direction is thematised, in particular this is done in three-dimensional space. This aspect is relevant in order to make the segregation process invariant to the choice of the coordinate system. The second topic is the packing of binary particle systems, which corrects the density computations of the granular flow equations in the case of binary particle systems.

For solving the set of equations, a finite volume approach is chosen. The segregation equation explicitly depends on the volume fraction of the granular system. Since the granular flow model is compressible, the segregation equation requires special numerical treatment. Therefore, a modified Godunov scheme is formulated based on the solutions of the underlying Riemann problems. The method guarantees that the system stays in a physically valid state. The model was implemented using the granular flow solver GRAIN, which is included in the software platform CoRheoS, developed at ITWM. The GRAIN solver was adapted to include the segregation equation and the modified version of the granular flow equations. The implementations for solving the segregation equation and the modifications concerning the granular flow equations derived in this work are made by the author. The used programming language is C++.

In the last part of this thesis, the final model is extensively tested using different frameworks in two- and three-dimensional space. Particularly, the influence of the granular flow model on the segregation process is pointed out in detail.

Zusammenfassung

Diese Arbeit beschäftigt sich mit dem Thema der Segregation in granularen Medien. Als Grundlage zur Beschreibung granularer Materialien dient ein hydrodynamisches Modell, ähnlich der Navier-Stokes Gleichungen. Das Ziel dieser Arbeit ist die Erweiterung dieses Modells. Für granulare Systeme, bestehend aus großen und kleinen Teilchen, soll das erweiterte Modell den Prozess der Segregation berücksichtigen und abbilden können.

Das Grundlagenmodell zur Beschreibung granularer Strömungen beinhaltet, zusätzlich zu den Navier-Stokes-Artigen Gleichungen, eine Gleichung zur Beschreibung der granularen Temperatur. Mittels dieser zusätzlichen Gleichung ist es möglich granulare Systeme sowohl in dichten, als auch dünnen Regimen zu beschreiben. Daher wird in einem ersten Abschnitt der Arbeit dieses Modell ausführlich beschrieben und die wichtigsten Eigenschaften und Abhängigkeiten dargelegt.

Zur Herleitung der Segregationsgleichung wird das Konzept der sogenannten "Mixture Theory" verwendet. Ein Hauptaugenmerk werden jeweils auf die Richtung des Segregationsprozesses, speziell im dreidimensionalen Raum und auf das Thema der Teilchenpackungen für Gemische zweier, unterschiedlich großer Teilchen gelegt. Der erste Schwerpunkt dient dem Bestreben den Segregationsprozess unabhängig vom gewählten Koordinatensystem zu machen. Der zweite Punkt korrigiert die Dichteberechnungen des granularen Modells für vermischte binäre Teilchensysteme.

Zur Lösung der Gleichungssysteme wird ein finite Volumen Ansatz gewählt. Numerisch bedarf das Lösen der Segregationsgleichung einer nicht standardisierten Behandlung. Das liegt daran, dass die Gleichung explizit von dem granularen Volumenanteil des Gesamtsystems abhängt, welches kompressibel ist. Daher wird, basierend auf den Lösungen der zugrundeliegenden Riemann Probleme, eine modifizierte Version der Godunov-Methode formuliert, mittels welcher die Segregationsgleichung gelöst werden kann. Die Methode garantiert, dass das System physikalisch zulässige Zustände nicht verlässt. Durch den am ITWM entwickelten granularen Strömungslöser GRAIN, welcher Teil der Softwareplattform CoRheoS ist, ist bereits ein Löser für das granulare System vorhanden. Die Implementierung des Lösers für die Segregationsgleichung und alle in dieser Arbeit hergeleiteten Änderungen am granularen Modell wurden durch den Autor vorgenommen. Die genutzte Programmiersprache ist C++.

Im letzten Teil der Arbeit wird das finale Modell an verschiedenen Beispielen, sowohl im zwei- als auch im dreidimensionalen Raum getestet und bewertet. Im Speziellen wird der Einfluss des granularen Strömungsmodells auf die Segregation hervorgehoben.

Contents

Acknowledgement **i**

Abstract **iii**

Contents **v**

Notation **vii**
Abbreviations vii
Symbols viii
Operators ix

1 Introduction and state of the art **1**
1.1 Granular material 1
1.1.1 Discrete models 2
1.1.2 Continuum models 2
1.2 Segregation 4

2 Mathematical models **9**
2.1 The granular flow model 9
2.1.1 The compressible isothermal viscous Navier-Stokes equations 10
2.1.2 The granular temperature equation 10
2.1.3 Constitutive relations for a hybrid model 11
2.1.4 Overview on the granular flow equations 15
2.1.5 Boundary conditions for the granular flow equations 18
2.1.6 The connection between temperature and shear rate 20
2.2 The segregation equation 20
2.2.1 Mixture theory 20
2.2.2 Deriving the segregation equation 22
2.2.3 The segregation direction 27
2.3 Maximum volume fraction 29
2.3.1 Packing of particles 30
2.3.2 Random close packing for binary mixtures 31
2.4 Modification of the granular flow model 34
2.5 Summary of the final model 36

3 Analysis **39**
3.1 Theory of hyperbolic conservation laws 39
3.2 Analysis of the segregation equation 46

3.3 Spatial dependent flux functions . . . 52
3.3.1 Introduction to discontinuous flux functions . . . 52
3.3.2 The segregation equation as non-linear resonant system . . . 54
3.3.3 Solving the Riemann problem for the segregation equation as non-linear resonant system . . . 56
3.3.4 Solution to the Riemann problem for the segregation equation with non-constant temperature . . . 68

4 Numerics **73**
4.1 Discretisation using finite volumes . . . 73
4.2 Numerical methods . . . 76
4.3 A Godunov method for the segregation flux . . . 78
4.3.1 The classical Godunov scheme . . . 79
4.3.2 The modified Godunov scheme . . . 80
4.4 The CFL condition . . . 83
4.5 Boundary conditions for the segregation equation . . . 84

5 Simulation and application **87**
5.1 Verification of the segregation direction . . . 87
5.2 Simulating segregation in one space dimension . . . 90
5.2.1 Gaining physical solutions by the modified Godunov method . . . 91
5.2.2 Convergence and the mixing entropy . . . 94
5.3 Simulating a two-dimensional shear cell . . . 99
5.3.1 The idealised case . . . 99
5.3.2 Influence of the granular flow equations . . . 102
5.3.3 Comparison to a shear cell experiment . . . 104
5.3.4 Verifying the shear-temperature relation . . . 108
5.4 Applications in the three-dimensional space . . . 108
5.4.1 The rotating tumbler . . . 109
5.4.2 Influence due to binary particle packings . . . 113
5.4.3 Discharging a silo . . . 114

6 Conclusion **117**

A Riemann solutions in the concave case **119**

Bibliography **127**

Notation

Abbreviations

BCRE Bouchaud-Cates-Ravi Prakash-Edwards (model)

CoRheoS Complex Rheology Solvers - A software framework for implementing flow solvers.

CFL Courant-Friedrichs-Lewy (condition)

DEM discrete element method

DPM discrete particle method

EC entropy condition

FVM finite volume method

LWR Lighthill-Witham-Richards (model)

MD molecular dynamics

MCM mechanical contraction model

NSE Navier-Stokes equations

ODE ordinary differential equation

PDE partial differential equation

QMOM quadrature-based method of moments

RCP random close packing

RLP random loose packing

Symbols

Symbol	Unit	Explanation
d		spacial space dimension
c	$[1]$	granular volume fraction
T	$[\frac{m^2}{s^2}]$	granular temperature
$\mathbf{u}$	$[\frac{m}{s}]$	macroscopic granular bulk velocity
p	$[\frac{m^2}{s^2}]$	granular pressure
$\boldsymbol{\sigma}$	$[\frac{m^2}{s^2}]$	stress-strain tensor
$\boldsymbol{\kappa}$	$[\frac{1}{s}]$	strain rate tensor
$\mathbf{q}$	$[\frac{m^3}{s^2}]$	granular heat flux
η	$[\frac{m^2}{s}]$	scaled shear viscosity
λ	$[\frac{m^2}{s}]$	scaled thermal conductivity
ε	$[\frac{1}{s}]$	scaled energy dissipation
η_0	$[m]$	shear viscosity factor
λ_0	$[m]$	thermal conductivity factor
ε_0	$[\frac{1}{m}]$	energy dissipation factor
ξ_k, ξ_y		kinetic and yield part of a granular constitutive expression, $\xi = \xi_k + \xi_y$
c_{max}, $c_{rcp}(\cdot)$	$[1]$	granular maximum volume fraction, random close packing
$c_{rlp}(\cdot)$	$[1]$	random loose packing
c_0	$[1]$	transition volume fraction between kinetic and yield regime (close to random loose packing)
T_0	$[\frac{m^2}{s^2}]$	yield parameter
$g(\cdot)$	$[1]$	compressibility factor
ϕ^ν	$[1]$	volume fraction of particle phase $\nu \in [s, l]$
$\hat{\phi}^\nu$	$[1]$	relative volume fraction of particle phase $\nu \in [s, l]$, $\hat{\phi}^\nu = \frac{\hat{\phi}^\nu}{c}$
$\mathbf{S}^{sl}$	$[\frac{m}{s}]$	segregation velocity
S_0^{sl}	$[\frac{s^2}{m}]$	segregation coefficient
$\dot{\gamma}$	$[\frac{1}{s}]$	shear rate
B	$[1]$	non-dimensional magnitude in definition of proportionality factors
μ	$[\frac{1}{s}]$	coefficient of inter-particle drag
$\mathbf{g}$	$[\frac{m}{s^2}]$	gravity vector
$\mathbf{d}_s$	$[1]$	segregation direction vector
r^ν, R	$[m]$	grain radius of particle phase $\nu \in [s, l]$ and radius ratio $R = \frac{r^s}{r^l}$
$\mathbf{F}$	$[\frac{m^3}{s^2}]$	force acting on particles
m	$[\frac{m^3}{s^2}]$	mass of a particle
$\mathbf{v}$	$[\frac{m^3}{s^2}]$	microscopic particle velocity
C_i		control volume of finite volume discretization
σ_k		face of control volume
$\mathbf{n}_{\sigma_k}$		outer normal vector of control volume's face
$\bar{F}^n_{\sigma_k}$		average flux through face σ_k at time step t_n
ξ_L, ξ_R		left and right Riemann state of some quantity ξ
$\check{\xi}$		correct Riemann solution at the interface of two control volumes
s	$[\frac{m}{s}]$	shock speed given by Rankine-Hugoniot condition

Operators

Throughout this thesis vectors and vector valued functions are typeset in bold font. As the components of vectors are scalar, they are not bold like all other scalar quantities or functions. Hence, the i-th component of the velocity vector $\mathbf{u}$ is given by u_i.
Furthermore, the following operators appear in this work.

Gradient

Let $\mathbf{e}_j$ be the j-th standard unit vector. For a *scalar valued function* $S\colon \mathbb{R}^d \to \mathbb{R}$ the gradient is defined as

$$grad(S) \coloneqq \nabla S = \sum_{i=1}^{d} (\partial_{x_i} S) \cdot \mathbf{e}_i$$

Divergence

The divergence of a *vector field* $\mathbf{F}\colon \mathbb{R}^d \to \mathbb{R}^d$ is defined as

$$div(\mathbf{F}) \coloneqq \nabla \cdot \mathbf{F} = \sum_{j=1}^{d} \partial_{x_j} F_j.$$

The extension of the divergence for a *tensor field* $\mathbf{T}\colon \mathbb{R}^d \to \mathbb{R}^{d\times d}$ is given by

$$div(\mathbf{T}) \coloneqq \nabla \cdot \mathbf{T} = \sum_{j=1}^{d} \sum_{j=1}^{d} (\partial_{x_j} T_{ji}) \cdot \mathbf{e}_i,$$

where $\mathbf{e}_i$ denotes the i-th unit vector.

Dyadic product

Let $\mathbf{u}$ and $\mathbf{v}$ be two vectors, then the *dyadic* or *outer vector product* is denoted by

$$\mathbf{u} \otimes \mathbf{v} = \mathbf{u}\mathbf{v}^T = (u_i \cdot v_j)_{ij}$$

Contraction

The *tensor contraction* for two tensors $\boldsymbol{\sigma}$ and $\boldsymbol{\kappa}$ is given by

$$\boldsymbol{\sigma} : \boldsymbol{\kappa} = \sum_{i=1}^{d} \sum_{j=1}^{d} \sigma_{ij} \kappa_{ij}.$$

Although it is quite common to denote the gradient and the divergence operator by $grad(\cdot)$ and $div(\cdot)$, respectively, the notation using the Nabla-Operator ∇ is preferred in this work. If a functional expression depends solely on one variable the prime-notation is used for derivatives in some cases. For example, the derivative of an integral curve with respect to the variable ξ, is simply written by $I'(\xi)$.

Chapter 1

Introduction and state of the art

1.1 Granular material

Granular materials consist of macroscopic particles of different size and kind. Examples range from avalanches and dunes in geophysics, grain filled silos in agriculture to powders in the cosmetic and pharmaceutical industry. They are omnipresent in humans daily lives. Many industrial and chemical processes have to deal with granular materials. The world-wide annual production of grains and aggregates reaches 10 billion metric tons and their processing consumes 10 % of all energy produced on earth. It is the most manufactured material in industry after water [23]. For these reasons granular materials have been the subject of intensive engineering research for many decades but fully understanding their dynamic behaviour still poses a major challenge to engineering science and physics. The natural and industrial processes described above can be quite complex, since granular materials can behave similar to either fluids or solids. For the aforementioned processes, the different regimes occur at the same time or consecutively. Due to the macroscopic size of the discrete particles, Brownian motion has no relevance for the collective behaviour. The dissipative forces acting on the particles, such as inelastic collisions and friction, lead to different material properties than conventional fluids, solids or gases. For a granular system to remain active, it needs to gain energy from external forces (gravity, electric or magnetic fields), shear or vibration. Thermal fluctuations are insufficient to move grains and therefore do not play a role for granular systems. Consequently, granular materials exhibit metastable steady states far from equilibrium [1]. All these aspects contribute to the difficulties one encounters in the modelling of granular flows.
The first true paper on granular matter appeared at the end of the eighteenth century written by Charles de Coulomb. In the following century, other well-known authors like Michael Faraday or Osborne Reynolds did first work in the field of granular flows. A good review of the use, the physics, and the history of granular materials can be found in the book of Duran [23].
Dealing with the aspect of simulation, there already exist several models to describe and compute the behaviour of granular materials. Those models are summarised in the upcoming subsections.

1.1.1 Discrete models

Discrete models exploit that granular materials are composed of single particles. In the discrete Element method (DEM) for example, the motion of each particle, associated with index i, is resolved. This is typically done by integrating Newton's equations of motion for the translational and rotational degrees of freedom given by

$$\begin{aligned} m_i \ddot{\mathbf{r}}_i &= \mathbf{F}_i + m_i \mathbf{g}, \\ \mathbf{I}_i \dot{\boldsymbol{\omega}}_i &= \mathbf{t}_i. \end{aligned} \tag{1.1}$$

In the set of equations (1.1), the position of particle i is $\mathbf{r}_i$, m_i is the mass, $\mathbf{F}_i$ the total force acting on this particle due to collisions, $\mathbf{I}_i$ the rotational inertia, $\boldsymbol{\omega}_i$ the angular velocity and $\mathbf{t}_i$ the total torque. The method has been proposed by Cundall in 1971 [16]. A precursor of the DEM is the Molecular Dynamics (MD) simulation, which was invented in the late 1950's. Today, the MD simulation is mainly used in the fields of chemical physics and material science to compute the interactions of atoms and molecules. In the MD simulation the rotational motion is ignored. Pretty often a simulation describing particle systems using equations of type (1.1) is also called Discrete Particle Method (DPM).

Each of these methods provides an accurate tool for the simulation of granular flows. However, they are numerically rather costly, which, for the high number of particles one encounters in industrial applications, would lead to excessive computational times or technical requirements. Therefore, researchers develop other approaches to describe granular flows. Despite the particles having macroscopic size, models like the Discrete Element Method are called microscopic because they describe each single particle. Even if these methods are costly, they are helpful, as they can partially substitute experiments.

1.1.2 Continuum models

Leaving the microscopic level, methods are derived via kinetic theory or by using phenomenological arguments. Approaches that are based on kinetic theory are derived from the Boltzmann equation. The Boltzmann equation is an equation of change of the particle probability distributions function $f(\mathbf{r}, \mathbf{v}, t)$. It is defined in such a way that

$$f(\mathbf{r}, \mathbf{v}, t) d\mathbf{v} d\mathbf{r} \tag{1.2}$$

denotes the probable number of particles in the spatial volume element $d\mathbf{r}$ located at $\mathbf{r}$ with a velocity in the range $d\mathbf{v}$ around $\mathbf{v}$ at time t. The Boltzmann equation assumes the following form:

$$\left(\partial_t + \mathbf{v} \cdot \nabla_{\mathbf{x}} + \frac{1}{m} \mathbf{F} \cdot \nabla_{\mathbf{v}} \right) f = \partial_t f|_{coll}, \tag{1.3}$$

where $\mathbf{F}$ is an external force and $\partial_t f|_{coll}$ the collision term. The equation describes the dynamics of a dilute granular gas and was devised by Ludwig Boltzmann in 1872. A well-known modification for denser gases was devised by David Enskog. Both equations differ just in the collision term. To derive equations like (1.3), the usual molecular-chaos assumption is used, which neglects correlations between colliding particles. Due to this fact, it can be a rather poor approximation for dense granular systems. More details

about kinetic theory can be found in the book of Brilliantov and Pöschel [9].
First of all and independently from each other, Sydney Chapman and David Enskog found a method to solve the Boltzmann equation using a perturbation expansion for f. The so-called Chapman-Enskog theory is described in [12].
Another theory is the Quadrature-based method of moments (QMOM), where a system of equations for the moments of the function f is solved. Information can be found in the work of Fox [26].
From the Boltzmann equation (1.3), one generally derives equations for independent hydrodynamic field variables by multiplying $\mathbf{1}, \mathbf{v}$, and $|\mathbf{v}|^{\mathbf{2}}$, respectively and integrating equation (1.3) over the particle velocity $\mathbf{v}$. Then, the field variables are the density ρ, the velocity $\mathbf{u}$, and the granular temperature T, which is the fluctuating kinetic energy. They are defined by

$$\begin{aligned} \rho &= m \int f d\mathbf{v}, \\ \rho\mathbf{u} &= m \int \mathbf{v} f d\mathbf{v}, \\ \rho T &= \frac{1}{2} m \int |\mathbf{v}|^2 f d\mathbf{v}. \end{aligned} \tag{1.4}$$

Hence, one obtains a mass, momentum and an energy conservation equation, which generally take the form

$$\begin{aligned} \partial_t \rho + \nabla \cdot (\rho\mathbf{u}) &= 0, \\ \partial_t (\rho\mathbf{u}) + \nabla \cdot (\rho\mathbf{u} \otimes \mathbf{u}) &= -\nabla \cdot \boldsymbol{\sigma} + \rho\mathbf{g}, \\ \partial_t (\rho T) + \nabla \cdot (\rho T \mathbf{u}) &= -\boldsymbol{\sigma} : \boldsymbol{\kappa} - \nabla \cdot \mathbf{q} + \varepsilon, \end{aligned} \tag{1.5}$$

where $\boldsymbol{\sigma}$ is the stress tensor, $\boldsymbol{\kappa}$ the strain-rate tensor, $\mathbf{q}$ the energy-flux vector and ε the energy dissipation rate. This set of equations describes the behaviour of the whole granular system and not all particles discretely. Therefore, this type of equations is called hydrodynamic or macroscopic. In engineering sciences as well as for phenomenological models it is common to call them continuum models. Summaries how to obtain hydrodynamic equations from kinetic theory can be found in the works of Dufty and Baskaran [22] and Hrenya [44].

Another way to derive macroscopic equations from a microscopic or mesoscopic level is presented in the work of Klar and Tiwari [49]. They start their derivations from the so-called Liouville equation associated with a microscopic N-particle system for the distribution function $f^{(N)}$, which is given by

$$\partial_t f^{(N)} + \sum_{i=1}^{N} \left(\nabla_{\mathbf{x}_i} \cdot (\dot{\mathbf{x}}_i f^{(N)}) + \nabla_{\mathbf{v}_i} \cdot (\dot{\mathbf{v}}_i f^{(N)}) \right) = 0. \tag{1.6}$$

Using several assumptions like the assumption of chaos and the assumption that particles are indistinguishable, one derives the mean field equation

$$\partial_t f + \mathbf{v} \cdot \nabla f + Sf = 0, \tag{1.7}$$

in the limit case $N \to \infty$. It is a integro-differential equation for the particle distribution function f as S is given in integral form defining the interaction information between the particles. Macroscopic equations can be derived in the same way as previously shown for the Boltzmann equation.
Furthermore, there are several phenomenological models where the continuum equations are mainly postulated and fitted to one specific flow behaviour occurring in a particular process. A popular model is the Bouchaud-Cates-Ravi Prakash-Edwards (BCRE) model, which combines the behaviour of flowing and static grains to describe the thin avalanches near the surface of sand piles [6, 7]. The model is a system of coupled differential equations for the evolution of the thickness of the avalanche R and of the static part of the sand pile h. Compactly, it can be written in the following form:

$$\begin{aligned} \partial_t h &= \Gamma(h, R) \\ \partial_t R &= v_d \partial_x R - \Gamma(h, R), \end{aligned} \tag{1.8}$$

where $\Gamma(h, R)$ is the exchange term between static and rolling grains and v_d the downhill velocity of the grains.

All introduced macroscopic methods can be used to describe the behaviour of liquids and gases or granular systems in the dilute regime as previously mentioned. However, they are not applicable to arbitrary industrial processes in general, in which the flow can come to rest. Latz and Schmidt modified a system of hydrodynamic equations of type (1.5) to cover the regime of fast dilute flows as well as slow dense flows, where the density of the granular material is close to the maximum packing density [55]. A more detailed description will be given in the upcoming chapter.

1.2 Segregation

As mentioned in the previous section, the modelling of granular flows is quite challenging. Researchers developed different models to simulate the behaviour of granular materials, but the field of granular physics is still a mixture of different modelling tools, concepts, and phenomenological theories. After all, there is no general hydrodynamic theory as the Navier-Stokes equations (NSE) for simple fluids, which can model a granular system with the same accuracy. Quite good results can be acquired from discrete models like DEM, but they are too costly to simulate entire industrial processes. With kinetic theory there exists a unified description for dilute systems of rapid grains, but it is not applicable for granular systems approaching close-packing density. For the latter, there are some promising extensions of hydrodynamic systems and phenomenological models as mentioned in the previous section.
Granular materials and simple fluids not only differ in their flow behaviour. There are many other discrepencies, such as pattern formation or segregation. These phenomena can differ when the interaction between particles exhibits additional features caused by an interstitial fluid, magnetisation or electrical charge. An extensive review of granular matter, pattern formation, and existing models is given in the work of Aranson and Tsimring [1]. Most granular models use the assumption of equal-sized grains with equal density. Consequently, they are not able to capture a phenomenon like segregation, which is a very important phenomenon in nature and industrial processes. Segregation

describes the demixing of poly-disperse granular matter. This effect is very helpful in the mining industry but leads to problems in most other industrial areas. In the pharmaceutical and the food industry, mixing processes using rotating tumblers are very common. Here, segregation can degrade the quality of the products.
There are several requirements and aspects of influence for segregation to take place in a granular system. Most important are the particle shape or differences in particle size or density. The particles in the system need to be in motion and gravity or shear needs to be present. Differences in particle size are the most perceived reason for segregation. Many people already encounter this effect in the morning, while they prepare their morning cereal - the larger grains always end up at the surface and the smaller ones on the ground. The same happens with a bag of nuts. Therefore, segregation is also called the Brazil-Nut effect. Today, the most accepted explanation for size segregation is the mechanism of gravity-driven void-filling. It says that during motion, it is easier for small particles to fall in void spaces in the granular system. Besides size segregation, density-segregation plays an important role, which can be explained by buoyancy effects due to differences in particle density. In general, small particles and particles with high material density are likely to percolate through the granular system to the ground. Accordingly, large particles can also segregate to the bottom of the system if they are heavy enough. This is called reverse Brazil-Nut effect. A good review of segregation, containing theory and experiments, is given by Kudrolli [51]. The review considers the intruder model (one big particle between many small particles) in the convective and non-convective regime as well as binary mixtures and also the influence of the direction of vibration.

The starting point for the derivation of most segregation models is to look at a simple process. Typically, granular avalanches of small and large particles flowing down an inclined plane serve as a common example. The equations are formulated such that x, y and z denote the down-slope, the cross-slope, and the depth direction, respectively. A first model to describe segregation was proposed in 1985 by Bridgwater et al. [8]. It is a simple one-dimensional advection-diffusion equation for the solid volume fraction of the small particle phase $\phi \in [0, 1]$. The equation,

$$\partial_t \phi + \partial_z \left(q\phi(1-\phi)^2 \right) = \partial_z \left(D \partial_z \phi \right), \tag{1.9}$$

acts only in the depth direction of a flowing granular system. The segregation flux in this equation shuts off when only one particle phase is present. The parameter q defines the segregation velocity and D the diffusion rate.
In 1988, Savage and Lun [71] used statistical mechanics and an information entropy approach to derive a segregation model for a system of small and large flowing particles. They assumed that due to shear between the different particle layers of an avalanche small voids appear randomly. Particles of the above adjacent layer fall into these gaps, where the smaller particles are statistically more likely to fill these void spaces than the large particles. This gravity-driven mechanism is called “random fluctuating sieve”. Additionally, particles can be squeezed out of their layer due to imbalances in contact forces. This mechanism is size-independent and is called “squeeze expulsion”. Savage and Lun combined these two mechanisms and derived a model for the small particle phase with a net flux to the base of the flow. The main drawback of their model was, that segregation happens even in the absence of gravity.

A postulated model based on observations is given by Dolgunin and Ukolov [21] in 1995. It is a two-dimensional time dependent model given by

$$\partial_t \phi + \partial_x(\phi u) + \partial_z(q\phi(1-\phi)) = \partial_z(D\partial_z\phi). \tag{1.10}$$

Similar to the model of Bridgwater, the segregation stops when the concentration reaches the values zero or one. They expressed q and D by further free parameters, which have to be fitted to experimental data.
While the above-mentioned models mainly focused on size segregation in inclined chute flows of granular solids, in 1997 Khakhar et al. [48] analysed density segregation in the flowing layer of a granular system in rotating cylinders. After performing experiments, they formulated a balance law for the segregation process. For their density segregation model, the work by Dolgunin and Ukolov served as orientation. The presented advection-diffusion models, especially the segregation flux, has a similar structure as given by equation (1.10).
In the last ten to fifteen years, mixture theory has been used extensively to develop models describing size segregation. In 2005 Gray and Thornton [37] proposed such a theory of particle-size segregation in shallow granular free surface flows. The model is formulated in terms of mass and momentum balance for the small and the large particle phase, respectively. Also, the theory of Gray and Thornton is closely related to those of Bridgwater, Savage & Lun, and Dolgunin & Ukolov, but the derivation is much more detailed and extensive. The key assumption of their theory is a pressure allocation. They assume that in an avalanche the big particles carry more of the load than the small particles.
Gray and Chugunov [36] modified the theory in 2006 and included a diffusion term that accounts for the remixing of particles. With this first extension for the model of 2005 the structure of the segregation equation is identical to the one given by Dolgunin and Ukolov (1.10), where a framework for the derivation of such an equation was still missing. In 2011, Gray and Ancey [34] generalized the theory to a system of n phases. In the recent past, Tunuguntla et al. [79] modified the Gray & Thornton model [37] to derive a conservation law for particle-size and particle-density segregation. To achieve this, they used an approach by Marks et al. [59] in 2012. Gray and Ancey [35] performed a similar extension in 2015 and analysed the model in detail analytically. Therefore, they especially focused on the fact that in the case of density segregation the bulk flow is no longer incompressible. Most of the mentioned models focus on gravity-driven segregation.
As opposed to this, Fan and Hill [24] derived a model for size segregation, which is not based on the classical gravity-driven mechanism but induced by shear rates. Their model segregates small particles to regions of low shear and the large particles in opposite direction. Later on, their work was extended to include the gravity-driven mechanism [42].
A different formulation of the already mentioned theories to describe segregation is given in the works by Larcher and Jenkins [53, 54]. They considered the evolution of segregation in dense granular flows of two particle types A and B differing slightly in size and mass. They derived a segregation equation, which is given by

$$\rho\partial_t X + \rho\mathbf{u}\nabla X + \nabla\cdot\left[\frac{m_A n}{4}(1-4X^2)(\bar{\mathbf{u}}_A - \bar{\mathbf{u}}_B)\right] = 0. \tag{1.11}$$

The equation is solved for the quantity $X \equiv (n_A - n_B)/(2n)$, which is the difference in the species number densities. They use an extension of kinetic theory to predict the

mixture density ρ, mixture velocity $\mathbf{u}$ and granular temperature of the mixture, which appears in the expressions for the relative velocities $\bar{\mathbf{u}}_A$ and $\bar{\mathbf{u}}_B$, respectively.

The theory of Gray and his colleagues has a nice structure. In the non-diffusive case, analytical solutions can be found using the method of characteristics. Hence, one provides good insight in the process of segregation and the behaviour of the equations. Details about the construction of this exact time-dependent solution and its stability can be found in the works of Gray et al. [39] and Shearer et al. [74]. The shock formation and wave breaking are discussed in Shearer and Giffen [73]. A short review of shock formation and stability for equations of this type can be found in Shearer et al. [75]. Furthermore, mixing zones and their evolution are analysed in McIntyre et al. [62]. For all these reasons this type of model is used extensively in this work. Hence, a detailed description is given in the next chapter.

Chapter 2

Mathematical models

In this chapter, all equations are derived to compute the flow behaviour of a granular system and to describe the effect of segregation. In the first section, the granular flow equations of Latz and Schmidt [55] are presented and explained. These equations serve as the basis for the final model. In section 2.2, the theory of mixtures is introduced, which is used to derive the segregation equation afterwards. Particular attention is paid to the direction of the segregation process and its determination. To modify the granular flow equations regarding the segregation effect, section 2.3 is addressed to the topic of random packings of particle systems. Finally, all modifications to the granular flow equations are pointed out and the final system of equations is summarised (section 2.4 and 2.5).

2.1 The granular flow model

The model of choice to describe the behaviour of flowing granular materials in this thesis is a version of the Latz-Schmidt model similar to that which has been derived in [55]. The derivation starts from kinetic theory descriptions of the granular system and uses Chapman-Enskog theory to obtain a hydrodynamic system of equations. There are mainly two regimes that need to be taken into account when dealing with granular materials. First, the fast dilute flow regime which is dominated by binary particle collisions. In this case, the mentioned kinetic gas theory can be applied.
For arresting granular flows, the assumption of binary particle collisions is not valid any more. This second regime is often called the static regime, where kinetic theory is no longer applicable. To include the static regime, Savage [70] developed an extension to the former model which is based on the theory of soil mechanics. This model has been simplified by Latz and Schmidt [55]. The granular properties required for a simulation with such a hydrodynamic model can be obtained from experiments. The simplifications of the model reduce the number of parameters that needs to be fitted. That makes the calibration of a system easier. Further improvements have been done by Zémerli [87].
The final hydrodynamic model is a hybrid model of kinetic theory and a soil mechanical approach to capture the dilute flow regime of granular materials as well as the static regime of arresting flows. The detailed derivations are far beyond the scope of this thesis. The necessary information can be found in Brilliantov and Pöschel [9], Savage [70], and Latz and Schmidt [55]. Details about the numerical treatment of the equations is given in the work of Schmidt [72]. Nevertheless, the equations and constitutive relations are

explained in this section. Another extensive summary of the granular model can be found in the work of Neusius [65].

2.1.1 The compressible isothermal viscous Navier-Stokes equations

The general framework of the hydrodynamic model consists of three equations. The first equation (2.1) and the second equation (2.2) are the isothermal compressible viscous Navier-Stokes equations (NSE). They are solved for the granular volume fraction c and the momentum $c\mathbf{u}$, where $\mathbf{u}$ defines the bulk velocity of the granular material.

$$\partial_t c + \nabla \cdot (c\mathbf{u}) = 0, \tag{2.1}$$

$$\partial_t (c\mathbf{u}) + \nabla \cdot (c\mathbf{u} \otimes \mathbf{u}) = \nabla \cdot \boldsymbol{\sigma} - \nabla p + \mathbf{F}. \tag{2.2}$$

The force term in the momentum balance (2.2) is assumed to be solely the gravitational force $\mathbf{F} = c\mathbf{g}$. Further, p defines the pressure and $\boldsymbol{\sigma}$ the deviatoric stress tensor. In this model an asymmetric stress-strain relation is used, i.e.,

$$\boldsymbol{\sigma} = \eta \boldsymbol{\kappa}, \tag{2.3}$$

$$\boldsymbol{\kappa} = \nabla \mathbf{u}, \tag{2.4}$$

where η defines a viscosity. The usage of the asymmetric stress-strain relation is a simplification compared to the standard NSE. Typically, the symmetric version of the stress is used. In an d-dimensional space, it is given by

$$\boldsymbol{\sigma}^S = 2\eta \boldsymbol{\kappa}^S + \left((\zeta - \frac{2}{d}\eta) \nabla \cdot \mathbf{u} \right) \mathbf{id}, \tag{2.5}$$

$$\boldsymbol{\kappa}^S = \frac{1}{2}(\nabla \mathbf{u} + (\nabla \mathbf{u})^T). \tag{2.6}$$

The choice of the less complex asymmetric stress-strain relation is not arbitrary. It is not exact, but it leads to a decoupling of the velocities in the numerical method which is a benefit in the implicit handled parts [55]. The advantage of the symmetric stress-strain relation in the NSE is that it ensures the conservation of angular momentum. This advantage is not given for granular flows as the conservation cannot be physically observed [65]. It is common that the equations are formulated and solved for the macroscopic density ρ of the granular material. The granular volume fraction $c \coloneqq \frac{\rho}{\rho^*}$, which is used here, is the scaled version of the granular density ρ by the constant material density of the particles ρ^*. Hence, the volume fraction is a dimensionless quantity and it holds

$$c \in [0, c_{max}) \text{ and } c_{max} \leq 1. \tag{2.7}$$

Further information about the granular volume fraction and its bounds are explained in section 2.3.

2.1.2 The granular temperature equation

The third and last equation of the hydrodynamic system is the granular temperature equation (2.10). The concept of a granular temperature is essential for continuum models

of granular materials, because it considers the energy transport due to particle movements and collisions. It is a measure of the random particle motion in the granular system.

There exists an analogy between the thermal motion of molecules in a gas and the random motion of particles in a granular system. Hence, the definition of the granular temperature T (2.9) is similar to the one of the thermodynamic temperature $\mathbb{T}$. Based on this similarity the granular temperature T can be defined in the following way:

The velocity $\mathbf{v}$ of each particle can be decomposed into a mean velocity with the bulk material $\mathbf{u}$ and a fluctuating velocity

$$\mathbf{v}_f \coloneqq \mathbf{v} - \mathbf{u} \tag{2.8}$$

relative to the mean. Then, the granular temperature is defined by the mean square of the fluctuating velocity of the particles

$$T \coloneqq \frac{1}{3} < \mathbf{v}_f^2 > . \tag{2.9}$$

Ogawa et al. [67] already postulated in 1980 that the mechanical energy in a granular system is first transformed into random particle motion before it dissipates into internal energy. More precisely, the energy transport in granular flows can be understood in the following way. Energy can enter the system only due to work that is performed on the system. Sources are body forces or the motion of system boundaries. Due to shear work, some of the kinetic energy of the mean motion converts into granular temperature which is the kinetic energy associated with the random particle velocities [46]. Finally, the granular temperature dissipates into internal energy like thermodynamic heat. This happens due to inelastic particle collisions. These dynamics can be described by a balance law derived from the Boltzmann equation, as done in the work of Brilliantov and Pöschel [9]. The final granular temperature equation is given by

$$\partial_t(cT) + \nabla \cdot (cT\mathbf{u}) = \frac{3}{2}(\eta \boldsymbol{\kappa} : \boldsymbol{\kappa} - \nabla \cdot \mathbf{q}) - \varepsilon c T. \tag{2.10}$$

It has the structure of a heat equation. More precisely, it is a convection diffusion equation. The diffusive part is given by the granular heat flux

$$\mathbf{q} = -\lambda \nabla T, \tag{2.11}$$

where λ denotes the temperature viscosity. Equation (2.10) has a source in the viscous heating term $\frac{3}{2}\eta\boldsymbol{\kappa} : \boldsymbol{\kappa}$ and a sink in the last term, where ε is the energy dissipation rate.

2.1.3 Constitutive relations for a hybrid model

The granular system consists of three equations (2.1), (2.2) and (2.10). It is solved for the unknowns c, $\mathbf{u}$, and T. At this state of modelling, the expressions for the stress tensor $\boldsymbol{\sigma}$ and the granular heat flux $\mathbf{q}$ are specified already, but the pressure p and the transport coefficients η, λ, ε are still unknowns. To obtain a closed system, constitutive relations for these variables need to be provided.

The compressibility factor

Essential for the closures is the concept of a compressibility factor for granular materials. It is an analogy to the compressibility factor for gases. In the field of thermodynamics, the ideal gas law

$$pV = n\mathcal{R}\mathbb{T} \tag{2.12}$$

gives a relation between the pressure, the density of the gas, and the temperature of ideal gases. The compressibility factor is a correction factor to make the ideal gas law applicable for real gases. For an ideal gas, it is equal to one.

To give a relation between the pressure, the volume fraction, and the temperature for granular materials, which holds for a wide range of volume fractions, a compressibility factor for granular materials is defined. In contrast to the thermodynamic version, the compressibility factor for granular materials depends on the volume fraction of the granular system [5, 11, 55, 70].
If the local volume fraction of the granular system is in a physically valid state $c < c_{max}$, the compressibility factor for granular materials is also essential to ensure that the solution of the granular system stays valid. It is the only position, where the bound c_{max} is used in the set of equations. The factor is defined by $g(c)\colon [0, c_{max}) \to [0, \infty)$,

$$g(c) \coloneqq \left(1 - \frac{c}{c_{max}}\right)^{-1}. \tag{2.13}$$

Although it is called compressibility factor, it is a non-constant function similar to the Carnahan-Starling formula [11] which is an equation of state for the three-dimensional hard sphere model [65].

In the dilute regime, the compressibility factor g is a measure for the frequency of binary particle collisions. The number of particle collisions in a certain time interval influences the most terms in the granular equations, as for instance, the transport coefficients. For this reason, the compressibility factor is not solely used in the constitutive relation for the pressure, as it is typically done for regular gases.
In the dense regime the kinetic assumption of solely binary particle collisions is not valid any more. To model the granular flow behaviour in the dense regime, equation (2.13) diverges for $c \to c_{max}$ which is the main difference to the Carnahan-Starling formula. Bocquet et al. [5] showed that, with a strongly increasing compressibility factor g, the numerical results in a dense regime are close to the experimental data as long as the granular temperature does not fall under a certain value. In the dense regime one has to add additional terms in the case of vanishing temperature, which will be shown later on.

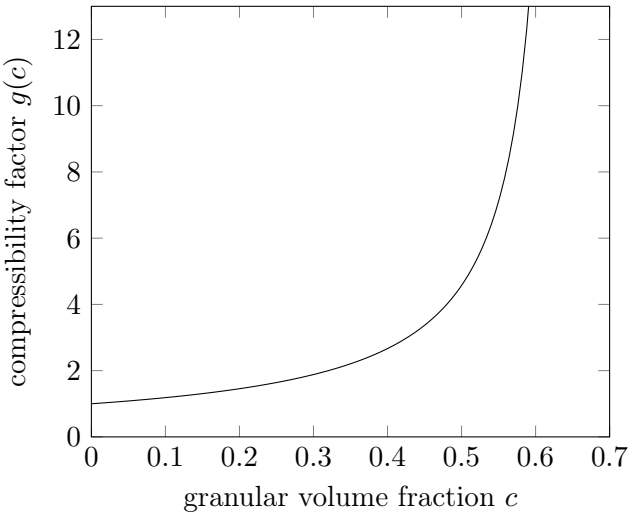

FIGURE 2.1: Plot of the compressibility factor $g(c)$ for $c_{max} = 0.64$. The compressibility factor diverges as $c \to c_{max}$.

The kinetic closures

As previously mentioned, one has to distinguish two regimes where the model should be applicable. Therefore, it is assumed that the closures for the pressure (2.14), the velocity viscosity (2.15), the temperature viscosity (2.16), and the dissipation factor (2.17)

$$p = p_k + p_y, \tag{2.14}$$
$$\eta = \eta_k + \eta_y, \tag{2.15}$$
$$\lambda = \lambda_k + \lambda_y, \tag{2.16}$$
$$\varepsilon = \varepsilon_k + \varepsilon_y \tag{2.17}$$

can be split in a purely kinetic and a so-called yield part. These parts are subscribed by k and y, respectively.

Starting from kinetic theory, Garzó and Dufty [29] derived expressions for p_k, η_k, λ_k, and ε_k. The expression for the kinetic pressure is formulated as

$$p_k \coloneqq cg(c)T. \tag{2.18}$$

Note that for low volume fractions, where $g(c)$ is almost constant, equation (2.18) is similar to the ideal gas law. For the kinetic parts of the transport coefficients, Bocquet et al. [5] showed that there are simpler expressions than those derived by Garzó and Dufty [29] which produce quantitatively correct results in shearing experiments. Furthermore, Schmidt [72] showed that the simpler form together with the upcoming extensions is applicable to various regimes of granular flow. The simplified kinetic parts for velocity diffusion, temperature diffusion, and temperature dissipation are given by

$$\eta_k \coloneqq \eta_0 c\sqrt{T}g(c), \tag{2.19}$$
$$\lambda_k \coloneqq \lambda_0 c\sqrt{T}g(c), \tag{2.20}$$
$$\varepsilon_k \coloneqq \varepsilon_0\sqrt{T}g(c). \tag{2.21}$$

All three relations are proportional to the compressibility factor $g(c)$, so they diverge in the same way for $c \to c_{max}$. This is necessary and leads to quantitatively correct simulation results which has been shown by Latz and Schmidt [55]. All parameters subscribed by 0 are material dependent constants that normally have to be validated by experiments. Some parameters can also be approximated via further relations. For instance, the temperature dissipation constant ε_0 can be computed with the help of the grain radius r and the particle coefficient of restitution e

$$\varepsilon_0 = \frac{4}{\sqrt{\pi} r}(1-e^2)\left(1 + \frac{3(1-e)(1-2e^2)}{81 - 17e + 30e^2(1-e)}\right) \tag{2.22}$$

as used in the work of Schmidt [72]. Further, Latz and Schmidt [55] used the relation

$$\tan(\varphi) = \sqrt{\varepsilon_0 \eta_0} \tag{2.23}$$

to determine η_0 with the help of the internal friction coefficient φ.

With the kinetic relations presented so far, the system can be closed and it leads to good results as long as the kinetic approximation of binary particle collisions is valid. For even denser flows, like shear flows or gravity-driven flows, good results can be obtained [5]. In these types of flows, enough energy enters the system that the granular temperature does not decrease to zero. In those cases the kinetic pressure is able to stabilise the granular system. As the kinetic pressure is proportional to the compressibility factor, this works also for increasing volume fractions.

The extensions for the yield regime

If a granular system comes to rest, the granular temperature decreases. As it holds for all materials, it contracts and the volume fraction increases. Strongly repulsive forces appear as the particles in the system are permanently touching multiple neighbours. The kinetic model does not account for these repulsive forces between the particles, except for the compressibility factor $g(c)$. However, if the granular temperature reaches zero faster than the volume fraction reaches its maximal value c_{max}, the pressure term vanishes and the system collapses. This collapse can be identified in the momentum balance (2.2) of the system.

In a static system, where $T = 0$ and $\mathbf{u} = \mathbf{0}$, the kinetic pressure term (2.18) and all kinetic transport coefficients (2.19), (2.20), and (2.21) vanish. Hence, the gravitational force cannot be compensated and the system will not stop contracting. This means that an additional expression independent of the temperature T is required.

Furthermore, particle shape and friction are responsible for the fact that granular materials reach a stable state already for $c = c_0 < c_{max}$ (see section 2.3). Without further forces acting on the granular system, the contraction must already stop for some transition volume c_0. To overcome the collapse of the system the so-called yield pressure is defined by

$$p_y \coloneqq \Theta(c - c_0) T_0 (c - c_0) g(c), \tag{2.24}$$

where $\Theta(\cdot)$ is the Heaviside step function and T_0 the yield parameter. The yield pressure has the same structure as the kinetic one for a constant temperature value T_0 but

only comes into play for volume fractions $c \geq c_0$. In this regime, the yield pressure compensates the vanishing kinetic pressure for temperatures tending to zero.

As already mentioned, the yield pressure can compensate the gravitational force. Certainly, the pressure gradient also works orthogonally to the direction of the earth acceleration. This force generated by the pressure gradient orthogonal to the earth acceleration would flatten each heap of granular materials. This has to be compensated by the transport coefficients. Schmidt [72] stated that this can be done under the following three requirements:

1. The transport coefficients must not vanish with vanishing temperature.
2. The viscosity η has to diverge with vanishing temperature.
3. The crossover from the kinetic regime to the yield regime must not modify the internal friction angle.

The derived yield expressions of the velocity diffusion, temperature diffusion, and temperature dissipation are given by

$$\eta_y \coloneqq \eta_k \frac{p_y}{p_k}, \tag{2.25}$$

$$\lambda_y \coloneqq \lambda_k \frac{p_y}{p_k}, \tag{2.26}$$

$$\varepsilon_y \coloneqq \varepsilon_k \frac{p_y}{p_k}. \tag{2.27}$$

Analogous to the kinetic expressions, the yield expressions are all of the same order. An evidence that the given expressions fulfil the stated requirements can be found in [72].

Originally, the concept of yield expressions comes from the field of soil mechanics where above a so-called yield surface only static deformations occur. In the field of soil mechanics, this regime is called plastic regime. First attempts to find a model combining the kinetic and the plastic regime were done by Savage [70]. The yield expressions used here were already used in the work of Schmidt [72]. They are simplified versions of those defined by Savage [70].

2.1.4 Overview on the granular flow equations

This subsection shortly summarises the granular flow model. In the presented form, the model serves as basis for further modelling steps throughout this thesis. The set of equations consists of the continuity equation, the momentum balance, and the granular temperature equation.

The granular flow equations

$$\partial_t c + \nabla \cdot (c\mathbf{u}) = 0, \tag{2.28a}$$
$$\partial_t (c\mathbf{u}) + \nabla \cdot (c\mathbf{u} \otimes \mathbf{u}) = \nabla \cdot \boldsymbol{\sigma} - \nabla p + c\mathbf{g}, \tag{2.28b}$$
$$\partial_t (cT) + \nabla \cdot (cT\mathbf{u}) = \frac{3}{2}(\eta \boldsymbol{\kappa} : \boldsymbol{\kappa} - \nabla \cdot \mathbf{q}) - \varepsilon c T. \tag{2.28c}$$

To close the system, several relations hold:

The closure relations

The stress and the granular heat flux are given by

$$\boldsymbol{\sigma} = \eta \boldsymbol{\kappa}, \qquad \boldsymbol{\kappa} = \nabla \mathbf{u}, \tag{2.29}$$
$$\mathbf{q} = -\lambda \nabla T. \tag{2.30}$$

The granular pressure fulfils

$$p = p_k + p_y, \tag{2.31a}$$
$$p_k = cTg(c), \tag{2.31b}$$
$$p_y = \Theta(c - c_0) T_0 (c - c_0) g(c), \tag{2.31c}$$

where the compressibility factor is given by

$$g(c) = \left(1 - \frac{c}{c_{max}}\right)^{-1}. \tag{2.32}$$

The transport coefficients for velocity diffusion, temperature diffusion and temperature dissipation are given by

$$\eta = \eta_k (1 + \frac{p_y}{p_k}), \qquad \eta_k = \eta_0 \sqrt{T} c g(c), \tag{2.33a}$$
$$\lambda = \lambda_k (1 + \frac{p_y}{p_k}), \qquad \lambda_k = \lambda_0 \sqrt{T} c g(c), \tag{2.33b}$$
$$\varepsilon = \varepsilon_k (1 + \frac{p_y}{p_k}), \qquad \varepsilon_k = \varepsilon_0 \sqrt{T} g(c). \tag{2.33c}$$

All coefficients are of the same order with respect to the granular temperature.

As already mentioned, the first two equations are similar to the compressible isothermal viscous NSE. In contrast to the density ρ of the granular material, the system is solved for the volume fraction c. An asymmetric stress-strain relation is used. This is

a simplification compared to the symmetric one which is normally used in the NSE. However, there are several points that make this system a much more challenging problem. For instance, there are the additional granular temperature equation and the particular closures which have a kinetic and a yield part to make this system applicable in the different regimes. In the dilute regime, the model is purely kinetic as the yield pressure term p_y is equal to zero and hence, all yield parameters are equal to zero, too. For volume fractions $c \geq c_0$, the yield parameters are non-zero which stabilises the granular system for increasing volume fractions and decreasing granular temperatures.

In a flowing system, each quantity of system (2.28) has to be transported with the material. Hence, each equation has a convection term on the left-hand side to transport each quantity with the bulk velocity $\mathbf{u}$ computed in the momentum balance (2.28b). Additionally, the pressure term ∇p in (2.28b) generates a velocity pointing from regions of high pressure to regions of lower pressure. This prevents the system from compressing above the maximal allowed value c_{max}.

A moving granular system stays in motion only if forces are present that perform work on the system. Otherwise, the granular material will come to rest. Due to particle collisions, the energy in the system diffuses. In the momentum balance (2.28b) and the granular temperature equation (2.28c), the diffusion terms $\nabla \cdot \boldsymbol{\sigma}$ and $\frac{3}{2}(\nabla \cdot \mathbf{q})$ reproduce this behaviour. In the dilute regime, the collisions are instantaneous and less frequent. For increasing volume fractions and increasing granular temperatures, the number of collisions increases and so the energy diffusion becomes larger. Hence, the diffusion parameters η and λ are proportional to $cg(c)$ and $\sqrt{T}$.

In the regime from dense to static granular materials, it is slightly different. Particle interactions are dominated by multi-contacts and contacts over long time durations. In this regime, it is not possible to accelerate one particle without accelerating a whole layer of particles as well. Therefore, large forces are necessary which has to increase even more for increasing volume fractions. This static friction of the adjacent particles is modelled by a large diffusion which is given in the yield terms of the model since they are proportional to $(c - c_0)g(c)$. The main difference to the dilute regime lies in the the granular temperature relation. If in a dense or static system the random motion of particles increases, the static friction decreases. Therefore, the yield terms are proportional to $\frac{1}{\sqrt{T}}$.

The magnitude of the granular temperature in equation (2.28c) depends on the ratio of generated temperature by shear work and its dissipation by inelastic particle collisions. Thus, the source and the sink term are essential for the granular temperature equation. The source is defined by the viscous heating term $\eta\boldsymbol{\kappa} : \boldsymbol{\kappa}$ which converts some of the kinetic energy of the bulk flow into kinetic energy of random particle motion. In (2.29), one can see that the viscous heating term states that any gradient in the granular velocity quadratically increases the granular temperature. If there are no forces acting on a moving granular system, it will rapidly come to rest due to the inelastic particle collisions. To model the constant loss of energy from the system, the sink εcT is necessary.

2.1.5 Boundary conditions for the granular flow equations

In this subsection, the mainly used boundary conditions for the granular model are sketched. The use of partial slip conditions, which are necessary for real applications, are explained in more detail. The given information and the notations used are mainly adopted from [65].

The boundary conditions for the granular volume fraction c at in- or outflow boundaries clearly depend on the application. However, for solid walls, a zero Neumann condition is used. An advective transport through the solid walls is omitted by the choice of the boundary conditions for the velocity field $\mathbf{u}$.

The same holds for the granular temperature T. Again, the advective flux is controlled by the velocity field. Hence, the boundary condition is almost always Neumann zero. This also ensures that there is no unwanted diffusive flux through the boundaries. It is important to note that temperature dissipates through the particle collisions with the solid walls, but this is already included in the terms of the granular temperature equation. If there are velocity differences between wall and granular material, shear forces increase the granular temperature which itself increases the dissipation factor ε.

Since there are Neumann zero conditions used for the granular volume fraction and also for the granular temperature, there are no pressure gradients at the solid walls. This is directly given due to the constitutive relation for the granular pressure (2.31). Nevertheless, strong pressure gradients can occur slightly inside the domain if the granular material compresses.

The boundary conditions for the granular velocity $\mathbf{u}$ are more particular. To handle the boundary conditions for the velocity, the velocity is split into a normal and a tangential component. The normal component usually is relevant for inflow boundaries, defined by a Dirichlet condition, and outflow boundaries, mostly the Neumann zero condition. For solid walls, a Dirichlet condition can be set at the tangential part to model friction between granular material and walls. A Dirichlet zero condition leads to the well-known no-slip condition which corresponds to infinite friction between granular material and walls. The other extreme is the slip condition which refers to walls that have no friction at all. For real applications both, slip and no-slip, are not useful as they are not physical. Therefore, a partial-slip condition is used which is defined as follows:

Let $0 \leq \varphi_{wall} \leq \frac{\pi}{2}$ be the wall friction angle, where $\varphi_{wall} = 0$ corresponds to the slip case and $\varphi_{wall} = \frac{\pi}{2}$ to the no-slip case. Based on the wall friction angle, a tangential boundary velocity $\mathbf{u}_B^t$ of the granular material is defined, which is used in the computations for the velocity diffusion term. According to a given wall point with tangential wall velocity $\mathbf{u}_W^t$, there is also an interior point with interior velocity $\mathbf{u}_I^t$. The infinitesimal distance between those two points is denoted by h. Assuming that the boundary velocity depends linearly on the wall velocity and the interior velocity, the partial-slip condition can be defined by

$$\mathbf{u}_B^t = \vartheta \mathbf{u}_I^t + (1 - \vartheta)\mathbf{u}_W^t \qquad \text{for some } \vartheta \in [0, 1]. \tag{2.34}$$

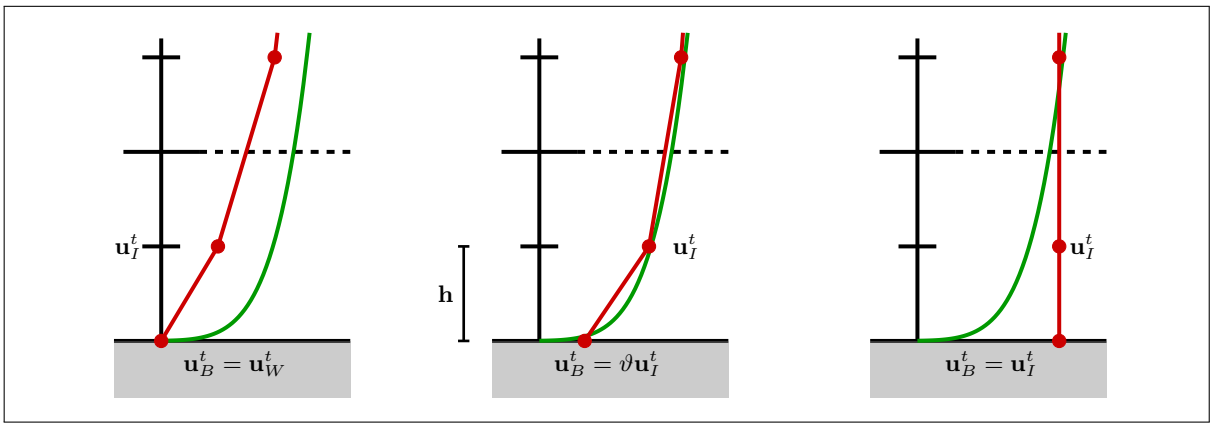

FIGURE 2.2: Sketch of the no-slip *(left)*, partial-slip *(middle)* and slip condition *(right)* to approximate the velocity profile of the granular material. The velocity profile is depicted in green and the different approximations for the velocity profile are depicted in red.

The slip and no-slip conditions are realised by

$$\mathbf{u}_B^t = \begin{cases} \mathbf{u}_I^t & \text{for } \vartheta = 1 \quad \textbf{(Slip)} \\ \mathbf{u}_W^t & \text{for } \vartheta = 0 \quad \textbf{(No-slip)}. \end{cases} \tag{2.35}$$

The boundary velocity cannot attain one fixed value. It depends on the relation of the normal wall stress

$$\mathcal{W}^n := n^T \cdot p\mathbf{I} \cdot n = p \tag{2.36}$$

and the tangential wall stress

$$(\mathcal{W}^t)_i := \eta \left| \frac{\partial u_i}{\partial n} \right| = \eta \frac{(u_I^t)_i - (u_W^t)_i}{h}. \tag{2.37}$$

From these stress terms, an expression for $\mathbf{u}_B^t$ can be found. In general it holds, if the tangential wall stress is locally less than the normal wall stress, i.e.,

$$(\mathcal{W}^t)_i \leq \mathcal{W}^n \tan(\varphi_{wall}), \tag{2.38}$$

the material still sticks to the wall and one has no-slip. For a tangential wall stress greater than the normal stress, the material slides. Fulfilling equation (2.38) with equality defines the point of transition.

One can define the modified tangential wall stress $\mathcal{W}_B^t$ on basis of the tangential boundary velocity by

$$(\mathcal{W}_B^t)_i := \eta \frac{(u_I^t)_i - (u_B^t)_i}{h}. \tag{2.39}$$

In the no-slip case, the boundary velocity needs to be chosen in such a way that condition (2.38) holds for $(\mathcal{W}_B^t)_i$ as long as it holds for $(\mathcal{W}^t)_i$. Furthermore, it should hold

$$(\mathcal{W}_B^t)_i = \mathcal{W}^n \tan(\varphi_{wall}) \tag{2.40}$$

for $(\mathcal{W}^t)_i > \mathcal{W}^n \tan(\varphi_{wall})$ to approximate the correct material wall friction that is defined by the value of φ_{wall}.
Exactly this can be fulfilled defining the tangential boundary velocity by

$$(u_B^t)_i \coloneqq (u_I^t)_i + \frac{h}{\eta} \min\{\mathcal{W}^n \tan(\varphi_{wall}), \mathcal{W}_i^t\} sgn((u_W^t)_i - (u_I^t)_i). \tag{2.41}$$

2.1.6 The connection between temperature and shear rate

Shear work, performed on the granular system, generates granular temperature. The shear work is a product of the shear stress and the strain rate, which is simply the velocity gradient of the granular velocity. In certain cases, it is helpful to introduce the shear rate

$$\dot{\gamma} \coloneqq \sqrt{\boldsymbol{\kappa} : \boldsymbol{\kappa}}. \tag{2.42}$$

With definition (2.42), the viscous heating term in the granular temperature equation (2.10) is simply given by $\frac{3}{2}\eta\dot{\gamma}^2$. The shear rate in the granular system can be approximated by the granular temperature. In a stationary uniform state, the equation for the granular temperature (2.10) can be written as

$$\frac{3}{2}\eta\dot{\gamma}^2 = \varepsilon c T. \tag{2.43}$$

The temperature equation is in the equilibrium between viscous heating and dissipation [87]. With the expressions (2.33a) and (2.33c), the shear rate is proportional to the square root of the granular temperature

$$\dot{\gamma} = \sqrt{\frac{2}{3}\frac{\varepsilon_0}{\eta_0} T}. \tag{2.44}$$

The expression (2.44) will be used for the derivation of the segregation equation in the upcoming subsection 2.2.2.

2.2 The segregation equation

In this section, the theory of mixtures is introduced. Afterwards, the segregation equation is modelled to extend the system of granular flow equations presented in the previous section. The framework of mixture theory serves as a tool for the derivation of the segregation equation. Especially, the direction of the segregation process is examined in some detail.

2.2.1 Mixture theory

Most commonly, mixture theory is used to model mixtures of different fluids, like oil and water. Each fluid defines one constituent or phase. In the case of dry granular materials, the phases are represented by the different particle types. Consider a mixture $\mathcal{M}$ of n different constituents $\mathcal{M}^\nu$. One assumes that concerning the motion of each constituent, the balance laws hold for each constituent $\mathcal{M}^\nu$ and the whole mixture $\mathcal{M}$. Further, one assumes that all constituents are simultaneously occupied at every point in the mixture. All quantities are expressed in terms of *partial* variables, defined per unit

mixture volume. Denoting the velocity of constituent $\mathcal{M}^\nu$ by $\mathbf{u}^\nu = (u_1^\nu, u_2^\nu, u_3^\nu)^T$ and the partial mass density by ρ^ν, the mass balance is given by

$$\partial_t \rho^\nu + \nabla \cdot (\rho^\nu \mathbf{u}^\nu) = m^\nu, \tag{2.45}$$

where m^ν defines the mass transfer between the constituents. This mass transfer can happen due to chemical reactions or especially in the framework of particles due to amalgamation and breakage. As the total mass of the mixture should be conserved, the mass balance for the whole mixture $\mathcal{M}$ is given by

$$\partial_t \rho + \nabla \cdot (\rho \mathbf{u}) = 0, \tag{2.46}$$

where ρ is the bulk density and $\mathbf{u} = (u_1, u_2, u_3)$ the bulk velocity of the whole mixture. Summing over all constituent equations,

$$\partial_t \sum_{\nu=1}^{n} \rho^\nu + \nabla \cdot \sum_{\nu=1}^{n} (\rho^\nu \mathbf{u}^\nu) = \sum_{\nu=1}^{n} m^\nu, \tag{2.47}$$

and comparing the sum to the whole mixture mass balance (2.46), one obtains relations between the constituent and the bulk variables. Hence, the bulk density and the bulk velocity are given by

$$\rho = \sum_{\nu=1}^{n} \rho^\nu \quad \text{and} \quad \rho \mathbf{u} = \sum_{\nu=1}^{n} (\rho^\nu \mathbf{u}^\nu). \tag{2.48}$$

Additionally, it holds

$$\sum_{\nu=1}^{n} m^\nu = 0, \tag{2.49}$$

which implies that the whole system neither loses nor gains mass. The momentum balance of the constituents and the whole mixture are given by

$$\partial_t (\rho^\nu \mathbf{u}^\nu) + \nabla \cdot (\rho^\nu \mathbf{u}^\nu \otimes \mathbf{u}^\nu) = \nabla \cdot \boldsymbol{\sigma}^\nu + \rho^\nu \mathbf{b}^\nu + \boldsymbol{\beta}^\nu, \tag{2.50}$$

$$\partial_t (\rho \mathbf{u}) + \nabla \cdot (\rho \mathbf{u} \otimes \mathbf{u}) = \nabla \cdot \boldsymbol{\sigma} + \rho \mathbf{b}, \tag{2.51}$$

where $\boldsymbol{\sigma}$, $\boldsymbol{\sigma}^\nu$ are the respective stress tensors, $\mathbf{b}$, $\mathbf{b}^\nu$ the body forces per unit mixture mass and $\boldsymbol{\beta}^\nu$ is the interaction force on phase ν by the other constituents. Summing over all constituent equations (2.50), and comparing the sum with the whole mixture momentum balance (2.51), gives the following relations for the body force, the stress tensor and the interaction forces:

$$\sum_{\nu=1}^{n} \rho^\nu \mathbf{b}^\nu = \rho \mathbf{b}, \tag{2.52}$$

$$\sum_{\nu=1}^{n} \boldsymbol{\sigma}^\nu = \boldsymbol{\sigma}, \tag{2.53}$$

$$\sum_{\nu=1}^{n} \boldsymbol{\beta}^\nu = 0, \tag{2.54}$$

where equation (2.54) ensures Newton's third law. An analogous procedure can be done for the energy balance and the entropy inequality. Depending on the constitutive relations one can gain a system of equations describing the behaviour of the mixture. An introduction to mixture theory can be found in Romano and Marasco [69]. More details of the general modelling approach can be found there.

2.2.2 Deriving the segregation equation

In this section, a model extension for the granular flow system from section 2.1 is derived. Therefore, it is assumed that the granular system consists of small and large particles. The extension describes the segregation process in such a bi-disperse system. The focus lies on avalanche-like flows of dry granular materials. In such a framework the segregation is a gravity-driven process that depends also on the shear rate [8]. Further, the effect of air on the granular material is negligibly small. Hence, the air phase just plays a passive role. It fills the void spaces but does not influence the granular material. Mind that with this restriction, it cannot generally be expected to obtain correct behaviour for frameworks like fluidised beds, where the process is driven by air. For the derivation process of the segregation equation, the framework of mixture theory is used.

Using the classic definitions of mixture theory, the whole mixture $\mathcal{M}$ consists of three constituents, the small particles $\mathcal{M}^s$, the large particles $\mathcal{M}^l$, and the air phase $\mathcal{M}^a$ which surrounds the granular material and fills the void spaces between the particles. The volume occupied by constituent ν is denoted by ϕ^ν and it holds

$$\phi^s + \phi^l + \phi^a = 1. \tag{2.55}$$

Consequently, the volume occupied by granular material is given by

$$\phi^s + \phi^l = c. \tag{2.56}$$

In literature, it is often assumed that in a granular avalanche the volume of air ϕ^a is constant. With the additional assumption of a passive air phase, it is argued that the air phase can be incorporated into the particle phases [37, 36, 34, 76, 81]. The mixture can be approximated by the particle phases which yields

$$\phi^s + \phi^l = 1. \tag{2.57}$$

Nevertheless, in this work, it is assumed that the volume fraction of the air phase can vary locally. This is consistent with the granular flow model which is compressible. For fulfilling (2.55), the air volume ϕ^a must change according to the granular volume c. Certainly, the volume fraction of a particle phase relative to the granular material can be defined analogously to ϕ^ν by

$$\hat{\phi}^\nu := \frac{\phi^\nu}{c}. \tag{2.58}$$

Throughout this thesis, $\hat{\phi}^\nu$ is simply called *relative* volume fraction of phase ν without further mentioning that it is relative to the granular volume. With definition (2.58), the saturation condition (2.56) rewrites

$$\hat{\phi}^s + \hat{\phi}^l = 1. \tag{2.59}$$

As previously mentioned, the quantities in mixture theory are expressed in terms of *partial* variables. These are linked to *intrinsic* variables, defining the quantity per unit volume of the pure phase. In general, the partial density ρ^ν of constituent ν is linked by a volume fraction scaling to the intrinsic density $\rho^{\nu*}$, whereas the partial and intrinsic velocities are the same,

$$\rho^\nu = \phi^\nu \rho^{\nu*}, \quad \mathbf{u}^\nu = \mathbf{u}^{\nu*}. \tag{2.60}$$

These are permissible relations as shown in the work of Morland [64]. Using this scaling, equations can easily be expressed by volume fractions instead of densities. Based on the assumptions of the mixture theory framework, a mass balance of type (2.45) and a momentum balance of type (2.50) for each phase is given. The exact form of the several terms in (2.45) and (2.50) depends on the following assumptions the model is restricted to:

1. The particles in the granular system do not amalgamate or break. Clearly, neither particles can become air nor vice versa. This implies that the mass transfer variable is equal to zero, $m^\nu = 0 \quad \forall \nu \in [s, l, a]$.

2. Just as stated for the granular flow model, the body force on each phase is solely the gravitational force, $\mathbf{b}^\nu = \mathbf{g} \quad \forall \nu \in [s, l, a]$.

3. The stress tensors for the particle phases in the segregation process are pressure dominated. They are approximated by lithostatic pressure fields, i.e. $\boldsymbol{\sigma}^\nu = -p^\nu \mathbf{I}$ [38].

4. The amount of stress in the mixture coming from air is negligibly small, i.e. $\boldsymbol{\sigma}^a = \mathbf{0}$.

5. There is no interaction force between the particle phases and the air phase, i.e. $\boldsymbol{\beta}^a = \mathbf{0}$.

With the assumptions made so far, the balance laws (2.45) and (2.50) for a particle phase ν are given by

$$\partial_t \rho^\nu + \nabla \cdot (\rho^\nu \mathbf{u}^\nu) = 0, \tag{2.61a}$$

$$\partial_t (\rho^\nu \mathbf{u}^\nu) + \nabla \cdot (\rho^\nu \mathbf{u}^\nu \otimes \mathbf{u}^\nu) = -\nabla p^\nu + \rho^\nu \mathbf{g} + \boldsymbol{\beta}^\nu. \tag{2.61b}$$

Especially, assumptions four and five state that one can focus on the particle phases and the combined granular system as mixture, as it is usually done in literature. With the fourth assumption, $\boldsymbol{\sigma}^a = \mathbf{0}$, the pressure of the whole mixture is equal to the granular pressure as equation (2.53) reduces to

$$p = p^s + p^l. \tag{2.62}$$

Furthermore, assumption five states that the relation of the interaction forces (2.54) reduces to

$$\boldsymbol{\beta}^s + \boldsymbol{\beta}^l = 0. \tag{2.63}$$

This means, there is no influence from air on the particle phases, besides its occupied volume. For this reason, the expression 'mixture' is used for the combination of the small and the large particle phase.

Starting from the balance law (2.61a) for one of the particle phases ν, one can derive an equation describing the change of this constituent. Introducing the relative velocity between phase ν and the bulk

$$\bar{\mathbf{u}}^\nu := \mathbf{u}^\nu - \mathbf{u}, \tag{2.64}$$

the mass balance can be rewritten in the form

$$\partial_t \rho^\nu + \nabla \cdot (\rho^\nu \mathbf{u}) = -\nabla \cdot (\rho^\nu \bar{\mathbf{u}}^\nu). \tag{2.65}$$

In this form, the left-hand side of equation (2.65) describes the transport of particle phase ν with the bulk velocity $\mathbf{u}$. The right-hand side represents the segregation. It is a motion relative to the bulk with velocity $\bar{\mathbf{u}}^\nu$. Segregation is a result of the interaction between the small and the large particles. This interaction is given in the momentum balance, especially due to the interaction force $\boldsymbol{\beta}^\nu$. Hence, an expression for the relative velocity can be obtained from the momentum balance (2.61b). With the assumption that the partial densities and momenta become quasi-steady even before the segregation starts [81], the momentum balance (2.61b) reduces to

$$0 = -\nabla p^\nu + \rho^\nu \mathbf{g} + \boldsymbol{\beta}^\nu. \tag{2.66}$$

Summing (2.66) over all constituents ν implies that the pressure field is lithostatic,

$$\nabla p = \rho \mathbf{g}, \tag{2.67}$$

as stated earlier. The key idea to derive an expression for the relative velocity is to introduce a pressure scaling that differs from the standard volume fraction scaling as it is used for the densities. The scaling, where the partial pressure depends linearly on the bulk pressure

$$p^\nu = f^\nu p \qquad \nu \in \{s, l\}, \tag{2.68}$$

was formulated by Gray and Thornton [37]. The idea arises from the assumption that small particles carry less of the overburden pressure than the large particles while they percolate to the ground of the mixture. The factor f^ν determines the proportion of the load carried by phase ν. Equation (2.68) automatically implies that

$$\sum_\nu f^\nu = 1. \tag{2.69}$$

Further, the proportionality factor f^ν must fulfil the condition if solely one of the phases is present, it has to carry all of the load,

$$f^\nu = 1 \quad \text{if} \quad \phi^\nu = 1 \quad \forall \nu. \tag{2.70}$$

Similar to [37] the expressions for each proportionality factor are chosen in such a way that they satisfy the conditions (2.69) and (2.70), i.e.,

$$f^l = \hat{\phi}^l + B\hat{\phi}^s\hat{\phi}^l, \tag{2.71a}$$

$$f^s = \hat{\phi}^s - B\hat{\phi}^s\hat{\phi}^l. \tag{2.71b}$$

The expressions in (2.71) are not unique. The chosen ones are the simplest but non-trivial expressions, where B is a non-dimensional magnitude. Gajjar and Gray [27] used different expressions in their work to model asymmetric flux functions.
Furthermore, an expression for the interaction force $\boldsymbol{\beta}^\nu$ is required. This expression is modelled by

$$\boldsymbol{\beta}^\nu = p\nabla f^\nu - \frac{\rho^\nu \mu}{\dot{\gamma}} \underbrace{(\mathbf{u}^\nu - \mathbf{u})}_{\bar{\mathbf{u}}^\nu} \qquad \nu \in \{s, l\}, \tag{2.72}$$

which satisfies the summation condition (2.63). The last term of expression (2.72) is a Darcy term, where μ is the coefficient of inter-particle drag. Its nature is poorly understood, thus it is basically chosen to be constant in literature. The Darcy term was already introduced by Morland [64] after observations that the segregation process of particles shows an analogy to the percolation of fluids through porous solids. The first term ensures that the percolation is driven by intrinsic than partial pressure gradients as in Darcy's law [37]. The segregation depends on the shear rate $\dot{\gamma}$. It is inversely proportional to the drag term as an increase in the shear rate decreases the friction between the particle layers. The first time, it appeared in a gravity-driven segregation model in the work of Marks et al. [59] but often, it is chosen to be constant in literature. It is allowed to vary in this work depending on the flow field. The expression for the interaction term (2.72) is the established form in the literature when dealing with gravity-driven segregation models [37, 27, 34, 79].

It is possible to extend the interaction term (2.72) on the right-hand side by

$$- \rho d \nabla \hat{\phi}^{\nu}, \tag{2.73}$$

such that it accounts for diffusive remixing. This extension of the interaction term was first given in 2006 by Gray and Chugunov [36]. It drives particles of phase ν from areas of high to areas of low concentration. The diffusion coefficient d determines the strength of the remixing force which generally is assumed to be constant. Note that the remixing term must depend on the relative volume fraction $\hat{\phi}^{\nu}$ instead of ϕ^{ν} like in the work of Gray and Chugunov [36], because the granular material is compressible. Otherwise a gradient would appear in a perfectly mixed granular system at every point where the ratio of granular material and air changes, i.e., $\nabla c \neq \mathbf{0}$. In this work, the remixing term is of low interest.

With the definition of the interaction term (2.72) and the pressure scaling (2.68), equation (2.66) is given by

$$0 = -f^{\nu} \nabla p + \rho^{\nu} \mathbf{g} - \frac{\rho^{\nu} \mu}{\dot{\gamma}} \bar{\mathbf{u}}^{\nu}. \tag{2.74}$$

In the most works (e.g. [8, 21, 24, 34, 36, 37, 53]) a segregation equation is derived for avalanches flowing down inclined planes with a constant angle. Further, it is assumed that the avalanche is incompressible with a constant height. In these gravity-driven shear flows, shear bands appear that are parallel to the inclined plane. In such a framework, the coordinate system can be rotated such that the avalanche flows in the positive x-direction and the segregation solely takes place in the z-direction. Especially, this means that the segregation direction will not change, neither over time nor locally in the spatial domain. To model the segregation process in such a case, one can focus solely on the z-direction as it has been done in the already mentioned literature.
In this work, the segregation equation should be coupled to the granular flow model where arbitrary flow directions are possible. Therefore, the modelling done here should be more general. Assume that the segregation direction at a point in space is given by the vector $\mathbf{d}_s$. This vector spans a one-dimensional subspace of $\mathbb{R}^d$, denoted by $\mathcal{D}$. To focus on this subspace one can define the projection $\mathbf{P} \colon \mathbb{R}^d \to \mathcal{D}$ by

$$\mathbf{P}\mathbf{x} \coloneqq < \mathbf{x}, \mathbf{d}_s > \mathbf{d}_s. \tag{2.75}$$

To be more precise, the direction of the segregation is perpendicular to the shear layer which depends on the velocity field.
Applying the projection on equation (2.74) gives

$$0 = -f^{\nu}\mathbf{P}\nabla p + \rho^{\nu}\mathbf{P}\mathbf{g} - \frac{\rho^{\nu}\mu}{\dot{\gamma}}\mathbf{P}\bar{\mathbf{u}}^{\nu}, \tag{2.76}$$

due to the linearity of $\mathbf{P}$. As the pressure field is lithostatic (2.67) and due to the volume fraction scaling of the densities each term in (2.76) is linear in ρ^*. Dividing by the intrinsic density leads to

$$\frac{\mu}{\dot{\gamma}}\phi^{\nu}\bar{\mathbf{u}}^{\nu} = (\phi^{\nu} - cf^{\nu})\mathbf{P}\mathbf{g}. \tag{2.77}$$

Note that the relative velocity $\bar{\mathbf{u}}^{\nu}$ is the segregation velocity. It lies in the image of the projection function $\mathbf{P}$ and therefore per definition it holds

$$\mathbf{P}\bar{\mathbf{u}}^{\nu} = \bar{\mathbf{u}}^{\nu}. \tag{2.78}$$

Finally, using the expressions for the load functions (2.71) the relative velocities for the small and large particle phases are given by

$$\bar{\mathbf{u}}^{s} = \left(\frac{B\dot{\gamma}}{\mu c}\mathbf{P}\mathbf{g}\right)\phi^{l}, \tag{2.79a}$$

$$\bar{\mathbf{u}}^{l} = -\left(\frac{B\dot{\gamma}}{\mu c}\mathbf{P}\mathbf{g}\right)\phi^{s}. \tag{2.79b}$$

With the expressions for the relative velocities (2.79), the balance law (2.65) modifies to

$$\partial_t\phi^{s} + \nabla\cdot(\phi^{s}\mathbf{u}) = \nabla\cdot\left(\mathbf{S}^{sl}\phi^{s}\frac{\phi^{l}}{c}\right), \tag{2.80a}$$

$$\partial_t\phi^{l} + \nabla\cdot(\phi^{l}\mathbf{u}) = \nabla\cdot\left(\mathbf{S}^{ls}\phi^{l}\frac{\phi^{s}}{c}\right), \tag{2.80b}$$

respectively. The segregation velocity is defined by

$$\mathbf{S}^{sl} \coloneqq -\frac{B\dot{\gamma}}{\mu}\mathbf{P}\mathbf{g}, \tag{2.81}$$

and it holds $\mathbf{S}^{ls} = -\mathbf{S}^{sl}$.
As previously mentioned, the shear rate is assumed to be non-constant in this work. It should depend on the state of the granular flow model. This can be done using the granular temperature. In section 2.1.6 the relation between the shear rate $\dot{\gamma}$ and the granular temperature T has been shown. With the derived expression (2.44) the segregation velocity can be rewritten as

$$\mathbf{S}^{sl} \;=\; -\underbrace{\frac{B}{\mu}\sqrt{\frac{2}{3}\frac{\varepsilon_0}{\eta_0}}}_{S_0^{sl}}\sqrt{T}\mathbf{P}\mathbf{g} \;=\; -S_0^{sl}\sqrt{T}\mathbf{P}\mathbf{g}, \tag{2.82}$$

where the segregation rate S_0^{sl} is constant. In general, the segregation rate depends on the properties of the respective granular material. Therefore, the segregation rate needs to

be fitted to the real granular system. Furthermore, S_0^{sl} is expected to be positive. In the upcoming chapter, simplified versions of the segregation equation are analysed. In these cases, there is no need to distinguish between segregation rate and segregation velocity. To gain a positive segregation velocity from a positive segregation rate, the negative sign convention in the definition of the segregation velocity (2.81) has been chosen.
To compute the behaviour of a granular system of small and large particles, it is not necessary to solve the respective balance law for both particle phases. Since the granular volume fraction c is known from the granular flow equations, it is enough to solve only one phase balance. In this work, the small particle phase is chosen. With the help of the saturation condition (2.56) the volume fraction of the large particle phase can be eliminated from the balance law, i.e.,

$$\partial_t \phi^s + \nabla \cdot (\phi^s \mathbf{u}) = \nabla \cdot \left(\mathbf{S}^{sl} \phi^s \frac{(c - \phi^s)}{c} \right). \tag{2.83}$$

The structure of the derived segregation equation (2.83) is similar to the presented models in section 1.2. The main differences are the non-constant granular volume fraction c and the dependence on the granular temperature T, which is non-constant as well. Not least, this will change the way the equation has to be handled numerically as it will be shown in the upcoming chapters. If one assumes constant granular temperature and constant granular volume fraction in the granular system the model reduces to the original model of Gray and Thornton [37].

Due to the restriction to the small particle phase, the superscript s is dropped for the upcoming chapters to simplify the notation. The superscripts are only used in specific sections where it helps to avoid confusion. From now on, the segregation equation for the bi-disperse particle system is given by

The segregation equation

$$\partial_t \phi + \nabla \cdot (\phi \mathbf{u}) = \nabla \cdot \left(\mathbf{S}^{sl} \phi \frac{(c - \phi)}{c} \right), \tag{2.84}$$

with

$$\mathbf{S}^{sl} = -\mathbf{S}_0^{sl} \sqrt{T} \mathbf{P} \mathbf{g}. \tag{2.85}$$

2.2.3 The segregation direction

For the modelling of the segregation equation, it has been assumed that a vector $\mathbf{d}_s$ is given that spans a subspace of $\mathbb{R}^d$ in which the segregation takes place. To solve the segregation equation such a vector needs to be found. It is well known that for gravity-driven shear flows, the segregation happens in the direction perpendicular to the local shear layer [8, 37, 54]. The shear depends on the velocity field of the granular system $\mathbf{u}$ or more precisely on the gradient of the velocity $\nabla \mathbf{u}$, such that $\mathbf{d}_s = \mathbf{d}_s(\nabla \mathbf{u})$. The question is: How to find the segregation direction?

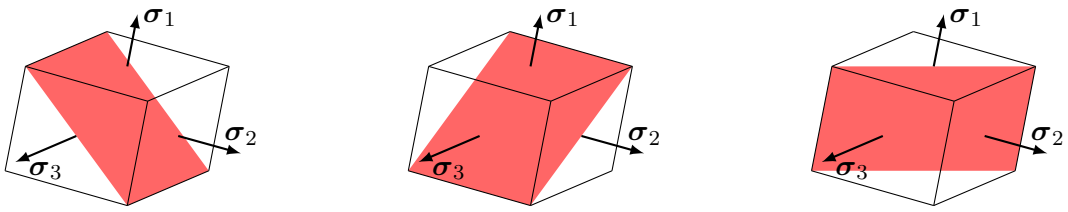

FIGURE 2.3: Orientation of the sectional planes of the principal shear stresses τ_{12} *(left)*, τ_{23} *(middle)*, and τ_{13} *(right)*. The normal vector to the sectional plane of the shear stress τ_{ij} is the angle bisector of the eigenvectors $\boldsymbol{\sigma}_i$ and $\boldsymbol{\sigma}_j$.

To solve this problem a concept from the field of mechanics is adapted. Assume a mechanical body under some stress. The Cauchy stress tensor $\boldsymbol{\sigma}$ describes the stress state of this mechanical body. From this stress tensor, it is possible to compute the shear stress acting in a sectional plane of the body. Therefore, an eigenvalue-eigenvector problem needs to be solved. In the following, the procedure is presented for $d = 3$. The 2d case is an even simpler analogue. Details of the presented concept can be found, for example, in the work of Wu [86].
Assume that the stress tensor $\boldsymbol{\sigma}$ is a symmetric 3×3 matrix. Then, the principal stresses are the real eigenvalues

$$\bar{\sigma}_1 \geq \bar{\sigma}_2 \geq \bar{\sigma}_3. \tag{2.86}$$

The corresponding normalised eigenvectors, given by $\boldsymbol{\sigma}_1$, $\boldsymbol{\sigma}_2$, and $\boldsymbol{\sigma}_3$, are mutually orthogonal. From the eigenvalues of the stress tensor, the principal shear stresses τ_{12}, τ_{23}, and τ_{13} are given by

$$\tau_{12} = \frac{|\bar{\sigma}_1 - \bar{\sigma}_2|}{2}, \qquad \tau_{23} = \frac{|\bar{\sigma}_2 - \bar{\sigma}_3|}{2}, \qquad \tau_{13} = \frac{|\bar{\sigma}_1 - \bar{\sigma}_3|}{2}. \tag{2.87}$$

These principal shear stresses act in sectional planes, where the normal vector to the plane of the shear stress τ_{ij} is the angle bisector of the eigenvectors $\boldsymbol{\sigma}_i$ and $\boldsymbol{\sigma}_j$. The orientation of the sectional planes are depicted in Figure 2.3. Under assumption (2.86) the maximal shear stress $\tau_{max} = \tau_{13}$ acts in the sectional plane depicted right in Figure 2.3.
The same procedure can be done with Cauchy's strain tensor which is given by the gradient of deformation. The principal strains can be computed and from this, the principal shear strains to find the planes where material failure happens. If the planes of the principal shear stress and the principal shear strain coincide, depends on the stress-strain relation.

Adapting this procedure to the framework of granular flows, the segregation direction can be computed by using the symmetric versions of the stress and the strain as given in (2.5) and (2.6). From the stress-strain relation, it can be deduced that the eigenvectors of stress and strain are equal. The corresponding eigenvalues might be different but have the same order in size. Hence, the planes of principal shear stress and principal shear strain coincide. As solely the orientation of the shear planes is of interest, it is enough to look at the symmetrised velocity gradient of the bulk flow which appears in the strain tensor (2.6) and is given by

$$\tilde{\boldsymbol{\kappa}} := \nabla \mathbf{u} + (\nabla \mathbf{u})^T.$$

The orientation of the principal shear planes is known from the computed eigenvectors $\tilde{\boldsymbol{\kappa}}_i$ of $\tilde{\boldsymbol{\kappa}}$. Searching the maximal shear stress τ_{max} by comparing combinations of the eigenvalues $\bar{\kappa}_i$, as formulated in (2.87), yields the respective shear plane. As the segregation direction is perpendicular to the shear layer, it is assumed that the normal vector to the shear plane, belonging to the largest principal shear, spans the space where the segregation happens. This vector is defined to be $\mathbf{d}_s$.

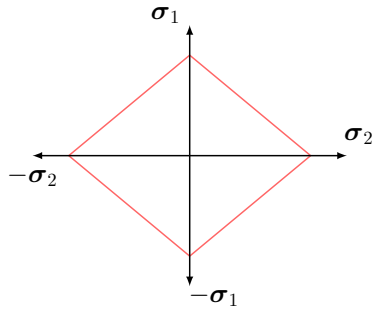

FIGURE 2.4: For solid mechanical bodies, the principal stress forces acting in the depicted planes are equal.

Unfortunately, normalised eigenvectors are not unique with respect to the algebraic sign. Hence, the planes depicted in Figure 2.3 are not unique. For mechanical bodies, the forces acting in the defined planes between, for example, all combinations of $\pm\boldsymbol{\sigma}_1$ and $\pm\boldsymbol{\sigma}_2$ are equal (see Figure 2.4). This is not the case for the granular system as it is not one solid body. Hence, it is assumed that the shear plane is the one which is mostly parallel to the velocity field. Summarising, Algorithm 2.1 states the procedure to compute the segregation direction.

Algorithm 2.1

1. *Compute the largest eigenvalue* $\bar{\kappa}_{max}$ *and the smallest eigenvalue* $\bar{\kappa}_{min}$ *of* $\tilde{\boldsymbol{\kappa}} = (\nabla\mathbf{u} + (\nabla\mathbf{u})^T)$.
2. *Compute the corresponding eigenvectors* $\tilde{\boldsymbol{\kappa}}_{max}$ *and* $\tilde{\boldsymbol{\kappa}}_{min}$.
3. *Define* $\mathbf{d}_s = \tilde{\boldsymbol{\kappa}}_{max} \pm \tilde{\boldsymbol{\kappa}}_{min}$ *depending which is mostly orthogonal to* $\mathbf{u}$.

Results of the presented computation scheme are illustrated in the simulation chapter in section 5.1. Several plots of different applications and flow fields are shown, depicting the computed segregation direction for each finite volume.

2.3 Maximum volume fraction

This section focuses on the maximum volume fraction for particle systems. The packing of particle systems is analysed and the so-called random close packing and the random loose packing are introduced. As already mentioned in section 1.1, the granular volume fraction c in the granular model is bounded by the value $c_{max} \leq 1$ which gives the maximum space the granular material can occupy. For the most particle systems, the value of c_{max} is really less than one. A value of one can, for example, only be reached

for ordered cubic particles but even cubes will not reach this value when they are placed randomly in a given volume. Therefore, for real applications, the correct value for the stated maximum volume fraction is exactly the mentioned random close packing as one will see in this section.

2.3.1 Packing of particles

The dense packing of particles, or objects in general, is a relevant topic for several hundreds of years. A system of spherical particles is not able to fill the whole allocated space of a given volume. There are always void spaces left due to the particles' structure. Already 1611, Johannes Kepler claimed that the maximum volume fraction of spherical objects of the same size is $\frac{\pi}{3\sqrt{3}} \approx 0.7405$. For such a system of equal spheres Carl Friedrich Gauß proofed in 1831 that this is the best value that can be reached for any regular lattice (see Figure 2.5). It is also independent of the spheres' radius.
The $2d$ equivalent for discs with equal size reaches a maximal value of $\frac{\pi}{2\sqrt{3}} \approx 0.9069$. Joseph Louis Lagrange proved this in 1773 for the regular case (see Figure 2.5). Many

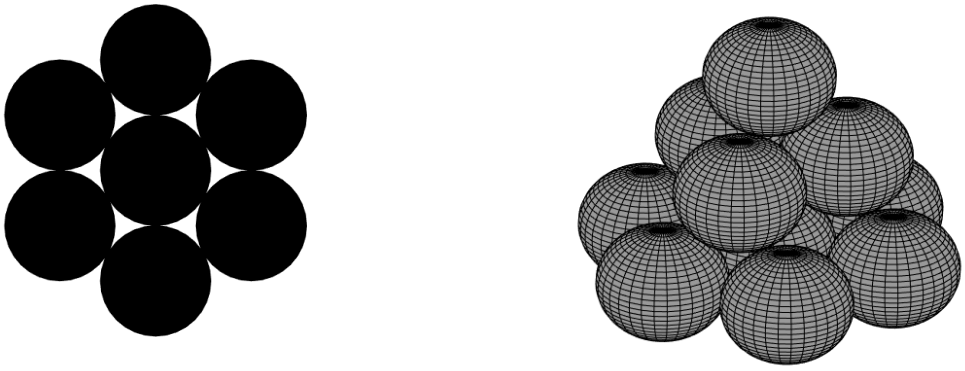

FIGURE 2.5: Sketch of the optimal packing of equal discs in $2d$ *(left)* and an optimal packing of spheres in $3d$ *(right)*. Approximately, the occupied volume for discs reaches a value of 90 %, whereas spheres reach a value of 74 %.

years later, general proofs were given by Hales et al. for the $3d$ case and by Tóth for the $2d$ variant [65].
In nature or industrial processes, the above-given value can never be achieved. Today, it is experimentally proven that any mono-disperse granular system of randomly distributed spherical particles can reach a packing value of approximately 64 %. This state is called random close packing (RCP). In general, additional forces like pressure or vibration are necessary to reach this value, due to the inter particle friction. Mechanically, a system becomes stable already for lower volume fractions. This loosest stable packing is called random loose packing (RLP). In the case of ideal, spherical, frictionless particles the RLP coincides with the onset of the RCP [52]. The packing fractions for the RCP and RLP are denoted by ϕ_{rcp} and ϕ_{rlp}, respectively. Note that both, the RCP and the RLP, depend on the shape of the particles but as long the system is mono-disperse, they have a constant value.
The random close packing of bi-disperse granular mixtures differs from a mono-disperse one. In a system of small and large particles, the smaller particles can fill the void spaces

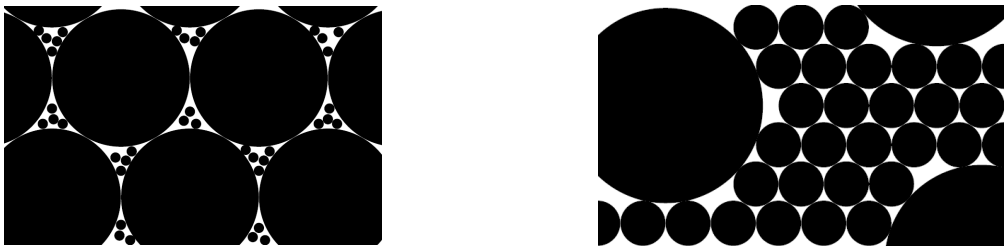

FIGURE 2.6: Sketch of dense packed large particles and loosely packed small particles *(left)* and vice versa *(right)*.

between the larger particles. As a consequence, a bi-disperse system can be packed denser than a mono-disperse system.

2.3.2 Random close packing for binary mixtures

The maximum packing value c_{rcp} of a bi-disperse particle system depends on both the radius ratio $R = \frac{r^s}{r^l}$ and the proportion of small and large particles. Furthermore, the packing of such a binary mixture cannot be given in general, but it is possible to give an analytic expression for an upper bound.

Binary mixture for size ratios approaching zero ($\mathbf{R \to 0}$)

The maximum value for the upper bound can be expressed by the volume fraction of a phase ν relative to the granular material c denoted by $\hat{\phi}^\nu$. To find the upper bound, one assumes that the particle types are that much different in size that each sub-system does not "influence" the packing of the other one. Then, there are two cases to look at.

First, one assumes that the large particles are jammed with $\phi^l = \phi_{rcp}$ and the small particles are packed in between (see Figure 2.6, left). Then, it holds

$$c = \phi^s + \phi_{rcp}. \tag{2.88}$$

This can be rewritten in terms of the particles' relative volume fraction (2.58)

$$c = c\hat{\phi}^s + \phi_{rcp} \tag{2.89}$$

$$\Leftrightarrow c = \frac{\phi_{rcp}}{1 - \hat{\phi}^s}. \tag{2.90}$$

In the second case, one assumes that the small particles are packed densely, i.e., $\phi^s = \phi_{rcp}$ and the large particles are packed loosely (see Figure 2.6, right). Then,

$$c = \phi^l + (1 - \phi^l)\phi_{rcp}. \tag{2.91}$$

Again with (2.58), one gains

$$c = c\hat{\phi}^l + (1 - c\hat{\phi}^l)\phi_{rcp} \tag{2.92}$$

$$\Leftrightarrow c = \frac{\phi_{rcp}}{(1 - \hat{\phi}^l(1 - \phi_{rcp})}. \tag{2.93}$$

With the saturation condition for the relative volume fractions

$$\hat{\phi}^s + \hat{\phi}^l = 1 \tag{2.94}$$

equation (2.93) can be written in terms of $\hat{\phi}^s$ instead of $\hat{\phi}^l$. Hence, the maximum packing for the bi-disperse system is given by

$$c_{rcp} = \min\left(\frac{\phi_{rcp}}{1-\hat{\phi}^s}, \frac{\phi_{rcp}}{(\hat{\phi}^s + (1-\hat{\phi}^s)\phi_{rcp}}\right). \tag{2.95}$$

In principle, the derived expression (2.95) suits for particles of arbitrary shape or surface roughness as long as one component of the mixture is much larger than the other one. It is quite intuitive that the argument of smaller particles packing in the void spaces of the larger particles, which increases the granular volume fraction, is not only applicable for closest packings but is also valid for looser ones. As already mentioned, particle shape and friction are responsible for the fact that granular materials reach a stable state already for $c_{rlp} \leq c_{rcp}$. Therefore, it is assumed that the random loose packing for bi-disperse systems fulfils an expression similar to (2.95) given by

$$c_{rlp} = \min\left(\frac{\phi_{rlp}}{1-\hat{\phi}^s}, \frac{\phi_{rlp}}{(\hat{\phi}^s + (1-\hat{\phi}^s)\phi_{rlp}}\right). \tag{2.96}$$

In their paper, Kyrylyuk et al. [52] derive the same expressions for the upper bound of the random close packing but with respect to the relative volume fraction of the large particle phase $\hat{\phi}^l$. Figure 2.7 shows the random close packing values for mixtures of spherical particles, where $\phi_{rcp} \approx 0.633$.

Random close packing for $\mathbf{R} \in (\mathbf{0}, \mathbf{1})$

For real applications it would be desirable to have an expression like (2.95) for an arbitrary mixture with radius ratio $R = \frac{r_s}{r_l}$. Unfortunately, "progress in this direction has not been rapid"[1]. There are simulation tools to compute the packing of bi-disperse particle mixtures.
Kyrylyuk et al. [52] used a mechanical contraction model (MCM) [85] to compute the maximum packing of binary mixtures of small and large particles. Their computations fit very well to experimental measurements.
Farr and Groot [25] constructed a greedy-algorithm that yields an accurate approximation for the random close packing density of hard spheres of any size distribution which is based upon a mapping onto a one-dimensional problem. Additionally, their model correctly reproduces the exact solution for particles with infinite size difference (2.95).
Besides the analytical packing expression derived above for systems differing that much in size that each sub-system does not influence the other one, Figure 2.7 shows results of the MCM simulations performed by Kyrylyuk et al. [52]. The random close packing for different mixtures of systems with particle size ratios $R = \frac{1}{2}$, $R = \frac{1}{3}$, $R = \frac{1}{5}$, and $R = \frac{1}{10}$ are depicted.

[1] Farr and Groot [25] $p.1f$

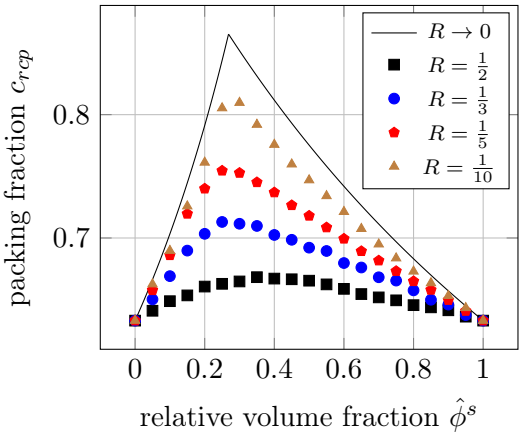

FIGURE 2.7: Plot of the random close packing for bi-disperse spherical particle mixtures. The *black line* shows the analytical solution for $R \to 0$. The values for the packings from $R = \frac{1}{2}$ to $R = \frac{1}{10}$ are results of the MCM simulations performed by Kyrylyuk et al. [52]. The random close packing for solely one of the two particle phases is 0.633.

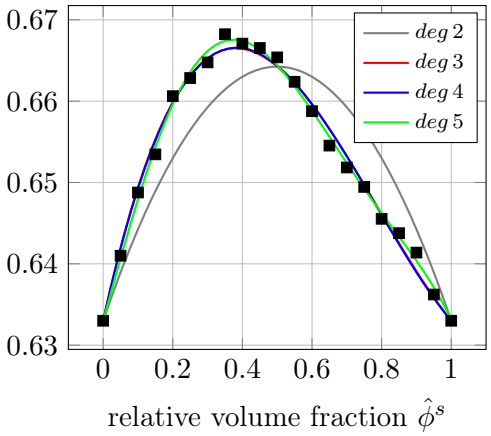

FIGURE 2.8: The black squares show the MCM computed random close packing data for $R = \frac{1}{2}$ performed by Kyrylyuk et al. [52]. The coloured lines show polynomial least square fits of degrees 2 - 5 for the depicted packing data. For the fitting the result is forced to exactly pass through the boundary points such that the packing value for a single phase is exact.

It is not the aim of this work to compute a perfect packing density for granular mixtures. For the purpose of this work, it is enough to have acceptable values for c_{rcp} and it is preferable to have an analytic expression that can be used in the computations. As already mentioned, there exists no analytical expression for computing the random close packing value from the particle size ratio R and the volume fraction $\hat{\phi}^s$, until today. This work restricts to a particle system with small and large particles of size ratio $R = \frac{1}{2}$. Therefore, a simple polynomial data fit is used to compute the random close packing c_{rcp}. The least square fit is forced to pass exactly through the packing values for solely small and solely large particles, respectively. This guarantees an exact packing value in mono-disperse regions. Figure 2.8 shows the polynomial fits of degrees 2-5. One can see that the polynomials of degree 3 and degree 4 are mainly identical. The fit of choice is the degree 5 polynomial, as it approximates the maximum best. Hence, the random close packing value can be written as

$$c_{rcp}(\hat{\phi}^s) = p(\hat{\phi}^s, \phi_{rcp}), \tag{2.97}$$

where $p(\psi, \zeta)$ is a polynomial of degree 5 which exactly passes through $(0, \zeta)$ and $(1, \zeta)$. It is given by

$$p(\psi, \zeta) = -0.4903\psi^5 + 1.2388\psi^4 - 0.9450\psi^3 + 0.0434\psi^2 + 0.1531\psi + \zeta. \tag{2.98}$$

Due to the structure of the chosen expression the value for the random loose packing can be written in a similar way,

$$c_{rlp}(\hat{\phi}^s) = p(\hat{\phi}^s, \phi_{rlp}). \tag{2.99}$$

2.4 Modification of the granular flow model

The granular flow model has been explained in detail in section 2.1. Now, the interplay between granular flow model and the derived segregation equation is stated. In a second step, some modifications for the granular flow model are presented. The modifications account for the changing particle distribution in the granular system due to segregation. As explained in section 2.2, the behaviour of a bi-disperse granular system can be described by equations for the granular mixture and an equation for only one of the particle phases. Information for the other particle phase can be gained directly from the saturation condition (2.56). In the simplest model extension, one solves the granular flow equations for $c, \mathbf{u}$, and T and uses the gained information to solve the segregation equation. With the velocity field $\mathbf{u}$, the transport of the small particle phase with the granular bulk can be computed. With the volume fraction c and the granular temperature T, the segregation process is controlled. In this case, the granular flow and the segregation model are only coupled one way as solely information from the granular flow equations are used for the computation of the segregation process but not vice versa. The segregation process does not influence the state of the granular mixture. This one-way coupled model is an adequate approximation to simulate the effect of segregation in a process of flowing granular material as it will be shown in chapter 5.

In the last section, it has been shown that the maximum packing value for an arbitrary granular system is the random close packing. This value is not constant any more for a bi-disperse system of small and large particles. Differently mixed regions in the granular system have different packing values. In the above described one-way coupling the differently packed regions in a granular system, which appear due to segregation, cannot be captured. Therefore, the information of the local particle distribution must be included in the granular flow model. This can be done by exchanging the constant value c_{max} by the function $c_{rcp}(\hat{\phi})$, which depends on the state of segregation.
Furthermore, the transition volume c_0 is important in the granular flow model. Normally, it is approximately given by the random loose packing of the granular system. In the previous section 2.3, it has been argued that the random loose packing cannot be a constant for bi-disperse mixtures as well. Therefore, the constant value c_0 is exchanged by the function $c_{rlp}(\hat{\phi})$.
Following, the compressibility factor $g(c)$ is now given by

$$g(c, c_{rcp}) = \left(1 - \frac{c}{c_{rcp}(\hat{\phi})}\right)^{-1}. \tag{2.100}$$

This modification appears in the pressure definitions and the varying random loose packing has influence on the activation of the yield model due to the yield pressure

$$p_k = cTg(c, c_{rcp}), \tag{2.101}$$
$$p_y = \Theta(c - c_{rlp})T_0(c - c_{rlp})g(c, c_{rcp}). \tag{2.102}$$

The variation of the random close packing also changes the behaviour of the flow parameters, since

$$\eta_k = \eta_0 \sqrt{T} c g(c, c_{rcp}), \tag{2.103}$$

$$\lambda_k = \lambda_0 \sqrt{T} c g(c, c_{rcp}), \tag{2.104}$$

$$\varepsilon_k = \varepsilon_0 \sqrt{T} g(c, c_{rcp}). \tag{2.105}$$

This is a permissible modification that does not change the interplay of the different parameters and the stability of the granular flow model. As mentioned in section 2.1, the granular flow parameters need to diverge in the same way for $c \to c_{rcp}$. Due to the modification in the compressibility factor, this is still valid. In the original model,

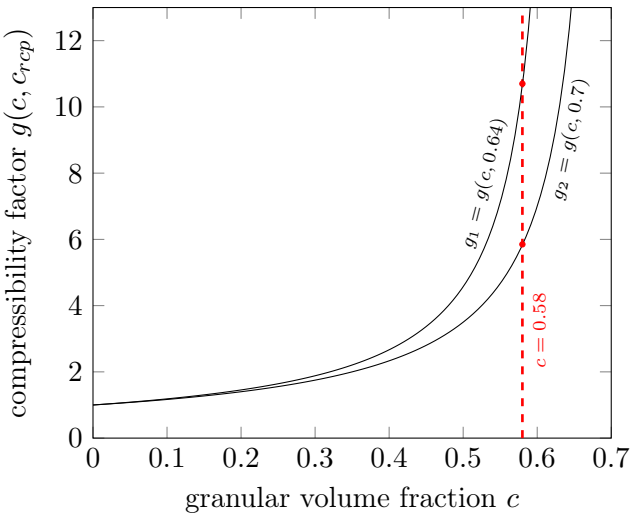

FIGURE 2.9: Comparison of the compressibility factor for $c_{rcp} = 0.64$ and $c_{rcp} = 0.7$. Even for the same value of c the difference in the compressibility factors g_1 and g_2 increases for increasing granular volume fractions.

the compressibility factor is already quite sensitive since it diverges for c approaching the random close packing. In the model using the back-coupling via the random close packing, the compressibility factor depends also on c_{rcp}. Hence, the value of $g(c, c_{rcp})$ can vary strongly even for the same value of c. Figure 2.9 shows the compressibility factor for two different values of c_{rcp}.

The computation procedure for the final model is done in an explicit way. First, the granular flow equations are solved to gain the granular velocity $\mathbf{u}$ and the scalar fields for granular volume fraction c and granular temperature T. With these data the segregation equation is solved, where $\mathbf{u}$ is needed for the transport with the granular bulk and c and T for the segregation strength. With the computed ϕ-field giving the volume fraction of the small particle phase, the local values for the random close packing $c_{rcp}(\hat{\phi})$ and the random loose packing $c_{rlp}(\hat{\phi})$ can be updated. Now this process can be repeated for each time step starting again with solving the granular flow system including the updated values for $c_{rcp}(\hat{\phi})$ and $c_{rlp}(\hat{\phi})$.

2.5 Summary of the final model

This chapter summarises all equations derived in the previous sections to give an overview of the final model. Again, the several terms are briefly explained.
The final model describes the behaviour of a granular mixture of small and large particles including the effect of segregation. It is a hybrid model to capture fast flowing regimes as well as arresting systems but does not include amalgamation or breakage of particles. The model equations are the scalar continuity equation (2.106a) for the granular mixture, the vectorial momentum balance (2.106b), the granular temperature equation (2.106c), and the segregation equation (2.106d) for the small particle phase.

The final model

$$\partial_t c + \nabla \cdot (c\mathbf{u}) = 0, \tag{2.106a}$$
$$\partial_t (c\mathbf{u}) + \nabla \cdot (c\mathbf{u} \otimes \mathbf{u}) = \nabla \cdot \boldsymbol{\sigma} - \nabla p + c\mathbf{g}, \tag{2.106b}$$
$$\partial_t (cT) + \nabla \cdot (cT\mathbf{u}) = \frac{3}{2}(\eta \boldsymbol{\kappa} : \boldsymbol{\kappa} - \nabla \cdot \mathbf{q}) - \varepsilon c T, \tag{2.106c}$$
$$\partial_t \phi + \nabla \cdot (\phi \mathbf{u}) = \nabla \cdot \left(\mathbf{S}^{sl} \phi \frac{(c - \phi)}{c} \right). \tag{2.106d}$$

In the four equations (2.106), the following relations hold:

The closure relations

$$\boldsymbol{\sigma} = \eta \boldsymbol{\kappa}, \tag{2.107}$$
$$\boldsymbol{\kappa} = \nabla \mathbf{u}, \tag{2.108}$$
$$\mathbf{q} = -\lambda \nabla T, \tag{2.109}$$
$$\mathbf{S}^{sl} = -\mathbf{S}_0^{sl} \sqrt{T} \mathbf{P} \mathbf{g}, \tag{2.110}$$

$$p = p_k + p_y, \tag{2.111a}$$
$$p_k = cTg(c, c_{rcp}), \tag{2.111b}$$
$$p_y = \Theta(c - c_{rlp}) T_0 (c - c_{rlp}) g(c, c_{rcp}), \tag{2.111c}$$

$$g(c, c_{rcp}) = \left(1 - \frac{c}{c_{rcp}} \right)^{-1}, \tag{2.112}$$

▶

The closure relations (cont)

$$\eta = \eta_k(1 + \frac{p_y}{p_k}), \qquad \eta_k = \eta_0\sqrt{T}cg(c, c_{rcp}), \tag{2.113a}$$

$$\lambda = \lambda_k(1 + \frac{p_y}{p_k}), \qquad \lambda_k = \lambda_0\sqrt{T}cg(c, c_{rcp}), \tag{2.113b}$$

$$\varepsilon = \varepsilon_k(1 + \frac{p_y}{p_k}), \qquad \varepsilon_k = \varepsilon_0\sqrt{T}g(c, c_{rcp}). \tag{2.113c}$$

The continuity equation models the advective transport of the granular mixture expressed by the granular volume fraction c. As our model is compressible, the volume fraction can vary, i.e., $c \in [0, c_{rcp}]$. In contrast to the original model, the upper bound c_{rcp} is not constant. It depends on the distribution of small and large particles. Therefore, it is a function of the small particles' relative volume fraction $\hat{\phi}$.
Similar to the continuity equation, the other equations also have an advective term,

$$\nabla \cdot (c\mathbf{u} \otimes \mathbf{u}),$$
$$\nabla \cdot (cT\mathbf{u}),$$
$$\nabla \cdot (\phi\mathbf{u}),$$

which transports the respective quantity with the velocity computed from the momentum balance. Additionally, the momentum balance has a diffusive transport $\nabla \cdot \boldsymbol{\sigma}$ which diffuses energy in form of velocity. The pressure gradient ∇p generates a velocity from regions of high to lower pressure to prevent the system from collapsing. A source term is given by the gravity term.
The granular temperature equation diffuses also energy in form of granular temperature, $\nabla \cdot \mathbf{q}$. The viscous heating term $\eta\boldsymbol{\kappa} : \boldsymbol{\kappa}$ generates granular temperature. It transforms shear work to microscopic random particle motion. Due to inelastic particle collisions, the granular temperature dissipates into internal energy given by the sink term εcT.
In contrast to the granular flow equations, the segregation equation has a second transport term $\nabla \cdot \left(\mathbf{S}^{sl}\phi\frac{(c-\phi)}{c}\right)$ which accounts for the segregation. This transport term depends on the distribution of the particles. The segregation stops if solely one particle phase is present. Additionally, it depends on the granular temperature (2.110) which guarantees that the segregation stops in a static system or in shear free regions. The transport happens in a direction perpendicular to the shear layers.
The constitutive relations for the pressure (2.111) close the granular system. They stabilise the system for $c \to c_{rcp}$, modelled using the compressibility factor (2.112) which, in the final set of equations, depends additionally on a non-constant value for the random close packing c_{rcp}. It also influences the granular parameters (2.113). Due to those, the most terms in the granular flow equations also behave differently depending on whether the system is in the kinetic or the yield regime.
To simulate the granular flow behaviour and the segregation effect in a natural or industrial process, several granular properties are required. Despite that there are some relations like (2.22) and (2.23), in general these properties cannot be gained from the particle properties. Therefore, experiments or simulations with the DEM are necessary

to calibrate the model. Besides the random close packing for the granular particles and the transition volume, all parameters subscribed by 0 are material dependent constants that need to be validated. This holds not only for flow parameters like η_0, λ_0, and ε_0 but also for the segregation rate S_0^{sl} in the segregation equation.

In general, it is known that the segregation rate depends on the size ratio R and also on the density ratio of the particles [51], where further effects come into play like the reverse Brazil nut problem [43]. Hence, models of combined size and density segregation are already topic of current research [35, 79]. Since there is no widely excepted expression for the segregation rate which explicitly depends on the size and the density ratio, in this work a constant value is used which needs to be fitted to the granular system. Throughout this work a size ratio of $R = \frac{1}{2}$ is assumed.

Chapter 3

Analysis

In this chapter, the focus lies on the analysis of the segregation equation. First, an extract of the theory of conservation laws is given to provide basic knowledge and to introduce several definitions in the scalar and the system case. Later on, analytic solutions for simplified versions of the segregation equation are derived and presented. For the simpler forms of the segregation equation, analytic solutions were already presented in several other works. Their results are also sketched. If the granular volume fraction c is not assumed to be constant, one is confronted with spatially varying flux functions. This topic is treated in a later part of this chapter. Proceeding from the results given in the upcoming sections, numerical methods for solving the segregation equation are derived in chapter 4.

3.1 Theory of hyperbolic conservation laws

To clarify the terminology for the upcoming sections, some general information about conservation laws are given starting with the scalar case. All definitions and results presented in this section can be found in the works of LeVeque [57] and Toro [77].

For completeness, the general definition of a conservation law is given, as well as the definition of hyperbolic conservation laws.

Definition 3.1 *Let* $\mathbf{q}(x,t)\colon \mathbb{R}^d \times \mathbb{R}^+ \to \mathbb{R}^n$ *be a function and* $\mathbf{F}^i = \mathbf{F}^i(\mathbf{q})\colon \mathbb{R}^n \to \mathbb{R}^n$ *for* $i = 1, \dots, d$. *Then*

$$\partial_t \mathbf{q} + \sum_{i=1}^{d} \partial_{x_i} \left(\mathbf{F}^i(\mathbf{q}) \right) = 0$$

is called a ***system of*** n ***conservation laws*** *in* $\mathbb{R}^d$ *with flux functions* $\mathbf{F}^i$.

Definition 3.2 *The system*

$$\partial_t \mathbf{q} + \sum_{i=1}^{d} \partial_{x_i} \left(\mathbf{F}^i(\mathbf{q}) \right) = 0$$

is called ***hyperbolic*** *if the following is fulfilled: Let* $\mathbf{DF}^i(\mathbf{q})$ *be the Jacobian of* $\mathbf{F}^i$ *given by*

$$(\mathbf{DF}^i(\mathbf{q}))_{1\leq j,k\leq n} = \left(\frac{\partial(\mathbf{F}^i)_j(\mathbf{q})}{\partial q_k}\right).$$

If for any $\mathbf{q} \in \mathbb{R}^n$ *and all* $\mathbf{w} \in \mathbb{R}^d$, $\mathbf{w} \neq \mathbf{0}$ *the matrix*

$$\mathbf{DF}(\mathbf{q}, \mathbf{w}) = \sum_{i=1}^{d} \mathbf{w}_i \mathbf{DF}^i(\mathbf{q})$$

has n *real eigenvalues* $\lambda_1(\mathbf{q}, \mathbf{w}) \leq \cdots \leq \lambda_n(\mathbf{q}, \mathbf{w})$ *and* n *linear independent corresponding eigenvectors* $\mathbf{v}_1, \ldots, \mathbf{v}_n$*, then the system is called* ***hyperbolic****. If all eigenvalues are different, it is called* ***strictly hyperbolic****.*

The segregation equation, as derived in chapter 2, is a scalar hyperbolic conservation law. For this reason, the following definitions are given for scalar conservation laws.

The scalar case

If a solution for a scalar hyperbolic conservation law exists, it cannot be unique without defining initial conditions.

Definition 3.3 *The* ***Cauchy-Problem*** *(Initial value problem) for scalar conservation laws is given by*

$$\begin{aligned} &\partial_t q + \partial_x f(q) = 0, && q\colon \mathbb{R} \times \mathbb{R}^+ \to \mathbb{R}, && f\colon \mathbb{R} \to \mathbb{R}, \\ &q(x,0) = q_0(x), && x \in \mathbb{R}. \end{aligned}$$

Solving these kind of equations, one cannot expect to find a classical solution. For a simple linear transport equation, the solution is a travelling discontinuous shock if the hyperbolic equation together with the initial condition form a Riemann problem.

Definition 3.4 *The Riemann problem is a Cauchy-Problem with piecewise constant initial data with a single jump discontinuity. Assume the discontinuity is located at* $x = 0$*, the initial data are given by*

$$q(x,0) = \begin{cases} q_l & \text{if } x < 0, \\ q_r & \text{if } x > 0. \end{cases} \tag{3.1}$$

Even for smooth initial data, the solution can be non-smooth if the conservation law is non-linear. For scalar conservation laws the information travel on characteristic curves in the state space. If the characteristics intersect, a shock forms, giving a discontinuous solution. Therefore, it is necessary to generalise the solution term.

Definition 3.5 *A function $q = q(x,t)$ is called a* ***weak solution*** *of the Cauchy-Problem*

$$\begin{aligned} &\partial_t q + \partial_x f(q) = 0, \\ &q(x,0) = q_0(x) \end{aligned}$$

if

$$\int_{\mathbb{R}} \int_0^\infty [q\partial_t \vartheta + f(q)\partial_x \vartheta] dt dx + \int_{\mathbb{R}} q_0(x)\vartheta(x,0)dx = 0 \qquad \forall \vartheta \in C_0^1(\mathbb{R} \times \mathbb{R}^+).$$

Note that each smooth solution is also a weak solution. It is helpful to have a more general solution term for conservation laws but solely stating initial conditions is not enough to guarantee a unique solution. As there can be several weak solutions, one wants to find the physically correct solution. These physical solutions are given by the viscose solution of the conservation law.

Definition 3.6 *The* ***viscose solution*** *of a conservation law is the weak solution, which is the limit $\epsilon \to 0$ of the viscose regularisation*

$$\partial_t q + \partial_x f(q) = \epsilon \partial_{xx} q.$$

Finding a viscose solution is quite inconvenient. An alternative solution concept can be introduced by using the notion of entropy. Therefore, the definition of an entropy-entropy flux pair is needed.

Definition 3.7 *Let q be a smooth solution of a conservation law*

$$\partial_t q + \partial_x f(q) = 0 \quad \Leftrightarrow \quad \partial_t q + f'(q)\partial_x q = 0$$

and let η and ψ be two convex functions, such that

$$\partial_t \eta(q) + \partial_x \psi(q) = 0 \quad \Leftrightarrow \quad \eta(q)'\partial_t q + \psi'(q)\partial_x q = 0.$$

Then (η, ψ) is called ***entropy-entropy flux pair*** *and it holds*

$$\eta(q)' f'(q) = \psi'(q).$$

With the help of the entropy-entropy flux pair, the concept of viscose solutions can be connected to the concept of entropy solutions (Definition 3.8). If q is a viscose solution of a conservation law, then it holds in the weak sense

$$\partial_t \eta(q) + \partial_x \psi(q) \leq 0.$$

This means that

$$\int_{\mathbb{R}} \int_0^\infty [\eta(q)\partial_t \vartheta + \psi(q)\partial_x \vartheta] dt dx + \int_{\mathbb{R}} \eta(q)(x,0)\vartheta(x,0)dx = 0 \qquad \forall \vartheta \in C_0^1(\mathbb{R} \times \mathbb{R}). \quad (3.2)$$

Definition 3.8 *Let q be a weak solution of a conservation law that additionally fulfils* (3.2) *for any entropy-entropy flux pair (η, ψ), then q is called an* ***entropy solution****.*

For an entropy solution, one can show uniqueness as stated in Kružhkov's theorem 3.2 at the end of this section. Checking definition 3.8 of an entropy solution, one realises that it is not applicable. It is impossible to check all infinitely many entropies that exist for scalar conservation laws. Fortunately, it can be shown that it is enough to find solely one convex entropy η, such that condition (3.2) holds for all entropies. Details are given in the cited literature [57, 77].
Finding and checking only one entropy is still quite inconvenient. This problem can be solved by introducing admissibility or more often called entropy conditions (EC) that can be checked more easily. A weak solution of a conservation law is the correct entropy solution if all discontinuities are admissible. For a discontinuity being admissible, conditions were stated by Lax and Oleinik. In the scalar case, a discontinuity can behave in different ways. First, it can travel as a shock, where the shock speed is given by the Rankine-Hugoniot condition.

Theorem 3.1 (Rankine-Hugoniot) *Let q_l be the left and q_r the right state of a Riemann problem* (3.1) *forming a shock propagating with speed s. Then*

$$s = \frac{f(q_l) - f(q_r)}{q_l - q_r} =: \frac{[f]}{[q]}. \tag{3.3}$$

Second, the discontinuity can smear out propagating as a rarefaction wave. As mentioned earlier, the information of the conservation law travels along characteristic curves. As time advances, a stable shock should have characteristics going into the shock. If the characteristics are coming out of a propagating discontinuity, then it is unstable. Hence, this discontinuity should propagate as a rarefaction wave and not as a shock wave. Based on these arguments, the following entropy conditions were formulated.

Entropy Condition 1 (Lax) *For a scalar conservation law with convex flux function f, a shock propagating with speed s, given by the Rankine-Hugoniot condition* (3.3)*, is admissible if*

$$f'(q_l) > s > f'(q_r). \tag{3.4}$$

A more general condition for not uniformly convex fluxes f, concerning admissible shocks, has been formulated by Oleinik.

Entropy Condition 2 (Oleinik) *For a non-uniformly convex scalar conservation law, a shock propagating with speed s is admissible if*

$$\frac{f(q) - f(q_l)}{q - q_l} \geq s \geq \frac{f(q) - f(q_r)}{q - q_r} \qquad \forall q \text{ between } q_l \text{ and } q_r. \tag{3.5}$$

Note that for convex flux functions f, EC 2 reduces to EC 1. Oleinik also stated a condition that is based on the spreading of characteristics in a rarefaction fan.

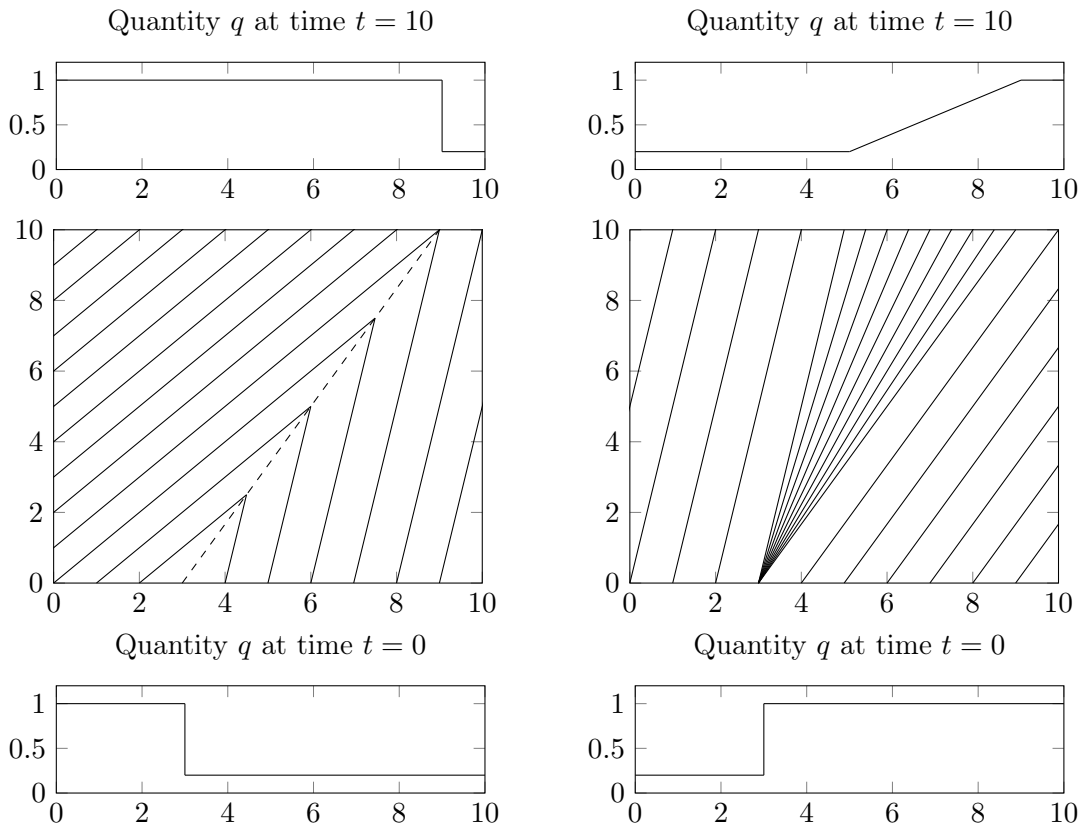

FIGURE 3.1: Entropy fulfilling shock *(left)* and rarefaction wave *(right)* for the simple conservation law $\partial_t q + \frac{1}{2}\partial_x(q^2) = 0$. The respective initial states *(bottom row)* and the final states after $10s$ *(top row)* are depicted. The characteristic curves are plotted in the x-t-space *(middle row)*.

Entropy Condition 3 (Oleinik) *Let f be the flux function of a scalar conservation law with $f''(q) > 0$. Then it holds, $q(x,t)$ is an entropy solution if there is a constant $E > 0$ such that $\forall h > 0$, $t > 0$ and $x \in \mathbb{R}$,*

$$\frac{q(x+h,t) - q(x,t)}{h} < \frac{E}{t}. \tag{3.6}$$

The presented conditions can not only be used to verify whether a solution behaves physically correct, they can directly be used to construct numerical schemes fulfilling the entropy conditions.
Finally, the Kružhkov-theorem is presented. Kružhkov's proof for the existence and uniqueness of entropy solutions for conservation laws was published in 1970 in [50].

Theorem 3.2 (Kružhkov) *The scalar conservation law*

$$\begin{aligned} &\partial_t q + \partial_x f(q) = 0, && f \in C^1(\mathbb{R}) \\ &q(x,0) = q_0(x), && q_0 \in L^\infty(\mathbb{R}) \end{aligned}$$

has a unique entropy solution $q \in L^\infty(\mathbb{R} \times \mathbb{R}^+)$, having the following properties:

1. $||q(\cdot,t)||_{L^\infty} \leq ||q_0(\cdot,t)||_{L^\infty}, \qquad t \in \mathbb{R}^+$
2. $q_0 \geq p_0 \Rightarrow q(\cdot,t) \geq p(\cdot,t), \qquad t \in \mathbb{R}^+$
3. $q_0 \in BV(\mathbb{R}) \Rightarrow q(\cdot,t) \in BV(\mathbb{R})$ *and* $TV(q(\cdot,t)) \leq TV(q_0)$
4. $q_0 \in L^1(\mathbb{R}) \Rightarrow \int_{\mathbb{R}} q(x,t)dx = \int_{\mathbb{R}} q_0(x)dx, \qquad t \in \mathbb{R}^+.$

The properties are called L^∞-stability, monotonicity, TV-stability and conservation property.

The appropriate function spaces for the proof given by Kružhkov were already defined in the work of Vol'pert [83]. For the sake of completeness, the function space of bounded variation is given in the following definition.

Definition 3.9 *Let $q \in L^\infty(\Omega)$, $\Omega \subset \mathbb{R}^n$ be open. Then, the **total variation** of q is defined by*

$$TV(q) = \limsup_{\epsilon \to 0} \frac{1}{\epsilon} \int_\Omega |q(x+\epsilon) - q(x)|dx.$$

The space of bounded variation is

$$BV(q) \coloneqq \{q \in L^\infty(\Omega) : TV(q) < \infty\}.$$

It should be noted, that the theorem is extendable to several space dimensions $x \in \mathbb{R}^d$. As opposed to this, it cannot generally be extended to the system case ($n > 1$). In such a case it is mostly necessary to use a weaker solution concept, called measure valued solutions.

The system case

In section 3.3, the segregation equation will be augmented into a system of equations. The following information is mainly an extension of those previously given for the scalar case. Let

$$\partial_t \mathbf{q} + \partial_x \mathbf{F}(\mathbf{q}) = 0 \tag{3.7}$$

be a non-linear strictly hyperbolic system of conservation laws. Writing the system in the linearised form, it is given by

$$\partial_t \mathbf{q} + \mathbf{DF}(\mathbf{q})\partial_x \mathbf{q} = 0, \tag{3.8}$$

where **DF** is the Jacobian. Further, let

$$\lambda_1(\mathbf{q}) < \lambda_2(\mathbf{q}) < \cdots < \lambda_n(\mathbf{q}) \tag{3.9}$$

denote the eigenvalues of the Jacobian with linear independent corresponding eigenvectors $\mathbf{r}_1(\mathbf{q}), \ldots, \mathbf{r}_n(\mathbf{q})$, which decompose the system into n characteristic fields. Following, the solution of the system consists of n waves, where the eigenvalues (3.9) are the characteristic speeds. In the system case, each state represents a point in the state space. Waves connecting different states travel along curves that can be depicted in the state space, where different wave solutions are possible. Like in the scalar case, a wave can travel as shock or as rarefaction wave, where the curves for shocks and rarefaction waves generally do not coincide. Furthermore, states can be connected by a contact discontinuity.

Definition 3.10 *The set of states* $\mathbf{q}$ *that can be connected by a shock to a state* $\bar{\mathbf{q}}$ *is called* ***Hugoniot-locus****. This set traces out a curve in the state space and fulfils the Rankine-Hugoniot condition* (3.3)*.*

In contrast to the shocks, the rarefaction waves travel along integral curves. In the p-th characteristic field a rarefaction wave travels with the characteristic speed λ_p. The eigenvectors $\mathbf{r}_p$ of the system define the integral curves.

Definition 3.11 *A smooth curve through the state space is an* ***integral curve*** *of the vector field defined by* $\mathbf{r}_p$ *if at each point the curve's tangent vector coincides with the eigenvector* $\mathbf{r}_p$ *of the system.*

Additionally to shocks and rarefactions like in the scalar case, contact discontinuities can appear for linearly degenerate fields. Generally, the n characteristic fields of the system can be distinct in the following way.

Definition 3.12 *The p-th characteristic field is called* ***genuinely non-linear*** *if*

$$\nabla\lambda_p(\mathbf{q}) \cdot \mathbf{r}_p(\mathbf{q}) \neq 0 \qquad \forall \mathbf{q} \in \Omega \subset \mathbb{R}^d. \tag{3.10}$$

The field is called ***linearly degenerate*** *if*

$$\nabla\lambda_p(\mathbf{q}) \cdot \mathbf{r}_p(\mathbf{q}) \equiv 0 \qquad \forall \mathbf{q} \in \Omega \subset \mathbb{R}^d. \tag{3.11}$$

For genuinely non-linear fields, the characteristic speed λ_p varies along the integral curves of $\mathbf{r}_p$. For linearly degenerate fields, λ_p stays constant along each integral curve. If the initial data is given by a jump discontinuity, the solution stays the same travelling with constant speed along the integral curve. Hence, it cannot be a rarefaction wave. Even if the solution propagates like a shock, it is none, as the characteristics in the x-t plane are parallel and do not merge. Therefore, these waves are called contact discontinuities. In the case of a linearly degenerate field, the integral curves and the Hugoniot-loci always coincide.
It still has to be clarified when a solution is admissible. For the system case, there exists a version of Lax's entropy condition.

Entropy Condition 4 (Lax) *For genuinely non-linear fields, a shock wave with speed* s*, given by the Rankine-Hugoniot condition* (3.3)*, is admissible if*

$$\lambda_p(\mathbf{q}_l) > s > \lambda_p(\mathbf{q}_r). \tag{3.12}$$

As contact discontinuities behave like shocks, it is possible to include them in the formulation of the Lax entropy condition by stating

$$\lambda_p(\mathbf{q}_l) \geq s \geq \lambda_p(\mathbf{q}_r). \tag{3.13}$$

3.2 Analysis of the segregation equation

To analyse and understand the behaviour of the segregation equation, a simple setting in a rectangular domain is used. The model is reduced to two space dimensions x and z. The granular bulk flows from left to right in the positive x-direction with velocity u. The segregation acts only in the z-direction. Hence, the segregation equation can be written as

$$\partial_t \phi + \partial_x(\phi u) - \partial_z(S\phi(c-\phi)) = 0, \tag{3.14}$$

with

$$S \coloneqq -S_0 \frac{\sqrt{T}}{c} g. \tag{3.15}$$

Furthermore, it is assumed that the volume fraction of the granular material c and the granular temperature T are constant and hence, the segregation velocity S is positive, since the gravitational acceleration g is typically negative. In this case, the segregation equation (3.14) is a scalar conservation law in two space dimension. As the flux terms fulfil the conditions stated in Kružhkov's theorem 3.2, there exists a unique solution to the problem under appropriate initial conditions. In this simplified form, the equation can be solved and analysed with the help of the method of characteristics.

As first example, assume a plug flow setting where the bulk velocity is constant, i.e., $u \equiv u_0$. Then, the Cauchy-Problem can be given in the quasi-linear form

$$\begin{aligned} \partial_t \phi + u_0 \partial_x \phi - S(c-2\phi)\partial_z \phi = 0, \\ \phi(x, z, t=0) = \phi_0(x, z). \end{aligned} \tag{3.16}$$

Defining a coordinate transformation $t' = t$, $x' = x - u_0 t$, and $z' = z$, the spatial variable in flow direction can be eliminated. With the chain rule, the derivative with respect to $\xi \in \{t,\, x\,, z\}$ is given by

$$\partial_\xi(\cdot) = \partial_\xi t' \partial_{t'}(\cdot) + \partial_\xi x' \partial_{x'}(\cdot) + \partial_\xi z' \partial_{z'}(\cdot). \tag{3.17}$$

Therefore, the differential operators are given by

$$\begin{aligned} \partial_t(\cdot) &= \partial_{t'}(\cdot) - u_0 \partial_{x'}(\cdot), \\ \partial_x(\cdot) &= \partial_{x'}(\cdot), \\ \partial_z(\cdot) &= \partial_{z'}(\cdot). \end{aligned} \tag{3.18}$$

To hold the notation simple, the prime is dropped for the transformed equations. As already mentioned, the Cauchy-Problem (3.16) simplifies to

$$\begin{aligned} \partial_t \phi - S(c-2\phi)\partial_z \phi = 0, \\ \phi(z, 0) = \phi_0(z). \end{aligned} \tag{3.19}$$

Parametrising the characteristic curves by s and the initial data by r, one ends with a system of ordinary differential equations (ODE), given by

$$\frac{dt}{ds}(r,s) = 1, \tag{3.20}$$

$$\frac{dz}{ds}(r,s) = S(2\psi - c), \tag{3.21}$$

$$\frac{d\psi}{ds}(r,s) = 0. \tag{3.22}$$

Solving (3.20) and (3.22) gives

$$t(r,s) = s + \zeta_1(r), \tag{3.23}$$
$$\psi(r,s) = \zeta_3(r). \tag{3.24}$$

From (3.24) it follows that ψ depends solely on r. Hence, the solution is constant along the characteristic curves and equation (3.21) can easily be integrated. One obtains

$$z(r,s) = S(2\zeta_3(r) - c)s + \zeta_2(r). \tag{3.25}$$

With the initial conditions

$$t(r,0) = 0, \tag{3.26}$$
$$z(r,0) = r, \tag{3.27}$$
$$\psi(r,0) = \phi_0(r), \tag{3.28}$$

the ζ_i, for all $i \in \{1, 2, 3\}$, can be found. The solutions of the ODEs (3.20), (3.21) and (3.22) are given by

$$t(r,s) = s, \tag{3.29}$$
$$z(r,s) = S(2\phi_0(r) - c)s + r, \tag{3.30}$$
$$\psi(r,s) = \phi_0(r). \tag{3.31}$$

For the backward transformation, r and s are written in terms of t and z, i.e.,

$$s(z,t) = t, \tag{3.32}$$
$$r(z,t) = z - S(2\psi - c)s. \tag{3.33}$$

Let $\phi(z,t) = \psi(r,s)$, then, the solution of the segregation equation is implicitly given by

$$\phi(z,t) = \phi_0(z - S(2\phi - c)t). \tag{3.34}$$

A sketch of the domain and a plot of the characteristics in the t-z-plane are illustrated in Figure 3.2. Initially, the domain of height h is filled with a mixed granular material $\phi = 0.6c$ and has a constant inflow of $\phi_{in} = 0.6c$. For the top and the bottom boundaries $\phi = 0$ and $\phi = c$ are chosen, respectively. Since a plug flow setting with $u \equiv u_0$ is assumed, each column of the granular flow field is independent of each other. A column of the flow field means the full depth of the granular flow (z-direction) at one specific position in x. The characteristics depicted in Figure 3.2 show the behaviour of the solution over time. The solution is identical for each column of the spatial x-axis under the given initial conditions. The information travel along the characteristics, which are straight lines. They merge in two shocks emanating from the left corners, one with positive and one with negative speed. Those also intersect after t_m time units. From this time on, the system is totally segregated, separated by a stable shock of speed zero. In the plug flow example, one can compute that for a given segregation rate S the time for total separation is given by $t_m = \frac{h}{Sc}$. The depicted solution is similar to the steady state solution in the spatial x-z-plane of the segregation equation

$$\begin{aligned} u_0 \partial_x \phi - S(c - 2\phi)\partial_z \phi = 0, \\ \phi(x,0) = \phi_0(z). \end{aligned} \tag{3.35}$$

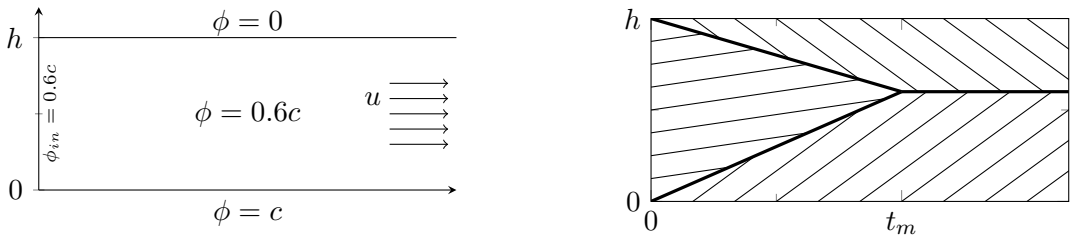

FIGURE 3.2: Sketch of the plug flow example. A rectangular domain of height h, initially filled with equally mixed granular material with $\phi = 0.6c$ and $u \equiv u_0$. The inflow at the left boundary has the same value $\phi_{in} = 0.6c$. The top and bottom boundaries are given by $\phi = 0$ and $\phi = c$, respectively *(left)*. Characteristics in the t-z-plane are straight lines. Two shocks emanate from the left corners, one with positive and one with negative speed. Both merge after $t_m = \frac{h}{Sc}$ time units. From this time on, the system is totally segregated, separated by a stable shock of speed zero *(right)*.

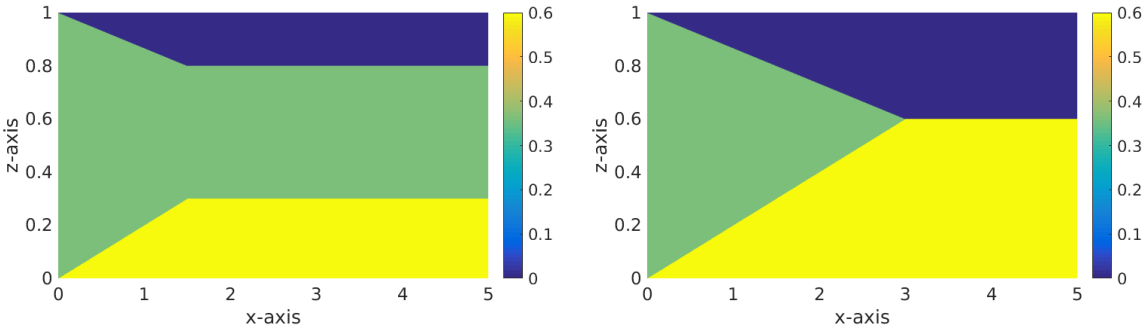

FIGURE 3.3: Solution of the plug flow example in the x-z-plane at $t = 1.5$ *(left)* and after the steady state has been reached $t \geq t_m$ *(right)*. The colour represents the volume fraction of the small particle phase. Yellow corresponds to solely small particles, whereas dark blue corresponds to solely large particles. The granular material has a volume fraction of $c = 0.6$ and flows from left to right with $u \equiv 1$. The segregation rate has been chosen to be $S = \frac{1}{3c}$. Initially, the domain is filled with a perfectly mixed material with value $\phi = 0.6c$. The inflow concentration ϕ_{in} at the left boundary is $0.6c$ as well.

It is even identical for $u_0 \equiv 1$. Due to the coordinate transformation, effectively, the steady state solution of the segregation equation has been solved as well. Solution plots are given in Figure 3.3 depicting the plug flow example in the x-z-plane at $t = 1.5$ and after the steady state has been reached. Mind that, due to the constant velocity, the final separating shock has to be located at a height of $z = 0.6h$, since the concentration of the small particle phase is chosen by $\phi = 0.6c$.

As already explained in chapter 2, segregation is also driven by shear. Since in a plug flow is no shear, there is rarely segregation happening. Therefore, the last example is not very realistic, but it serves quite good for getting a feeling of the behaviour of the equation and the characteristic curves. To look at a more realistic example, the bulk velocity is assumed to depend on z but still does not vary over time. A simple but general form for u is chosen depending on a parameter α,

$$u^{\alpha}(z) = \alpha + 2(1 - \alpha)z, \qquad 0 \leq \alpha \leq 1. \tag{3.36}$$

With this definition, u^α defines a plug flow for $\alpha = 1$ and a simple shear flow with no-slip at the bottom for $\alpha = 0$. For all values in between, a shear flow is defined with different slip values at the bottom of the flow. The general form (3.36) has already been used by Shearer et al. [74] and McIntyre et al. [62] to investigate the classical Gray-Thornton model.

Assume now, the segregation equation is given with the bulk velocity defined by u^α (3.36). The velocity field depends solely on the z-variable, hence, the quasi-linear form of the segregation equation can again directly be written as

$$\begin{aligned} \partial_t \phi + u^\alpha(z)\partial_x \phi - S(c - 2\phi)\partial_z \phi = 0, \\ \phi(x, z, 0) = \phi_0(x, z) \end{aligned} \tag{3.37}$$

This time the transport with the bulk cannot be eliminated that easy. The system of ODEs has four equations. They are given with the corresponding initial conditions by

$$\frac{dt}{d\tau} = 1 \qquad t(r, s, 0) = 0, \tag{3.38}$$

$$\frac{dx}{d\tau} = u^\alpha(z) \qquad x(r, s, 0) = r, \tag{3.39}$$

$$\frac{dz}{d\tau} = S(2\phi - c) \qquad z(r, s, 0) = s, \tag{3.40}$$

$$\frac{d\phi}{d\tau} = 0 \qquad \phi(r, s, 0) = \phi_0(r, s). \tag{3.41}$$

From (3.38) one gains

$$t = \tau \tag{3.42}$$

and from (3.41) it follows, identically to the plug flow example, that the solution along the characteristics is constant. Then, the solution to (3.40) is given by

$$z(t) = S(2\phi - c)t + s. \tag{3.43}$$

With the expression for the velocity field and the solution (3.43), the x-characteristic is given by

$$x(t) = (1 - \alpha)S(2\phi - c)t^2 + (2s - 2\alpha s + \alpha)t + r. \tag{3.44}$$

A general solution depends on the representation of the initial condition and can be implicitly written as

$$\phi(x, z, t) = \phi_0(r(x, z, t), s(x, z, t)), \tag{3.45}$$

where

$$r(x, z, t) = x - (1 - \alpha)S(2\phi - c)t^2 + (2s(z, t) - 2\alpha s(z, t) + \alpha)t, \tag{3.46}$$

$$s(z, t) = z - S(2\phi - c)t. \tag{3.47}$$

One can see that due to the shear flow the columns in the flow field are not independent any more. It is easy to proof that this dependence cancels out for a plug flow, which is given for $\alpha = 1$. By eliminating the time, the characteristics can be given in the x-y-phase

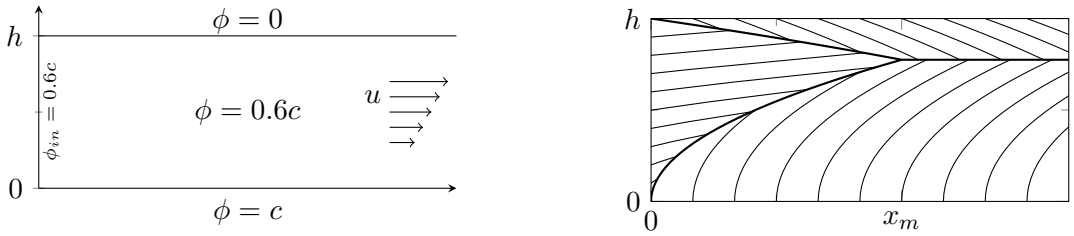

FIGURE 3.4: Sketch of the simple shear flow example. A rectangular domain of height h with $u(z) = 2z$. Initially, the domain is filled with equally mixed granular material with $\phi = 0.6c$. The inflow at the left boundary has the same value. The top and bottom boundaries are given by $\phi = 0$ and $\phi = c$, respectively *(left)*. Characteristics in the x-z-plane are curved lines, as the bulk velocity decreases with the depth of the granular bed. The characteristics intersect in two shocks emanating from the left corners, one with positive and one with negative speed. Both merge at $x_m = \frac{h^2}{Sc}$. From this point on the system is totally segregated, separated by a stable shock of speed zero *(right)*.

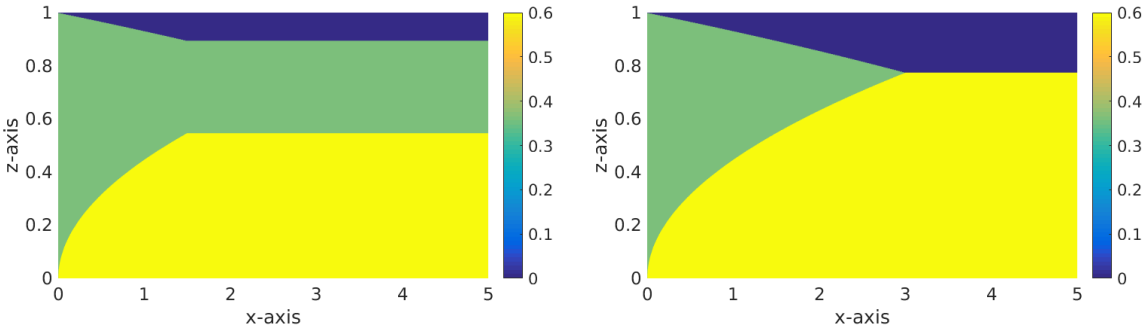

FIGURE 3.5: Solution of the simple shear flow example in the x-z-plane at $t = 1.5$ *(left)* and after the steady state has been reached *(right)*. The colour represents the volume fraction of the small particle phase. Yellow corresponds to solely small particles, whereas dark blue corresponds to solely large particles. The granular material has a volume fraction of $c = 0.6$ and flows from left to right with $u = 2z$. The segregation rate has been chosen to be $S = \frac{1}{3c}$. Initially, the domain is filled with a perfectly mixed material with value $\phi = 0.6c$. The inflow concentration ϕ_{in} at the left boundary is $0.6c$ as well.

space, which makes it easier to depict the segregation process (Figure 3.4). For a starting point (x_0, z_0) a characteristic curve is given by a parabola

$$x(z) = x_0 + \frac{(z - z_0)(\alpha + (1 - \alpha)(z + z_0))}{S(2\phi - c)}. \tag{3.48}$$

Along the characteristic curves the solution is constant again. The initial, boundary, and inflow conditions in the example, depicted in Figure 3.4, are identical to those chosen in the previous plug flow example (Figure 3.2). However, due to the z-dependent velocity field the information travels on non straight characteristics. Again the characteristics merge in two shocks emanating from the left corners, one with positive and one with negative speed. They also intersect and form a stable shock of speed zero. In contrast to the plug flow example, the final shock separating small and large particles is not located at a height of $z = 0.6h$, although the inflow volume fraction is $\phi_{in} = 0.6c$. Since the upper layers of the flow field are faster, the large particles in the top layers move faster

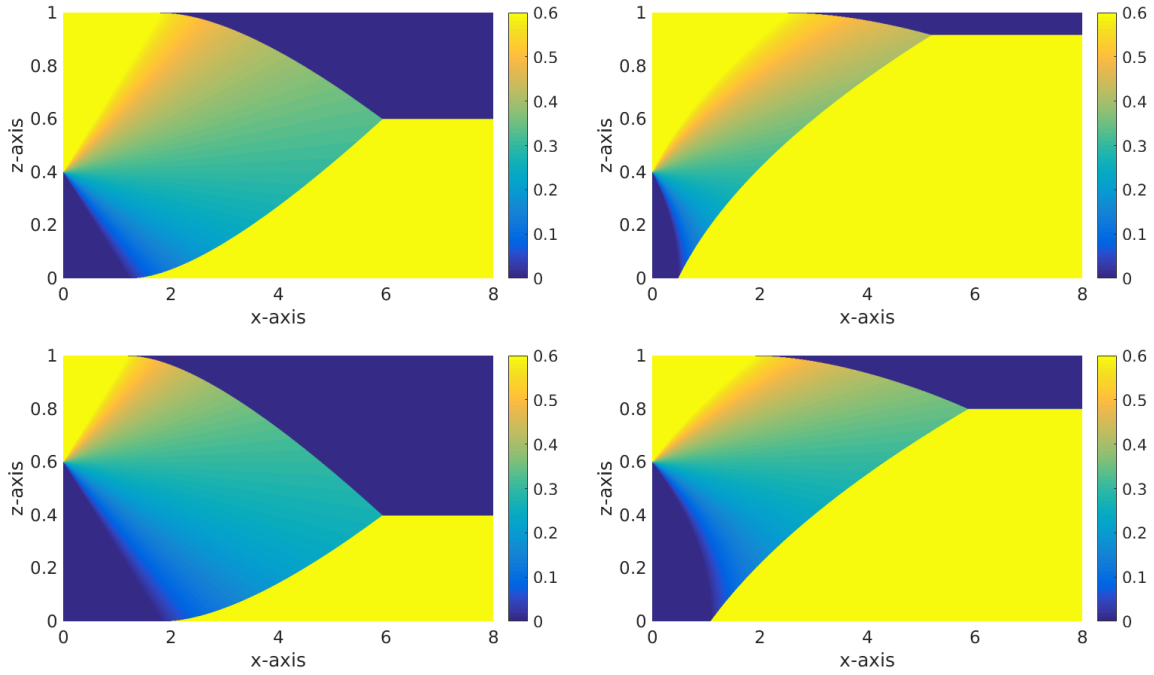

FIGURE 3.6: Steady state solution of a plug flow $u \equiv 1$ *(left)* and a simple shear flow example $u = 2z$ *(right)* in the x-z-plane with height $h = 1$. The colour represents the volume fraction of the small particle phase. Yellow corresponds to solely small particles, whereas dark blue corresponds to solely large particles. The granular material has a volume fraction of $c = 0.6$. The segregation rate has been chosen to be $S = \frac{1}{3c}$. The inflowing material is unmixed with small particles above the large ones separated by a jump at $z_r = 0.4h$ *(top)* and $z_r = 0.6h$ *(bottom)*, respectively. The jump smears out in a rarefaction fan, before again a stable shock forms with inversely graded particles.

than the small particles in the lower parts of the domain. Actually, the separating shock is located at $z = \sqrt{0.6}h$. Solution plots are given in Figure 3.5 depicting the simple shear flow example in the x-z-plane at $t = 1.5$ and after the steady state has been reached.

Similar examples of a simplified segregation equation based on the derived model of Gray and Thornton can be found in [37, 39, 62, 74]. Several authors analysed the behaviour of these types of segregation equations in more detail. The shock formation and stability is discussed in Shearer et al. [75]. Further, wave breaking under certain conditions and the evolution of the mixing zones is analysed in McIntyre et al. [62]. In Shearer and Giffen [73] the authors analysed shock formation and wave breaking for a generalised equation given by

$$\partial_t \phi + u(z)\partial_x \phi + \partial_z f(\phi) = 0, \tag{3.49}$$

where the flux function $f : [0, 1] \to \mathbb{R}$ is smooth, strictly convex and satisfies

$$f(0) = 0 = f(1). \tag{3.50}$$

Even for the generalised case, it can be shown that a shock is stable if the large particles are located above the small particles. In Figure 3.6, solution plots as in Figure 3.3 and Figure 3.5 show the segregation process in the steady state for plug and shear flow. The only difference to the previous examples lies in the inflow condition. The inflowing

material is perfectly separated. It has a unstable jump at $z = z_r$ with small particles above the large particles. One can see that this jump smears out in a rarefaction fan before a stable shock forms again with inversely graded particles. Figure 3.6 shows this situation for $z_r = 0.4h$ and $z_r = 0.6h$.

For less simplified versions of the segregation equation, it becomes even harder to solve the equation. If the granular bulk velocity u depends not only on z but also on the variable x, the information along the characteristics vary by ϕu_x and will not stay constant any longer. However, if the segregation flux becomes less simple, even with ignoring the bulk flow, the solution cannot be found explicitly. Mostly, solely the structure of the solution can be characterized. In the work of May et al. [61], the authors assume a one-dimensional segregation equation in the general form

$$\partial_t \phi + \partial_z (sa(z) f(\phi)) = 0, \quad 0 < z < 1, \quad t > 0, \tag{3.51}$$

where $a(z)$ defines a spatial dependent shear rate and $f(\phi)$ is defined similar as in equation (3.49). Again, ϕ is not constant along the characteristics. The same can be expected for the segregation equation that has been derived in chapter 2 if the granular temperature is not constant. May et al. [61] have also examined that only for specific expressions of $a(z)$ the existence theory of Kružhkov is applicable. If an additional spatial dependence of the segregation flux cannot be separated from the ϕ-terms, even more theory breaks down. This is the case for the equation derived in chapter 2, due to the dependence on the granular volume fraction c. Therefore, the next section is addressed to the topic of spatially varying flux functions.

3.3 Spatial dependent flux functions

This section deals with hyperbolic conservation laws with discontinuous flux functions. One has to distinguish two different cases. The flux function can be discontinuous with respect to the quantity q or the discontinuity can occur from a spatial dependence of the flux function. The latter case pertains to the segregation equation as mentioned at the end of the last section. However, the first case is also summarised in this section.

3.3.1 Introduction to discontinuous flux functions

For conservation laws with discontinuous flux functions the existence and uniqueness of a solution cannot directly be deduced from Kružhkov's theorem 3.2. In its proof, the continuity of the flux function is essential [50]. Assume the Cauchy-Problem

$$\begin{aligned} &q_t + \nabla \cdot \mathbf{F}(q) = 0, && q \colon \mathbb{R}^d \times \mathbb{R}^+ \to \mathbb{R}, && \mathbf{F} \colon \mathbb{R} \to \mathbb{R}^d, \\ &q(\mathbf{x}, 0) = q_0(\mathbf{x}), && \mathbf{x} \in \mathbb{R}^d, \end{aligned}$$

where $\mathbf{F}$ contains a jump discontinuity with respect to q. For this case Bulíček et al. [10] introduced a concept of entropy solutions that is different but equivalent to the usual one. With this concept they extended the definition of an entropy solution to fluxes with jump discontinuities. Their strategy is inspired by implicit constitutive theory. In their work, they identified a given discontinuous flux function $\mathbf{F}$ with a continuous curve G that is

given by a graph of $\mathbf{F}$ and abscissae that fill the jumps. Consequently, they dealt with the implicit relation

$$G(\mathbf{F}, q) = 0.$$

They showed existence and uniqueness of entropy weak solutions for conservation laws with fluxes that are α-Hölder continuous at the jump.
Further results for discontinuous flux functions were already given by Gimse [31] and Dias et al. [18]. The derived results are only given for the one-dimensional case, $d = 1$. Gimse [31] has not formulated any entropy condition, whereas Dias et al. [18] derived a generalised entropy solution concept. For a discontinuity at $q = 0$ and fluxes given by

$$F \coloneqq g(q) + (f(q) - g(q))H(q), \tag{3.52}$$

where $f(q)$ and $g(q)$ are smooth and $H(q)$ denotes the Heaviside function, the authors established the existence and uniqueness of a weak solution fulfilling the generalised entropy concept.

Pretty much work has already been done in the framework of conservation laws with spatially dependent flux functions (also called spatially varying flux functions). In this case the flux function $F(q(x,t), x)$ is continuous in the quantity q but not in the spatial variable x. The problem can generally be formulated by

$$\partial_t q + \partial_x F(q, x) = 0, \tag{3.53}$$

$$q(x, 0) = q_0(x), \tag{3.54}$$

where the flux F is discontinuous in a finite number of points x. Authors, who analysed this problem, typically restrict to one discontinuity in $x = 0$, such that

$$F \coloneqq g(q) + (f(q) - g(q))H(x). \tag{3.55}$$

Again, Kružhkov's theorem is not applicable, due to the missing Lipschitz continuity of the flux function in x, which is needed in the proof. In this discontinuous case, an entropy solution is not unique under the classical entropy conditions [13]. Furthermore, an additional jump wave may occur besides the classical ones as solution of a Riemann problem. Authors, who dealt with the uniqueness of a solution for conservation laws with discontinuous flux functions generalised or added an entropy condition to guarantee the uniqueness.
A first paper on discontinuous flux functions for hyperbolic conservation laws is the one by Gimse and Risebro [32]. They considered a model for two phase flows through a porous medium and used a front tracking method to prove the existence of a weak solution.
In his publications [19, 20], Diehl considered different conservation laws modelling sedimentation processes in a clarifier-thickener unit. He formulated the viscous profile condition, which is based on the entropy condition stated by Oleinik (EC 2) and an equivalent, called condition Γ. With the formulated condition Γ, a suitable flux over the jump can be found. This corresponds to a choice a Riemann solver has to make at the discontinuity. Later on, existence and uniqueness for small time have been proven, assuming regularity and monotonicity along the discontinuity $x = 0$.
Chen et al. [13] compared different entropy conditions suggested in the literature. They focused on a family of discontinuous flux functions that can be written as

$$F(q, x) = \eta(x)h(q), \tag{3.56}$$

where $\eta(x)$ is continuous except on a set of measure zero and $h(q)$ is Lipschitz continuous. They showed existence and combined it with the uniqueness proof given by Audusse and Perthame [4]. Garavello et al. [28] summarised concepts given by different authors and concluded that depending on the physics of the underlying application, various models need different solution concepts, although they are based on the same equation (3.53). Furthermore, they also provided a formulation in terms of Riemann solvers for an equation of type (3.53) motivated by a traffic flow model, where f and g are strictly concave functions. They determined the class of Riemann solvers which provide existence by a front tracking method and uniqueness of the corresponding weak entropy solution.

3.3.2 The segregation equation as non-linear resonant system

In the upcoming subsection, the focus lies on the segregation flux term. The bulk flow is ignored, such that the segregation equation reduces to a one-dimensional model acting only in the spatial z-direction. Assume that the granular temperature T is constant as in the last sections, but the granular volume fraction c varies in the spatial variable z defining a c-profile in the depth (z-direction) of the granular system. Starting from a classical Riemann problem, the structure of an entropy fulfilling solution is going to be characterised. For the following procedure, the equation is written in a system of equations as it already has been done by Jin and Zhang [47] for a concave traffic flow model of similar structure.
Start with the one-dimensional segregation equation with constant granular temperature

$$\partial_t \phi - \partial_z \underbrace{\left(S \frac{(c-\phi)}{c} \phi \right)}_{f(\phi,c)} = 0. \tag{3.57}$$

As c solely depends on the spatial variable, one can introduce an additional conservation law $\partial_t c = 0$. Then, equation (3.57) can be augmented into a system of conservation laws

$$\partial_t \mathbf{U} + \partial_z \mathbf{F}(\mathbf{U}) = 0, \tag{3.58}$$

where $\mathbf{U} = (\phi, c)^T$ and the flux $\mathbf{F}(\mathbf{U}) = (f(\phi, c), 0)^T$. The system can be written in the linearised form and can be analysed by looking at the eigenvalues and the corresponding eigenvectors of the Jacobian. Writing the system in the linearised form

$$\partial_t \mathbf{U} + \mathbf{DF}(\mathbf{U}) \partial_z \mathbf{U} = 0, \tag{3.59}$$

it is given by

$$\partial_t \begin{pmatrix} \phi \\ c \end{pmatrix} + \begin{pmatrix} S(2\frac{\phi}{c} - 1) & -S\frac{\phi^2}{c^2} \\ 0 & 0 \end{pmatrix} \partial_z \begin{pmatrix} \phi \\ c \end{pmatrix} = 0. \tag{3.60}$$

The eigenvalues of the Jacobian $\mathbf{DF}$ are

$$\lambda_0 = 0, \qquad \lambda_1 = S\left(2\frac{\phi}{c} - 1\right) \tag{3.61}$$

and the corresponding right eigenvectors are

$$\mathbf{r}_0 = \begin{pmatrix} \frac{\phi^2}{c^2} \\ 2\frac{\phi}{c} - 1 \end{pmatrix}, \qquad \mathbf{r}_1 = \begin{pmatrix} 1 \\ 0 \end{pmatrix}. \tag{3.62}$$

The system has two characteristic fields, where the 0-field is linearly degenerate, as

$$\nabla\lambda_0(\mathbf{U}) \cdot \mathbf{r}_0(\mathbf{U}) \equiv 0 \quad \forall \mathbf{U}. \tag{3.63}$$

The 1-field is genuinely non-linear, as

$$\nabla\lambda_1(\mathbf{U}) \cdot \mathbf{r}_1(\mathbf{U}) = S\frac{2}{c} \neq 0 \quad \forall \mathbf{U}. \tag{3.64}$$

Mind that $c > 0$. From the eigenvalues, it follows that the system is non-strictly hyperbolic, since for several states in the system, it holds

$$\lambda_0 = \lambda_1. \tag{3.65}$$

A state $\mathbf{U}^* = (\phi^*, c^*)^T$ is called critical if

$$\lambda_1(\mathbf{U}^*) = 0 = \lambda_0. \tag{3.66}$$

In the **U**-space, all critical points form a smooth curve. This curve is called transition curve and is defined by

$$\Gamma = \{\mathbf{U} | \lambda_1(\mathbf{U}) = 0\} \tag{3.67}$$

$$= \{(\phi, c)^T | c = 2\phi\}. \tag{3.68}$$

The Jordan normal form of the linearised system (3.60) in a critical state is

$$\begin{pmatrix} \tilde{\phi} \\ \tilde{c} \end{pmatrix}_t + \begin{pmatrix} 0 & 1 \\ 0 & 0 \end{pmatrix} \begin{pmatrix} \tilde{\phi} \\ \tilde{c} \end{pmatrix}_z = 0. \tag{3.69}$$

The solution of this system, given by

$$\tilde{\phi}(z,t) = \tilde{c}'(z)t + k, \tag{3.70}$$

blows up for $t \to \infty$. It is said, resonant behaviour occurs. These systems are called **non-linear resonant systems** and were characterised in the work of Isaacson and Temple [45]. At any point on the curve Γ, given by the critical states, the wave speed of the 0-family and the 1-family are the same and it follows that the system (3.58) is singular. This makes wave interactions significantly more complicated than in a strictly hyperbolic system, since "the wave speeds are not distinct, and so the number of times a pair of waves can interact in a given solution cannot be bounded a priori"[1]. Or in other words, no distinct eigenvectors are given in such points to show the correct direction to connect two states in the **U**-space.
In their work, Isaacson and Temple [45] proved that under several conditions, the Riemann problem of a non-linear resonant system of type (3.58) has a unique solution. Based on this work, Lin et al. [58] discussed numerical methods for such resonant systems. The original theorem, stating unique solutions in the work of Isaacson and Temple [45], is formulated as follows:

[1] Isaacson and Temple [45] *p.* 1261

Theorem 3.3 *Assume that in a neighbourhood of a state* $\mathbf{U}^* = (\mathbf{q}^*, a^*)$ *the* $n \times n$ *system*

$$\partial_t \mathbf{q} + \partial_x \mathbf{F}(\mathbf{q}, a) = \mathbf{0}$$

is strictly hyperbolic for each fixed value of a*, and is either genuinely non-linear or linearly degenerate in each characteristic field. Let*

$$\lambda_1(\mathbf{q}, a) < \lambda_2(\mathbf{q}, a) < \cdots < \lambda_n(\mathbf{q}, a)$$

denote the eigenvalues of this system with corresponding right eigenvectors $\mathbf{r}_1, \ldots, \mathbf{r}_n$ *and left eigenvectors* $\mathbf{l}_1, ..., \mathbf{l}_n$*. Assume that the function* $\mathbf{F}$ *satisfies the following conditions at the state* $\mathbf{U}^*$*:*

1. $\lambda_k(\mathbf{q}^*, a^*) = 0$,
2. $\nabla \lambda_k \cdot r_k|_{U^*} \neq 0$,
3. $l_k \cdot \partial_a \mathbf{F}|_{U^*} \neq 0$,

where $k \in \{1, \ldots, n\}$*. Then, there exists a unique solution of the Riemann problem in a neighbourhood of* $\mathbf{U}^*$*, and this solution depends continuously in physical space on the left and right states. Moreover, for every* $\mathbf{F}$ *in this class, the solution exhibit the same qualitative behaviour.*

Based on their results, the authors were able to formulate an additional entropy condition which ensures a unique solution.

Entropy Condition 5 *A 0-wave, which connects two states on the same integral curve by a contact discontinuity of speed zero, is admissible if it does* ***not*** *cross the transition curve* Γ*.*

Applying theorem 3.3 on the segregation problem, the mentioned $n \times n$ system is simply the one dimensional equation (3.57). For a fixed c, the equation is strictly hyperbolic. It is easily checked that all other conditions, stated in theorem 3.3, for the system augmented from the segregation equation (3.57) are fulfilled. Following, the Riemann problem can be uniquely solved if one regards the additional entropy condition (EC 5).

3.3.3 Solving the Riemann problem for the segregation equation as non-linear resonant system

In this subsection the integral curves and Hugoniot-loci for the system (3.58), given by

$$\partial_t \phi + \partial_z \left(S\left(\frac{\phi}{c} - 1\right) \phi \right) = 0, \tag{3.71a}$$

$$\partial_t c = 0, \tag{3.71b}$$

are constructed and the admissible waves, fulfilling the classical Lax entropy condition (EC 4) and additionally EC 5, are worked out. The starting point is the Riemann problem given by the equations (3.71) and the initial condition

$$\mathbf{U}(z, t=0) = \begin{cases} \mathbf{U}_L \text{ if } z < 0, \\ \mathbf{U}_R \text{ if } z > 0, \end{cases} \tag{3.72}$$

with constant states $\mathbf{U}_L$ and $\mathbf{U}_R$. A state in the state space is defined by $\mathbf{U} = (\phi, c)^T$.

Shock solution

For the shock solution, the Hugoniot-locus to a state in $\mathbf{U}$-space needs to be found. A shock that can be connected to an arbitrary fixed state $\bar{\mathbf{U}} = (\bar{\phi}, \bar{c})^T$ with speed s must fulfil the Rankine-Hugoniot condition 3.1. Hence,

$$S\left(\frac{\phi}{c} - 1\right)\phi - S\left(\frac{\bar{\phi}}{\bar{c}} - 1\right)\bar{\phi} = s(\phi - \bar{\phi}), \tag{3.73}$$

$$0 = s(c - \bar{c}). \tag{3.74}$$

To fulfil equation (3.74) one has to distinguish two cases. First, with the assumption $s = 0$, equation (3.73) modifies to

$$S\left(\frac{\phi}{c} - 1\right)\phi - S\left(\frac{\bar{\phi}}{\bar{c}} - 1\right)\bar{\phi} = 0. \tag{3.75}$$

Solving equation (3.75) for c yields

$$c = \frac{\phi^2}{\left(\frac{\bar{\phi}}{\bar{c}} - 1\right)\bar{\phi} + \phi}. \tag{3.76}$$

This can be parametrised by ϕ, such that the Hugoniot-locus in the $\mathbf{U}$-space is given by

$$H_0(\xi) = \begin{pmatrix} \xi \\ \frac{\xi^2}{\left(\frac{\bar{\phi}}{\bar{c}} - 1\right)\bar{\phi} + \xi} \end{pmatrix}. \tag{3.77}$$

As the shock speed s is zero, the curve $H_0(\xi)$ belongs to the linear degenerate field with $\lambda_0 = 0$. The only admissible wave along H_0 is a contact discontinuity. Contact discontinuities with speed zero are often called standing waves. Note that for an admissible solution, the standing wave along H_0 is not allowed to cross the transition curve Γ (Entropoy Condition 5).

For the second case assume $s \neq 0$. From equation (3.74), it directly follows that $c = \bar{c}$. The Hugoniot-locus needs to be a straight line in $\mathbf{U}$-space defined by the set

$$\mathbb{H}_1 = \{\mathbf{U} | c = \bar{c} \text{ and } \phi \in \mathbb{R}_0^+\}. \tag{3.78}$$

The Hugoniot-locus can be given as a parametrised curve

$$H_1(\xi) = \begin{pmatrix} \xi \\ \bar{c} \end{pmatrix} \tag{3.79}$$

and the shock speed is given by

$$\begin{aligned} s(\phi) &= S\frac{\left(\frac{\phi^2}{\bar{c}} - \phi\right) - \left(\frac{\bar{\phi}^2}{\bar{c}} - \bar{\phi}\right)}{\phi - \bar{\phi}} \\ &= S\frac{\frac{(\phi-\bar{\phi})(\phi+\bar{\phi})}{\bar{c}} - (\phi - \bar{\phi})}{\phi - \bar{\phi}} \\ &= S\left(\frac{\phi + \bar{\phi}}{\bar{c}} - 1\right) \end{aligned} \tag{3.80}$$

From Lax's entropy condition (EC 4), it follows that a state $\mathbf{U}$ can only be connected to the state $\bar{\mathbf{U}}$ on the same curve H_1 by an admissible shock if

$$\lambda_1(\mathbf{U}) > s > \lambda_1(\bar{\mathbf{U}}) \tag{3.81}$$

Hence, it must hold

$$\lambda_1(\mathbf{U}) = S\left(2\frac{\phi}{\bar{c}} - 1\right) > \underbrace{S\left(\frac{\phi + \bar{\phi}}{\bar{c}} - 1\right)}_{s} > S\left(2\frac{\bar{\phi}}{\bar{c}} - 1\right) = \lambda_1(\bar{\mathbf{U}}). \tag{3.82}$$

This is fulfilled if

$$\phi > \bar{\phi}, \tag{3.83}$$

which geometrically means that, for the chosen coordinate system, $\mathbf{U}$ must be located right of $\bar{\mathbf{U}}$ in the state space.

Rarefaction waves

Each eigenvector $\mathbf{r}_k$ of the given system defines a vector field in state space. The rarefaction waves travel along the integral curves of these vector fields. As the tangent vector in an arbitrary point of the integral curve is given by the eigenvector defining the vector space, a parametrisation for the respective integral curve can be found. At every point in the state space, the eigenvector of the 1-family is given by $\mathbf{r}_1 = (1, 0)^T$. Since the eigenvector r_1 needs to be a tangent vector at every point of the integral curve, it holds that the derivative of the integral curve takes the form

$$I_1'(\xi) = \alpha(\xi) \cdot \mathbf{r}_1(\xi). \tag{3.84}$$

Set $\alpha(\xi) \equiv 1$, assuming the integral curve is parametrised by ϕ and is passing through a point $\bar{\mathbf{U}} = (\bar{\phi}, \bar{c})^T$, the integral curve is given by

$$I_1(\xi) = \begin{pmatrix} \xi \\ \bar{c} \end{pmatrix}. \tag{3.85}$$

It can be seen that for the 1-family, the curve defining the Hugoniot-locus H_1 (3.79) coincides with the integral curve I_1 (3.85).
In the previous subsection, it has been shown that the 0-field is linearly degenerate with constant eigenvalue $\lambda_0 = 0$. The integral curve and the Hugoniot-locus in a linear degenerate field always coincide. This can easily be verified in this case. Starting with

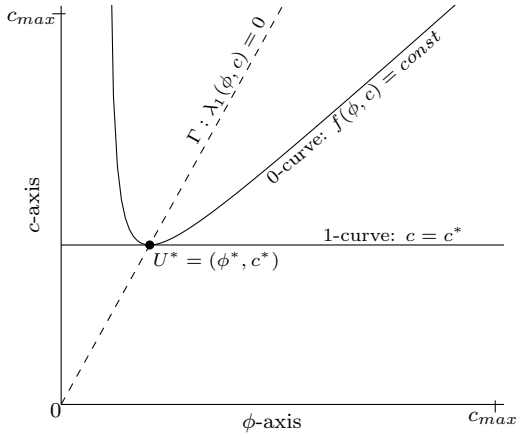

FIGURE 3.7: Plot of the integral curves passing through a critical point $\mathbf{U}^* = (\phi^*, c^*)^T$ and the transition line Γ in state space.

the same approach as for the 1-field, the parametrisation of the integral curve of the 0-field with eigenvector $\mathbf{r}_0$ leads to a curve that is identical to the one defining the Hugoniot-locus $H_0(\xi)$ (3.77). As the speed along a curve H_0 does not vary, it has been deduced that the only admissible solution is a standing wave and cannot be a rarefaction wave.

The Hugoniot-loci coincide with the integral curves for both fields. Therefore, they will not be distinguished and will be called in the following 0-curve and 1-curve. A plot of the state space with these two curves, passing through a critical state together with the transition curve Γ is shown in Figure 3.7. One can see, that the 0-curve is convex and the 1-curve is a straight line. Both curves intersect the transition line only ones. Following, there is only one critical point on each 0-curve and each 1-curve. At a critical state, the 1-curve is a tangent to a 0-curve passing through the same critical state. For an arbitrary state $\mathbf{U}$, there is only one curve of both kinds passing it.

Similar to (3.78), the 0-curve can be given by the set

$$\mathbb{H}_0 = \{\mathbf{U} | f(\mathbf{U}) = const.\} \tag{3.86}$$

This can directly be seen, since

$$\mathbf{r}_0 = \left(\frac{\phi^2}{c^2}, 2\frac{\phi}{c} - 1\right)^T = (\partial_c f, -\partial_\phi f)^T \tag{3.87}$$

which is the tangent vector to a level line of the scalar field defined by the segregation flux f. Hence, the integral curve is given by a level line of the flux function defined by (3.86). With the found expressions for the integral curves and the entropy conditions, the Riemann problem can be uniquely solved. Summarising the results, the following procedure shows how an admissible combination of waves can be constructed.

Scheme 3.1
A unique solution to the Riemann problem (3.72)-(3.71) *can be found by fulfilling the following conditions:*

1. *A contact discontinuity with speed zero (standing wave) travels along the* 0 *- curve but is not allowed to cross the transition curve* Γ.

2. *A shock connecting two states* $\mathbf{U}_L$ *and* $\mathbf{U}_R$ *travels along the* 1*-curve and is only admissible if* $\mathbf{U}_L$ *is located right of* $\mathbf{U}_R$ *(*$\phi_L > \phi_R$*).*

3. *A rarefaction wave connecting two states* $\mathbf{U}_L$ *and* $\mathbf{U}_R$ *travels along the* 1*-curve and is only physical if* $\mathbf{U}_L$ *is located left of* $\mathbf{U}_R$ *(*$\phi_L < \phi_R$*).*

To guarantee that a solution does not become double valued, the speeds of a combination of waves must increase. Mind that the chosen name of the integral curves has no bear on the order waves must travel the curves. Despite the waves along the 0-curve always have speed zero, the wave speed along the 1-curve can be both, positive and negative. This depends on the location of the states, as the transition line Γ separates the state space in a region where $\lambda_1 > 0$ and a region where $\lambda_1 < 0$.
Depending on the location of the left Riemann state $\mathbf{U}_L$ in relation to the transition line, one can find ten different combinations of waves to connect to a state $\mathbf{U}_R$. Hence, there are ten different regions in the state space for the position of $\mathbf{U}_R$ that lead to one of the ten wave combinations. In Figure 3.8, these regions are plotted. Six regions if $\mathbf{U}_L$ is located left of the transition line Γ and four if $\mathbf{U}_L$ is located right of Γ. Each area is numbered and coloured to distinguish from the others. The regions are mainly separated by curves passing through the points $\mathbf{U}^*$ and $\tilde{\mathbf{U}}$, where $\mathbf{U}^*$ is the intersection of the 1-curve through $\mathbf{U}_L$ and the transition line Γ. The state $\tilde{\mathbf{U}}$ is the intersection point of the 0-curve through $\mathbf{U}_L$ and the transition line. The volume fraction of a particle phase must not be larger than the granular volume fraction c. Therefore, all states in the state space where $\phi > c$ are forbidden.

Following the previously stated procedure, one can find the admissible wave solutions for each of the 10 configurations. A solution of a strictly hyperbolic system consists of a combination of two, not necessarily different, waves. As the system is not strictly

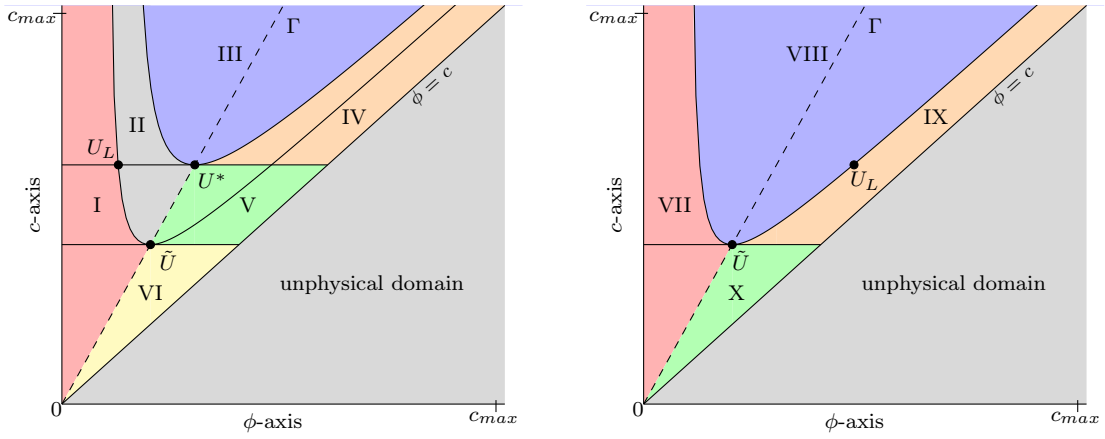

FIGURE 3.8: Different regions for $\mathbf{U}_R$ depending on $\mathbf{U}_L$ which yield different Riemann solutions for a convex segregation flux. Six regions if $\mathbf{U}_L$ is located left of the transition line Γ *(left Picture)* and four regions if $\mathbf{U}_L$ is located right of Γ *(right Picture)*. The lower right part defines an unphysical area, as $\phi > c$.

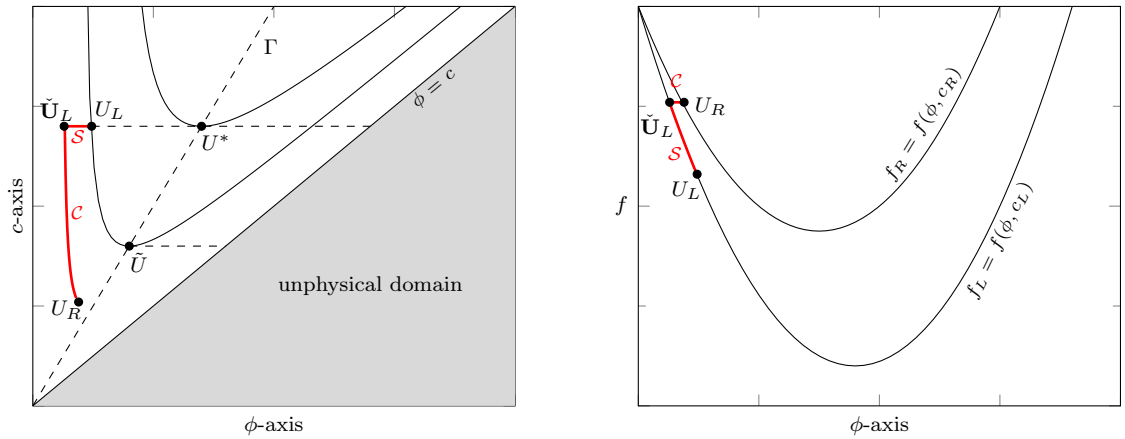

FIGURE 3.9: **(1)** Example showing the wave solution in state space *(left)*. $\mathbf{U}_L$ is located left of the transition line Γ and $\mathbf{U}_R$ in region I shown in Figure 3.8, where $\phi_R < \frac{c_R}{2}$ and $f(\mathbf{U}_R) > f(\mathbf{U}_L)$. The solution consists of two basic waves, a shock $(\mathbf{U}_L, \check{\mathbf{U}}_L)$ with negative speed $s = (f(\check{\mathbf{U}}_L) - f(\mathbf{U}_L))/(\check{\phi}_L - \phi_L) < 0$ and a contact discontinuity $(\check{\mathbf{U}}_L, \mathbf{U}_R)$ with speed zero (standing wave). Furthermore, the flux function for a left and a right state is plotted *(right)*. The wave solution is highlighted. The flux curves are connected by the contact discontinuity. The resulting average boundary flux is given by $\bar{F} = f(\mathbf{U}_R)$.

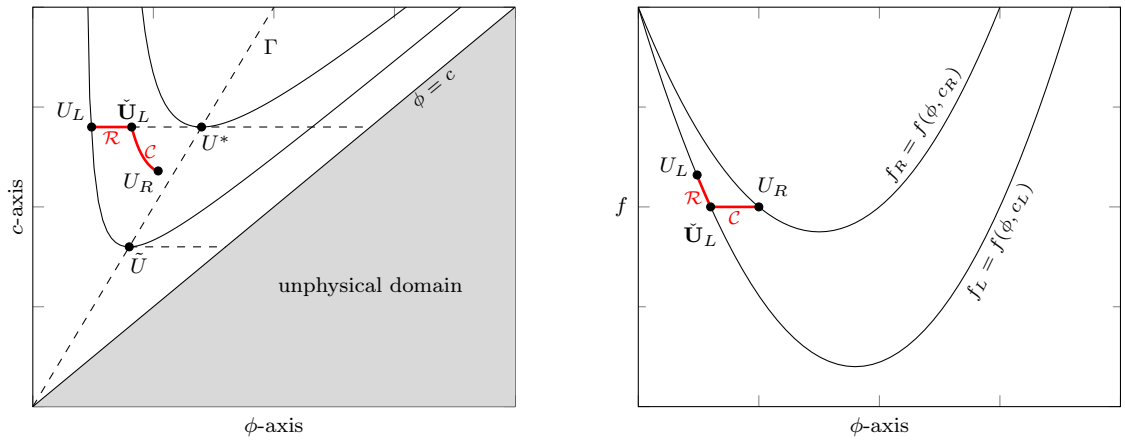

FIGURE 3.10: **(2)** Example showing the wave solution in state space *(left)*. $\mathbf{U}_L$ is located left of the transition line Γ and $\mathbf{U}_R$ in region II shown in Figure 3.8, where $\phi_R < \frac{c_R}{2}$ and $f(\mathbf{U}^*) \leq f(\mathbf{U}_R) < f(\mathbf{U}_L)$. The solution consists of two basic waves, a rarefaction $(\mathbf{U}_L, \check{\mathbf{U}}_L)$ with characteristic speed $\lambda_1(\phi, c_L) < 0$ and a contact discontinuity $(\mathbf{U}_1, \mathbf{U}_R)$ with speed zero (standing wave). Furthermore, the flux function for a left and a right state is plotted *(right)*. The wave solution is highlighted. The flux curves are connected by the contact discontinuity. The resulting average boundary flux is given by $\bar{F} = f(\mathbf{U}_R)$.

hyperbolic, the solution of the Riemann problem can consist of up to three different waves as one will see soon. The solution to each of the 10 cases is plotted in the Figures 3.9-3.18, where shock waves are denoted by $\mathcal{S}$, rarefaction waves by $\mathcal{R}$, and contact discontinuities by C.

With the constructed solutions for the Riemann problem (3.72), it is possible to construct a finite volume method for computing the admissible solutions, which will be done in the

upcoming chapter. Therefore, the average flux at the cell boundary at $z = 0$ over some time interval Δt is of interest. It is defined by

$$\bar{F}_0 = \frac{1}{\Delta t} \int_0^{\Delta t} f(\mathbf{U}(0,t))dt. \tag{3.88}$$

An admissible approximation for this boundary flux can be deduced from the solutions of the Riemann problem. As already mentioned, the Figures 3.9-3.18 present the solutions and give the boundary flux $\bar{F}$. Additionally, for each case, the fluxes of the left and right states are plotted. For physical left and right states, the fluxes are convex curves with $f(\phi, c) \leq 0$. The connected states and wave solutions are highlighted in these plots.

Example 3.1 (Two-Wave-Solution)
Assume the case, where $\mathbf{U}_L$ is located left of the transition line, i.e.,

$$\phi_L < \frac{c_L}{2}.$$

Further, assume $\mathbf{U}_R$ is in region I shown in Figure 3.8. It holds

$$\phi_R < \frac{c_R}{2}$$

and

$$f(\mathbf{U}_R) \geq f(\mathbf{U}_L).$$

Then, the solution depicted in Figure 3.9 consists of two basic waves with the intermediate state $\check{\mathbf{U}}_L = (\check{\phi}_L, c_L)$, where $f(\check{\mathbf{U}}_L) = f(\mathbf{U}_R)$.

1. *The wave $(\mathbf{U}_L, \check{\mathbf{U}}_L)$ is a shock with negative speed $s = \frac{f(\check{\mathbf{U}}_L) - f(\mathbf{U}_L)}{\check{\phi}_L - \phi_L} < 0$.*
2. *The wave $(\check{\mathbf{U}}_L, \mathbf{U}_R)$ is a contact discontinuity with speed zero (standing wave).*

The resulting average boundary flux for Example 3.1 is given by $\bar{F} = f(\check{\mathbf{U}}_L) = f(\mathbf{U}_R)$. A solution consisting of three different waves is depicted in Figure 3.11.

Example 3.2 (Three-Wave-Solution)
Let $\mathbf{U}_L$ be located left of the transition line, i.e.,

$$\phi_L < \frac{c_L}{2}.$$

The right state $\mathbf{U}_R$ is located in region III shown in Figure 3.8. It holds

$$f(\mathbf{U}_R) < f(\mathbf{U}^*) < f(\mathbf{U}_L).$$

1. *The wave $(\mathbf{U}_L, \mathbf{U}^*)$ is a rarefaction with characteristic speed $\lambda_1(\phi, c_L) < 0$.*
2. *$(\mathbf{U}^*, \check{\mathbf{U}}_R)$ is a standing wave.*

3. *The wave* $(\check{\mathbf{U}}_R, \mathbf{U}_R)$ *is a shock with positive speed. The shock speed is given by* $s = \frac{f(\mathbf{U}_R) - f(\check{\mathbf{U}}_R)}{\phi_R - \check{\phi}_R} > 0$.

In the case given in example 3.2, an admissible average boundary flux is different to the fluxes gained from the left or right state. The boundary flux is given by $\bar{F} = f(\mathbf{U}_1) = f(\mathbf{U}^*)$. The state $\mathbf{U}^* = (\frac{c_L}{2}, c_L)$ is known, as it lies on the transition line. It defines the minimum of the flux function, i.e.,

$$\mathbf{U}^* = \underset{\mathbf{U}=(\phi, c_L)}{\operatorname{argmin}} f(\mathbf{U}). \tag{3.89}$$

In the following, the minimum of the flux function with fixed state c_L is denoted by f_L^{min}. Hence, $\bar{F} = f_L^{min}$.

Assume that the states $\mathbf{U}_L$ and $\mathbf{U}_R$ are physically admissible states of the system, i.e., $c > 0$ and $0 \leq \phi \leq c$. Then, it can be shown that for all found solutions, each state on one of the connecting integral curves and therefore, all intermediate states are also physically admissible states. Checking the given solutions in Figure 3.9-3.18, it can be seen that an unphysical state can theoretically only be reached for the regions I (Figure 3.9), VI (Figure 3.14), VII (Figure 3.15), $VIII$ (Figure 3.16) and X (Figure 3.18) if the 0-curve leaves the domain into the area where $\phi < 0$ or $\phi > c$. Let $f(\mathbf{U})$ be the segregation flux function and define

$$h(\mathbf{U}) \coloneqq \frac{f(\mathbf{U})}{S}, \tag{3.90}$$

then the 0-curve through a state $\bar{\mathbf{U}}$ can be given as graph of the function

$$g_{\bar{\mathbf{U}}}(\phi) = \frac{\phi^2}{h(\bar{\mathbf{U}}) + \phi}. \tag{3.91}$$

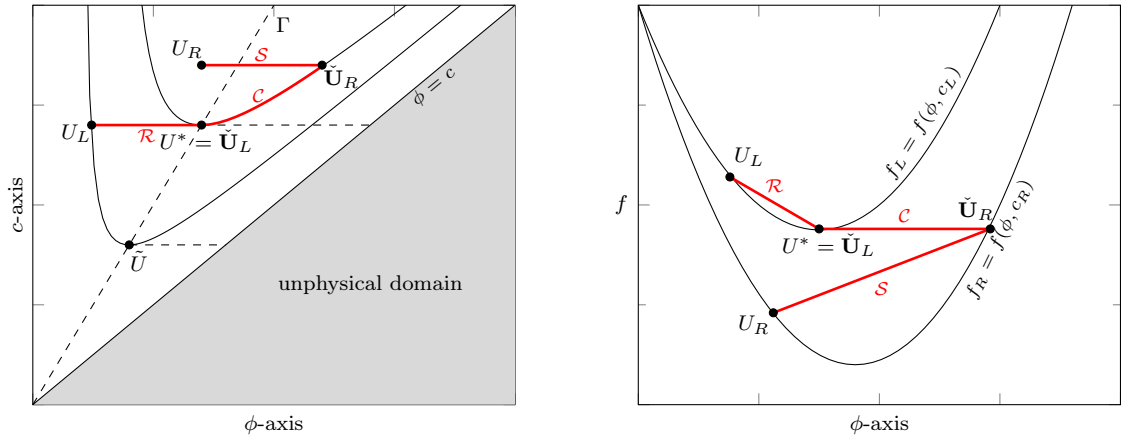

FIGURE 3.11: **(3)** Example showing the wave solution in state space *(left)*. $\mathbf{U}_L$ is located left of the transition line Γ and $\mathbf{U}_R$ in region III shown in Figure 3.8, where $f(\mathbf{U}_R) < f(\mathbf{U}^*) < f(\mathbf{U}_L)$. The solution consists of three basic waves, a rarefaction wave $(\mathbf{U}_L, \mathbf{U}^*)$ with characteristic speed $\lambda_1(\phi, c_L) < 0$, a standing wave $(\mathbf{U}^*, \check{\mathbf{U}}_R)$, and a shock wave $(\check{\mathbf{U}}_R, \mathbf{U}_R)$ with positive speed, given by $s = (f(\mathbf{U}_R) - f(\check{\mathbf{U}}_R)/(\phi_R - \check{\phi}_R) > 0$. Furthermore, the flux function for a left and a right state is plotted *(right)*. The wave solution is highlighted. The flux curves are connected by the contact discontinuity. The resulting average boundary flux is given by $\bar{F} = f_L^{min}$.

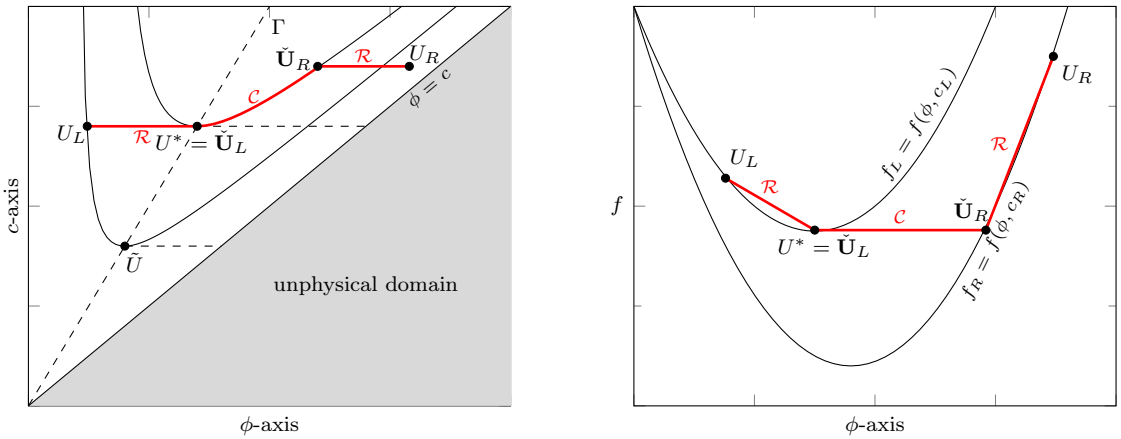

FIGURE 3.12: **(4)** Example showing the wave solution in state space *(left)*. $\mathbf{U}_L$ is located left of the transition line Γ and $\mathbf{U}_R$ in region IV shown in Figure 3.8, where $\phi_R > \frac{c_R}{2}$, $c_R > c^* = c_L$, and $f(\mathbf{U}_R) > f(\mathbf{U}^*)$. The solution consists of three basic waves, a rarefaction wave $(\mathbf{U}_L, \mathbf{U}^*)$ with characteristic speed $\lambda_1(\phi, c_L) < 0$, a standing wave $(\mathbf{U}^*, \check{\mathbf{U}}_R)$, and a second rarefaction wave $(\check{\mathbf{U}}_R, \mathbf{U}_R)$ with characteristic speed $\lambda_1(\phi, c_R) > 0$. Furthermore, the flux function for a left and a right state is plotted *(right)*. The wave solution is highlighted. The flux curves are connected by the contact discontinuity. The resulting average boundary flux is given by $\bar{F} = f_L^{min}$.

As the segregation flux for the small particle phase is less or equal to zero for all admissible states, $f(\mathbf{U}) \leq 0$, it holds $h(\mathbf{U}) \leq 0$, as $S > 0$. Therefore, it can be seen that $g_{\bar{\mathbf{U}}}$ has a pole at $\phi = -h(\bar{\mathbf{U}})$. Hence, the graph tends to infinity inside the admissible domain without reaching the area where $\phi < 0$.
Furthermore, the graph of $g_{\bar{\mathbf{U}}}$ approaches an asymptote given by

$$A_{\bar{\mathbf{U}}}(\phi) = \phi - h(\bar{\mathbf{U}}), \tag{3.92}$$

as $\phi \to \infty$. The asymptote is a line inside the physical domain, which is parallel to the boundary of the physical space defined by $\phi = c$. The 0-curve also does not cross the asymptote $A_{\bar{\mathbf{U}}}$, since it is convex between the pole and the asymptote. Hence, a physical state cannot leave the physical domain along the 0-curve.

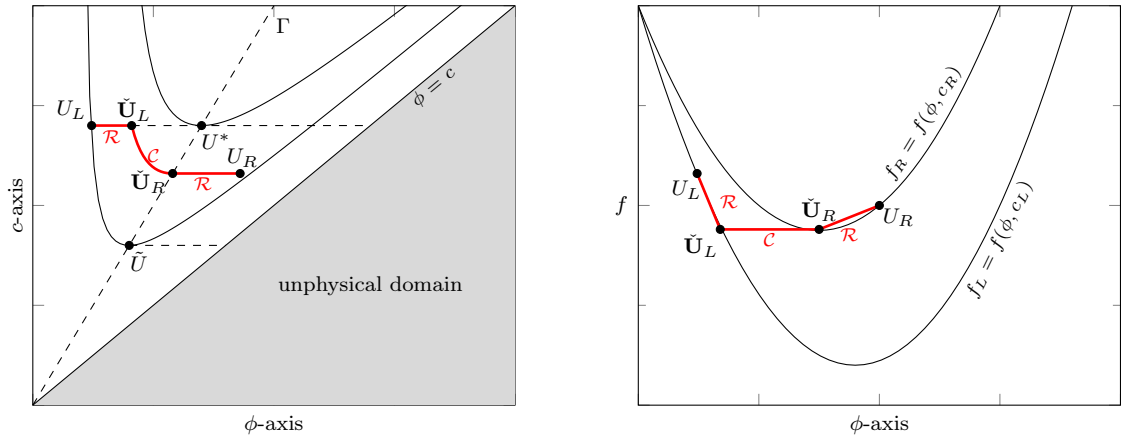

FIGURE 3.13: **(5)** Example showing the wave solution in state space *(left)*. $\mathbf{U}_L$ is located left of the transition line Γ and $\mathbf{U}_R$ in region V shown in Figure 3.8, where $\phi_R > \frac{c_R}{2}$, $\tilde{c} < c_R < c^* = c_L$, and $f(\mathbf{U}_R) > f(\mathbf{U}^*)$. The solution consists of three basic waves, a rarefaction wave $(\mathbf{U}_L, \check{\mathbf{U}}_L)$ with characteristic speed $\lambda_1(\phi, c_L) < 0$, a standing wave $(\check{\mathbf{U}}_L, \check{\mathbf{U}}_R)$, and a second rarefaction wave $(\check{\mathbf{U}}_R, \mathbf{U}_R)$ with characteristic speed $\lambda_1(\phi, c_R) > 0$. Furthermore, the flux function for a left and a right state is plotted *(right)*. The wave solution is highlighted. The flux curves are connected by the contact discontinuity. The resulting average boundary flux is given by $\bar{F} = f_R^{min}$.

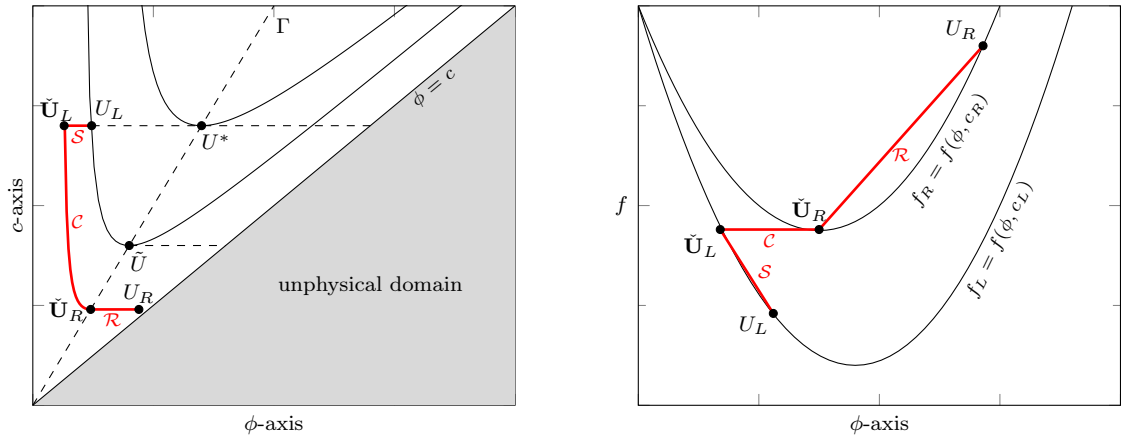

FIGURE 3.14: **(6)** Example showing the wave solution in state space *(left)*. $\mathbf{U}_L$ is located left of the transition line Γ and $\mathbf{U}_R$ in region VI shown in Figure 3.8, where $\phi_R > \frac{c_R}{2}$, $c_R < \tilde{c}$, and $f(\mathbf{U}_R) > f(\mathbf{U}_L)$. The solution consists of three basic waves, a negative shock $(\mathbf{U}_L, \check{\mathbf{U}}_L)$ with speed $s = (f(\check{\mathbf{U}}_L) - f(\mathbf{U}_L)/(\check{\phi}_L - \phi_L) < 0$, a standing wave $(\check{\mathbf{U}}_L, \check{\mathbf{U}}_R)$, and a rarefaction wave $(\check{\mathbf{U}}_R, \mathbf{U}_R)$ with characteristic speed $\lambda_1(\phi, c_R) > 0$. Furthermore, the flux function for a left and a right state is plotted *(right)*. The wave solution is highlighted. The flux curves are connected by the contact discontinuity. The resulting average boundary flux is given by $\bar{F} = f_R^{min}$.

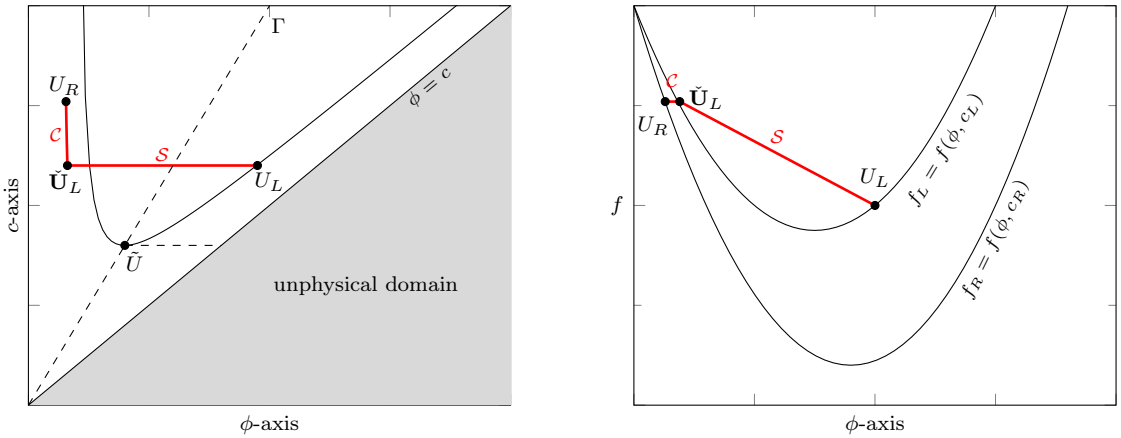

FIGURE 3.15: **(7)** Example showing wave solution in state space *(left)*. $\mathbf{U}_L$ is located right of the transition line Γ and $\mathbf{U}_R$ in region VII shown in Figure 3.8, where $\phi_R < \frac{c_R}{2}$ and $f(\mathbf{U}_R) > f(\mathbf{U}_L)$. The solution consists of two basic waves, a negative shock $(\mathbf{U}_L, \check{\mathbf{U}}_L)$ with speed $s = (f(\check{\mathbf{U}}_L) - f(\mathbf{U}_L)/(\check{\phi}_L - \phi_L) < 0$ and a standing wave $(\check{\mathbf{U}}_L, \mathbf{U}_R)$. Furthermore, the flux function for a left and a right state is plotted *(right)*. The wave solution is highlighted. The flux curves are connected by the contact discontinuity. The resulting average boundary flux is given by $\bar{F} = f(\mathbf{U}_R)$.

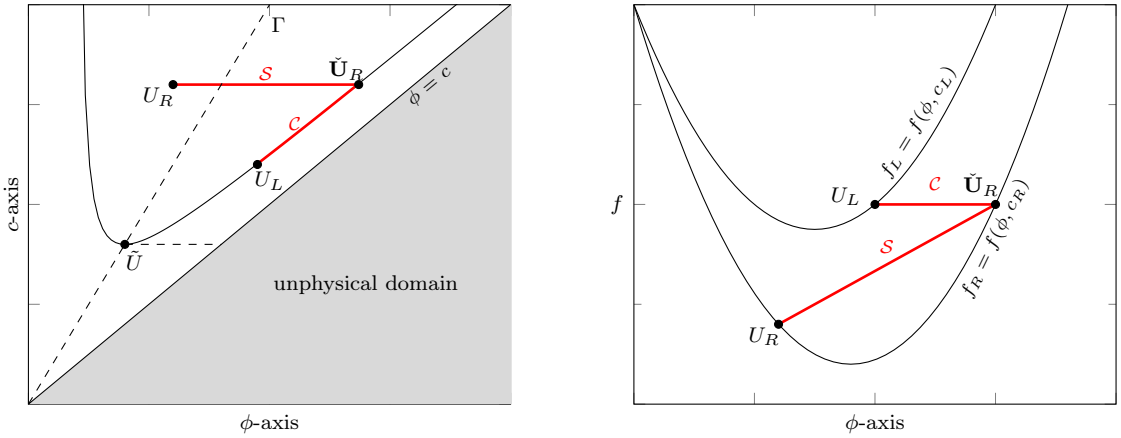

FIGURE 3.16: **(8)** Example showing the wave solution in state space *(left)*. $\mathbf{U}_L$ is located right of the transition line Γ and $\mathbf{U}_R$ in region VIII shown in Figure 3.8, where $f(\mathbf{U}_R) < f(\mathbf{U}_L)$. The solution consists of two basic waves, a standing wave $(\mathbf{U}_L, \check{\mathbf{U}}_R)$ and a positive shock $(\check{\mathbf{U}}_R, \mathbf{U}_R)$ with speed $s = (f(\mathbf{U}_R) - f(\check{\mathbf{U}}_R)/(\phi_R - \check{\phi}_R) > 0$. Furthermore, the flux function for a left and a right state is plotted *(right)*. The wave solution is highlighted. The flux curves are connected by the contact discontinuity. The resulting average boundary flux is given by $\bar{F} = f(\mathbf{U}_L)$.

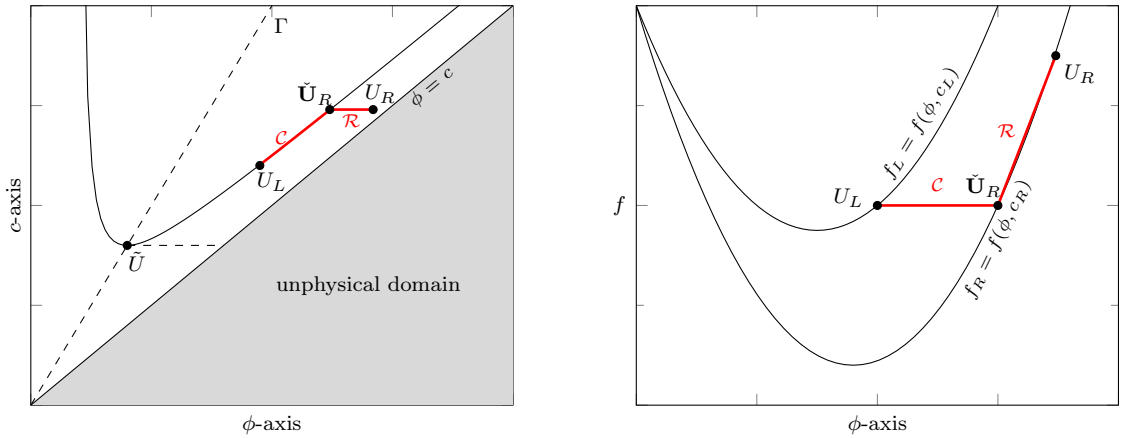

FIGURE 3.17: **(9)** Example showing the wave solution in state space *(left)*. $\mathbf{U}_L$ is located right of the transition line Γ and $\mathbf{U}_R$ in region IX shown in Figure 3.8, where $\phi_R > \frac{c_R}{2}$, $c_R > \tilde{c}$, and $f(\mathbf{U}_R) > f(\mathbf{U}_L)$. The solution consists of two basic waves, a standing wave $(\mathbf{U}_L, \check{\mathbf{U}}_R)$ and a rarefaction wave $(\check{\mathbf{U}}_R, \mathbf{U}_R)$ with characteristic speed $\lambda_1(\phi, c_R) > 0$. Furthermore, the flux function for a left and a right state is plotted *(right)*. The wave solution is highlighted. The flux curves are connected by the contact discontinuity. The resulting average boundary flux is given by $\bar{F} = f(\mathbf{U}_L)$.

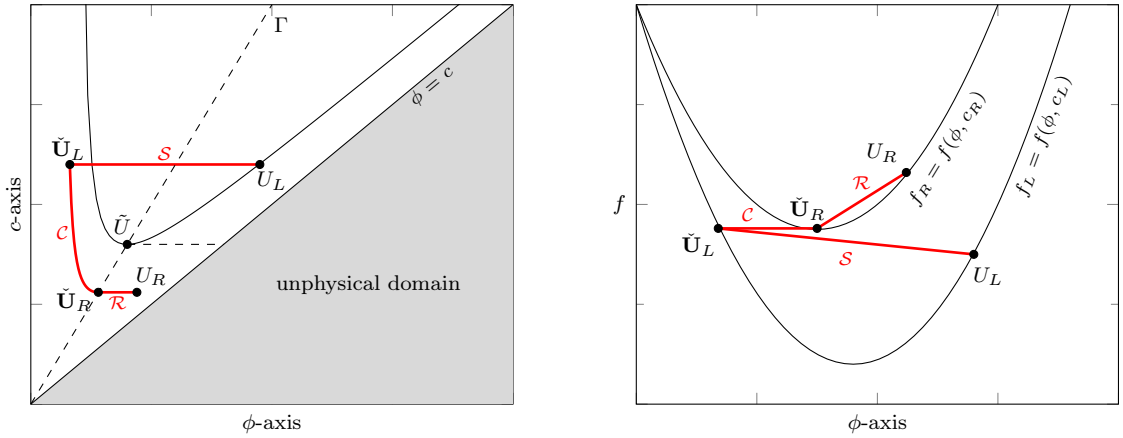

FIGURE 3.18: **(10)** Example showing the wave solution in state space *(left)*. $\mathbf{U}_L$ is located right of the transition line Γ and $\mathbf{U}_R$ in region X shown in Figure 3.8, where $\phi_R > \frac{c_R}{2}$, $c_R < \tilde{c}$, and $f(\mathbf{U}_R) > f(\mathbf{U}_L)$. The solution consists of three basic waves, a negative shock $(\mathbf{U}_L, \check{\mathbf{U}}_L)$ with speed $s = (f(\check{\mathbf{U}}_L) - f(\mathbf{U}_L)/(\check{\phi}_L - \phi_L) < 0$, a standing wave $(\check{\mathbf{U}}_L, \check{\mathbf{U}}_R)$, and a rarefaction wave $(\check{\mathbf{U}}_R, \mathbf{U}_R)$ with characteristic speed $\lambda_1(\phi, c_R) > 0$. Furthermore, the flux function for a left and a right state is plotted *(right)*. The wave solution is highlighted. The flux curves are connected by the contact discontinuity. The resulting average boundary flux is given by $\bar{F} = f_R^{min}$.

3.3.4 Solution to the Riemann problem for the segregation equation with non-constant temperature

Now assume that the temperature depends also on the spatial variable. For simplicity, $\gamma \coloneqq \sqrt{T}$ is used instead of the granular temperature to overcome the square root term. Analogous to the case where the temperature is constant, one can introduce another additional equation for γ and augment the segregation equation into a system of equations. In this case, the system is given by

$$\partial_t \phi + \partial_z \left(S\gamma \left(\frac{\phi}{c} - 1 \right) \phi \right) = 0, \tag{3.93a}$$

$$\partial_t c = 0, \tag{3.93b}$$

$$\partial_t \gamma = 0. \tag{3.93c}$$

Initially, the Riemann problem is given by

$$\mathbf{U}(z, t=0) = \begin{cases} \mathbf{U}_L \text{ if } z < 0, \\ \mathbf{U}_R \text{ if } z > 0, \end{cases} \tag{3.94}$$

with constant states $\mathbf{U}_L$ and $\mathbf{U}_R$, where the states in the state space are defined by $\mathbf{U} = (\phi, c, \gamma)^T$. Note that the state space is now three-dimensional. The linearised form of the system is

$$\partial_t \begin{pmatrix} \phi \\ c \\ \gamma \end{pmatrix} + \begin{pmatrix} S\gamma \left(2\frac{\phi}{c} - 1\right) & -S\gamma\frac{\phi^2}{c^2} & S\left(\frac{\phi}{c} - 1\right)\phi \\ 0 & 0 & 0 \\ 0 & 0 & 0 \end{pmatrix} \partial_z \begin{pmatrix} \phi \\ c \\ \gamma \end{pmatrix} = 0. \tag{3.95}$$

The eigenvalues of the system are

$$\lambda_0 = 0, \qquad \lambda_1 = 0, \qquad \lambda_2 = S\gamma \left(2\frac{\phi}{c} - 1 \right) \tag{3.96}$$

and the corresponding right eigenvectors are

$$\mathbf{r}_0 = \begin{pmatrix} \frac{\phi^2}{c^2} \\ \left(2\frac{\phi}{c} - 1\right) \\ 0 \end{pmatrix}, \qquad \mathbf{r}_1 = \begin{pmatrix} \left(1 - \frac{\phi}{c}\right)\phi \\ 0 \\ \gamma\left(2\frac{\phi}{c} - 1\right) \end{pmatrix}, \qquad \mathbf{r}_2 = \begin{pmatrix} 1 \\ 0 \\ 0 \end{pmatrix}. \tag{3.97}$$

The system has three characteristic fields, where the 0-field and the 1-field are linearly degenerate. Since no segregation happens in a static system, where the granular temperature is zero, one can restrict to the case that $T > 0$, and therefore $\gamma > 0$. Under these assumptions the 2-field is genuinely non-linear, as

$$\nabla\lambda_2(\mathbf{U}) \cdot \mathbf{r}_2(\mathbf{U}) \;=\; S\gamma\frac{2}{c} \;\neq\; 0 \quad \forall \mathbf{U}. \tag{3.98}$$

Similar to the analysed two-dimensional system, a critical state $\mathbf{U}^* = (\phi^*, c^*, \gamma^*)^T$ is defined by

$$\lambda_2(\mathbf{U}^*) = 0. \tag{3.99}$$

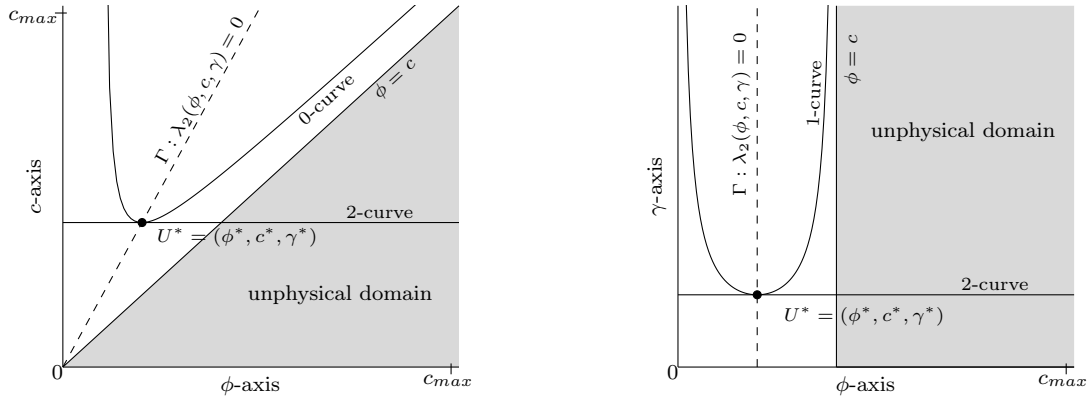

FIGURE 3.19: Plot of the integral curves, defined in (3.103), passing through a critical point $\mathbf{U}^* = (\phi^*, c^*, \gamma^*)^T$ and the transition line Γ. The curves are depicted in the state space, where the 0-curve lies in the ϕ-c-plane *(left)* and the 1-curve lies in the ϕ-γ-plane *(right)*.

In the three-dimensional system, the set of critical states forms a transition surface

$$\Gamma = \{\mathbf{U} | \lambda_2(\mathbf{U}) = 0\} \tag{3.100}$$

$$= \{(\phi, c, \gamma)^T | c = 2\phi, \quad \gamma \in \mathbb{R}^+\}. \tag{3.101}$$

Let $\bar{\mathbf{U}}$ be a state in the state space. As the Hugoniot-loci and the integral curves again coincide for all three fields, a parametrisation can be found starting from the ansatz

$$I_k'(\xi) = \alpha(\xi) \cdot \mathbf{r}_k. \tag{3.102}$$

Parametrising by ϕ and assuming that $I(\bar{\phi}) = (\bar{\phi}, \bar{c}, \bar{\gamma})^T$, the three curves can be written by

$$I_0(\xi) = \begin{pmatrix} \xi \\ \frac{\xi^2}{\left(\frac{\bar{\phi}}{\bar{c}} - 1\right)\bar{\phi} + \xi} \\ \bar{\gamma} \end{pmatrix}, \qquad I_1(\xi) = \begin{pmatrix} \xi \\ \bar{c} \\ \frac{\bar{\gamma}\bar{\phi}(\bar{\phi} - \bar{c})}{\xi(\xi - \bar{c})} \end{pmatrix}, \qquad I_2(\xi) = \begin{pmatrix} \xi \\ \bar{c} \\ \bar{\gamma} \end{pmatrix}. \tag{3.103}$$

The 0-wave and the 1-wave are contact discontinuities with speed zero, whereas along the 2-curve either shocks, or rarefaction waves can be the admissible solution. The respective curves defined in (3.103) are plotted in Figure 3.19.

The derived 0-curve and the 1-curve lie in the ϕ-c-plane and the ϕ-γ- plane, respectively. The representation of the 0-curve is identical to the one described in the last subsection for the constant temperature case. Hence, the 0-curve does not leave the physically admissible domain. The same holds true for the 1-curve, which can be given by a graph in the ϕ-γ-plane. Defining

$$h(\mathbf{U}) \coloneqq \frac{c f(\mathbf{U})}{S}, \tag{3.104}$$

where $f(\mathbf{U})$ is the segregation flux function, the graph representing the 1-curve through a state $\bar{\mathbf{U}}$ can be given by

$$g_{\bar{\mathbf{U}}}(\phi) = \frac{h(\bar{\mathbf{U}})}{\phi(\phi - \bar{c})}. \tag{3.105}$$

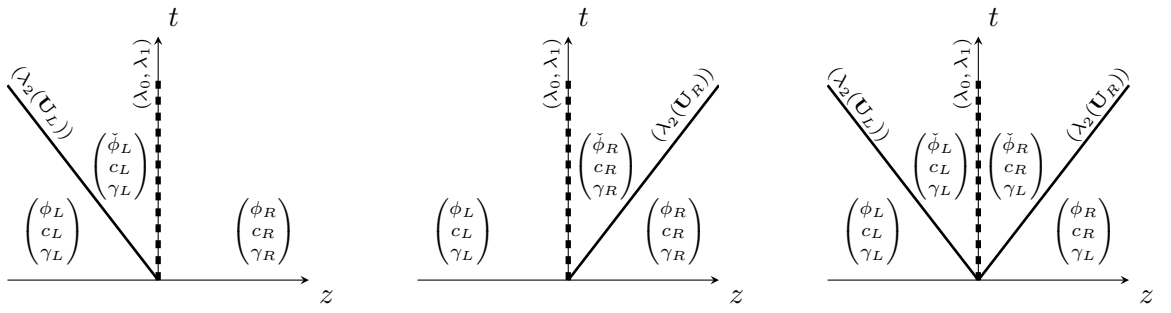

FIGURE 3.20: Structure of the Riemann solution with non-constant temperature. The solution consists either of a left going wave and a contact discontinuity with speed zero *(left)*, a contact discontinuity and a right going wave *(middle)*, or a left going wave, a contact discontinuity and a right going wave *(right)*. Each wave can be a shock or a rarefaction. The algebraic sign of the characteristic speed, given by λ_2, depends on the location of the respective state. To distinguish the contact discontinuity and the t-axis, the contact discontinuity is drawn by a dashed line.

To stay in the admissible domain the curve must not enter the region where $\phi < 0$ or $\phi > \bar{c}$. Since $h(\mathbf{U})$ is bounded, it holds

$$g_{\bar{\mathbf{U}}}(\phi) \to \infty \tag{3.106}$$

for $\phi \to 0$ and also for $\phi \to \bar{c}$. Hence, the 1-curve stays in the admissible domain and therefore, a combination of the 0-curve and the 1-curve.
This is relevant, since the defined curves are not the unique wave paths. As $\lambda_0 = \lambda_1$, each linear combination of the respective eigenvectors $\mathbf{r}_0$ and $\mathbf{r}_1$ is again an eigenvector and would define a suitable direction for a wave in the state space. In general, such a problem has no unique solution as the path in the state space is not clear.

However, it turns out that it is not necessary to know the exact path of the standing waves to finally solve the problem. As it has been done for the smaller system in the last section, applying entropy condition 5 solves the problem how to handle a solution around the transition plane, where also $\lambda_2 = 0$. Hence, one has to deal with the 0-curve and 1-curve on the respective side of the transition plane. Fortunately, the given system does not lead to problems, as both fields are linearly degenerate. This case coincides with the system of Euler equations in multiple space dimensions, where for each space dimension a contact discontinuity is given with equal characteristic speed (compare Toro [77]). For the segregation equation, the solution can be depicted as shown in Figure 3.20. The solution is similar to the solution derived for the system with constant temperature in the last subsection. It consists either of a left going wave and a contact discontinuity with speed zero or a contact discontinuity and a right going wave or a left going wave, a contact discontinuity and a right going wave.
Each wave can be a shock or a rarefaction depending on the states. The shock speed connecting an arbitrary state $\mathbf{U}$ to a state $\bar{\mathbf{U}}$ can be computed by the Rankine-Hugoniot condition 3.1 and yields similar to (3.80)

$$s = S\bar{\gamma}\left(\frac{\phi + \bar{\phi}}{\bar{c}} - 1\right) \tag{3.107}$$

The admissibility of a shock solution can be verified by Lax's entropy condition (EC 4). It follows that an entropy fulfilling shock wave is given if

$$\phi > \bar{\phi}. \tag{3.108}$$

Although the exact path of the contact discontinuity in state space is not known, it will be shown in subsection 4.3.2 and section 5.2 that a natural extension of the derived numerical method of the constant temperature system yields similar good results.

Chapter 4

Numerics

The software platform CoRheoS (Complex Rheology Solvers) is a development of the department "Flow and Material Simulation" of Fraunhofer ITWM. It includes the granular finite volume solver GRAIN. The granular flow model, which has been explained in section 2.1 is implemented in this solver. One goal of this thesis is to extend the GRAIN solver by the segregation model derived in section 2.2. This chapter deals with numerically solving the segregation equation in an adequate way to combine it with the already existing implementations in GRAIN.
Several tools to solve partial differential equations numerically are applicable today, like finite differences, finite volumes or finite element methods. This work is restricted to the method of finite volumes for several reasons. One is to fit into the framework of the GRAIN solver. Another is concerned with the mathematical properties of the segregation equation. As already experienced in the previous sections, the solution of non-linear hyperbolic equations, like the segregation equation, can contain discontinuities which lead to computational difficulties. Methods like the finite difference method which approximate derivatives by finite differences may break down near those discontinuities. Further, the number of particles of a specific type and therefore its volume fraction, which is of interest, is a quantity that should be conserved. As finite volume methods are based on the integral form of the differential equation, they conserve quantities per construction if the underlying differential equation can be given in conservation form. After introducing words about finite volumes and dealing with the discretisation of the segregation equation, a modified version of Godunov's scheme is presented, based on the solution of the Riemann problem analysed in section 3.3. The information stated in this chapter and even more details can be found in [57] or [77].

4.1 Discretisation using finite volumes

The finite volume method (FVM) is based on the subdivision of a spatial domain into non-overlapping "finite volumes", also called control volumes or grid cells. Let

$$\partial_t q + \nabla \cdot \mathbf{f}(q) = 0 \tag{4.1}$$

be a scalar conservation law on the spatial domain $\Omega \subset \mathbb{R}^d$. Further, let C_i denote the i-th control volume of the mesh subdividing the domain. Then it holds

$$\Omega = \bigcup_{i \in \mathcal{I}} C_i, \tag{4.2}$$

FIGURE 4.1: Top- and bottom-view of a control volume C_i of some equidistant grid in three-dimensional space showing the notation of the different faces. The cell wall σ_E is highlighted in red. In both views σ_S, which is located opposite of σ_N, is hidden.

where $\mathcal{I}$ defines some index set. In this work, a cell-centred finite volume scheme is used, which means that discrete evaluations of the quantity of the conservation law (4.1) are made in the centre point $\mathbf{x}_i \in \mathbb{R}^d$ of cell C_i.

The FVM works with the integral of q over each of the control volumes C_i and updates them over time by evaluating the fluxes through the parts of the boundary of each control volume. The approximated average value of q over the i-th control volume at some time t_n can be given by

$$Q_i^n \approx \frac{1}{|C_i|} \int_{C_i} q(\mathbf{x}, t_n)\, d\mathbf{x}. \tag{4.3}$$

For the discretisation with the finite volume method, one integrates the equation (4.1) over the control volume C_i, which leads to

$$\int_{C_i} \partial_t q(\mathbf{x}, t)\, d\mathbf{x} + \int_{C_i} \nabla \cdot \mathbf{f}(q(\mathbf{x}, t))\, d\mathbf{x} = 0. \tag{4.4}$$

For the second term, the Gauß theorem can be applied, giving

$$\int_{C_i} \partial_t q(\mathbf{x}, t)\, d\mathbf{x} + \int_{\partial C_i} \mathbf{f}(q(\mathbf{x}, t)) \cdot \mathbf{n}_{C_i}\, ds = 0, \tag{4.5}$$

where $\mathbf{n}_{C_i}$ defines the control volume's outer normal vector. Furthermore, the boundary of the control volume ∂C_i can be subdivided into parts. If the control volume C_i is a polyhedron, one normally chooses each boundary part σ_k equal to one of the polyhedrons faces. Hence,

$$\int_{C_i} \partial_t q(\mathbf{x}, t)\, d\mathbf{x} + \sum_k \int_{\sigma_k} \mathbf{f}(q(\mathbf{x}, t)) \cdot \mathbf{n}_{\sigma_k}\, ds = 0. \tag{4.6}$$

In this work, it is assumed that the underlying grid for the discretisation is equidistant and rectangular. Each control volume is given by a cube where the face outer normal vectors are given by the canonical unit vectors. For a better understanding the faces are denoted by σ_N (north), σ_E (east), σ_S (south), σ_W (west), σ_T (top), and σ_B (bottom), in the three-dimensional case as depicted in Figure 4.1.
Defining

$$f_{\sigma_k}(t) = \int_{\sigma_k} f(q(\mathbf{x}, t)) \cdot \mathbf{n}_{\sigma_k}\, ds, \tag{4.7}$$

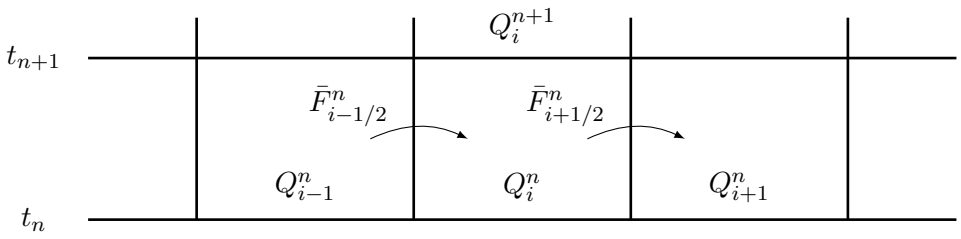

FIGURE 4.2: Sketch of the finite volume method. Updating process of Q_i^n by the fluxes through the cell walls of a one-dimensional equation depicted in x-t-space.

equation (4.6) can shortly be written as

$$\int_{C_i} \partial_t q(\mathbf{x}, t)\, d\mathbf{x} + \sum_k f_{\sigma_k}(t) = 0. \tag{4.8}$$

Integrating equation (4.8) over the time interval $[t_n, t_{n+1}]$ and additionally dividing by $|C_i|$ yields

$$\frac{1}{|C_i|}\int_{C_i} q(\mathbf{x}, t_{n+1})\, d\mathbf{x} = \frac{1}{|C_i|}\int_{C_i} q(\mathbf{x}, t_n)\, d\mathbf{x} - \frac{1}{|C_i|}\sum_k \int_{t_n}^{t_{n+1}} f_{\sigma_k}(t)\, dt. \tag{4.9}$$

Using (4.3), a numerical method to update the cell averages of q, which is explicit in time, takes the form

$$Q_i^{n+1} = Q_i^n - \frac{\Delta t}{|C_i|}\sum_k \bar{F}_{\sigma_k}^n, \tag{4.10}$$

where

$$\bar{F}_{\sigma_k}^n \approx \frac{1}{\Delta t}\int_{t_n}^{t_{n+1}} f_{\sigma_k}(t)\, dt \tag{4.11}$$

defines an approximation of the average flux through the boundary part σ_k and $\Delta t = t_{n+1} - t_n$ is the time step. Procedure (4.10) simply states that the cell average at the new time step t_{n+1} is given by the cell average at the old time step t_n and the flux through all parts of the control volume's boundary in the given time interval Δt.

This can be clarified, assuming only one space dimension $\Omega = (a, b)$, as depicted in Figure 4.2, which sketches the FVM in the x-t-space. The equidistant grid is given by $a = x_{-1/2} < x_0 < \cdots < x_N < x_{N+1/2} = b$ and the grid cells are defined by

$$C_i = (x_{i-1/2}, x_{i+1/2}), \tag{4.12}$$

where x_i defines the midpoint of cell i. The size of a cell is given by $\Delta x = x_{i+1/2} - x_{i-1/2}$. Then, equation (4.10) can be given more precisely by

$$Q_i^{n+1} = Q_i^n - \frac{\Delta t}{\Delta x}(\bar{F}_{i+1/2}^n - \bar{F}_{i-1/2}^n), \tag{4.13}$$

where $\bar{F}_{i-1/2}^n$ is some approximation to the average flux along $x = x_{i-1/2}$.
To get a fully discrete method, the average fluxes $\bar{F}^n$ need to be computed from the values Q^n. There are several methods on the market that obtain $\bar{F}_{i-1/2}^n$ based on the values of

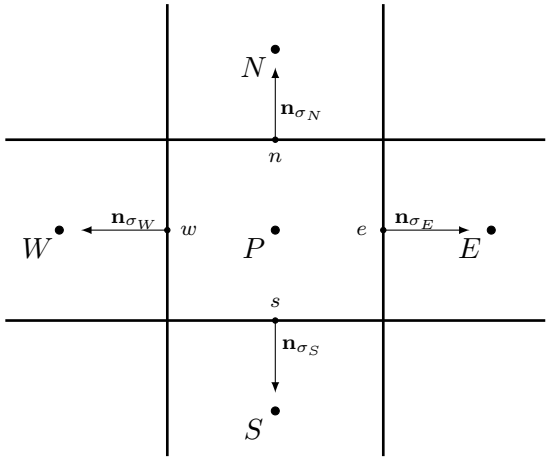

FIGURE 4.3: Sketch of a control volume with centre point P in the x-y-space showing the notation of the most important points for evaluations. All points $\mathbf{x}_k$ are given in the abbreviated form, written by k. Additionally, the outer normal vectors are drawn.

the neighbouring two cells Q_{i-1}^n and Q_i^n. This can be written using the notation of a numerical flux function

$$\bar{F}_{i-1/2}^n = \mathcal{F}(Q_{i-1}^n, Q_i^n). \tag{4.14}$$

The method (4.13) can be rewritten as

$$Q_i^{n+1} = Q_i^n - \frac{\Delta t}{\Delta x}(\mathcal{F}(Q_i^n, Q_{i+1}^n) - \mathcal{F}(Q_{i-1}^n, Q_i^n)), \tag{4.15}$$

which results in an explicit method with a three-point stencil. To obtain higher order methods, bigger stencils are necessary and thus, the values of more cells need to be taken into account in the numerical flux functions.
Having a cartesian grid in d-dimensional space with $d > 1$, the flux can be assumed to be one-dimensional in each coordinate direction. For example, the numerical flux of the cell wall σ_N depends on the state values of the cell midpoints of the neighbouring cells, depicted by P and N in Figure 4.3. For the different dimensions, only the size of the cell walls and the volume of the cells differs.

As mentioned in the beginning of this section, the work focuses on cell-centred cubic finite volumes. The only exception made, is in the simulation chapter 5 where the already implemented cut-cell method, as introduced in Neusius [65], is used to improve the approximation of the domain boundary. In these cut and, in some circumstances, merged cells, the cell information is not located in the geometric centre of the cell any more. Therefore, interpolations have to be made. Detailed descriptions and explanations are given in [65].

4.2 Numerical methods

After discussing the case of a general conservation law, the specific form of the segregation equation is investigated. In accordance to the previous section, the following question can be posed: How to find an appropriate boundary flux for the segregation equation which

takes into account the given data of the neighbouring cells? The segregation equation (2.106d), derived in chapter 2, can be given in the general form

$$\partial_t \phi + \nabla \cdot \mathbf{f}^t(\phi) + \nabla \cdot \mathbf{f}^s(\phi) = 0, \tag{4.16}$$

where $\mathbf{f}^t$ is the transport flux with the bulk material and $\mathbf{f}^s$ the segregation flux. For each cell wall σ_k, a numerical flux approximation is needed for both defined fluxes, $\mathbf{f}^t$ and $\mathbf{f}^s$. To simplify the notation presenting the numerical schemes in accordance to Figure 4.3, the evaluation of a function or quantity Υ at a specific position $\mathbf{x}_k$ at time t_n is denoted by $\Upsilon(k)$.
The flux function defining the transport with the granular bulk is given by

$$\mathbf{f}^t(\phi) = \phi \mathbf{u}. \tag{4.17}$$

The numerical scheme which is used for the transport of the small particle phase ϕ with the granular bulk, should coincide with the scheme which is used for the transport of the granular volume fraction c, computed by the mass balance (2.106a). This is done by using the upwind method.
Given a cell wall, e.g. σ_W, the flux $\bar{F}^t_{\sigma_W}$ is approximated with the data at time t_n. It holds

$$\bar{F}^t_{\sigma_W} \approx \int_{\sigma_W} \mathbf{f}^t(\phi(\mathbf{x}, t_n)) \cdot \mathbf{n}_{\sigma_W} \, ds_W. \tag{4.18}$$

Using the midpoint rule to compute the integral over the cell wall yields

$$\bar{F}^t_{\sigma_W} = \mathbf{f}^t(w) \cdot \mathbf{n}_{\sigma_W} |\sigma_W|, \tag{4.19}$$

where

$$\mathbf{f}^t(w) = \phi(w)\mathbf{u}(w). \tag{4.20}$$

The bulk velocity is known from the granular flow equations and is given in the cell centres. The value at the wall $\mathbf{u}(w)$ is a linear interpolation of the values in P and W. The value of $\phi(w)$ is unknown but can be approximated by the upwind scheme. The upwind scheme chooses the value at a cell wall depending on the transport velocity, i.e.,

$$\phi(w) = \begin{cases} \phi(W) & \text{if } \mathbf{u}(w) \cdot \mathbf{n}_{\sigma_W} > 0, \\ \phi(P) & \text{if } \mathbf{u}(w) \cdot \mathbf{n}_{\sigma_W} < 0. \end{cases} \tag{4.21}$$

For a transport process with given transport velocity, the upwind method leads to good numerical results. For non-linear flux functions like the segregation flux other methods are preferable, as it will be shown later on. The general idea to handle the segregation flux numerically is based on the scheme of Godunov. The following Algorithm 4.1 is a natural development to solve hyperbolic conservation laws numerically. It is called REA algorithm, which stands for *reconstruct-evolve-average*. The original approach given by Godunov uses this procedure with simple constant functions as reconstruction in each control volume.

Algorithm 4.1 (REA)

1. *Reconstruct a piecewise polynomial function $\tilde{q}(\mathbf{x}, t_n)$, defined for all $\mathbf{x}$, from the cell averages Q_i^n. In the simplest case, take a piecewise constant function given by*

$$\tilde{q}(\mathbf{x}, t_n) = Q_i^n \qquad \forall \mathbf{x} \in C_i.$$

2. *Evolve the hyperbolic equation exactly (or approximately) with this initial data to obtain $\tilde{q}(\mathbf{x}, t_{n+1})$ one time step Δt later.*

3. *Average this function over each control volume to obtain new cell averages*

$$Q_i^{n+1} = \frac{1}{|C_i|} \int_{C_i} \tilde{q}(\mathbf{x}, t_{n+1})\, d\mathbf{x}.$$

4. *Repeat the whole procedure for each time step.*

Using Godunov's approach with constant data in each cell, the "evolve"-step 2 coincides with solving a Riemann problem at each cell wall. If the solution of the Riemann problem at the cell wall σ_W is known, one can define the numerical flux and gains a numerical scheme of the desirable form (4.10).
As the cell data are constant, the value $\tilde{q}^n(\mathbf{x}_w, t)$ defined in Algorithm 4.1 is constant over the time interval $t_n < t < t_{n+1}$ under certain stability conditions (see section 4.4).
Let $\check{Q}_w$ be the solution of the Riemann problem at the cell wall σ_W, then $\check{Q}_w = \tilde{q}^n(\mathbf{x}_w, t)$ and the numerical flux is given by

$$\begin{aligned} \bar{F}^n_{\sigma_W} &= \frac{1}{\Delta t} \int_{t_n}^{t_{n+1}} f(\check{Q}_w) \cdot \mathbf{n}_{\sigma_W} |\sigma_W|\, dt \\ &= f(\check{Q}_w) \cdot \mathbf{n}_{\sigma_W} |\sigma_W|. \end{aligned} \tag{4.22}$$

Hence, Godunov's method can generally be given by Algorithm 4.2.

Algorithm 4.2 (Godunov)

1. *Solve the Riemann problem for each cell wall σ_k to obtain $\check{Q}_k$.*

2. *Define the numerical flux $\bar{F}^n_{\sigma_k} = f(\check{Q}_k) \cdot \mathbf{n}_{\sigma_k} |\sigma_k|$.*

3. *Apply the flux differencing formula $Q_i^{n+1} = Q_i^n - \frac{\Delta t}{|C_i|} \sum_k \bar{F}^n_{\sigma_k}$.*

Depending on the conservation law, the solution to a Riemann problem can directly be given, which simplifies the computation. In the next section, it will be shown that for the spatially depending segregation flux this classical version of Godunov's method leads to undesired behaviour in the numerical solution. Therefore, a modified version is derived.

4.3 A Godunov method for the segregation flux

In the last section, the flux differencing formula has been derived. To compute the states of the new time step, the evaluation of the boundary fluxes is essential. Doing this for the segregation flux, the approach of Godunov (Algorithm 4.2) should be used, which needs the solution of the Riemann problem at the cell wall. First, a compact form of the numerical Godunov flux is presented. A modified version is derived afterwards.

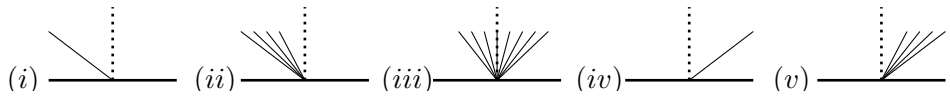

FIGURE 4.4: Five possible Riemann solutions in the z-t-space between the states Q_{i-1}^n and Q_i^n: (i) a left going shock, $\check{Q}_{i-1/2} = Q_i^n$; (ii) a left going rarefaction wave, $\check{Q}_{i-1/2} = Q_i^n$; (iii) a transonic rarefaction fan, $\check{Q}_{i-1/2} = q_s$; (iv) a right going shock, $\check{Q}_{i-1/2} = Q_{i-1}^n$; or (v) a right going rarefaction wave, $\check{Q}_{i-1/2} = Q_{i-1}^n$.

4.3.1 The classical Godunov scheme

The focus lies on the segregation flux. Therefore, the model is reduced to a one-dimensional segregation equation as it has already been done in chapter 3 to analyse the flux term. Let

$$\partial_t q + \partial_z f(q) = 0$$

be a conservation law with convex flux function $f(q)$. The flux differencing formula in the one-dimensional case is given by

$$Q_i^{n+1} = Q_i^n - \frac{\Delta t}{\Delta z}(\bar{F}_{i+1/2}^n - \bar{F}_{i-1/2}^n).$$

As stated in Algorithm 4.2, the flux at $z_{i-1/2}$ is given by

$$\bar{F}_{i-1/2}^n = f(\check{Q}_{i-1/2}). \tag{4.23}$$

For a non-linear flux function $f(q)$ there are five possible Riemann solutions, (i) a left going shock, (ii) a left going rarefaction wave, (iii) a transonic rarefaction fan, which is a rarefaction fan spreading in both directions, (iv) a right going shock, or (v) a right going rarefaction wave as depicted in Figure 4.4. If the waves travel either to the left or to the right, the solution $\check{Q}_{i-1/2}$ at $z_{i-1/2}$ is given by either Q_i^n or Q_{i-1}^n, respectively. For the rarefaction fan spreading in both directions $\check{Q}_{i-1/2} = q_s$, where $Q_{i-1}^n < q_s < Q_i^n$ is the stagnation point fulfilling $f'(q_s) = 0$. Then, the Godunov flux for a convex scalar conservation law is given by

$$\bar{F}_{i-1/2}^n = \begin{cases} f(Q_{i-1}^n) & \text{if } s > 0 \text{ and } Q_{i-1}^n > q_s, \\ f(Q_i^n) & \text{if } s < 0 \text{ and } Q_i^n < q_s, \\ f(q_s) & \text{if } Q_{i-1}^n < q_s < Q_i^n, \end{cases} \tag{4.24}$$

where s is the shock speed given by the Rankine-Hugoniot condition 3.1. The formula (4.24) can be written even more compactly as

$$\bar{F}_{i-1/2}^n = \begin{cases} \min\limits_{q \in [Q_{i-1}^n, Q_i^n]} f(q) & \text{if } Q_{i-1}^n \leq Q_i^n, \\ \max\limits_{q \in [Q_i^n, Q_{i-1}^n]} f(q) & \text{if } Q_{i-1}^n > Q_i^n. \end{cases} \tag{4.25}$$

With this formula, the flux through the cell walls can be computed directly from the neighbouring states. Unfortunately, formula (4.25) cannot directly be applied to the segregation equation. Due to the spatial dependence of the segregation flux function, one has to be more cautious as described in [57]. Assume that the flux function depends explicitly on z, then the conservation law is given by

$$\partial_t q + \partial_z f(q, z) = 0. \tag{4.26}$$

Discretising the flux, one obtains a flux function $f_i(q)$ associated with the i-th grid cell giving a Riemann problem at $z_{i-1/2}$ with states Q^n_{i-1} and Q^n_i by

$$\begin{aligned} \partial_t q + \partial_z f_{i-1}(q) = 0 \quad &\text{if } z < z_{i-1/2}, \\ \partial_t q + \partial_z f_i(q) = 0 \quad &\text{if } z > z_{i-1/2}. \end{aligned} \tag{4.27}$$

Solving such a Riemann problem generally consists of finding a state $\check{Q}_L$ that can be connected with left going waves to Q^n_{i-1} and a state $\check{Q}_R$ that can be connected with right going waves to Q^n_i, such that additionally

$$f_{i-1}(\check{Q}_L) = f_i(\check{Q}_R). \tag{4.28}$$

One or both of the states $\check{Q}_L$ and $\check{Q}_R$ do not have to coincide with the states Q^n_{i-1} and Q^n_i. The classical Godunov flux approximation of the directly dicretised flux fails in this case, because the chosen states do not fulfil condition (4.28). In the next chapter, in subsection 5.2.1, the effect on the solution choosing states that do not fulfil (4.28) is shown.

4.3.2 The modified Godunov scheme

Assume the one-dimensional segregation equation is given by

$$\partial_t \phi - \partial_z \left(S\sqrt{T} \left(\frac{c-\phi}{c} \right) \phi \right) = 0. \tag{4.29}$$

The flux function is non-linear and, since $0 \leq \phi \leq c$, $T > 0$ and $S > 0$, it is convex. Due to the spatial dependence of the granular volume fraction and the granular temperature, a z-dependence is given in the flux function.

Segregation flux with constant temperature

Similarly to section 3.3, it is assumed that the granular temperature is constant for now, such that the segregation equation can simply be given by

$$\partial_t \phi - \partial_z \left(S \left(\frac{c-\phi}{c} \right) \phi \right) = 0 \tag{4.30}$$

with a segregation flux $f(\phi, c)$. Discretising the segregation flux, like in (4.27), a Riemann problem at $z = 0$ with left and right states ϕ_L and ϕ_R is given by

$$\begin{aligned} \partial_t \phi + \partial_z f_L(\phi) = 0 \quad &\text{if } z < 0, \\ \partial_t \phi + \partial_z f_R(\phi) = 0 \quad &\text{if } z > 0, \end{aligned} \tag{4.31}$$

where $f_L(\phi) = f(\phi, c_L)$. This problem is identical to the Riemann problem (3.71)-(3.72) with states $\mathbf{U}_L$ and $\mathbf{U_R}$, where $\mathbf{U} = (\phi, c)^T$, which has been explicitly solved in section 3.3 of the previous chapter. From the solutions plotted in the Figures 3.9-3.18, the correct boundary fluxes, fulfilling condition (4.28), can be found. The states fulfilling condition (4.28) can be identified directly in the solution plots, which depict the flux functions f_L and f_R. In this plot the mentioned states must be connected by a horizontal line. The conditions for each Riemann solution and the resulting boundary flux are listed

Case	Figure	left state	condition of right state	$\bar{F}$
1	3.9	$\phi_L < \frac{c_L}{2}$	$\phi_R < \frac{c_R}{2}$, $f(\mathbf{U}_R) > f(\mathbf{U}_L)$	$f(\mathbf{U}_R)$
2	3.10	$\phi_L < \frac{c_L}{2}$	$\phi_R < \frac{c_R}{2}$, $f(\mathbf{U}^*) \leq f(\mathbf{U}_R) < f(\mathbf{U}_L)$	$f(\mathbf{U}_R)$
3	3.11	$\phi_L < \frac{c_L}{2}$	$f(\mathbf{U}_R) < f(\mathbf{U}^*) < f(\mathbf{U}_L)$	f_L^{min}
4	3.12	$\phi_L < \frac{c_L}{2}$	$\phi_R > \frac{c_R}{2}$, $c_R > c^* = c_L$, $f(\mathbf{U}_R) > f(\mathbf{U}^*)$	f_L^{min}
5	3.13	$\phi_L < \frac{c_L}{2}$	$\phi_R > \frac{c_R}{2}$, $\tilde{c} < c_R < c^* = c_L$, $f(\mathbf{U}_R) > f(\mathbf{U}^*)$	f_R^{min}
6	3.14	$\phi_L < \frac{c_L}{2}$	$\phi_R > \frac{c_R}{2}$, $c_R < \tilde{c}$, $f(\mathbf{U}_R) > f(\mathbf{U}_L)$	f_R^{min}
7	3.15	$\phi_L > \frac{c_L}{2}$	$\phi_R < \frac{c_R}{2}$, $f(\mathbf{U}_R) > f(\mathbf{U}_L)$	$f(\mathbf{U}_R)$
8	3.16	$\phi_L > \frac{c_L}{2}$	$f(\mathbf{U}_R) < f(\mathbf{U}_L)$	$f(\mathbf{U}_L)$
9	3.17	$\phi_L > \frac{c_L}{2}$	$\phi_R > \frac{c_R}{2}$, $c_R > \tilde{c}$, $f(\mathbf{U}_R) > f(\mathbf{U}_L)$	$f(\mathbf{U}_L)$
10	3.18	$\phi_L > \frac{c_L}{2}$	$\phi_R > \frac{c_R}{2}$, $c_R < \tilde{c}$, $f(\mathbf{U}_R) > f(\mathbf{U}_L)$	f_R^{min}

Table 4.1: Conditions and the resulting solutions for the boundary fluxes of the Riemann problem (3.71)-(3.72).

in Table 4.1. One can see that the resulting boundary flux in all 10 cases is equal to one of four quantities. In the cases 1, 2, and 7, it is given by the downstream flow rate $f(\mathbf{U}_R) = f_R(\phi_R)$ and in the cases 8 and 9 by the upstream flow rate $f(\mathbf{U}_L) = f_L(\phi_L)$. The remaining cases are different. The averaged boundary flux coincides with one of the extrema of the fluxes f_L and f_R. In the cases 3 and 4, it is given by $f_L^{min} = f_L(\phi_L^{min})$, where $\phi_L^{min} = \frac{c_L}{2}$ is the point where f_L takes its minimum and in the cases 5, 6, and 10, it is given by $f_R^{min} = f_R(\phi_R^{min})$, where $\phi_R^{min} = \frac{c_R}{2}$ is the point where f_R takes its minimum. From the given results, a formula can be deduced which yields the right boundary flux under the respective conditions. Defining the upstream supply by

$$f^{up} = \begin{cases} f_L(\phi_L) & \text{if } \phi_L > \phi_L^{min} \\ f_L^{min} & \text{if } \phi_L \leq \phi_L^{min}, \end{cases} \tag{4.32}$$

and the corresponding downstream supply by

$$f^{down} = \begin{cases} f_R(\phi_R) & \text{if } \phi_R < \phi_R^{min}, \\ f_R^{min} & \text{if } \phi_R \geq \phi_R^{min}, \end{cases} \tag{4.33}$$

the average boundary flux is directly given by

$$\bar{F}^G = \max\{f^{up},\, f^{down}\}. \tag{4.34}$$

A similar formula can be deduced for the large particle phase, where the flux functions are concave. In this case the flux functions have maxima and the four possible quantities for the boundary flux are $f_L(\phi_L)$, $f_R(\phi_R)$, f_L^{max} and f_R^{max}. All solution plots of the Riemann problem for the large particle phase and a compact formula for the boundary flux are given in Appendix A.

The notation of the presented flux formula is taken from Jin and Zhang [47]. In their work, the authors analysed a spatially dependent Riemann problem for the Lighthill-Witham-Richards (LWR) traffic flow model. The concave flux function, they dealt with, is similar to the flux function of the large particle phase's segregation equation. It turned out that the Riemann solutions which they found are identical with those for the large particle's

segregation equation. Independently from each other, Daganzo [17] and Lebacque [56] also found identical solutions for the LWR traffic flow model. In 2008 Towers et al. [78] extended the work done in [17], [47], and [56] and gave the first completely rigorous convergence proof for the Godunov scheme with the above mentioned flux formula. Furthermore, they introduced a more compact formula for the boundary flux, which clearly fits also for the large particle flux. Modifying this formula such that it suits for the convex flux function of the small particle phase, the computation formula for the extended Godunov scheme can be given by

$$\bar{F}^G = \max\left\{f_L(\max\{\phi_L, \phi_L^{min}\}),\, f_R(\min\{\phi_R, \phi_R^{min}\})\right\}. \tag{4.35}$$

One can easily check that the Godunov flux formula (4.35) is in accordance with the previously derived formulas (4.32)-(4.34). Furthermore, the modified Godunov scheme, using the flux (4.35), reduces to the classical Godunov version if the granular volume fraction is constant. Mostly, the modified flux version produces the same result as the classical flux approximation anyhow. Only in the upstream or the downstream case, where the boundary flux typically is given by the left state $f_L(\phi_L)$ or the right state $f_R(\phi_R)$, the chosen value can be different.
A different choice happens in the upstream case with flux candidate $f_L(\phi_L)$ if

$$f_L(\phi_L) < f_R(\phi), \quad \forall \phi \in [0,\, c_R]. \tag{4.36}$$

Analogously, a different choice happens also in the downstream case with flux candidate $f_R(\phi_R)$ if

$$f_R(\phi_R) < f_L(\phi), \quad \forall \phi \in [0,\, c_L]. \tag{4.37}$$

This can be seen in the flux plots of Figure 3.9 and Figure 3.18. In both cases the necessary condition (4.28) can not be fulfilled. Accordingly, the modified Godunov flux chooses the "strongest" flux value that is allowed for both, the left and the right flux function f_L and f_R. Strongest coincides with the flux' extrema and is meant in the sense of absolute values. In the upstream case, the chosen value becomes

$$f_L(\check{\phi}_L) = f_R^{min} \tag{4.38}$$

and in the downstream case

$$f_R(\check{\phi}_R) = f_L^{min}. \tag{4.39}$$

Mind that in the concave case of the large particle segregation equation, the differences appear if relation (4.36) and (4.37) are formulated with ">".

It should be mentioned that already in 2007 Garavello et al. [28] determined a class of Riemann solvers for a hyperbolic conservation law with discontinuous flux in the field of traffic flow models. This class provides existence and uniqueness of the corresponding weak entropic solutions. However, they impose more conditions to the structure of the flux as in the work of Towers et al. [78].

Segregation flux with non-constant temperature

The spatial dependence of the segregation equation is not only given due to the granular volume fraction c but also due to the granular temperature T as it can be seen in

equation (4.29). Solving the equation numerically, this additional dependence makes no big difference. Analogously to the statements previously done, the numerical scheme can be used almost in the same way including the granular temperature. Discretising the segregation flux, a Riemann problem at $z = 0$ with left and right states ϕ_L and ϕ_R is equivalently given to (4.31) by

$$\begin{aligned} \partial_t \phi + \partial_z f_L(\phi) = 0 \quad &\text{if } z < 0, \\ \partial_t \phi + \partial_z f_R(\phi) = 0 \quad &\text{if } z > 0, \end{aligned}$$

where this time $f_L(\phi) = f(\phi, c_L, T_L)$. The solution to the Riemann problem has been sketched at the end of the last chapter in Figure 3.20. The depicted solutions coincide with those for the constant temperature case. The only difference is that the contact discontinuity additionally compensates the difference between T_L and T_R. The only condition for a suitable flux approximation is again (4.28). If this condition can not be fulfilled in some upstream or downstream case as in relation (4.36) or relation (4.37), the flux value of choice is the "strongest" that is applicable for both, f_L and f_R. Hence, the explicit description of the modified Godunov flux can be written in the exact same way as for the equation with constant temperature. It is given by

$$\bar{F}^G = \max\left\{ f_L(\max\{\phi_L, \phi_L^{min}\}),\ f_R(\min\{\phi_R, \phi_R^{min}\}) \right\}.$$

Clearly, the defined numerical flux reduces to the classical Godunov approach for constant temperature and constant volume fraction.
If condition (4.28) is not fulfilled, problems appear, since the boundary flux entering the control volume might be overestimated. Some examples to demonstrate these problems, and to show that they do not appear for the derived modified Godunov flux, are presented in section 5.2.

4.4 The CFL condition

The stability of numerical methods, especially explicit schemes, is typically adjusted by the choice of the time step. For finite volume methods, the relation between the time and the spatial grid is relevant. For explicit methods, the time step must be decreased with decreasing spatial grid size to hold the scheme stable. The well-known Courant-Friedrichs-Lewy (CFL) condition, which was first suggested in 1928, gives a condition to ensure stability [15]. For convection problems, the so-called Courant number for a d-dimensional problem is defined by

$$\Delta t \sum_{i=1}^{d} \frac{v_i}{h_i} = C_{cfl}, \tag{4.40}$$

where Δt is the time step size, v_i the maximal transport velocity and h_i the spatial step size in direction i. For $d = 3$, it holds that $h_i \in \{\Delta x,\ \Delta y,\ \Delta z\}$. A method is stable if the wave solutions do not interact within one time step. For a method like the previously derived one, this can be guaranteed if a wave does not reach the opposite cell wall within one time step *(compare Figure 4.4)*. Hence, it must hold that

$$C_{cfl} < 1. \tag{4.41}$$

For solving the segregation equation, the upwind method is used for the transport with the granular bulk and the modified Godunov scheme for the segregation flux. In direction i, the bulk transport happens with the granular velocity u_i and the effective transport due to the segregation term is given by $\partial_\phi f_i^s$. Hence,

$$v_i = u_i + S_i\sqrt{T}\frac{(c-2\phi)}{c}. \tag{4.42}$$

As $0 \leq \phi \leq c$, (4.42) can be estimated by

$$v_i = u_i + S_i\sqrt{T}. \tag{4.43}$$

Consequently, an appropriate time step for solving the segregation equation depends on the maximal values of the granular velocity $\mathbf{u}$ and the granular temperature T.

One should keep in mind that solving the granular flow equations also subjects to stability conditions. From experiences with the granular flow equations, it is already known that $C_{cfl} \ll 1$ is necessary [65]. Additionally, a second condition is relevant for the system stability. It is important that the relative pressure gradient $\frac{\nabla p}{|C_i|}$ stays bounded, which appears to be more restrictive than the classical CFL-condition quite often [65].
In this context, it has been experienced that the stability restrictions to the granular flow model usually dominate the restrictions to the segregation equation. Additional use of the cut-cell method also reduces the admissible time step that can be used as the cell volume shrinks for several cut cells.

4.5 Boundary conditions for the segregation equation

Choosing an appropriate boundary condition for the segregation equation clearly depends on the type of domain boundary (inflow, outflow, solid walls). Let the wall of a control volume that coincides with the domain boundary be denoted by σ_{bound}. Using the flux differencing formula (4.10), which already has been introduced, it is necessary to define the flux over the domain boundary $\bar{F}_{\sigma_{bound}}$. As formulated in equation (4.16), the flux of the segregation equation can be subdivided into a transport flux and a segregation flux, where both can be evaluated separately.

At **inflows**, Dirichlet data are used depending on the application. At the boundary, it holds $\phi|_{\sigma_{bound}} = \phi_{in}$. For all quantities of the granular flow equations also Dirichlet data are used describing a specific value at the inflow walls. The fluxes can directly be computed by

$$\begin{aligned}\bar{F}^t_{\sigma_{bound}} &= \mathbf{f}^t(\phi_{in}, \mathbf{u}_{in}) \cdot \mathbf{n}_{\sigma_{bound}} |\sigma_{bound}| \\ \bar{F}^s_{\sigma_{bound}} &= \mathbf{f}^s(\phi_{in}, c_{in}, T_{in}) \cdot \mathbf{n}_{\sigma_{bound}} |\sigma_{bound}|\end{aligned}$$

Normally, there is nothing to be done for **outflows** if the flux is advective. When the material is flowing out of the domain, the wall flux is evaluated in the cell centre where all information are known. As the segregation flux is non-linear, it is not known whether the

effective transport velocity of a particle phase is pointing out of the domain. Therefore, a zero Neumann condition $\partial_n \phi = 0$ is implemented for the segregation flux if needed. Hence, the segregation flux at the outflow boundary is always given by the values in the cell centre

$$\bar{F}^s_{\sigma_{bound}} = \mathbf{f}^s(\phi(P), c(P), T(P)) \cdot \mathbf{n}_{\sigma_{bound}} |\sigma_{bound}|.$$

For solid **walls**, the conditions are different again. In section 2.1, the boundary conditions used for the granular flow equations are explained shortly. The boundary condition for the granular volume fraction c at solid walls is defined to be the Neumann zero condition. The outflow of the material is omitted due to the boundary condition for the granular bulk velocity $\mathbf{u}$. At solid walls, the transport flux $\bar{F}^t_{\sigma_{bound}}$ for the particle phase ϕ is handled in the same way to coincide with the existing implementations for the granular flow model. Similarly, the zero normal velocity at such a wall results in no flux through the boundary $\bar{F}^t_{\sigma_{bound}} = 0$.
Also there should be no flux through solid walls due to segregation, $\bar{F}^s_{\sigma_{bound}} \stackrel{!}{=} 0$, which simply means $\mathbf{f}^s(\phi, c, T) \stackrel{!}{=} 0$. This cannot be realised by Neumann zero conditions. Simply stating Dirichlet conditions

$$\phi|_{\sigma_{bound}} = c|_{\sigma_{bound}} \quad \text{or} \quad \phi|_{\sigma_{bound}} = 0$$

would result in a no flux condition, due to the structure of the flux function. However, this already would imply that one knows which particle phase will concentrate at this wall. As this should not be defined in advance, the boundary flux is defined to be zero to guarantee no segregation flux through solid walls,

$$\bar{F}^s_{\sigma_{bound}} := 0.$$

Chapter 5

Simulation and application

In this chapter, the focus lies on the numerical simulation of the previously derived equations. One essential extension of the model is the introduced segregation direction vector. In the first section of this chapter, results of the computation of the segregation direction are shown. In the second section, several one-dimensional test cases are used to validate the behaviour of the one-dimensional segregation equation and the applicability of the derived numerical schemes. Afterwards, the interplay of the segregation equation and the granular flow equations is examined in two-dimensional domains. Finally, in the last section, further results and applications are presented in the three-dimensional space.

5.1 Verification of the segregation direction

In the modelling chapter, it has been mentioned that for granular shear flows the segregation acts mainly orthogonal to the shear bands. Therefore, a computation scheme has been derived in subsection 2.2.3 to gain this direction from the underlying flow field. This procedure is given in Algorithm 2.1. To verify the results of these computations,

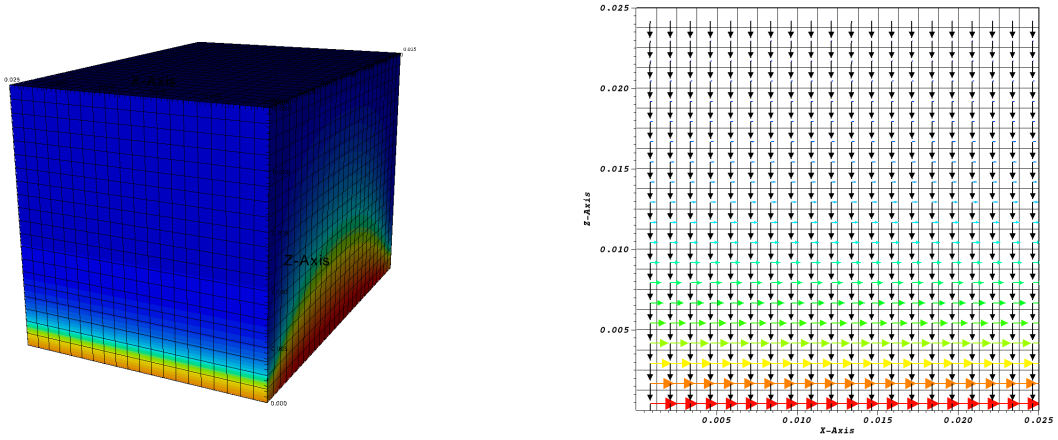

FIGURE 5.1: Part of a three-dimensional shear cell *(left)* with moving bottom plate. The domain additionally shows the velocity magnitude from low velocities (blue) to high velocities (red). The two-dimensional slice of the domain, orthogonal to the y-axis *(right)*, shows the computed segregation directions depicted by black arrows. The velocities are depicted by coloured arrows.

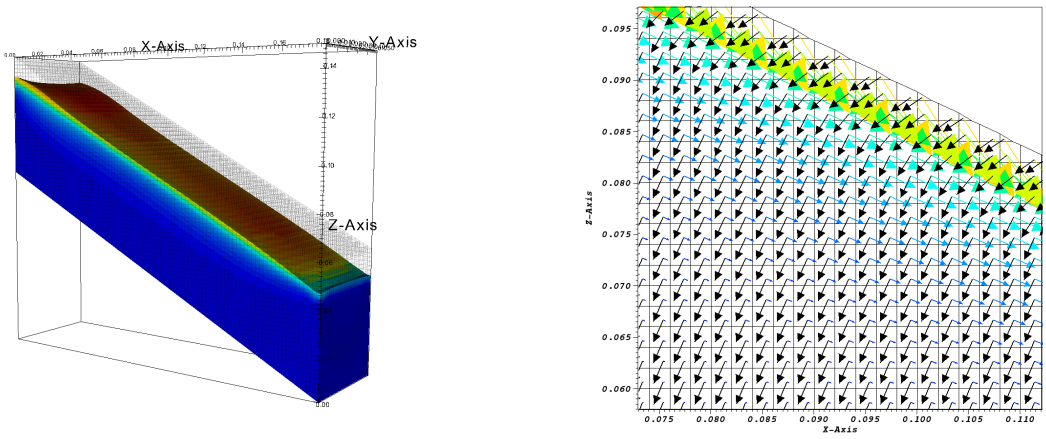

FIGURE 5.2: Three-dimensional chute *(left)* showing the velocity magnitude of the granular material from low velocities (blue) to high velocities (red). The two-dimensional slice shows a close-up view of the domain orthogonal to the y-axis *(right)*. The computed segregation directions are depicted by black arrows. The velocities are depicted by coloured arrows.

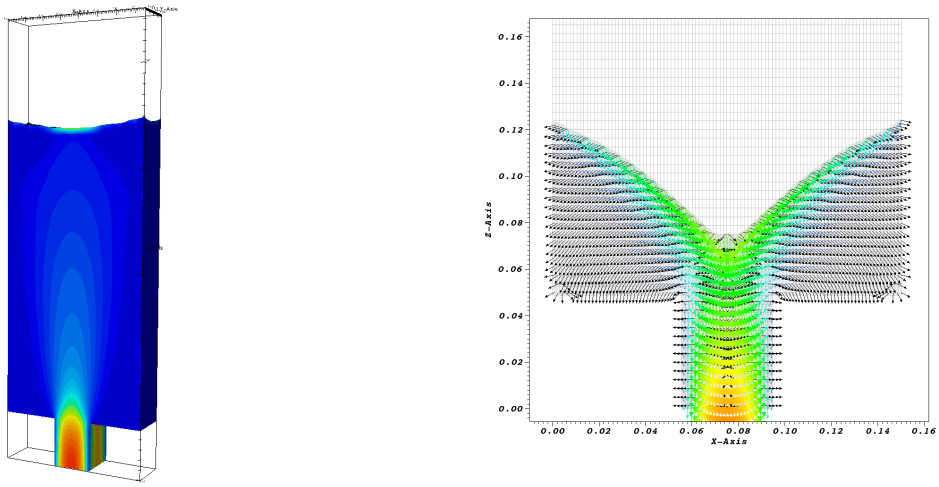

FIGURE 5.3: Three-dimensional silo *(left)* showing the velocity magnitude of the granular material from low velocities (blue) to high velocities (red) while discharging the silo. The two-dimensional slice shows a close-up view of the domain orthogonal to the y-axis *(right)* at a later state in time. The amount of granular material is depicted in light grey. The computed segregation directions are given by black arrows. The velocities are given by coloured arrows.

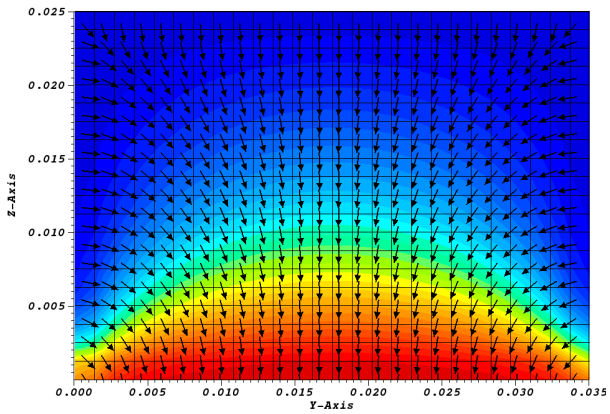

FIGURE 5.4: Two-dimensional slice, orthogonal to the x-axis, of the shear cell which is depicted in the previously shown Figure 5.1. The segregation direction is given by black arrows.

three different test cases in a three-dimensional domain have been simulated. The first domain is a cuboid representing a part of a three-dimensional shear cell. The second one is a chute where the cut-cell method has been used to observe a better representation of the domain boundaries. The third domain is a silo. All domains are depicted at the left side in the respective Figures 5.1, 5.2, and 5.3. The three plots additionally show the velocity magnitude from low velocities *(blue)* to high velocities *(red)* during the process of shearing, flowing down the chute, and discharging the silo, respectively. In the shear cell simulation, the granular material flows in positive x-direction accelerated through the bottom of the cell. For the left and right domain boundaries, periodic conditions are used such that the leaving material re-enters the domain. Hence, a shear flow emerges parallel to the x-axis. This can be seen in the right plot of Figure 5.1 which shows a two-dimensional slice of the domain, orthogonal to the y-axis. The slice plot depicts the velocity field by arrows that correspond in length and colour to the velocity magnitude. The computed segregation direction for each control volume is given by a black arrow. The slice of the shear cell shows a perfectly parallel shear flow. The computed segregation direction matches the expectations.
For the chute simulation, periodic boundary conditions have once more been used to re-enter the material which is flowing out. Due to gravity, a shear flow emerges at the upper layers of the granular material. It can be seen in the close-up view of Figure 5.2 *(right)* that the computation of the segregation direction leads to good results even though the flow field is not parallel to one of the coordinate axes or the orientation of the control volumes any more. Furthermore, the direction is exactly as mentioned in literature for avalanches flowing down chutes (e.g. [37, 36, 34])
While discharging a silo, dead zones appear in the lower left and right corners. The close-up view in Figure 5.3 *(right)* shows the process at a late state in time. The material flows to the discharge while the segregation directions point to the dead zones. The only region where the computation results for the segregation direction seem to be quite random is close to the corners of the silo. This happens, because the velocities are close to zero. As the material is at rest, these directions do not influence the segregation process.
One also obtains good results in the third coordinate direction, which can be seen in

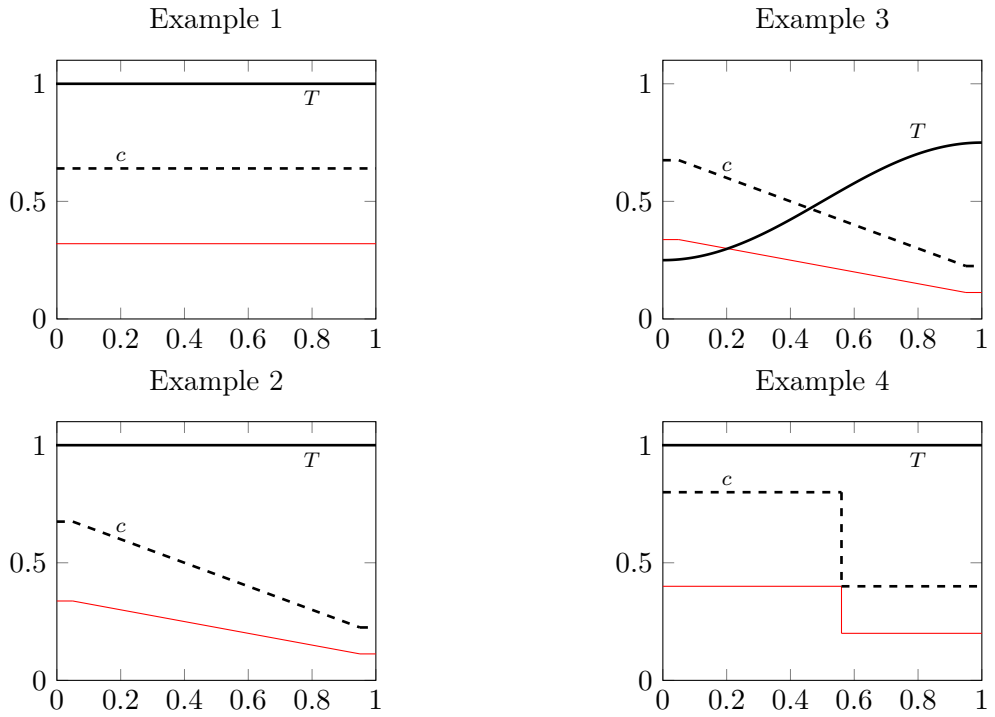

FIGURE 5.5: Illustration of the four examples chosen for the one-dimensional segregation mechanism. The black line depicts the distribution of the granular temperature T over the domain. The dashed line shows the granular volume fraction c which is an upper bound for all particle phases. The initial state of the particle phases is depicted in red which corresponds to a perfectly mixed initial state, $\phi = \frac{c}{2}$. In the four examples, c is chosen to be either constant, linearly decreasing or piecewise constant with a jump. The temperature is either constant or non-linearly increasing.

Figure 5.4. Due to the deceleration of the material by the outer walls of the shear cell, the flow field is not constant along the y-axis. This results in curved shear bands. Hence, the segregation direction not only points downwards but also to the middle of the domain.

The presented examples show that the procedure to compute the segregation direction, described in subsection 2.2.3, can be applied to granular material flows. In the case of shear flows, the results are promising which is of major importance in this work.

5.2 Simulating segregation in one space dimension

In this section, some numerical results for the one-dimensional segregation equation are presented. Therefore, four test cases are used. The spatial domain is the unit interval $[0, 1]$ in z-direction, which is assumed to be the direction of the segregation process. The chosen examples differ solely in the choice of the granular volume fraction c and the granular temperature T. For all examples, the volume fraction of a particle phase is initially chosen by $\phi = \frac{c}{2}$ which corresponds to an equally mixed initial state. Example 1 is the simplest test case with a constant value for the granular volume fraction c and the granular temperature T. In example 2, the granular volume fraction is linearly decreasing with increasing domain height. As opposed to example 2, the granular temperature is

non-linearly increasing with decreasing granular volume fraction in example 3. The last example has a constant granular temperature but a jump in the granular volume fraction. The initial states of the four examples are illustrated in Figure 5.5.

5.2.1 Gaining physical solutions by the modified Godunov method

The previously mentioned examples 2, 3, and 4 are used to compare the modified Godunov scheme, which has been derived in the last sections, to the upwind and the classical Godunov scheme. In these cases, either one or both of the granular volume fraction c and the granular temperature T are non-constant. The simplest test case given by example 1 is omitted, as in this case, the modified Godunov method reduces to the classical one. In all simulations, the one-dimensional equation for the small particle phase and also the large particle phase are solved. The volume fractions are plotted over the z-axis. The two equations are given by

$$\partial_t \phi \mp \partial_z \left(S\sqrt{T} \left(\frac{c-\phi}{c} \right) \phi \right) = 0, \tag{5.1}$$

where the segregation rate is set to one in the whole section, i.e., $S = 1$. The computation of the numerical flux of the large particle phase can be determined using the flux approximation formula (A.2) given in Appendix A.
Initially, the system is perfectly mixed with $\phi = \frac{c}{2}$ defining the initial condition for both particle phases in all chosen test cases. Throughout all three examples, the small particle phase is plotted in red and the large particle phase in blue. The line style implies the chosen numerical method. For the modified Godunov scheme the regular line style is used, whereas the classical Godunov scheme is plotted by a dotted and the upwind scheme by a dashed line.

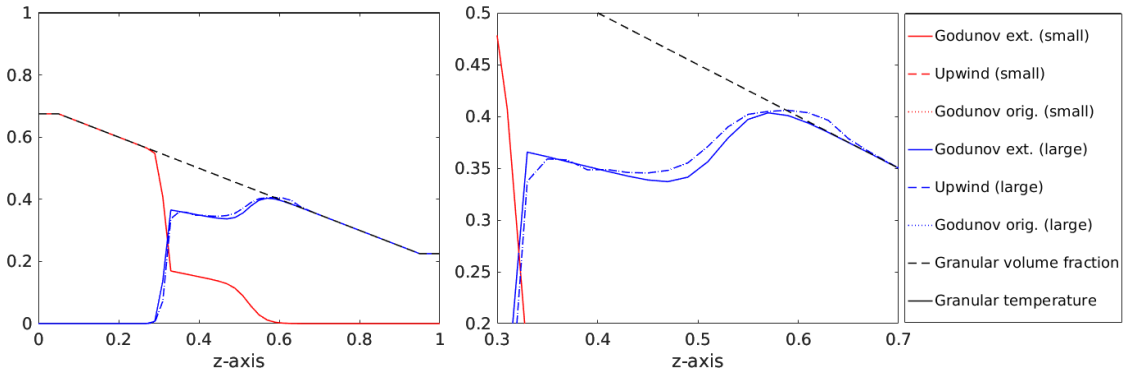

FIGURE 5.6: Simulation result of the one-dimensional segregation process in z-direction for the small and large particle phase using different numerical schemes at $t = 0.75$ *(left)*. A close-up view shows the problematic region *(right)*. The black dashed line depicts the granular volume fraction c, which is an upper bound for both particle phases and decreases linearly. The granular temperature is chosen to be $T = 1$ and the segregation rate is chosen to be $S = 1$. Initially, the system is perfectly mixed. Over time, the small particles concentrate at the left (bottom of the granular bed) and the large particles at the right (top of the granular bed). Only the modified Godunov scheme prevents a particle phase from overshooting c.

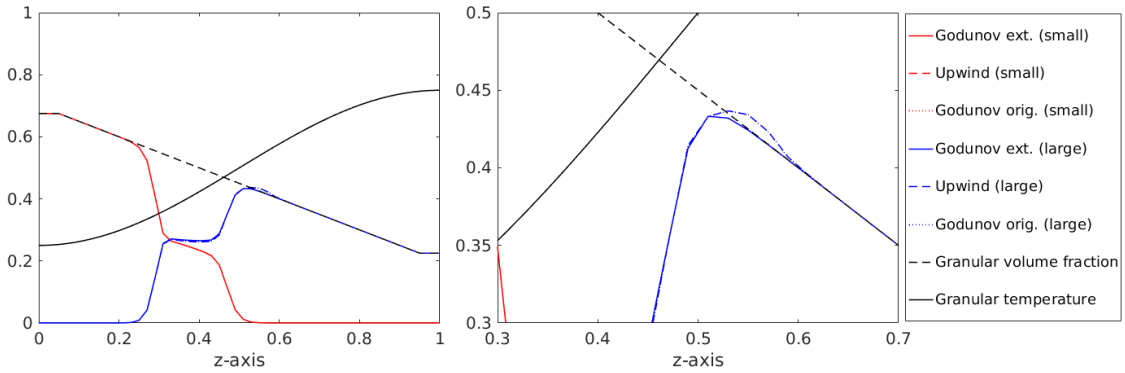

FIGURE 5.7: Simulation result of the one-dimensional segregation process in z-direction for the small and large particle phase using different numerical schemes at $t = 1.1$ *(left)*. A close-up view shows the problematic region *(right)*. The black dashed line depicts the granular volume fraction c, which is an upper bound for both particle phases and decreases linearly. The granular temperature increases non-linearly. The segregation rate is chosen to be $S = 1$. Initially, the system is perfectly mixed. Over time, the small particles concentrate at the left (bottom of the granular bed) and the large particles at the right (top of the granular bed). Only the modified Godunov scheme prevents a particle phase from overshooting c.

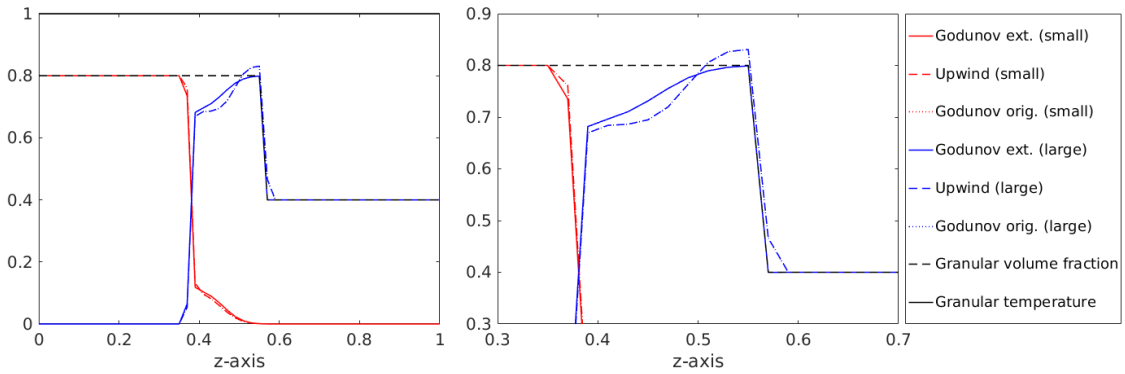

FIGURE 5.8: Simulation result of the one-dimensional segregation process in z-direction for the small and large particle phase using different numerical schemes at $t = 1$ *(left)*. A close-up view shows the problematic region *(right)*. The black dashed line depicts the granular volume fraction c, which is an upper bound for both particle phases and has an unsteady jump. The granular temperature is chosen to be $T = 1$ and the segregation rate is chosen to be $S = 1$. Initially, the system is perfectly mixed. Over time, the small particles concentrate at the left (bottom of the granular bed) and the large particles at the right (top of the granular bed). Only the modified Godunov scheme prevents a particle phase from overshooting c.

	Example 2		Example 3		Example 4	
h	L^∞	rate	L^∞	rate	L^∞	rate
8.00e-02	0.06702	-	0.06741	-	0.34160	-
4.00e-02	0.03041	1.140	0.02478	1.444	0.32870	0.056
2.00e-02	0.01690	0.847	0.01427	0.796	0.28748	0.193
1.00e-02	0.00969	0.803	0.00731	0.966	0.30736	-0.096
5.00e-03	0.00484	1.001	0.00382	0.934	0.30397	0.016
2.50e-03	0.00260	0.899	0.00196	0.961	0.30226	0.008
1.25e-03	0.00137	0.926	0.00100	0.976	0.30141	0.004
6.25e-04	0.00068	1.004	0.00051	0.971	0.30099	0.002
3.125e-04	0.00035	0.966	0.00026	0.978	0.30078	0.001

Table 5.1: Overview of the overshooting error and the convergence rates for the examples 2-4 shown in the Figures 5.6, 5.7, and 5.8. The listed values are equal for the upwind and the classical Godunov scheme.

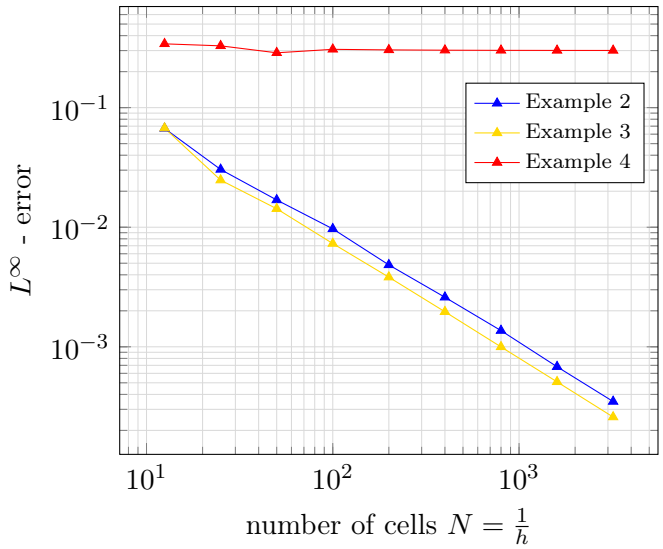

FIGURE 5.9: Plot of the overshooting error for different spatial grid sizes. The time step is chosen to hold the CFL number constant. The error decreases for example 2 (Figure 5.6) and example 3 (Figure 5.7), both with a convergence rate that is approximately 1. The error for example 4 (Figure 5.8) nearly stays constant (compare Table 5.1).

Figure 5.6 shows the simulation result for example 2 *(left)* at time $t = 0.75$. Additionally, a close-up view is plotted *(right)*. The granular temperature is chosen to be $T = 1$. The granular volume fraction decreases linearly from left to right in the region between $x = 0.05$ and $x = 0.95$, depicted by a black dashed line. This means that the granular system is less dense at the top of the granular system than at the bottom. The granular volume fraction is an upper bound for both particle phases. Due to the segregation process, the small particles concentrate on the left (bottom of the granular bed) and the large particles on the right (top of the granular bed). The classical Godunov scheme and the upwind method lead to quite identical results in all plots. Even the modified Godunov scheme leads to almost the same result for the small particle phase. A different

result is gained for the large particle phase. In the close-up view, one can see that solely the modified Godunov scheme does not overestimate the flux values. The two other methods overshoot the value of the granular material's volume fraction. In particular, this happens if the material flows in the direction of decreasing volume fraction. In these cases, the chosen flux values do not fulfil condition (4.28).
In example 3, which is shown in Figure 5.7, not only c but also the granular temperature T is non-constant. The granular temperature increases non-linearly from left to right, which is depicted by the black curve. This means that the temperature is higher in the upper layers of the granular system. As in the previous test case, the granular volume fraction decreases linearly. The plot shows the simulation results at time $t = 1.1$. One can see, that the modified Godunov scheme still prevents the particle phases from overshooting c even if both, c and T, vary.

Figure 5.8 shows the simulation result of example 4. The setup is mainly identical to example 2, but the granular volume fraction c is constant with a large jump at $z = 0.56$. This is not very realistic for granular systems, but it is helpful to show the quality of the numerical method. Again, the small particles concentrate at the left (bottom of the granular bed) and the large particles at the right (top of the granular bed). The simulation result is shown at time $t = 1$, where the system is not yet fully segregated. Especially in the close-up view, one can see that again only the modified Godunov scheme does not overshoot the granular volume fraction c.

Several simulations have shown that the overshoot produced by the classical Godunov and the upwind scheme can mostly be decreased by decreasing the spatial grid size. Nevertheless, it cannot be avoided. This is illustrated in Figure 5.9 and the corresponding Table 5.1. The overshoot can be defined by

$$\varepsilon_{over} := max\{0, \phi - c\}. \tag{5.2}$$

The largest overshoot appearing during the segregation process is given by $\|\varepsilon_{over}\|_{L^\infty}$. If $\|\varepsilon_{over}\|_{L^\infty} = 0$, a solution is physical. Figure 5.9 shows the overshooting error for the three previously presented examples (Figure 5.6, 5.7, and 5.8). The time steps used in the simulations for the different grid sizes are chosen in such a way that the CFL number is constant, i.e., $C_{cfl} \equiv const$. The computed errors and the corresponding convergence rates are given in Table 5.1. In Figure 5.9, as well as in Table 5.1, only one set of data is shown for each example, since the upwind scheme and the classical Godunov scheme produce the same simulation results. It can be seen that for example 2 and example 3 the methods converge linearly to a physical solution whereas the errors for example 4 nearly stay constant. The modified Godunov scheme fulfils $\|\varepsilon_{over}\|_{L^\infty} = 0$ for all three examples.

5.2.2 Convergence and the mixing entropy

After validating the physical admissibility of the modified Godunov scheme with respect to overshooting, the quality of the method is further analysed. The examples 1-3, depicted in Figure 5.5, serve as test cases for the validation. Since an analytical solution can not be given in general, the concept of the experimental order of convergence (EOC) [40] is used to show grid convergence of the method. Therefore, a simulation on a fine grid serves as

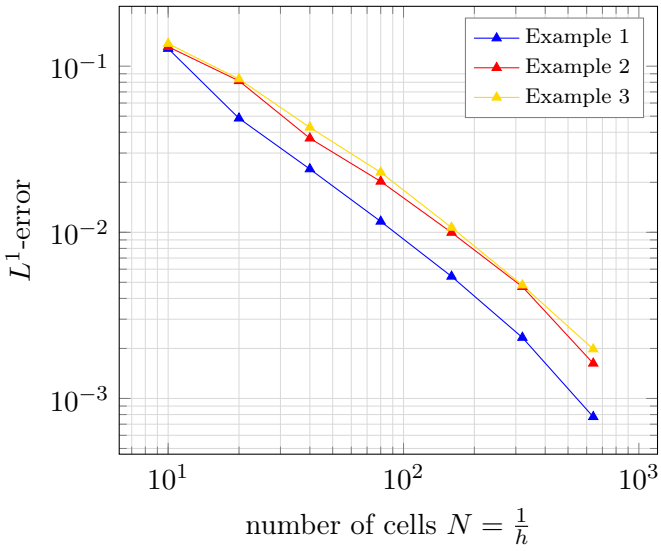

FIGURE 5.10: Plots of the relative errors for examples 1-3 at time $t_n = 0.5$. The grid and the time step size decrease equally such that the CFL number is constant. The convergence order, measured in the L^1-norm, is approximately one for all three examples.

	Example 1		Example 2		Example 3	
h	L^1	rate	L^1	rate	L^1	rate
1.00e-01	0.12756	-	0.13094	-	0.13664	-
5.00e-02	0.04854	1.394	0.08152	0.684	0.08367	0.708
2.50e-02	0.02402	1.015	0.03680	1.147	0.04279	0.967
1.25e-02	0.01162	1.047	0.02024	0.863	0.02295	0.899
6.25e-03	0.00542	1.100	0.00996	1.022	0.01068	1.103
3.125e-03	0.00232	1.222	0.00470	1.084	0.00480	1.152
1.5625e-03	0.00077	1.585	0.00163	1.532	0.00198	1.278

Table 5.2: Overview of the relative L^1-errors and the convergence rates for examples 1-3, evaluated at time $t_n = 0.5$. The corresponding convergence plots are depicted in Figure 5.10.

a reference. Generally, the relative error of some quantity Υ_h, evaluated for grid size h, to the reference solution Υ_{ref} is computed in some L^p-norm. The relative error is given by

$$\varepsilon_{rel} = \frac{\|\Upsilon_h - \Upsilon_{ref}\|_{L^p}}{\|\Upsilon_{ref}\|_{L^p}}. \tag{5.3}$$

For the one-dimensional examples the reference grid has $N = 1280$ cells. Hence, the grid size is $h = 7.8125\text{e-}04$.

In Figure 5.10, the results of the error computations for the three examples are depicted. The exact values and convergence rates are given in Table 5.2. For the simulations, the grid and the time step size decrease equally such that the CFL number is constant. The evaluation is made after running the simulations until $t_n = 0.5$. The convergence order, measured in the L^1-norm, is approximately one for all three examples as expected.

Characterising the mixing process leads to another method to compare different simulations and also to compare simulations to experiments. Introducing a mixing entropy, the degree of mixing or segregation can be quantified over time. Using Boltzmann's expression, a local mixing entropy for a bi-disperse system of particles can be defined by

$$e(\mathbf{x},t) = -\sum_{\nu\in\{s,l\}} \ln(\hat{\phi}^{\nu}(\mathbf{x},t))\,\hat{\phi}^{\nu}(\mathbf{x},t). \tag{5.4}$$

For the whole domain Ω, the global entropy in the system can be given by

$$E(t) = \int_{\Omega} e(\mathbf{x},t)c(\mathbf{x},t)d\mathbf{x}. \tag{5.5}$$

To obtain the global entropy, the local entropy (5.4) is weighted by the granular volume fraction c. For the discretised system, the domain is subdivided into control volumes C_i. It holds true, that

$$\Omega = \bigcup_{i\in\mathcal{I}} C_i, \tag{5.6}$$

where $\mathcal{I}$ defines some index set. Since only the small particle phase is used for the simulations, the exponent is dropped. To eliminate the other phase's variable, the saturation condition (2.59) is used. Then, for each control volume C_i, the discretised version of the local entropy at some point in time is given by

$$e_i = -\ln(\hat{\phi}_i)\hat{\phi}_i - \ln(1-\hat{\phi}_i)(1-\hat{\phi}_i) \tag{5.7}$$

and the global entropy by

$$E = \sum_{i\in\mathcal{I}} e_i c_i |C_i|. \tag{5.8}$$

In literature, different methods are used to describe the degree of mixing. A similar quantification, as used here, is given in [2, 3]. It is based on particle numbers to analyse DEM simulations. In analogy to the authors in [2, 3], a mixing parameter is introduced by

$$\Psi = \frac{E - E_{seg}}{E_{mix} - E_{seg}}, \tag{5.9}$$

which is a normalisation of the global entropy. For the mixing parameter, one has $\Psi \in [0,1]$ where $\Psi = 0$ is a fully segregated system and $\Psi = 1$ is a perfectly mixed system. The quantities E_{seg} and E_{mix} are the global entropies for a perfectly segregated system and a perfectly mixed system, respectively. In the following test cases, and also in the already introduced examples, the discretisation and the volume ratio of small and large particles are chosen such that $E_{seg} \approx 0$. Specifically, E_{mix} strongly depends on the initial conditions of the system as well as the definition of a perfectly mixed system itself. It is assumed that a system is perfectly mixed if $\hat{\phi}$ is constant over the whole domain. However, the exact value varies depending on the proportion of small and large particles in the system. The initial condition for all examples depicted in Figure 5.5 is a perfectly mixed system. In such a case, E_{mix} can be chosen as the global entropy of the initial configuration of the system.

As already mentioned, the mixing parameter Ψ quantifies the process of mixing and segregation. The examples 1-3 can be analysed by computing this quantity from the

	Example 1		Example 1		Example 1	
h	L^∞	rate	L^1	rate	L^2	rate
1.00e-01	0.11619	-	0.16532	-	0.13665	-
5.00e-02	0.05817	0.998	0.08301	0.994	0.07084	0.948
2.50e-02	0.02863	1.023	0.04110	1.014	0.03563	0.991
1.25e-02	0.01385	1.047	0.01995	1.043	0.01744	1.031
6.25e-03	0.00647	1.100	0.00932	1.097	0.00820	1.089
3.125e-03	0.00277	1.222	0.00400	1.221	0.00354	1.211
1.5625e-03	0.00092	1.585	0.00133	1.584	0.00120	1.558

Table 5.3: Overview of the relative errors and the convergence rates of the mixture entropies in example 1. The corresponding convergence plots and entropy curves are depicted in Figure 5.11 *(top row)*.

results of the performed simulations. Then, for each of the three examples, it can be seen how the segregation process behaves and at what time the process ends. The value E_{mix} to normalise the mixing entropy for the three examples is given by

$$E_{mix} = \begin{cases} 0.4436 & \text{for example 1,} \\ 0.3119 & \text{for examples 2, 3,} \end{cases} \tag{5.10}$$

respectively. Figure 5.11 shows the mixing parameter for some of the performed grid sizes and the convergence of the mixing parameter for all three examples, which have been simulated. For example 1, the granular temperature, the granular volume fraction, and the segregation rate S are constantly equal to one. Hence, the segregation time, denoting the time needed for the system to reach the final segregated state, is also equal to one. One can see that for a decreasing grid size the segregation time converges to this value. Furthermore, it can be seen that the segregation time changes for the different configurations given by example 2 and example 3. Particularly the varying temperature distribution in example 3 has a large influence on the segregation speed and thus, on the segregation time. However, the chosen method performs well as can be seen in the convergence plots *(Figure 5.11, right side)*. For all three examples, an expected convergence rate of approximately one can be confirmed. The exact values of the computed relative errors and the corresponding convergence rates are given in Table 5.3, Table 5.4, and Table 5.5, respectively.

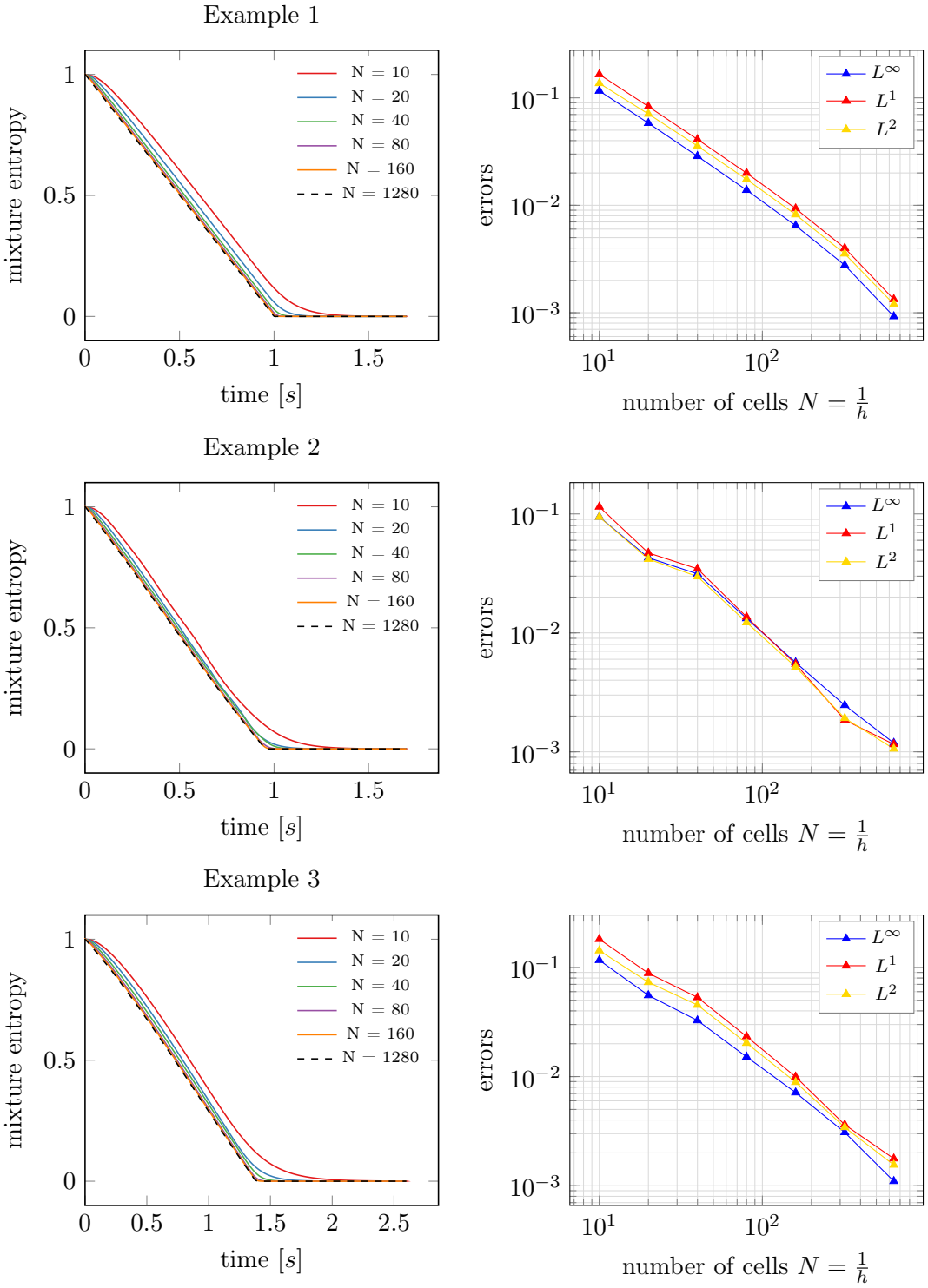

FIGURE 5.11: Mixture entropy (left) and relative errors (right) for the examples 1-3. Time step is chosen such that the CFL number is fixed. The segregation speed depends on c and the granular temperature in the system, which can be seen in the entropy plots. The detailed error values and convergence rates are given in Tables 5.3, 5.4, and 5.5.

	Example 2		Example 2		Example 2	
h	L^∞	rate	L^1	rate	L^2	rate
1.00e-01	0.09442	-	0.11481	-	0.09411	-
5.00e-02	0.04282	1.141	0.04701	1.288	0.04174	1.173
2.50e-02	0.03134	0.45	0.03458	0.443	0.02974	0.489
1.25e-02	0.01323	1.244	0.01362	1.344	0.01223	1.282
6.25e-03	0.00563	1.232	0.00546	1.318	0.00517	1.242
3.125e-03	0.00247	1.193	0.00185	1.562	0.00192	1.432
1.5625e-03	0.00119	1.056	0.00116	0.678	0.00106	0.856

Table 5.4: Overview of the relative errors and the convergence rates of the mixture entropies in example 2. The corresponding convergence plots and entropy curves are depicted in Figure 5.11 *(middle row)*.

	Example 3		Example 3		Example 3	
h	L^∞	rate	L^1	rate	L^2	rate
1.00e-01	0.11645	-	0.18139	-	0.14262	-
5.00e-02	0.05547	1.070	0.08852	1.035	0.07311	0.964
2.50e-02	0.03265	0.765	0.05315	0.736	0.04522	0.693
1.25e-02	0.01516	1.107	0.02332	1.189	0.02027	1.158
6.25e-03	0.00713	1.088	0.00995	1.229	0.00888	1.190
3.125e-03	0.00308	1.211	0.00362	1.457	0.00343	1.374
1.5625e-03	0.00110	1.487	0.00177	1.032	0.00155	1.144

Table 5.5: Overview of the relative errors and the convergence rates of the mixture entropies in example 3. The corresponding convergence plots and entropy curves are depicted in Figure 5.11 *(bottom row)*.

5.3 Simulating a two-dimensional shear cell

In this section, the test case of choice is a two-dimensional shear cell. To verify the results from the previous section an idealised Couette flow is used, as depicted in Figure 5.12 *(left plot)*. In contrast to the one-dimensional case, the granular flow equations come into play for the two-dimensional variant. Therefore, the influence of the granular flow equations on the segregation process is analysed. The dimensions of the shear cell setting are chosen to be similar to the experimental setup in the works of Golick and Daniels [33] and May et al. [60]. The resulting shear thinning flow, which is topic of the upcoming subsection 5.3.2, is sketched in Figure 5.12 *(right plot)*. Hence, the same system can be used in the last part of this section to compare the computed segregation process to the experimental measurements. Since the dimension for all upcoming test cases are chosen similar to experiments, all domains, quantities, and parameters are given in SI units.

5.3.1 The idealised case

After analysing the one-dimensional case in the last section, simulations in two space dimensions are performed. As already mentioned, a shear cell setting is chosen, based

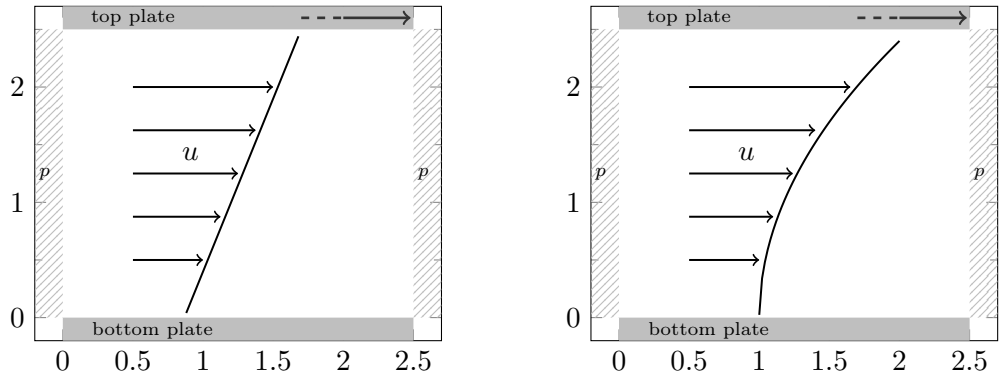

FIGURE 5.12: Sketches of two-dimensional shear cells with periodic boundary conditions at the left and right domain boundaries and different velocity profiles. Linearly increasing velocity profile which results in a constant shear rate and thus, in a constant temperature field *(left)*. Shear thinning flow with non-constant shear rate and granular temperature *(right)*.

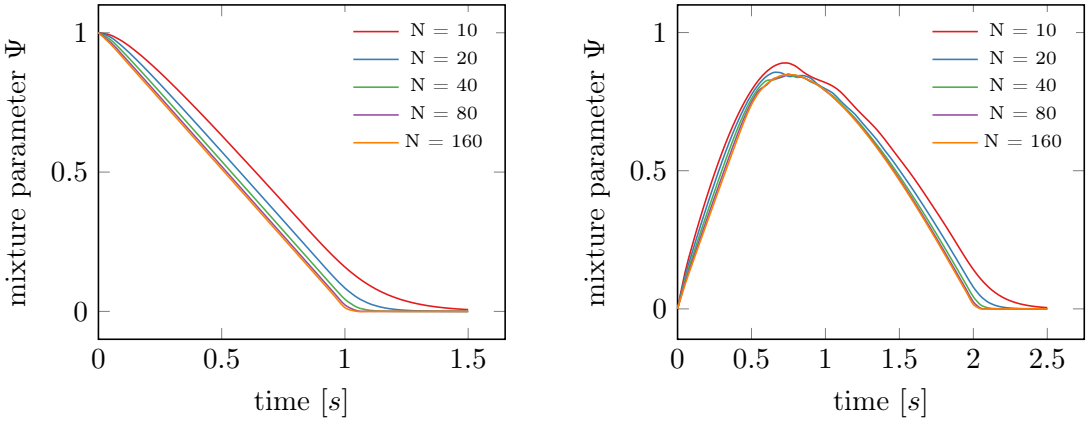

FIGURE 5.13: Normed mixture entropy for the idealised two-dimensional shear cell for different grid sizes. The time step is chosen such that the CFL number is constant. The system segregates from a perfectly mixed initial state like in the one-dimensional case *(left)*. Starting from an inversely graded initial state, the system mixes before it re-segregates *(right)*.

on an experiment performed by Golick and Daniels [33] and May et al. [60]. In the experiment, small and large glass beads, with a size ratio of $R = \frac{1}{2}$ and a mean diameter of $3mm$, segregate in a Couette shear cell. To measure the velocity profile and the segregation process, the authors used high-speed digital imaging and particle tracking. The scanned shear cell part has a size of $0.025 \times 0.025\, m^2$. The chosen domain for the simulation is given by

$$\Omega = [0, 0.025] \times [0, 0.025]. \tag{5.11}$$

For the first two-dimensional simulation, only the dimension of the considered domain part is fitted to the experiment. The granular volume fraction is set to a constant value $c = 0.64$ in the whole domain. Also, the granular bulk velocity is pre-defined to guarantee a linear velocity profile and a constant temperature distribution, as depicted in Figure 5.12 *(left plot)*. This configuration adds the effect of the granular transport to the segregation

(A) Initial state.

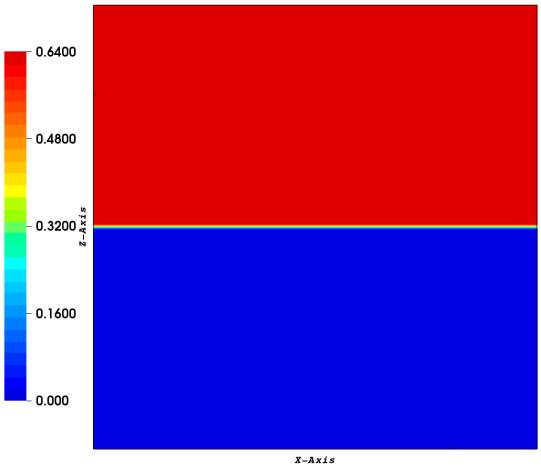

(B) State after 0.5 s.

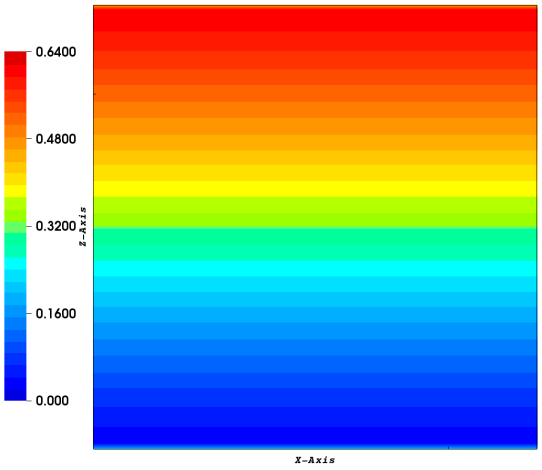

(C) State after 0.75 s.

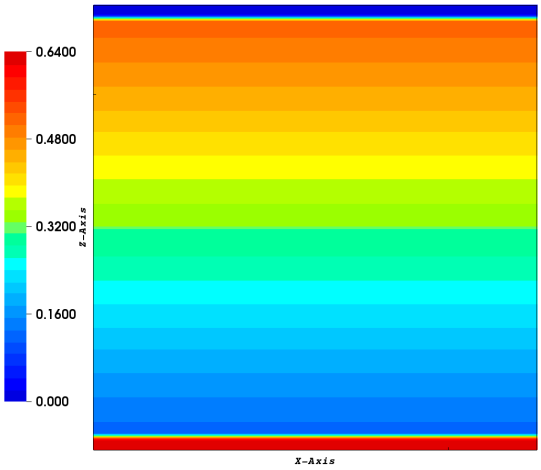

(D) State after 1.0 s.

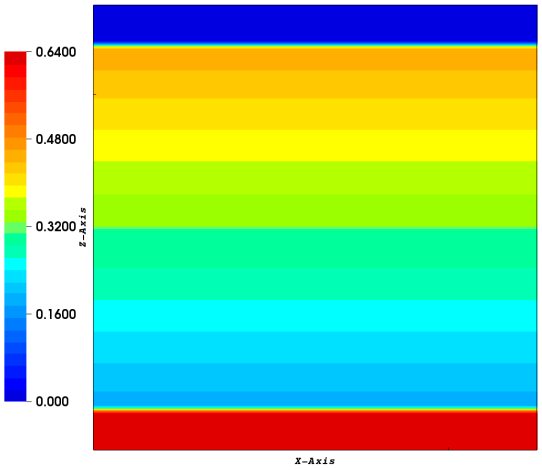

(E) State after 1.5 s.

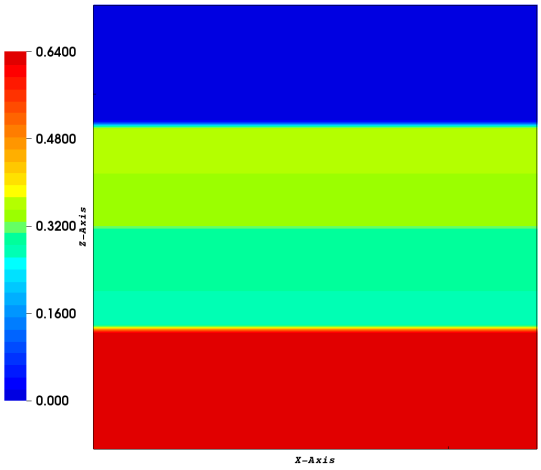

(F) Final state.

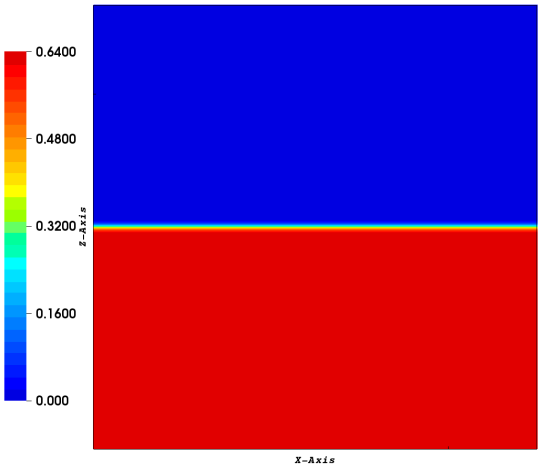

FIGURE 5.14: Simulation result of the idealised two-dimensional shear cell. The plot shows the volume fraction of the small particles at the initial state, after 0.5 s, 0.75 s, 1.0 s, 1.5 s, and 2 s. The system starts inversely graded. After a mixing phase the system re-segregates.

equation, but the granular flow equations do not have to be used. The segregation rate S_0^{sl} is chosen such that the segregation velocity

$$S^{sl} = -S_0^{sl}\sqrt{T}\mathbf{Pg} = 0.025\,\tfrac{m}{s}. \tag{5.12}$$

As initial condition, a fully mixed system with$\hat{\phi} = 0.5$ is chosen. Using these configurations, one can expect the same segregation time as for the one-dimensional example 1.

In fact, one observes that the segregation behaviour is identical. Figure 5.13 shows the normed mixture entropy Ψ for different grids for the idealised two-dimensional shear cell. The left picture shows the segregation process under the aforementioned configurations. The entropy plots for the different grids are almost identical to the one-dimensional example 1, depicted in Figure 5.11 *(left picture, top row)*.
In the right plot of Figure 5.14 the segregation process of an initially different distribution of particles is shown. Starting from an inversely graded system with all small particles are located above a layer of purely large particles, the system mixes before it re-segregates. In Figure 5.14, the simulation result is shown for different points in time. It can also be seen that the system never reaches a perfectly mixed state. While the system still mixes in the middle part of the domain, layers near the top and the bottom plate are already in the final segregated state. This can also be seen in Figure 5.13 where the mixing parameter Ψ never reaches its maximum value.

5.3.2 Influence of the granular flow equations

After performing a simulation under idealised conditions, the setting is now chosen to be more realistic. This has been done by using the full system of equations, as summarised in section 2.5, fitted to the mentioned experiment. The only simplification made, is the omission of the back-coupling from segregation equation to the granular flow model. Changing RLP and RCP values would lead to a loss of contact between the glass beads and the top plate, since the domain size is fixed. In the experiment, the top plate of the shear cell is free to move vertically which ensures the contact of the plate and the material, even when the system changes its volume due to the segregation process. In this more realistic test case, a shear thinning flow is observed with a velocity profile decreasing exponentially. The simulation setting deviates from the experiment in one aspect. In the experiment the bottom plate is accelerated, while in the simulation the top plate accelerates the granular material. This makes it easier to gain a similar velocity profile due to the gravitational force. A sketch is shown in Figure 5.12 *(right plot)*.

Before the segregation process itself is considered, the focus lies on the granular flow equations. The aim is to validate their influence on the segregation equation. To simulate the bulk material, a set of parameters is needed. These are given in Table 5.6. The viscosity η_0 is used as fitting parameter and has been chosen in such a way that the resulting flow profile is similar to the one identified in the shear cell experiment. The other parameters are taken from Niedziela et al. [66], in which the same granular flow equations as here were used to simulate glass beads. To easily hit the experimentally measured velocities near the top and bottom plate, these values are used as Dirichlet boundary conditions. For the fast top plate the velocity is set to $u_{top} = 0.0055\,\frac{m}{s}$ and for the bottom plate the

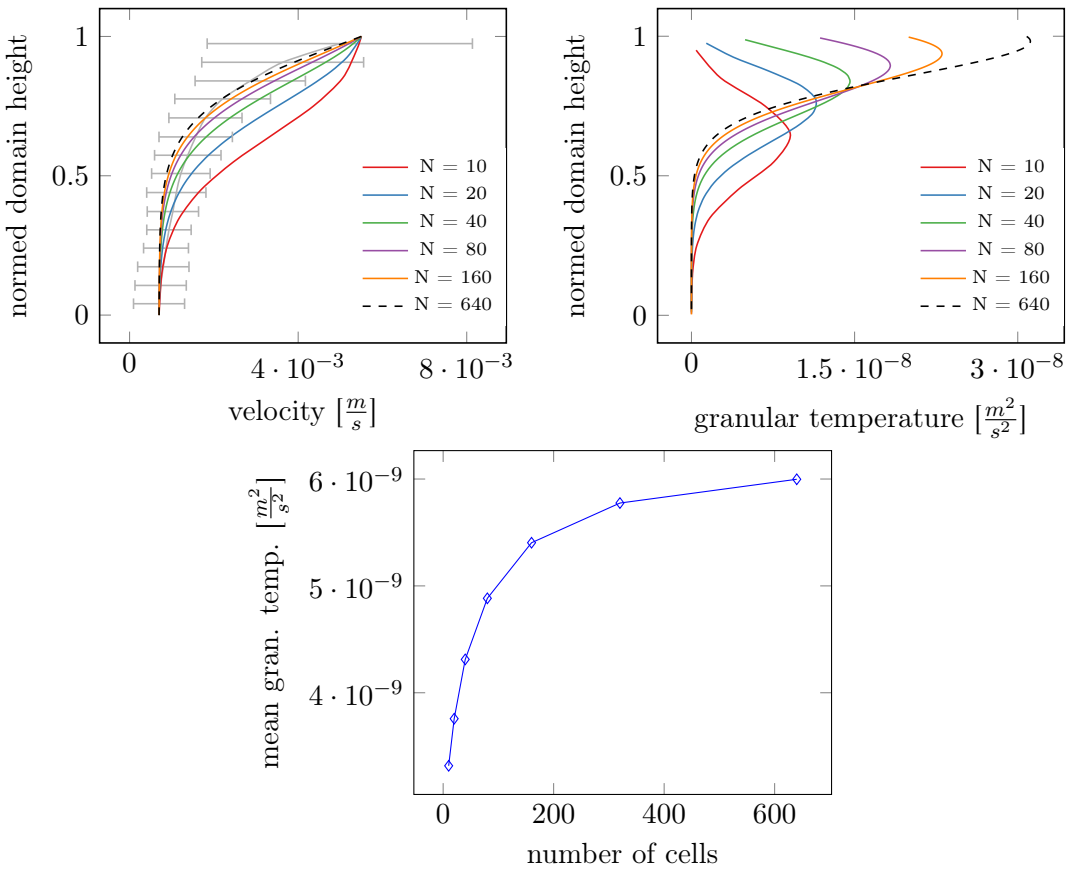

FIGURE 5.15: Velocity profile *(left)* for different grid sizes in a two-dimensional shear cell which is sketched in Figure 5.12. The horizontal grey lines represent the confidence intervals for the velocities measured in [60]. The grey curve connects the midpoints of the confidence intervals. In some regions, the velocity gradients increase due to the convergence of the velocity profile. This leads to an increase of the granular temperature in these regions *(right)*. Furthermore, an increase of the mean granular temperature in the granular system can be observed *(bottom)*.

symbol	value	unit	symbol	value	unit
η_0	1.3e-04	$[m]$	T_0	1.8	$[\frac{m^2}{s^2}]$
λ_0	3.4e-04	$[m]$	ϕ_{rlp}	0.5757	[1]
ε_0	1477.15	$[\frac{1}{m}]$	ϕ_{rcp}	0.632	[1]

Table 5.6: Parameters for the granular flow equations as used for simulating glass beads in [66], except for η_0.

velocity is set to $u_{bottom} = 0.0007\,\frac{m}{s}$. The initial volume fraction of the granular material is chosen to be $c = 0.6$, which lies above the RLP value to ensure contact with the top plate.

Figure 5.15 shows the resulting velocity profile *(upper, left picture)* and the temperature distribution *(upper, right picture)* over the normed domain height for different grids. One can see that the velocity profile converges. As it changes for different grid sizes, the temperature distribution changes accordingly. The maximum of the granular tempera-

ture increases for finer grids, because the velocity gradients increase, too. Additionally, the mean granular temperature in the domain is plotted *(lower picture)*. It can be seen that the mean granular temperature converges but increases noticeably with decreasing grid size.

In the previous subsections, non-constant but pre-defined velocity and temperature fields have been used to show grid convergence for the segregation equation. Dealing with the full system of equations, these fields are a solution of the granular flow equations. Due to the grid convergence of the velocity and the temperature field presented in Figure 5.15, grid convergence is also ensured for the segregation equation, when using the full system of equations.

To validate the influence of the granular flow equations on the segregation process in more detail, the computations for the different grids are used. These already provide slightly different velocity and temperature profiles. For the validation the results, which are obtained from the experiment, are used for comparison. In Figure 5.15, one can see that the computed velocity profile lies within the confidence intervals for grids of at least 40 cells per dimension. However, the velocity and the velocity gradients are slightly underestimated compared to the mean of the confidence intervals. The confidence intervals for the velocity are depicted by grey bars. The mean value is given by a grey curve. The temperature field changes accordingly.

The described velocity and temperature fields for different grids influence the segregation process in different ways. The bulk velocity is relevant in the segregation equation for the transport with the granular material. A change of the velocity profile merely changes the flow behaviour of the granular system but has no direct influence on the segregation process. Especially for the perfectly parallel shear flow in the shear cell setting, there is no effect on the segregation pattern.
An indirect influence of the granular velocity field is given by the granular temperature, since both influence each other in the granular flow equations. This influence of the granular temperature to the segregation process is strong, since the segregation velocity scales with $\sqrt{T}$. A higher granular temperature leads to a higher segregation velocity in these regions. As the mean granular temperature in the system increases for finer grids, one would expect that the segregation reaches its final state faster. This is not generally the case as it will be shown in the upcoming subsection. More important than the total amount of the granular temperature in the system is the distribution of the granular temperature. The temperature distribution obtained for finer grids in the shear cell case leads to faster segregation close to the fast top plate. However, the region with low granular temperature also grows in the bottom half of the shear cell. Hence, a bottleneck for the segregation process emerges. This increases the time until a final state can be reached.

5.3.3 Comparison to a shear cell experiment

In this subsection, the focus lies on a more detailed comparison of the simulations and the shear cell experiment, especially concerning the segregation process. In Figure 5.15, it

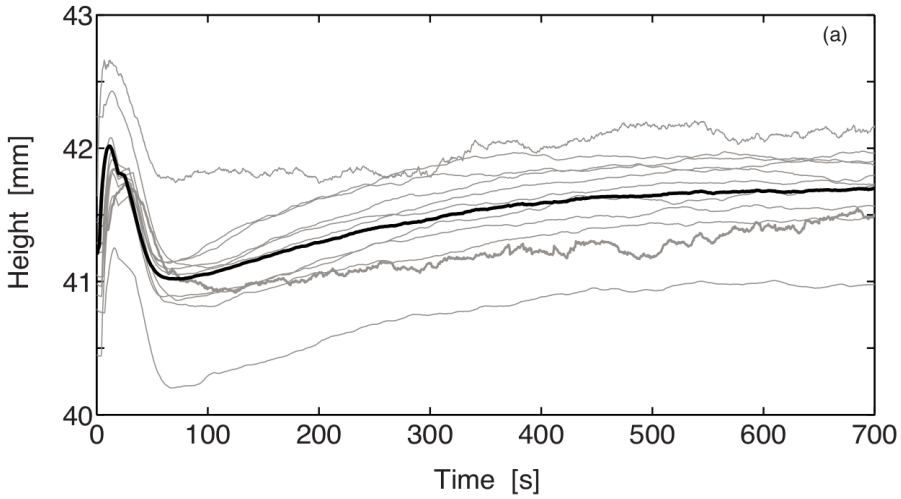

FIGURE 5.16: Height plot of the sheared granular bed for 11 experimental runs *(grey lines)*. The thick black line is the average of the 11 runs. Plot taken from [60].

has already been shown that the velocity profile converges to a profile that is lying within the confidence intervals measured in the experiment. However, comparing to the mean of the measurements, the simulations underestimate the velocity and the velocity gradient in the bottom half. This results in very low granular temperature values in this region.

To analyse the segregation process, more information from the shear cell experiment can be used. It already has been mentioned that the top plate of the shear cell is free to move vertically in the experiment performed by May et al. [60]. This ensures the contact between the top plate and the material, even when the system changes its volume due to the segregation process. The authors measured the vertical movement of the top plate to track the segregation process over time. Figure 5.16 shows the movement of the top plate for all eleven runs of the experiment in grey. The black curve shows the mean value of all runs. The first peak is mainly a result of the transition of the granular material from a static to a flowing regime. After that, the measured height decreases as the inversely graded particles start to mix before the re-segregation process starts. The segregation process ends after $700\,s$. This information can be used to fit the segregation rate S_0^{sl}.

Figure 5.18 shows the segregation process for a simulation with a space discretisation of 80 cells per dimension. The segregation rate is chosen to be $S_0^{sl} = 4.56$, such that the segregation process in the numerical simulation ends like in the experiment. Due to the non-linear velocity profile and the resulting temperature distribution, the segregation patterns during the whole process differ from the idealised case, which is depicted in Figure 5.14. Since the temperature is not constant over the whole domain, the segregation velocity changes with domain height. Therefore, large particles reach the top plate much earlier than small particles reach the bottom plate. The general behaviour fits to the experiments. After a slight mixing of the system in a short time interval, a long period of time is needed to reach the final re-segregated state. This can also be seen in Figure 5.17, which shows the behaviour of the mixture entropy in the system for different grids. The segregation rate, $S_0^{sl} = 4.56$, is the same for all grids and corresponds to the

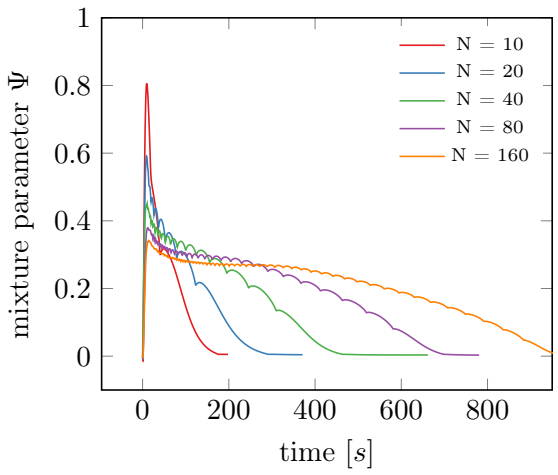

FIGURE 5.17: Mixture parameter for different grids. The segregation rate, $S_0^{sl} = 4.56$, is chosen such that the simulation with a grid resolution of 80 cells per dimension fits the experiment. The time to reach the final state increases for finer grids.

N	S_0^{sl}
10	1.28
20	2.01
40	3.08
80	4.56
160	6.24

TABLE 5.7: Segregation rate for different grids. The value is fitted to the time needed to reach the final state in the experiment.

shown simulation result in Figure 5.18. The segregation process differs for the different grids. For a coarse grid, the system mixes more rapidly and the final re-segregation time is much shorter than for finer grids. This verifies the observations from the previous subsection. For a coarse grid, the maximum of the granular temperature profile lies further in the centre than for finer grids. Furthermore, the region where the granular temperature is close to zero is small for a coarse grid. This region grows for decreasing grid size. The emerging bottleneck increases the final re-segregation time considerably. Fitting the simulation for each grid to the experimental measured segregation time, the segregation rates range between $S_0^{sl} = 1.28$ and $S_0^{sl} = 6.24$ as can be seen in Table 5.7. However, it can be assumed that most segregation rates given in Table 5.7 are overestimated. This results from the fact that the velocity profile computed by the granular flow equations does not exactly hit the mean of the measured velocities in the experiment. Especially the velocity gradients close to the bottom plate are too small in the performed simulations compared to the experiment.

Summarising the above, it can be said that the general behaviour of the segregation process works well. The grid convergence ensures also the convergence of S_0^{sl}. However, the segregation process depends strongly on the distribution of the granular temperature and therefore, on a good agreement of the granular flow equations to the real material. It is almost more important to hit the velocity gradients than the absolute values of the velocity. Otherwise, a suitable segregation rate can vary a lot.

(A) Initial state.

(B) State after 13 s.

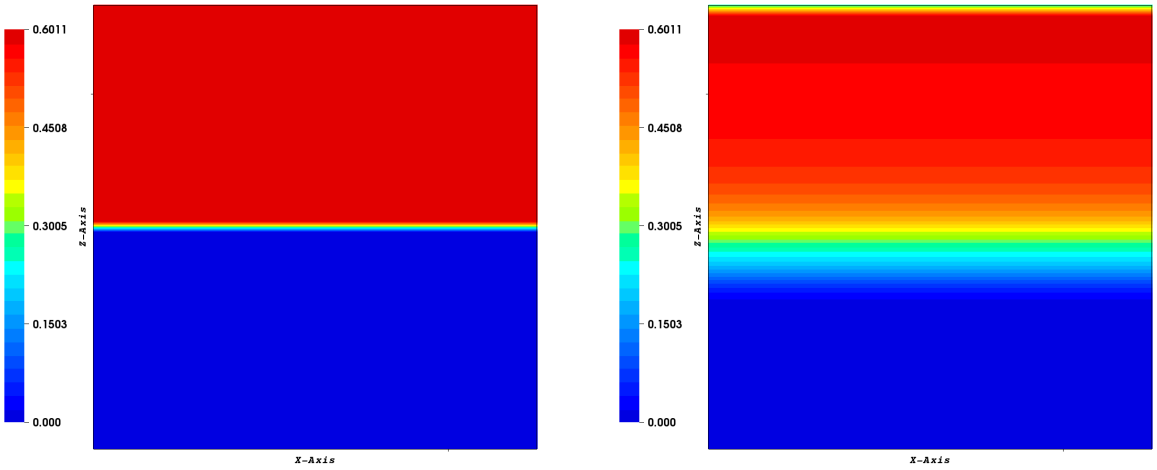

(C) State after 26 s.

(D) State after 132 s.

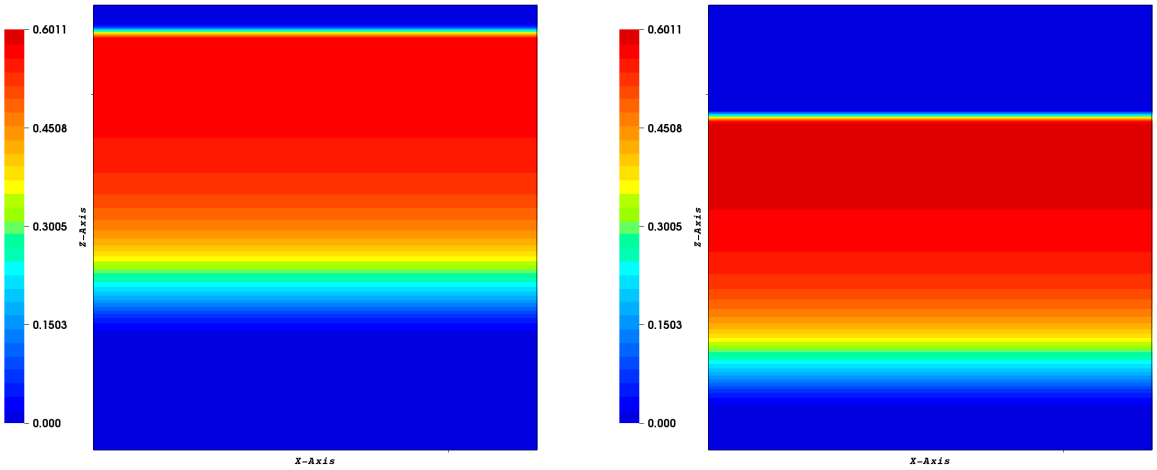

(E) State after 330 s.

(F) State after 660 s.

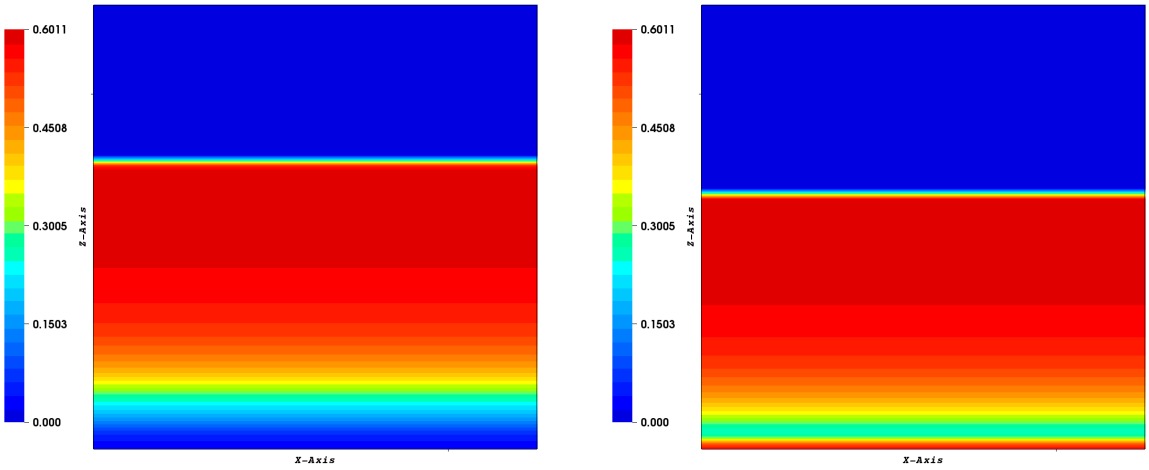

FIGURE 5.18: Simulation result of the two-dimensional shear cell with a grid resolution of 80 cells per dimension. The plots show the volume fraction of the small particles at the initial state and the states after 13 s, 26 s, 132 s, 330s, and 660 s. The system starts inversely graded. After a mixing phase the system re-segregates. The segregation rate is $S_0^{sl} = 4.56$, such that the process ends after 700 s.

5.3.4 Verifying the shear-temperature relation

In contrast to many other models presented in literature, the segregation equation derived in chapter 2.2 depends on the square root of the granular temperature and not on the shear rate. Therefore, the relation

$$\dot{\gamma} = \underbrace{\sqrt{\frac{2}{3}\frac{\varepsilon_0}{\eta_0}}}_{=:\frac{1}{k}} \sqrt{T}$$

has been derived in 2.1.6. This expression is an approximation attained from the granular temperature equation. In Figure 5.19, one can see the $k\dot{\gamma}$ and $\sqrt{T}$-profile in the two-dimensional shear cell setting, computed using the granular flow equations with a grid resolution of 80 cells per dimension. Both profiles are not identical, but they behave the same. They mainly vary by a scalar factor of approximately 0.692. Therefore, one can say that for shear flows the chosen relation is a valid approximation. In these cases, the segregation equation produces the same result using the square root of the granular temperature or the shear rate if the segregation rate is chosen appropriately.

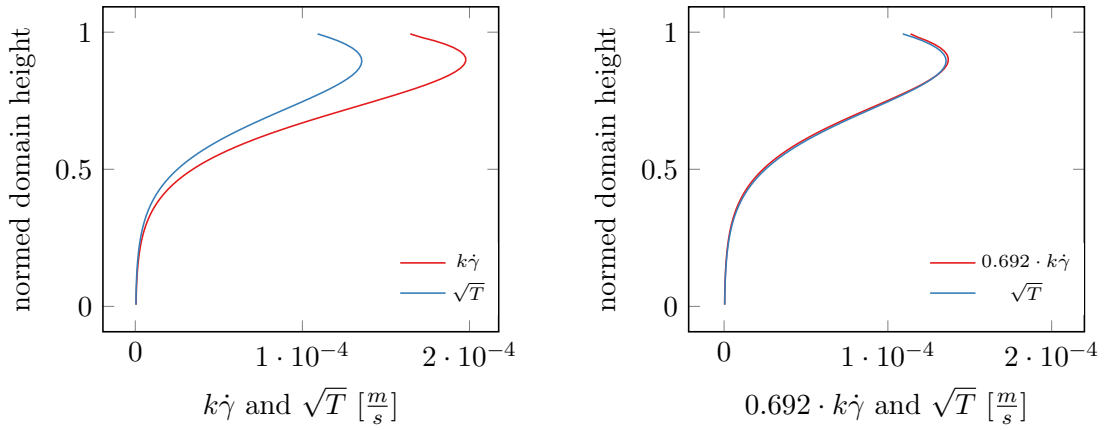

FIGURE 5.19: Plot of the $k\dot{\gamma}$-profile and the $\sqrt{T}$-profile in the two-dimensional shear cell setting *(left)*, computed by the granular flow equations with a grid resolution of 80 cells per dimension. The profiles are close to identical besides a scalar factor of approximately 0.692 as shown in the right plot.

5.4 Applications in the three-dimensional space

This last section focuses on simulations in the three-dimensional space. These simulations are most important for real applications. The use case of choice is a plain rotating tumbler for several reasons. First of all, the general behaviour of the granular material in such a tumbler is already well known, since it is used in industrial processes and therefore, a thoroughly investigated case in literature. Furthermore, the granular material shows different regimes during the rotation of the tumbler. There are flowing regimes where segregation takes place as well as static regimes.
The behaviour of the granular material in a rotating tumbler depends not only on the material properties but also on the rotation speed. Additionally, the filling height and

the wall friction can influence the regime of the granular material. Mellmann [63] gives an extensive overview of the different conditions and regimes. All types of bed motion can be subdivided into three forms, called

- slipping motion,
- cascading (tumbling) motion,
- cataracting motion.

The two types of slipping motion, sliding and surging, only appear for low rotational velocities and unfavourable frictional conditions between granular material and the walls of the tumbler. In these two regimes, the tumbler walls need to be very smooth, such that the material slides as static block relative to the tumbler wall, which is of no interest in this work.
Of high interest in industrial processes and also in this work is the cascading regime, which formally can be subdivided into three states of motion, namely slumbing, rolling, and cascading. The slumbing regime is also of low interest, because of the very low rotational speed. The other two states of motion are quite similar and they are characterised by a uniform flow of granular material on the surface and a large part of the granular bed that is moving statically with the rotation of the tumbler. Past and current research has concentrated on this regime ([2, 3, 41, 48, 68, 82]).
For very high rotational speeds, the motion of the granular bed becomes turbulent in the cataracting regime, which formally includes also the centrifuging state of motion.

5.4.1 The rotating tumbler

The first simulated test case, is situated in the rolling regime. The tumbler has a diameter of $0.1\,m$ with periodic boundary conditions at the end walls. This guarantees a large granular bed and lower computational costs compared to simulating a tumbler of extended thickness. For the granular material, the parameter set for the glass beads is used as has been done in the shear cell experiment. The parameters are given in Table 5.6. The segregation rate is set to $S_0^{sl} = 1$, which is in the order of the rates gained for the shear cell simulations. In contrast to the shear cell simulations treated in the previous section, no contact with a top wall has to be guaranteed. Hence, the full model can be used, including the back-coupling from the segregation equation to the granular flow model. This leads to varying RCP and RLP values during the segregation process. For the interaction between material and side wall, a wall friction angle of $11°$ is chosen (compare 2.1.5), which corresponds to a smooth side wall. The tumbler rotates in a clockwise direction with a speed of 0.1 revolutions per second (rps).

The rotation of the tumbler is realised with a software module for moving and rotating domains, which is provided in CoRheoS. Using this module, the set of equations is solved in the rotating reference frame. In this rotating reference frame, the domain and the grid are static, but the gravity vector rotates. Additionally, fictitious forces, like the centrifugal force and the Coriolis force, have to be added. For solving the whole set of

(A) Initial state. (B) State after 2 s.

(C) State after 5 s. (D) State after 25 s.

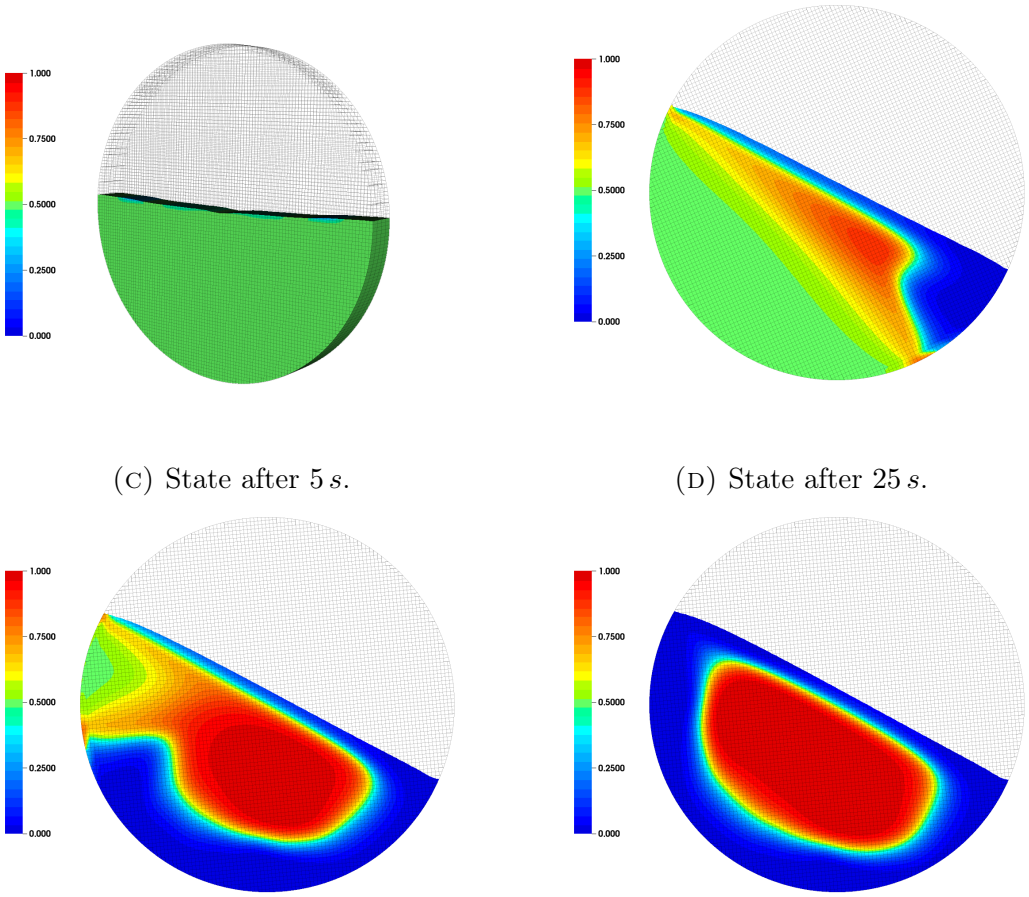

FIGURE 5.20: Half-filled rotating tumbler showing the perfectly mixed initial state and the further segregation process at time 2 s, 5 s, and 25 s. Due to the segregation process, a core of small particle forms and the large particles are located at the periphery. The plots show the relative volume fraction $\hat{\phi}$ of the small particle phase.

equations in the rotating reference frame, only the body force term given by the gravity vector has to be replaced by the rotating gravity vector and the fictitious forces, i.e.,

$$\mathbf{F}_{gravity} = \mathbf{F}^{rot}_{gravity} + \mathbf{F}_{centrifugal} + \mathbf{F}_{Coriolis}. \tag{5.13}$$

For the illustration, the whole grid is simply transformed back to the inertial system.

The initial state of the simulation is a half-filled tumbler in a perfectly mixed state with equal volume fractions for small and large particles. From literature *(e.g. [1])*, the segregation behaviour for the rolling regime is known. In this setup, a special pattern forms due to the rotation. Near the surface, the particles are in motion while the bulk of the granular material beneath the surface layer stays in a static state. The segregation is then concentrated in the shearing top layers. Here, the system segregates with small particles percolating downwards and large particles are lifted to the surface. In the static regime below, the material rotates with the tumbler without further segregation. This behaviour can be accurately observed in Figure 5.20. As expected, a core of small particles is formed due to the segregation, whereas the large particles eventually wander

to the periphery. In the plots, the relative volume fraction $\hat{\phi}$ of the small particle phase is shown. Accordingly, the colour bar is fixed between 0 and 1.

It is known, that the segregation pattern is sensitive to changes in the filling height. This can be observed in the simulation. Again small particles percolate downwards in the sheared regime near the granular surface. However, the small particles do not even reach the core of the granular material, due to the increased height of the granular bed. Finally, a ring of small particles forms around a completely unchanged core. The large particles accumulate next to the walls. Figure 5.23 shows the simulation result of a rotating tumbler filled to a height of 75 % after 25 *s (top row, left)*. One can see exactly the described pattern. Besides the filling height, the whole setup is chosen identical to the half-filled tumbler.

Similar results are given by Arntz et al. [2, 3]. The authors studied the segregation process in horizontal rotating tumblers using DEM simulations. Especially, they focused on the influence of the rotation speed on the segregation process. To quantify the degree of mixing, they used an entropy expression based on their DEM data. The method is similar to the mixture entropy defined in 5.2.2 which is based on the data gained from the continuum fields. They found that for a fill level of 50 %, the segregation effect is strong for slow rotating tumblers. With increasing rotation speed the system tends to a mixed state. A maximal plateau of this process begins with the beginning of the cataracting regime, where the motion becomes turbulent. If the rotation speed is increased further, the particles start to demix again, which is where the cataracting-centrifuging regime begins. In this regime, all particles are pressed to the outer walls, where the smaller particles tend to accumulate.

Figure 5.21 shows the normalised mixture entropy for the simulation of the rotating tumbler with different rotation speeds in the rolling and cascading regime. The value E_{mix} to normalise the mixing entropy for the use case of the half-filled tumbler is given by $E_{mix} = 1.717\text{e-}05$. The slowest rotation speed of $0.1\,rps$ lies in the rolling regime and the fastest in the cascading regime with a rotation speed of $1.5\,rps$. Latter rotation speed is already quite close to the beginning of the cataracting regime where Arntz et al. [2] gained the mixed granular system. Similar to the results described in [2], the system with the lowest rotation speed segregates until a certain point, where the system stays with small periodic fluctuations appearing with every revolution of the tumbler. For increasing rotation speeds, the entropy value of the final state increases. The granular beds are less segregated. The system with the highest rotation speed barely changes and stays in an almost perfectly mixed state. For even faster rotation speeds, it can not generally be expected that the model, derived in this work, is applicable, since turbulent flows have not been considered deriving the segregation equation.
The tendency of the granular system to mix or segregate for different rotation speeds fits the results presented in the work of Arntz et al. [2]. However, the simulation results shown in Figure 5.21 reach their final state faster than the DEM simulations performed in [2]. Furthermore, the entropy values of the steady states in the simulation range from 0.3 to 0.93. The values in [2] vary between 0.6 and 0.98. However, the large discrepancy between the two lower values suggests that the segregation rate is too large for this use

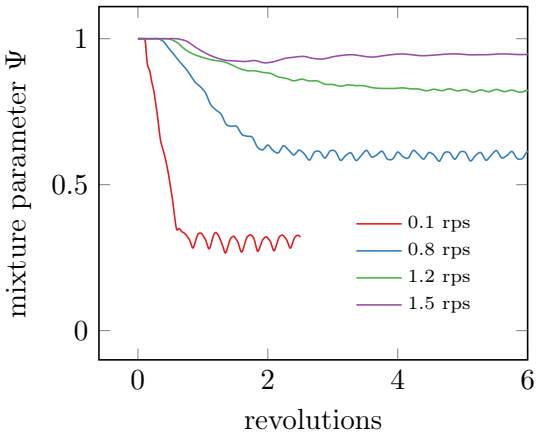

FIGURE 5.21: Normalised mixture entropy for the simulation of the rotating tumbler with different rotation speeds in the rolling and cascading regime. The slowest rotation speed of 0.1 *rps* lies in the rolling regime and the fastest in the cascading regime with a rotation speed of 1.5 *rps*. The influence of the segregation process decreases with increasing rotation speed in these regimes as observed in [2].

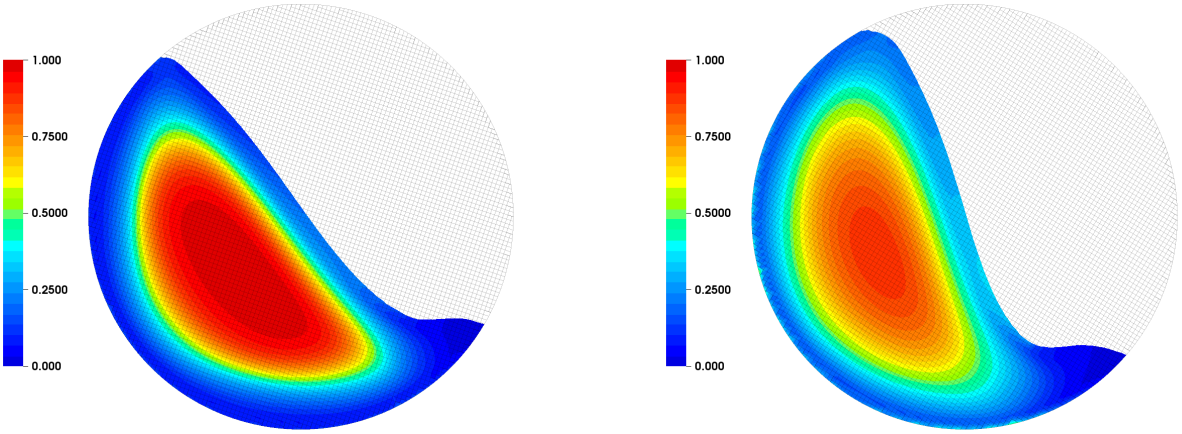

FIGURE 5.22: Half-filled rotating tumbler at time 25 *s* with a rotation speed of 0.8 *rps (left)* and 1.2 *rps (right)*. Due to increasing rotation speeds the typical segregation pattern is less strong, as observed in Figure 5.20. The plots show the relative volume fraction $\hat{\phi}$ of the small particle phase.

case. Two examples of the performed simulations for the rotation speeds 0.8 *rps* and 1.2 *rps* are shown in Figure 5.22.

Not only the segregation rate can control the segregation process but also an additional remixing term in the model could improve the results. As already mentioned in chapter 1 and 2, such a term is already discussed in the literature, but the ratio between segregation rate and diffusivity is still unclear. If a suitable form and the dependences of such an additional term can be found, the model can be improved further. A physically correct interplay of segregation and remixing probably can improve the simulation results much more than only fitting the segregation rate.

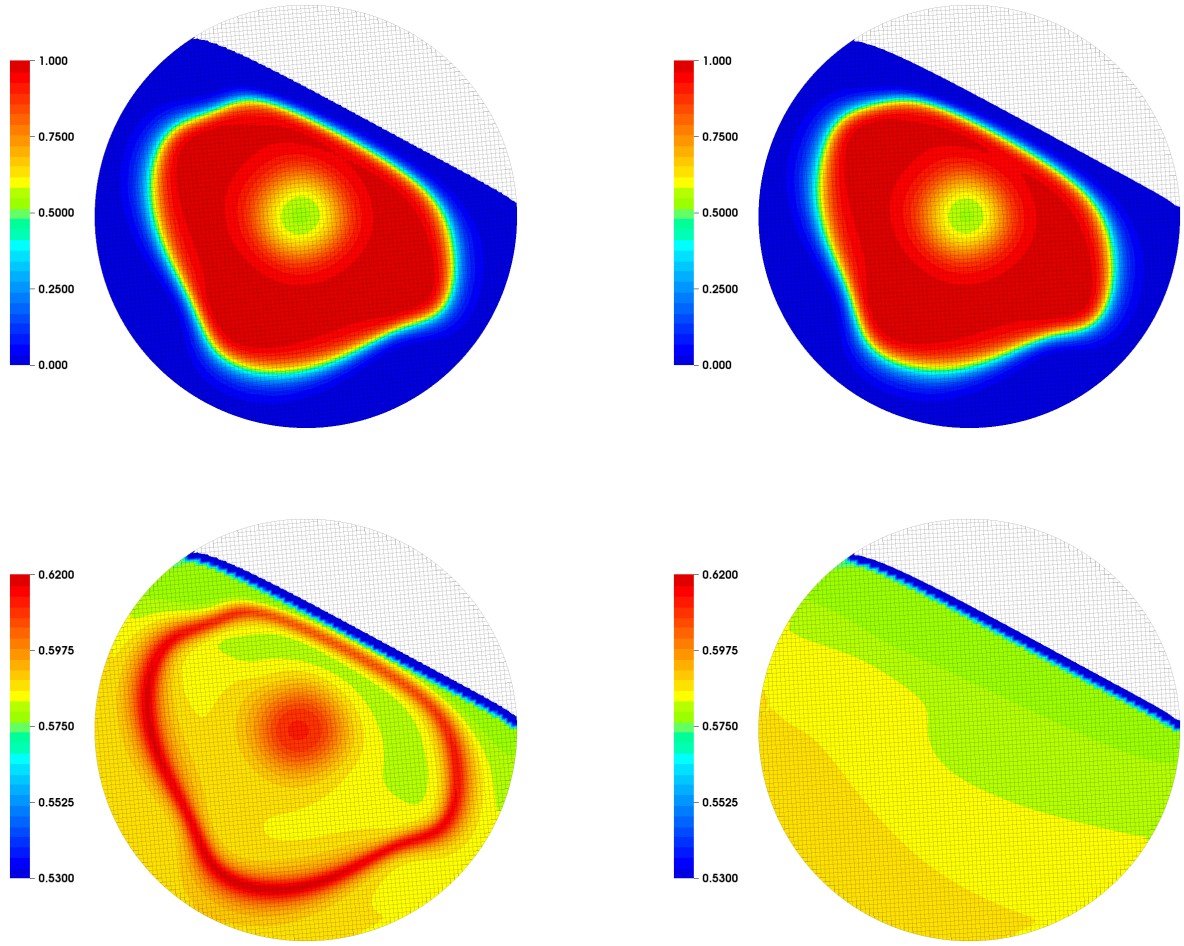

FIGURE 5.23: Segregation pattern *(top row)* in a tumbler filled to a height of 75 %. The plot shows the relative volume fraction $\hat{\phi}$ of the small particle phase. Additionally, the granular volume fraction c is shown *(bottom row)*. The same simulation has been done with back-coupling *(left)* and without back-coupling *(right)*. All plots show the respective state after 25 s.

5.4.2 Influence due to binary particle packings

The final model, as given in section 2.5, uses varying RCP and RLP values depending on the relative volume fraction $\hat{\phi}$ of the small particle phase. To show the effect of these varying packing values, the rotating tumbler with a filling height of 75 % has been simulated with and without varying packing values. This means the model is solved with and without a back-coupling from the segregation equation to the granular flow equations. The resulting segregation pattern after 25 s is shown in Figure 5.23 *(top row)*. Additionally, the granular volume fraction profile is shown *(bottom row)*. The plots on the left show the simulation with and the plots on the right without varying packing values. One can see that both simulations yield almost identical segregation patterns. However, the advantage of the varying packing values can be seen in the granular volume fraction plots. The profile for the simulation without varying RCP and RLP values simply shows a lithostatic profile which is characteristic for a mono-disperse system. In the case of varying packing values, the lithostatic profile is superimposed by a profile that is similar to the segregation pattern. One can see that the volume fraction is much higher in regions where

the system is partially mixed than in regions where solely one particle phase is present. The packing values that have been reached in the mixed regions are much higher than any value in the volume fraction profile for the simulation without back-coupling, which is in agreement with the expectations.
In summary, one can say that a simple version of the final model without back-coupling is applicable to reproduce correct segregation patterns. However, back-coupling from the segregation equation to the granular flow model leads to more realistic results for the volume fraction profiles in the case of binary particle systems.

5.4.3 Discharging a silo

After performing several simulations for the rotating tumbler, another entirely different test case has been studied. The process of interest in this section is the discharge of a silo filled with some granular material. Therefore, also the properties of the granular material are modified compared to the tumbler simulations. Assuming the surface of the used particles is less smooth than the glass beads simulated before, the RLP is chosen to be smaller, than that in the tumbler simulation. All parameters that have been used for the model are given in Table 5.8. The silo has a flat bottom plate and a free discharge located in the middle of the bottom plate. The silo has a dimension of $0.5 \times 0.145 \times 0.04\,m^3$ and is filled with small and large granular particles with an average diameter of $3.3\,mm$. The size ratio is $R = \frac{1}{2}$. Initially, the system is perfectly mixed. For the interaction of the particles and the wall, a wall friction angle of 30° has been chosen. Figure 5.24 shows the full domain and the relative volume fraction $\hat{\phi}$ of the small particle phase. One can see that due to the discharge of the silo a segregation pattern forms.

Combarros Garcia et al. [14] have performed several experiments discharging silos of different kind and shape. The silos had a transparent side wall to image the resulting segregation patterns. They have also performed an experiment for a silo with a flat bottom plate and free discharge. Images of their experiment at different states in time during the discharging process are shown in Figure 5.25. The small particles in the experiment are

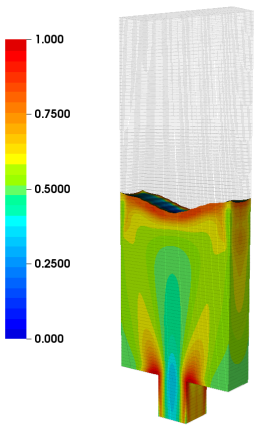

FIGURE 5.24: Segregation pattern as a result of simulating a discharging silo. The plot shows the relative volume fraction $\hat{\phi}$ of the small particle phase.

symbol	value	unit
η_0	0.00175	$[m]$
λ_0	3.4e-04	$[m]$
ε_0	126.984	$[\frac{1}{m}]$
T_0	1.5	$[\frac{m^2}{s^2}]$
ϕ_{rlp}	0.4	[1]
ϕ_{rcp}	0.64	[1]
S_0^{sl}	0.2	[1]

TABLE 5.8: Set of parameters that have been used in the final model for simulating the discharging silo.

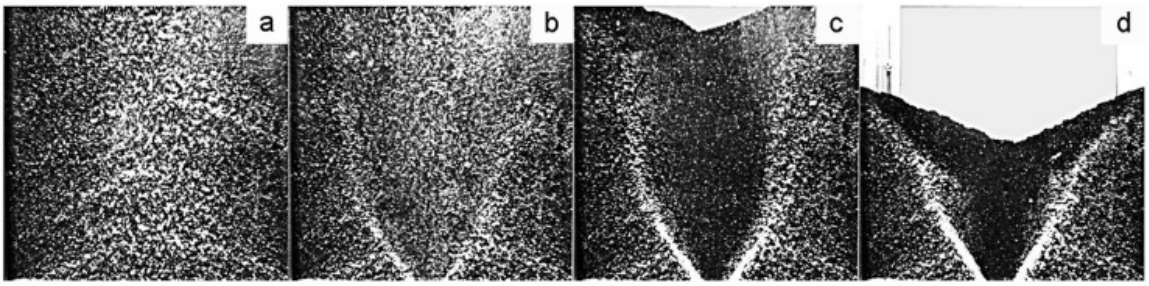

FIGURE 5.25: Segregation patterns for a discharge out of a silo with a flat bottom and free discharge at different states. The large particles are darker than the small particles. Pictures taken from Combarros Garcia et al. [14].

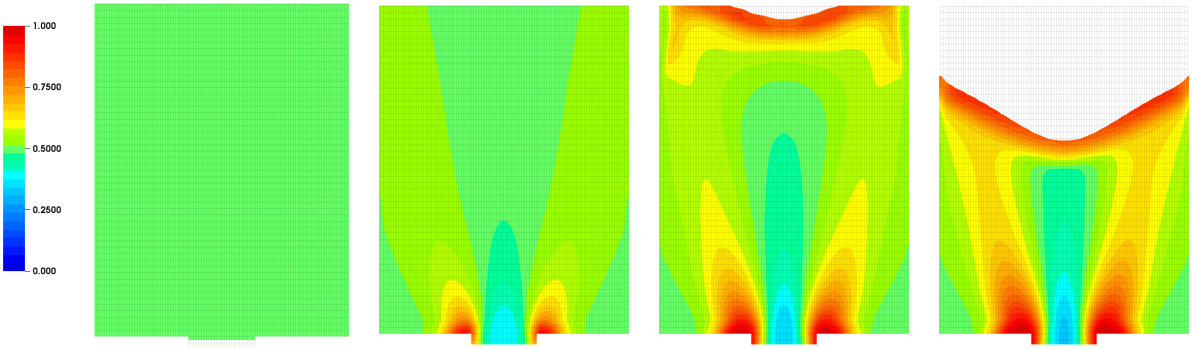

FIGURE 5.26: Segregation patterns for a discharge out of a silo with a flat bottom and free discharge at different states. The simulation result shows the lower part of the silo. The red areas show a high concentration of small particles given by the relative volume fraction $\hat{\phi}$.

light and the large particles dark. During the discharging process, a V-shaped layer of small particles emerges from the corners of the discharge. This is a characteristic pattern for a silo with a flat bottom plate.
Figure 5.26 shows the simulation result in the lower part of the silo during the discharging process. Similar to the experiment performed in [14], a V-shaped layer of small particles emerges. Hence, the main characteristic pattern can be reproduced.

Chapter 6

Conclusion

This work investigates the simulation of granular material flows with segregation. The used model extends a set of Navier-Stokes-like equations with a non-Newtonian and non-linear rheology model, to incorporate the segregation process of binary granular systems with small and large particles in up to three space dimensions.

The segregation equation has been derived using mixture theory. Due to the coupling of the segregation equation to the granular temperature, the segregation process is regulated in the different regimes. Depending on the behaviour computed by the granular flow equations, segregation takes place in regimes where the granular material is sheared or random particle movement can be observed. In contrast to this, the segregation is inactive for plug flows or static systems.

Unlike most other models in literature, the segregation equation derived in this work depends explicitly on the local value of the granular volume fraction. The volume fraction is non-constant over the whole domain, since the granular flow equations are compressible. Therefore, due to the varying granular volume fraction field, the segregation equation needs to be treated numerically in a special way. Therefore, a Riemann problem for each possible combination of left and right states has been solved. Additionally, all solutions have been illustrated in the phase space. Based on these solutions, a modified version of Godunov's method has been formulated for the small particle phase (convex). The corresponding solutions and the formulation of the scheme for the large particle phase (concave) are given in Appendix A.

To make the model applicable to a wide field of applications, where the flow direction might change, a local segregation direction vector has been introduced. This segregation direction is computed based on the granular flow field which also makes the segregation process invariant to the choice of the coordinate system. An advantage compared to common models of a similar type is that the segregation process does not have to act in the same direction in the whole domain.

Section 2.3 has addressed the topic of particle packings. The packing fraction of binary particle systems differs depending on the ratio of the particles' radii and especially on the proportion of small and large particles. Therefore, the granular flow equations have

been modified to account for this property. Depending on the state of segregation, which is computed by the segregation equation, the random close packing value and also the random loose packing value for the granular system change.

In chapter 5, the derived model has been tested for different test cases in different space dimensions. It has been shown that the derived numerical scheme prevents the system from reaching unphysical states. For the segregation equation, first order convergence has been observed. Furthermore, the model performs well for the chosen examples. However, it has been pointed out that for real applications it is quite important to accurately fit the basic model to the real material, since the temperature field has a strong influence on the segregation process.

All numerical results presented in two and three-dimensional space have been computed using the finite volume solver GRAIN, which is included in the software platform CoRheoS, developed at ITWM. The implementation of the segregation equation, as well as the modifications to the granular flow model were implemented by the author using C++.

The final system of equations have shown good results for the different test cases. To further increase the accuracy of the model, some additional modifications and extensions could be investigated. As pointed out in this work, the structure of the segregation equation leads to a strong influence of the granular temperature on the segregation process. Therefore, it is advisable to compare the granular flow equations to more experiments of different kinds. To obtain suitable results for a large variety of flows in almost arbitrary domains, it is currently expected that some aspects of the model need to be improved.
Moreover, it is not easy to identify the parameters of the granular flow model to fit a real material. Currently, there is no standard procedure to obtain all parameters from particle properties or simple experimental measurements. A promising approach to obtain macroscopic properties is the combination of DEM simulations and upscaling methods such as coarse graining [80, 84].
Concerning the segregation process itself, several further improvements are already topic of the current research. This includes a diffusive remixing term in the segregation equation which has already been modelled and thoroughly discussed, e.g. in [36]. A physically correct interplay of segregation and remixing probably could improve the simulation results a lot. However, the ratio between segregation velocity and diffusivity is still unclear.
Other improvements of interest are a segregation rate that explicitly depends on the particle sizes [59], the extension to n-particle phases [34] or the density segregation. Also, models of combined size and density segregation [35, 79] are an interesting research topic, as further effects come into play like the reverse Brazil nut problem.
An extension of the current model to n-particle phases, as has been done in [34], could easily be achieved. The same holds true for a segregation rate that explicitly depends on the particle sizes. It should furthermore be investigated, how to include diffusive remixing or the combined size and density segregation in a consistent way.

Appendix A

Riemann solutions for the large particle phase

Let $\phi = \phi^l$ be the volume fraction of the large particle phase. Similarly to the equation of the small particle phase (4.30), one can augment the simplified equation for the large particle phase

$$\partial_t \phi + \partial_z \left(S \left(\frac{c - \phi}{c} \right) \phi \right) = 0 \tag{A.1}$$

into a resonant system. A Riemann problem can be solved in the same way as presented in Chapter 3. For the large particle phase, the segregation flux is concave. In this case, the integral curves in the state space are identical to the convex case of the small particle phase but the allowed paths in the state space are different. The state space can, depending on the position of the left Riemann state $\mathbf{U}_L$, be decomposed into 10 regions for the location of $\mathbf{U}_R$, which results in different wave combinations. These regions are depicted in Figure A.1. The different Riemann solutions are depicted in Figure A.2 - A.11. The conditions for each combination of wave solutions and the resulting approximated boundary fluxes are listed in Table A.1. Since the flux curves are concave, their extrema are maxima. Hence, these values are denoted by f_L^{max} and f_R^{max}, whereas the corresponding arguments are denoted by ϕ_L^{max} and ϕ_R^{max}, respectively. The resulting numerical flux function of Godunov type in the concave case can be written by

$$\bar{F}^G = \min \left\{ f_L(\min\{\phi_L, \phi_L^{max}\}),\ f_R(\max\{\phi_R, \phi_R^{max}\}) \right\}, \tag{A.2}$$

where $f_L(\phi) = f(\phi, c_L)$.

For the segregation equation of the large particle phase without constant temperature,

$$\partial_t \phi + \partial_z \left(S\sqrt{T} \left(\frac{c - \phi}{c} \right) \phi \right) = 0, \tag{A.3}$$

the average flux over the cell boundary can be given by expression (A.2) as well, where $f_L(\phi) = f(\phi, c_L, T_L)$.

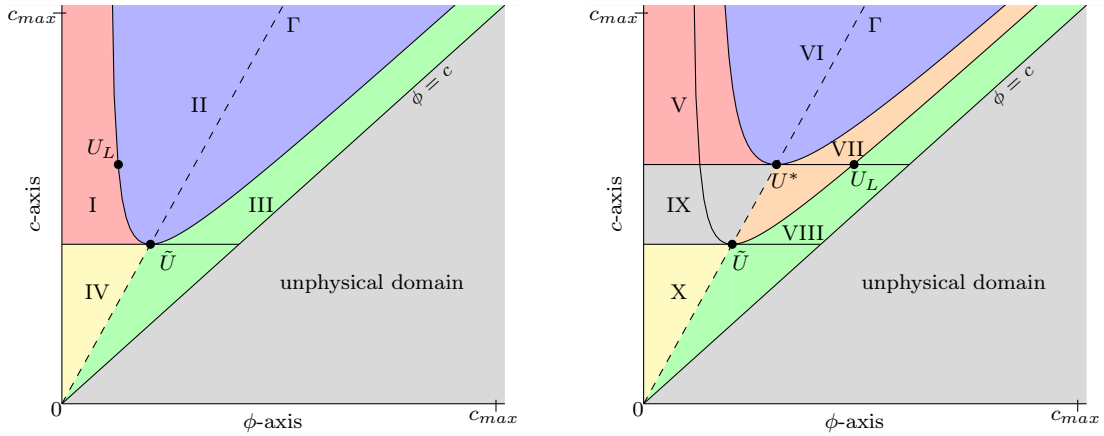

FIGURE A.1: Different regions for $\mathbf{U}_R$ depending on $\mathbf{U}_L$ which yield different Riemann solutions for a concave segregation flux. Four regions if $\mathbf{U}_L$ is located left of the transition line Γ *(left Picture)* and six regions if $\mathbf{U}_L$ is located right of Γ *(right Picture)*. The lower right part defines an unphysical area, as $\phi > c$.

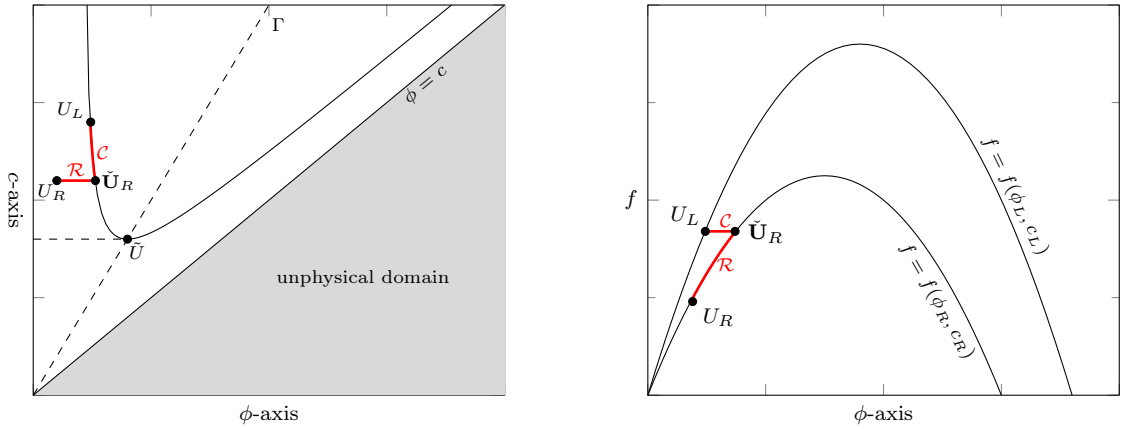

FIGURE A.2: **(1)** Example showing the wave solution in state space *(left)*. $\mathbf{U}_L$ is located left of the transition line Γ and $\mathbf{U}_R$ in region I shown in Figure A.1, where $\phi_R < \frac{c_R}{2}$, $c_R > \tilde{c}$, and $f(\mathbf{U}_R) < f(\mathbf{U}_L)$. The solution consists of two basic waves, a standing wave $(\mathbf{U}_L, \check{\mathbf{U}}_R)$ and a rarefaction wave $(\check{\mathbf{U}}_R, \mathbf{U}_R)$ with characteristic speed $\lambda_1(\phi, c_R) > 0$. Furthermore, the flux function for a left and a right state is plotted *(right)*. The wave solution is highlighted. The flux curves are connected by the contact discontinuity. The resulting average boundary flux is given by $\bar{F} = f(\mathbf{U}_L)$.

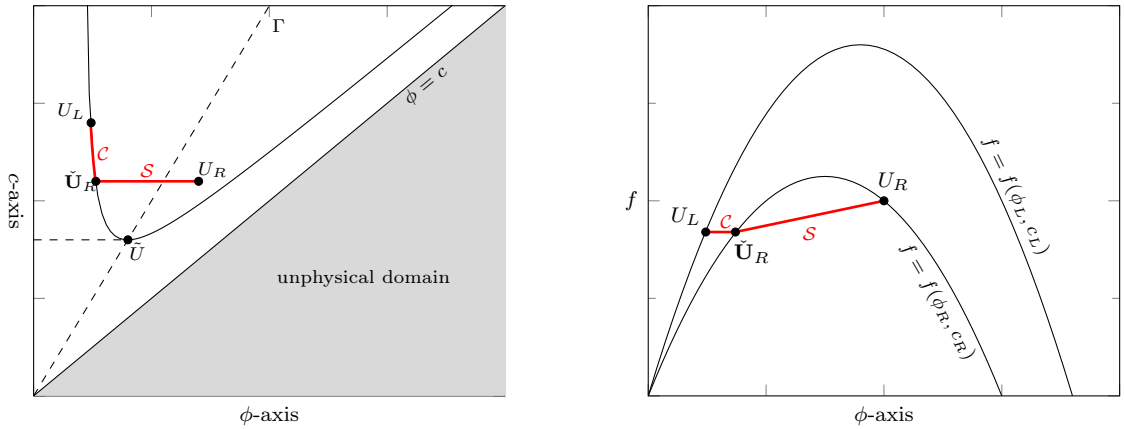

FIGURE A.3: **(2)** Example showing the wave solution in state space *(left)*. $\mathbf{U}_L$ is located left of the transition line Γ and $\mathbf{U}_R$ in region II shown in Figure A.1, where $f(\mathbf{U}_R) > f(\mathbf{U}_L)$. The solution consists of two basic waves, a standing wave $(\mathbf{U}_L, \check{\mathbf{U}}_R)$ and a shock wave $(\check{\mathbf{U}}_R, \mathbf{U}_R)$ with positive speed, given by $s = (f(\mathbf{U}_R) - f(\check{\mathbf{U}}_R)/(\phi_R - \check{\phi}_R) > 0$. Furthermore, the flux function for a left and a right state is plotted *(right)*. The wave solution is highlighted. The flux curves are connected by the contact discontinuity. The resulting average boundary flux is given by $\bar{F} = f(\mathbf{U}_L)$.

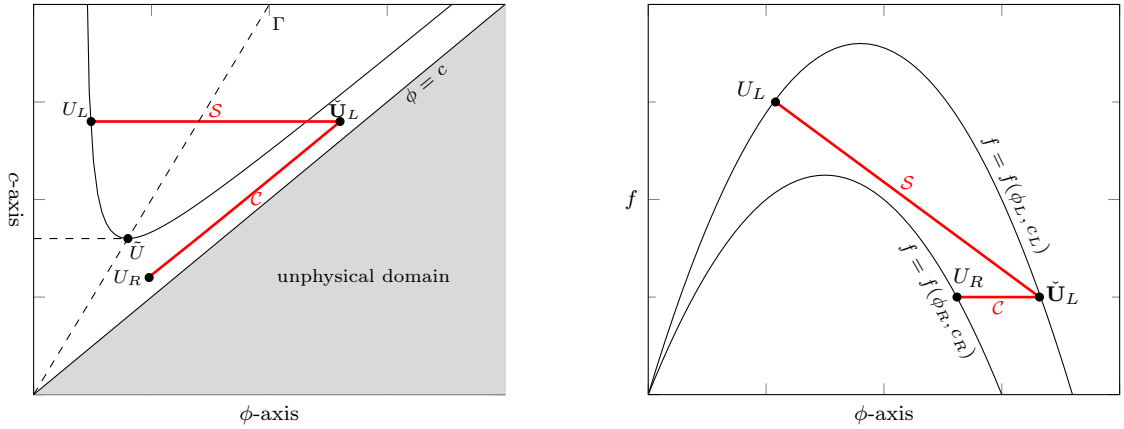

FIGURE A.4: **(3)** Example showing the wave solution in state space *(left)*. $\mathbf{U}_L$ is located left of the transition line Γ and $\mathbf{U}_R$ in region III shown in Figure A.1, where $\phi_R > \frac{c_R}{2}$ and $f(\mathbf{U}_R) > f(\mathbf{U}_L)$. The solution consists of two basic waves, a shock wave $(\mathbf{U}_L, \check{\mathbf{U}}_L)$ with negative speed, given by $s = (f(\check{\mathbf{U}}_L) - f(\mathbf{U}_L)/(\check{\phi}_L - \phi_L) < 0$ and a standing wave $(\check{\mathbf{U}}_L, \mathbf{U}_R)$. Furthermore, the flux function for a left and a right state is plotted *(right)*. The wave solution is highlighted. The flux curves are connected by the contact discontinuity. The resulting average boundary flux is given by $\bar{F} = f(\mathbf{U}_R)$.

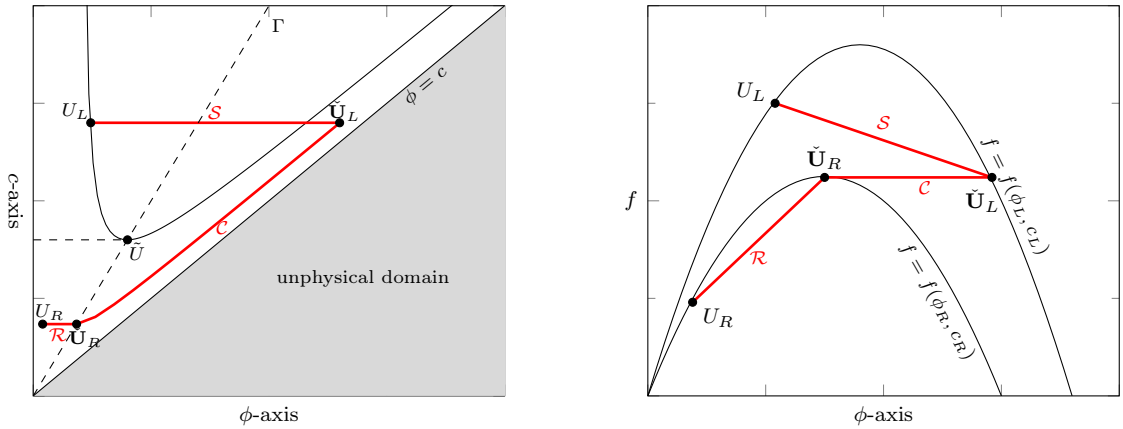

FIGURE A.5: **(4)** Example showing the wave solution in state space *(left)*. $\mathbf{U}_L$ is located left of the transition line Γ and $\mathbf{U}_R$ in region IV shown in Figure A.1, where $\phi_R < \frac{c_R}{2}$, $c_R < \tilde{c}$, and $f(\mathbf{U}_R) < f(\mathbf{U}_L)$. The solution consists of three basic waves, a shock wave $(\mathbf{U}_L, \check{\mathbf{U}}_L)$ with negative speed, given by $s = (f(\check{\mathbf{U}}_L) - f(\mathbf{U}_L)/(\check{\phi}_L - \phi_L) < 0$, a standing wave $(\check{\mathbf{U}}_L, \check{\mathbf{U}}_R)$, and a rarefaction wave $(\check{\mathbf{U}}_R, \mathbf{U}_R)$ with characteristic speed $\lambda_1(\phi, c_R) > 0$. Furthermore, the flux function for a left and a right state is plotted *(right)*. The wave solution is highlighted. The flux curves are connected by the contact discontinuity. The resulting average boundary flux is given by $\bar{F} = f_R^{max}$.

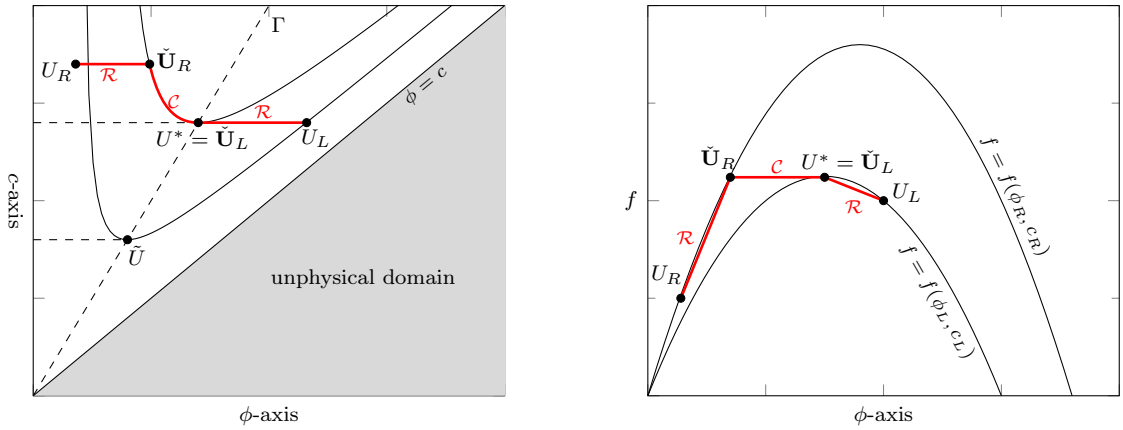

FIGURE A.6: **(5)** Example showing the wave solution in state space *(left)*. $\mathbf{U}_L$ is located right of the transition line Γ and $\mathbf{U}_R$ in region V shown in Figure A.1, where $\phi_R < \frac{c_R}{2}$, $c_R > c^*$, and $f(\mathbf{U}_R) < f(\mathbf{U}^*)$. The solution consists of three basic waves, a rarefaction wave $(\mathbf{U}_L, \mathbf{U}^*)$ with characteristic speed $\lambda_1(\phi, c_L) < 0$, a standing wave $(\mathbf{U}^*, \check{\mathbf{U}}_R)$, and a second rarefaction wave $(\check{\mathbf{U}}_R, \mathbf{U}_R)$ with characteristic speed $\lambda_1(\phi, c_R) > 0$. Furthermore, the flux function for a left and a right state is plotted *(right)*. The wave solution is highlighted. The flux curves are connected by the contact discontinuity. The resulting average boundary flux is given by $\bar{F} = f_L^{max}$.

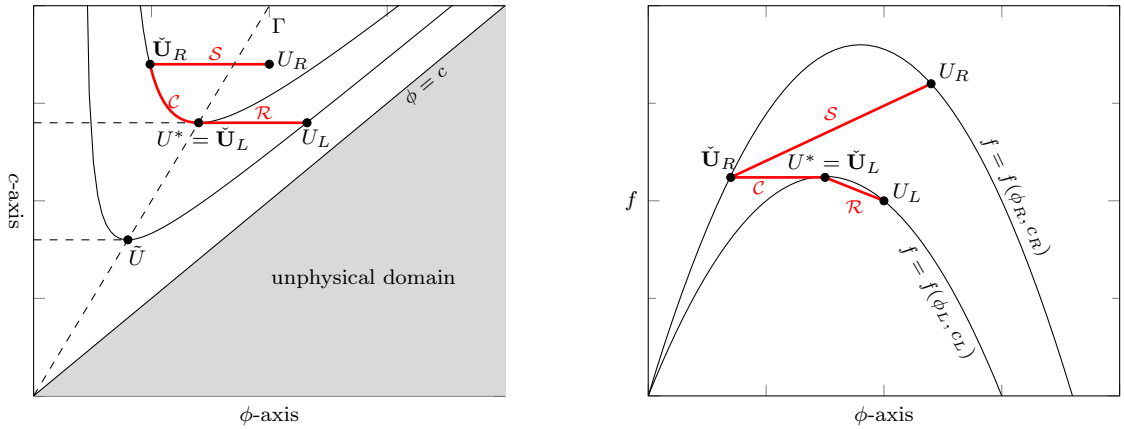

FIGURE A.7: **(6)** Example showing the wave solution in state space *(left)*. $\mathbf{U}_L$ is located right of the transition line Γ and $\mathbf{U}_R$ in region VI shown in Figure A.1, where $f(\mathbf{U}_R) > f(\mathbf{U}^*)$. The solution consists of three basic waves, a rarefaction wave $(\mathbf{U}_L, \mathbf{U}^*)$ with characteristic speed $\lambda_1(\phi, c_L) < 0$, a standing wave $(\mathbf{U}^*, \check{\mathbf{U}}_R)$, and a shock wave $(\check{\mathbf{U}}_R, \mathbf{U}_R)$ with positive speed, given by $s = (f(\mathbf{U}_R) - f(\check{\mathbf{U}}_R)/(\phi_R - \check{\phi}_R) > 0$. Furthermore, the flux function for a left and a right state is plotted *(right)*. The wave solution is highlighted. The flux curves are connected by the contact discontinuity. The resulting average boundary flux is given by $\bar{F} = f_L^{max}$.

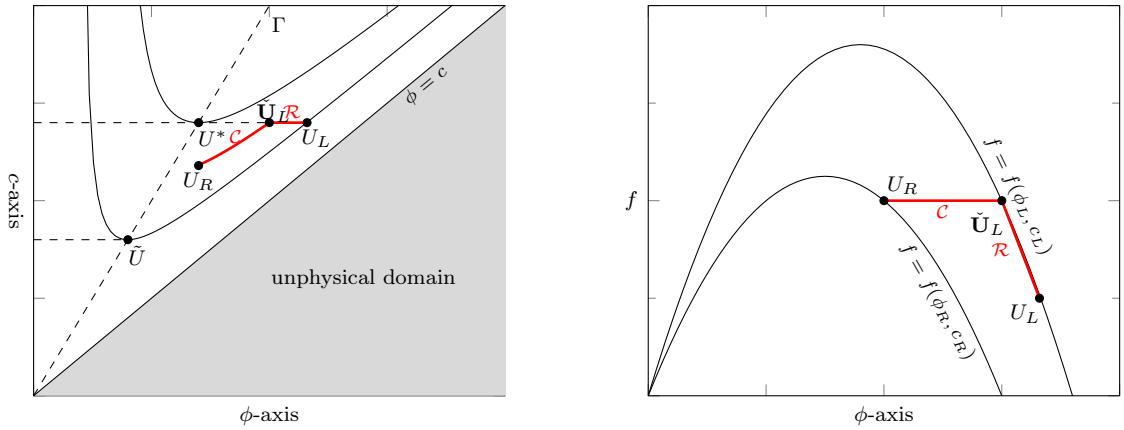

FIGURE A.8: **(7)** Example showing the wave solution in state space *(left)*. $\mathbf{U}_L$ is located right of the transition line Γ and $\mathbf{U}_R$ in region VII shown in Figure A.1, where $\phi_R > \frac{c_R}{2}$ and $f(\mathbf{U}_L) < f(\mathbf{U}_R) \leq f(\mathbf{U}^*)$. The solution consists of two basic waves, a rarefaction wave $(\mathbf{U}_L, \check{\mathbf{U}}_L)$ with characteristic speed $\lambda_1(\phi, c_L) < 0$ and a standing wave $(\check{\mathbf{U}}_L, \mathbf{U}_R)$. Furthermore, the flux function for a left and a right state is plotted *(right)*. The wave solution is highlighted. The flux curves are connected by the contact discontinuity. The resulting average boundary flux is given by $\bar{F} = f(\mathbf{U}_R)$.

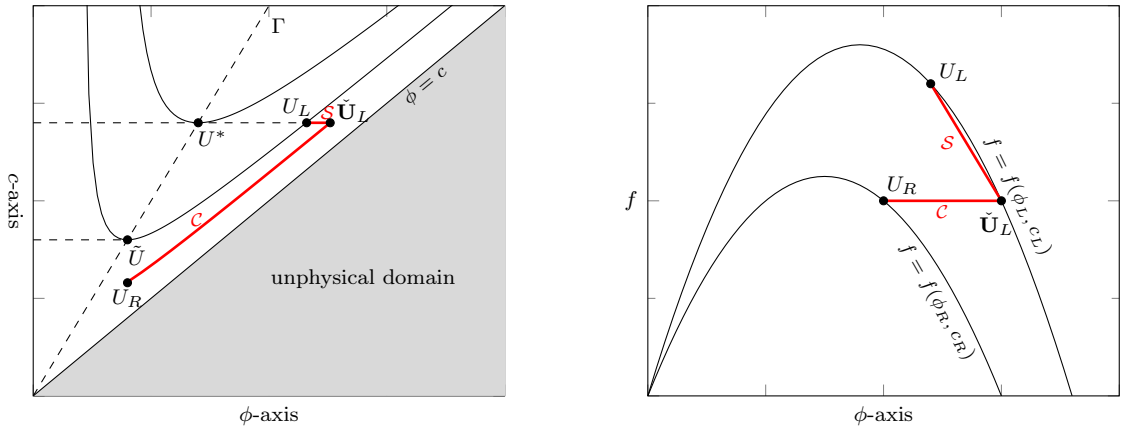

FIGURE A.9: **(8)** Example showing the wave solution in state space *(left)*. $\mathbf{U}_L$ is located right of the transition line Γ and $\mathbf{U}_R$ in region VIII shown in Figure A.1, where $\phi_R > \frac{c_R}{2}$ and $f(\mathbf{U}_R) > f(\mathbf{U}_L)$. The solution consists of two basic waves, a shock wave $(\mathbf{U}_L, \check{\mathbf{U}}_L)$ with negative speed, given by $s = (f(\check{\mathbf{U}}_L) - f(\mathbf{U}_L)/(\check{\phi}_L - \phi_L) < 0$ and a standing wave $(\check{\mathbf{U}}_L, \mathbf{U}_R)$. Furthermore, the flux function for a left and a right state is plotted *(right)*. The wave solution is highlighted. The flux curves are connected by the contact discontinuity. The resulting average boundary flux is given by $\bar{F} = f(\mathbf{U}_R)$.

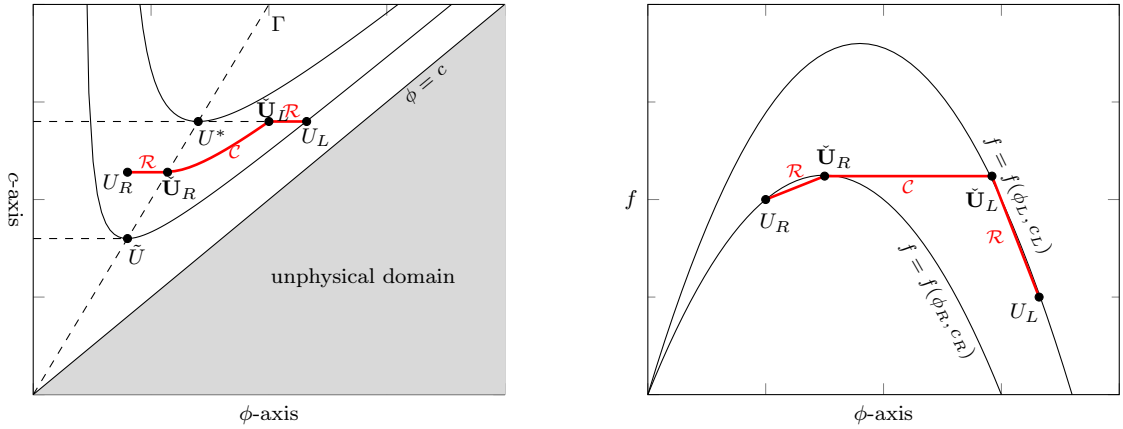

FIGURE A.10: **(9)** Example showing the wave solution in state space *(left)*. $\mathbf{U}_L$ is located right of the transition line Γ and $\mathbf{U}_R$ in region IX shown in Figure A.1, where $\phi_R < \frac{c_R}{2}$, $\tilde{c} < c_R < c^*$, and $f(\mathbf{U}_R) > f(\mathbf{U}^*)$. The solution consists of three basic waves, a rarefaction wave $(\mathbf{U}_L, \check{\mathbf{U}}_L)$ with characteristic speed $\lambda_1(\phi, c_L) < 0$, a standing wave $(\check{\mathbf{U}}_L, \check{\mathbf{U}}_R)$, and a second rarefaction wave $(\check{\mathbf{U}}_R, \mathbf{U}_R)$ with characteristic speed $\lambda_1(\phi, c_R) > 0$. Furthermore, the flux function for a left and a right state is plotted *(right)*. The wave solution is highlighted. The flux curves are connected by the contact discontinuity. The resulting average boundary flux is given by $\bar{F} = f_R^{max}$.

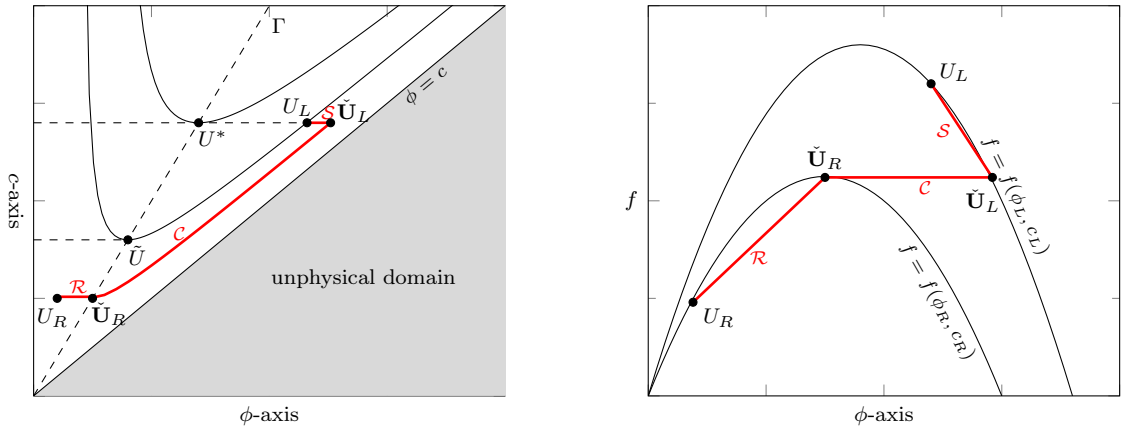

FIGURE A.11: **(10)** Example showing the wave solution in state space *(left)*. $\mathbf{U}_L$ is located right of the transition line Γ and $\mathbf{U}_R$ in region X shown in Figure A.1, where $\phi_R < \frac{c_R}{2}$, $c_R < \tilde{c}$, and $f(\mathbf{U}_R) > f(\mathbf{U}_L)$. The solution consists of three basic waves, a shock wave $(\mathbf{U}_L, \check{\mathbf{U}}_L)$ with negative speed, given by $s = (f(\check{\mathbf{U}}_L) - f(\mathbf{U}_L)/(\check{\phi}_L - \phi_L) < 0$, a standing wave $(\check{\mathbf{U}}_L, \check{\mathbf{U}}_R)$, and a rarefaction wave $(\check{\mathbf{U}}_R, \mathbf{U}_R)$ with characteristic speed $\lambda_1(\phi, c_R) > 0$. Furthermore, the flux function for a left and a right state is plotted *(right)*. The wave solution is highlighted. The flux curves are connected by the contact discontinuity. The resulting average boundary flux is given by $\bar{F} = f_R^{max}$.

Case	Figure	left state	condition of right state	$\bar{F}$
1	A.2	$\phi_L < \frac{c_L}{2}$	$\phi_R < \frac{c_R}{2}$, $c_R > \tilde{c}$, $f(\mathbf{U}_R) < f(\mathbf{U}_L)$	$f(\mathbf{U}_L)$
2	A.3	$\phi_L < \frac{c_L}{2}$	$f(\mathbf{U}_R) > f(\mathbf{U}_L)$	$f(\mathbf{U}_L)$
3	A.4	$\phi_L < \frac{c_L}{2}$	$\phi_R > \frac{c_R}{2}$, $f(\mathbf{U}_R) > f(\mathbf{U}_L)$	$f(\mathbf{U}_R)$
4	A.5	$\phi_L < \frac{c_L}{2}$	$\phi_R < \frac{c_R}{2}$, $c_R < \tilde{c}$, $f(\mathbf{U}_R) < f(\mathbf{U}_L)$	f_R^{max}
5	A.6	$\phi_L > \frac{c_L}{2}$	$\phi_R < \frac{c_R}{2}$, $c_R > c^*$, $f(\mathbf{U}_R) < f(\mathbf{U}^*)$	f_L^{max}
6	A.7	$\phi_L > \frac{c_L}{2}$	$f(\mathbf{U}_R) > f(\mathbf{U}^*)$	f_L^{max}
7	A.8	$\phi_L > \frac{c_L}{2}$	$\phi_R > \frac{c_R}{2}$, $f(\mathbf{U}_L) < f(\mathbf{U}_R) \leq f(\mathbf{U}^*)$	$f(\mathbf{U}_R)$
8	A.9	$\phi_L > \frac{c_L}{2}$	$\phi_R > \frac{c_R}{2}$, $f(\mathbf{U}_R) > f(\mathbf{U}_L)$	$f(\mathbf{U}_R)$
9	A.10	$\phi_L > \frac{c_L}{2}$	$\phi_R < \frac{c_R}{2}$, $\tilde{c} < c_R < c^*$, $f(\mathbf{U}_R) > f(\mathbf{U}^*)$	f_R^{max}
10	A.11	$\phi_L > \frac{c_L}{2}$	$\phi_R < \frac{c_R}{2}$, $c_R < \tilde{c}$, $f(\mathbf{U}_R) > f(\mathbf{U}_L)$	f_R^{max}

Table A.1: Conditions and the resulting solutions for the boundary fluxes of the Riemann problem in the concave flux case corresponding to the large particle phase.

Bibliography

[1] Igor S. Aranson and Lev S. Tsimring. Patterns and collective behavior in granular media: Theoretical concepts. *Reviews of Modern Physics*, 78(2):641–692, 2006. ISSN 0034-6861. doi: 10.1103/RevModPhys.78.641.

[2] M.M.H.D. Arntz, W. K. den Otter, W. J. Briels, P. J. T. Bussmann, H. H. Beeftink, and R. M. Boom. Granular mixing and segregation in a horizontal rotating drum: A simulation study on the impact of rotational speed and fill level. *AIChE Journal*, 54(12):3133–3146, 2008. ISSN 00011541. doi: 10.1002/aic.11622.

[3] M.M.H.D. Arntz, H. H. Beeftink, W. K. den Otter, W. J. Briels, and R. M. Boom. Segregation of granular particles by mass, radius, and density in a horizontal rotating drum. *AIChE Journal*, 60(1):50–59, 2014. ISSN 00011541. doi: 10.1002/aic.14241.

[4] Emmanuel Audusse and Benoît Perthame. Uniqueness for scalar conservation laws with discontinuous flux via adapted entropies. *Proceedings of the Royal Society of Edinburgh: Section A Mathematics*, 135(2):253–265, 2005. ISSN 0308-2105. doi: 10.1017/S0308210500003863.

[5] L. Bocquet, W. Losert, D. Schalk, T. C. Lubensky, and J. P. Gollub. Granular shear flow dynamics and forces: experiment and continuum theory. *Physical review. E, Statistical, nonlinear, and soft matter physics*, 65(1 Pt 1):011307, 2002. ISSN 1539-3755. doi: 10.1103/PhysRevE.65.011307.

[6] J.-P. Bouchaud, M. E. Cates, J. Ravi Prakash, and S. F. Edwards. A model for the dynamics of sandpile surfaces. *Journal de Physique I*, 4(10):1383–1410, 1994. ISSN 1155-4304. doi: 10.1051/jp1:1994195.

[7] J.-P. Bouchaud, M. E. Cates, J. Ravi Prakash, and S. F. Edwards. Hysteresis and metastability in a continuum sandpile model. *Physical Review Letters*, 74(11): 1982–1986, 1995. ISSN 0031-9007.

[8] J. Bridgwater, W. S. Foo, and D. J. Stephens. Particle mixing and segregation in failure zones—theory and experiment. *Powder Technology*, 41(2):147–158, 1985. ISSN 0032-5910. doi: 10.1016/0032-5910(85)87033-9.

[9] N. Brilliantov and Thorsten Pöschel. *Kinetic theory of granular gases*. Oxford graduate texts. Oxford University Press, Oxford, 2004. ISBN 0198530382.

[10] M. Bulíček, P. Gwiazda, and Málek, J. and Świerczewska-Gwiazda A. On scalar hyperbolic laws with discontinuous flux. *Mathematical Models and Methods in Applied Sciences*, 21(1):89–113, 2011. ISSN 0218-2025.

[11] Norman F. Carnahan and Kenneth E. Starling. Equation of state for nonattracting rigid spheres. *The Journal of chemical physics*, 51(2):635–636, 1969. ISSN 1089-7690. doi: 10.1063/1.1672048.

[12] Sydney Chapman and T. G. Cowling. *The mathematical theory of non-uniform gases; An account of the kinetic theory of viscosity, thermal conduction and diffusion in gases*. Cambridge University Press, [Cambridge, Eng.], 3rd ed. edition, 1970. ISBN 9780521408448.

[13] Gui-Qiang Chen, Nadine Even, and Christian Klingenberg. Hyperbolic conservation laws with discontinuous fluxes and hydrodynamic limit for particle systems. *Journal of Differential Equations*, 245(11):3095–3126, 2008. ISSN 00220396. doi: 10.1016/j.jde.2008.07.036.

[14] M. Combarros Garcia, H. J. Feise, S. Strege, and A. Kwade. Segregation in heaps and silos: Comparison between experiment, simulation and continuum model. *Powder Technology*, 293:26–36, 2016. ISSN 0032-5910. doi: 10.1016/j.powtec.2015.09.036.

[15] R. Courant, K. Friedrichs, and H. Lewy. Über die partiellen differenzengleichungen der mathematischen physik. *Mathematische Annalen*, 100(1):32–74, 1928. ISSN 0025-5831. doi: 10.1007/BF01448839.

[16] P. A. Cundall. A computer model for simulating progressive large scale movements in blocky rock systems. *Proceedings Symposium Int. Soc. Rock Mech.*, 1(II-8), 1971.

[17] Carlos F. Daganzo. The cell transmission model, part ii: Network traffic. *Transportation Research Part B: Methodological*, 29(2):79–93, 1995. ISSN 01912615. doi: 10.1016/0191-2615(94)00022-R.

[18] João-Paulo Dias, Mário Figueira, and José-Francisco Rodrigues. Solutions to a scalar discontinuous conservation law in a limit case of phase transitions. *Journal of Mathematical Fluid Mechanics*, 7(2):153–163, 2005. ISSN 1422-6928. doi: 10.1007/s00021-004-0113-y.

[19] S. Diehl. Scalar conservation laws with discontinuous flux function: I. the viscous profile condition. *Communications in Mathematical Physics*, 176(1):23–44, 1996. ISSN 1432-0916. doi: 10.1007/BF02099361. URL `https://doi.org/10.1007/BF02099361`.

[20] Stefan Diehl. On scalar conservation laws with point source and discontinuous flux function. *SIAM Journal on Mathematical Analysis*, 26(6):1425–1451, 1995. ISSN 0036-1410. doi: 10.1137/S0036141093242533.

[21] V. N. Dolgunin and A. A. Ukolov. Segregation modeling of particle rapid gravity flow. *Powder Technology*, 83(2):95–103, 1995. ISSN 0032-5910. doi: 10.1016/0032-5910(94)02954-M.

[22] James W. Dufty and Aparna Baskaran. Hydrodynamic equations from kinetic theory. In Sreekanth Pannala, Madhava Syamlal, and Thomas J. O'Brien, editors, *Computational gas-solids flows and reacting systems*, pages 66–101. Engineering

Science Reference, Hershey, Pa., 2011. ISBN 9781615206513. doi: 10.4018/978-1-61520-651-3.ch002.

[23] Jacques Duran. *Sands, powders, and grains: An introduction to the physics of granular materials*. Partially ordered systems. Springer, New York and London, 2000. ISBN 0-387-98656-1.

[24] Yi Fan and K. M. Hill. Theory for shear-induced segregation of dense granular mixtures. *New Journal of Physics*, 13(9):95009, 2011. ISSN 1367-2630. doi: 10.1088/1367-2630/13/9/095009.

[25] Robert S. Farr and Robert D. Groot. Close packing density of polydisperse hard spheres. *The Journal of chemical physics*, 131(24):244104, 2009. ISSN 1089-7690. doi: 10.1063/1.3276799.

[26] R. O. Fox. A quadrature-based third-order moment method for dilute gas-particle flows. *Journal of Computational Physics*, 227(12):6313–6350, 2008. ISSN 00219991. doi: 10.1016/j.jcp.2008.03.014.

[27] P. Gajjar and J.M.N.T. Gray. Asymmetric flux models for particle-size segregation in granular avalanches. *Journal of Fluid Mechanics*, 757:297–329, 2014. ISSN 0022-1120. doi: 10.1017/jfm.2014.503.

[28] Mauro Garavello, Roberto Natalini, Benedetto Piccoli, and Andrea Terracina. Conservation laws with discontinuous flux. *Networks and Heterogeneous Media*, 2 (1):159–179, 2007. ISSN 1556-1801. doi: 10.3934/nhm.2007.2.159.

[29] V. Garzó and J. W. Dufty. Dense fluid transport for inelastic hard spheres. *Physical Review E*, 59(5):5895–5911, 1999. ISSN 1539-3755. doi: 10.1103/PhysRevE.59.5895.

[30] Dominik Gilberg, Axel Klar, Konrad Steiner, F. Radjai, S. Nezamabadi, S. Luding, and J. Y. Delenne. A hydrodynamic model for granular material flows including segregation effects. *EPJ Web of Conferences*, 140:11008, 2017. doi: 10.1051/epjconf/201714011008.

[31] Tore Gimse. *Conservation laws with discontinuous flux functions*, volume 1991,23 of *Preprint series / Institute of Mathematics, University of Oslo Pure mathematics*. Inst., Univ, Oslo, 1991. ISBN 9788255307600.

[32] Tore Gimse and Nils Henrik Risebro. Solution of the cauchy problem for a conservation law with a discontinuous flux function. *SIAM Journal on Mathematical Analysis*, 23(3):635–648, 1992. ISSN 0036-1410. doi: 10.1137/0523032.

[33] Laura A. Golick and Karen E. Daniels. Mixing and segregation rates in sheared granular materials. *arXiv:0906.3207*, 2009.

[34] J.M.N.T. Gray and C. Ancey. Multi-component particle-size segregation in shallow granular avalanches. *Journal of Fluid Mechanics*, 678:535–588, 2011. ISSN 0022-1120. doi: 10.1017/jfm.2011.138.

[35] J.M.N.T. Gray and C. Ancey. Particle-size and -density segregation in granular free-surface flows. *Journal of Fluid Mechanics*, 779:622–668, 2015. ISSN 0022-1120. doi: 10.1017/jfm.2015.438.

[36] J.M.N.T. Gray and V. A. Chugunov. Particle-size segregation and diffusive remixing in shallow granular avalanches. *Journal of Fluid Mechanics*, 569:365–398, 2006. ISSN 0022-1120. doi: 10.1017/S0022112006002977.

[37] J.M.N.T. Gray and A. R. Thornton. A theory for particle size segregation in shallow granular free-surface flows. *Proceedings of the Royal Society A: Mathematical, Physical and Engineering Sciences*, 461(2057):1447–1473, 2005. ISSN 1364-5021. doi: 10.1098/rspa.2004.1420.

[38] J.M.N.T. Gray, Y.-C. TAI, and S. NOELLE. Shock waves, dead zones and particle-free regions in rapid granular free-surface flows. *Journal of Fluid Mechanics*, 491:161–181, 2003. ISSN 0022-1120. doi: 10.1017/S0022112003005317.

[39] J.M.N.T. Gray, M. Shearer, and A. R. Thornton. Time-dependent solutions for particle-size segregation in shallow granular avalanches. *Proceedings of the Royal Society A: Mathematical, Physical and Engineering Sciences*, 462(2067):947–972, 2006. ISSN 1364-5021. doi: 10.1098/rspa.2005.1580.

[40] Christian Grossmann and Hans-G. Roos. *Numerische Behandlung partieller Differentialgleichungen*. Vieweg+Teubner Verlag, 03 edition, 2005. ISBN 978-3-519-22089-3.

[41] Suman K. Hajra and D. V. Khakhar. Radial segregation of ternary granular mixtures in rotating cylinders. *Granular Matter*, 13(4):475–486, 2011. ISSN 1434-5021. doi: 10.1007/s10035-011-0259-2.

[42] Kimberly M. Hill and Yi Fan. Granular temperature and segregation in dense sheared particulate mixtures. *KONA Powder and Particle Journal*, 33(0):150–168, 2016. ISSN 0288-4534. doi: 10.14356/kona.2016022.

[43] Daniel C. Hong, Paul V. Quinn, and Stefan Luding. Reverse brazil-nut problem: Competition between percolation and condensation. *Physical Review Letters*, 86 (15):3423–3426, 2001. ISSN 0031-9007. doi: 10.1103/PhysRevLett.86.3423.

[44] Christine M. Hrenya. Kinetic theory for granular materials. In Sreekanth Pannala, Madhava Syamlal, and Thomas J. O'Brien, editors, *Computational gas-solids flows and reacting systems*, pages 102–127. Engineering Science Reference, Hershey, Pa., 2011. ISBN 9781615206513. doi: 10.4018/978-1-61520-651-3.ch003.

[45] Eli Isaacson and Blake Temple. Nonlinear resonance in systems of conservation laws. *SIAM Journal on Applied Mathematics*, 52(5):1260–1278, 1992. ISSN 0036-1399. doi: 10.1137/0152073.

[46] Hugo A. Jakobsen. *Chemical reactor modeling: Multiphase reactive flows*. Springer, Cham [u.a.], 2. ed. edition, 2014.

[47] W.-L. Jin and H. M. Zhang. The inhomogeneous kinematic wave traffic flow model as a resonant nonlinear system. *Transportation Science*, 37(3):294–311, 2003. URL http://www.jstor.org/stable/25769155.

[48] D. V. Khakhar, J. J. McCarthy, and J. M. Ottino. Radial segregation of granular mixtures in rotating cylinders. *Physics of Fluids*, 9(12):3600, 1997. ISSN 10706631. doi: 10.1063/1.869498.

[49] A. Klar and S. Tiwari. A multiscale meshfree method for macroscopic approximations of interacting particle systems. *Multiscale Modeling & Simulation*, 12(3):1167–1192, 2014. ISSN 1540-3459. doi: 10.1137/130945788.

[50] S. N. Kružkov. First order quasilinear equations in several independent variables. *Mathematics of the USSR-Sbornik*, 10(2):217–243, 1970. ISSN 0025-5734. URL http://stacks.iop.org/0025-5734/10/i=2/a=A06.

[51] Arshad Kudrolli. Size separation in vibrated granular matter. *Reports on Progress in Physics*, 67(3):209–247, 2004. ISSN 0034-4885. doi: 10.1088/0034-4885/67/3/R01.

[52] Andriy V. Kyrylyuk, Alan Wouterse, and Albert P. Philipse. Percolation and jamming in random heterogeneous materials with competing length scales. In Seyda Bucak, editor, *Trends in colloid and interface science XXIII*, pages 29–33. Springer Berlin Heidelberg, Berlin, Heidelberg, 2010. ISBN 978-3-642-13460-9. doi: 10.1007/978-3-642-13461-6{\textunderscore}7.

[53] Michele Larcher and James T. Jenkins. Segregation and mixture profiles in dense, inclined flows of two types of spheres. *Physics of Fluids*, 25(11):113301, 2013. ISSN 1070-6631. doi: 10.1063/1.4830115.

[54] Michele Larcher and James T. Jenkins. The evolution of segregation in dense inclined flows of binary mixtures of spheres. *Journal of Fluid Mechanics*, 782: 405–429, 2015. ISSN 0022-1120. doi: 10.1017/jfm.2015.549.

[55] Arnulf Latz and Sebastian Schmidt. Hydrodynamic modeling of dilute and dense granular flow. *Granular Matter*, 12(4):387–397, 2010. ISSN 1434-5021. doi: 10.1007/s10035-010-0187-6.

[56] J. P. Lebacque. The godunov scheme and what it means for first order traffic flow models. *The International Symposium on Transportation and Traffic Theory*, 1996.

[57] Randall J. LeVeque. *Finite volume methods for hyperbolic problems*. Cambridge texts in applied mathematics. Cambridge University Press, Cambridge and New York, 2002. ISBN 0521009243.

[58] L. Lin, J. B. Temple, and J. Wang. A comparison of convergence rates for godunov's method and glimm's method in resonant nonlinear systems of conservation laws. *SIAM Journal on Numerical Analysis*, 32(3):824–840, 1995. ISSN 0036-1429. doi: 10.1137/0732038.

[59] Benjy Marks, Pierre Rognon, and Itai Einav. Grainsize dynamics of polydisperse granular segregation down inclined planes. *Journal of Fluid Mechanics*, 690: 499–511, 2012. ISSN 0022-1120. doi: 10.1017/jfm.2011.454.

[60] Lindsay B. H. May, Laura A. Golick, Katherine C. Phillips, Michael Shearer, and Karen E. Daniels. Shear-driven size segregation of granular materials: modeling and experiment. *Physical Review E*, 81(5), 2010. ISSN 1539-3755. doi: 10.1103/PhysRevE.81.051301. URL `http://arxiv.org/pdf/0911.4138v1`.

[61] Lindsay B. H. May, Michael Shearer, and Karen E. Daniels. Scalar conservation laws with nonconstant coefficients with application to particle size segregation in granular flow. *J. Nonlinear Sci. (Journal of Nonlinear Science)*, 20(6):689–707, 2010. doi: 10.1007/s00332-010-9069-7.

[62] M. McIntyre, E. L. Rowe, M. Shearer, J.M.N.T. Gray, and A. R. Thornton. Evolution of a mixing zone in granular avalanches. *Applied Mathematics Research eXpress*, 2008. ISSN 1687-1200. doi: 10.1093/amrx/abm008.

[63] J. Mellmann. The transverse motion of solids in rotating cylinders: forms of motion and transition behavior. *Powder Technology*, (118):251–270, 2001. ISSN 0032-5910.

[64] L. W. Morland. Flow of viscous fluids through a porous deformable matrix. *Surveys in Geophysics*, 13:209–268, 1992.

[65] David Neusius. *Advanced interpolation cut-cell method for numerically solving continuum granular flow equations*. Fraunhofer Verlag, Stuttgart, 2016. ISBN 978-3-8396-1086-2.

[66] Dariusz Niedziela, Sebastian Rau, Konrad Steiner, Simone de Vita, Marion Lutsche, Meike Richter, Mattias Schmidt, and Christopher Stoltz. Virtual characterization of dense granular flow through a vertically rotating feeding experiment. *Chemical Engineering & Technology*, 40(9):1599–1604, 2017. ISSN 09307516. doi: 10.1002/ceat.201600589.

[67] Satoru Ogawa, Akira Umemura, and Nobunori Oshima. On the equations of fully fluidized granular materials. *Journal of Applied Mathematics and Physics*, 31(4): 483–493, 1980. doi: 10.1007/BF01590859.

[68] J. M. Ottino and D. V. Khakhar. mixing and segregation of granular materials. *Annual Review of Fluid Mechanics*, 32(1):55–91, 2000. ISSN 0066-4189. doi: 10.1146/annurev.fluid.32.1.55.

[69] Antonio Romano and Addolorata Marasco. *Continuum Mechanics*. Birkhäuser Boston, Boston, 2010. ISBN 978-0-8176-4869-5. doi: 10.1007/978-0-8176-4870-1.

[70] S. B. Savage. Analyses of slow high-concentration flows of granular materials. *Journal of Fluid Mechanics*, 377:1–26, 1998. ISSN 0022-1120. doi: 10.1017/S0022112098002936.

[71] S. B. Savage and C. K. K. Lun. Particle size segregation in inclined chute flow of dry cohesionless granular solids. *Journal of Fluid Mechanics*, 189:311–335, 1988. ISSN 0022-1120.

[72] Sebastian Schmidt. *On numerical simulation of granular flow.* Phd-thesis, University of Kaiserslautern, 2009.

[73] M. Shearer and N. Giffen. Shock formation and breaking in particle size-segregation. *Reprint*, 2009.

[74] M. Shearer, J.M.N.T. Gray, and A. R. Thornton. Stable solutions of a scalar conservation law for particle-size segregation in dense granular avalanches. *European Journal of Applied Mathematics*, 19(01), 2008. ISSN 0956-7925. doi: 10.1017/S0956792507007280.

[75] M. Shearer, Lindsay B. H. May, N. Giffen, and Karen E. Daniels. The gray-thornton model of granular segregation. *IUTAM-ISIMM Symposium on Mathematical Modeling and Physical Instances of Granular Flows*, 2009.

[76] Anthony R. Thornton, Thomas Weinhart, Stefan Luding, and ONNO BOKHOVE. Modeling of particle size segregation: calibration using the discrete particle method. *International Journal of Modern Physics C*, 23(08):1240014, 2012. ISSN 0129-1831. doi: 10.1142/S0129183112400141.

[77] Elewterio F. Toro. *Riemann solvers and numerical methods for fluid dynamics.* Springer, Dordrecht u.a., 3. ed. edition, 2009. ISBN 978-3-540-49834-6.

[78] John Towers, Kenneth Karlsen, Antonio García, and Raimund Bürger. Difference schemes, entropy solutions, and speedup impulse for an inhomogeneous kinematic traffic flow model. *Networks and Heterogeneous Media*, 3(1):1–41, 2008. ISSN 1556-1801. doi: 10.3934/nhm.2008.3.1.

[79] D. R. Tunuguntla, O. Bokhove, and A. R. Thornton. A mixture theory for size and density segregation in shallow granular free-surface flows. *Journal of Fluid Mechanics*, 749:99–112, 2014. ISSN 0022-1120. doi: 10.1017/jfm.2014.223.

[80] Deepak R. Tunuguntla, Anthony R. Thornton, and Thomas Weinhart. From discrete elements to continuum fields: Extension to bidisperse systems. *Computational Particle Mechanics*, 3(3):349–365, 2016. ISSN 2196-4378. doi: 10.1007/s40571-015-0087-y.

[81] Deepak R. Tunuguntla, Thomas Weinhart, and Anthony R. Thornton. Comparing and contrasting size-based particle segregation models. *Computational Particle Mechanics*, 4(4):387–405, 2017. ISSN 2196-4378. doi: 10.1007/s40571-016-0136-1.

[82] Watson L. Vargas, Suman K. Hajra, Deliang Shi, and J. J. McCarthy. Suppressing the segregation of granular mixtures in rotating tumblers. *AIChE Journal*, 54(12): 3124–3132, 2008. ISSN 00011541. doi: 10.1002/aic.11640.

[83] A. I. Vol'pert. The spaces bv and quasilinear equations. *Mathematics of the USSR-Sbornik*, 2(2):225–267, 1967. ISSN 0025-5734. URL `http://stacks.iop.org/0025-5734/2/i=2/a=A06`.

[84] Thomas Weinhart, Carlos Labra, Stefan Luding, and Jin Y. Ooi. Influence of coarse-graining parameters on the analysis of dem simulations of silo flow. *Powder Technology*, 293:138–148, 2016. ISSN 0032-5910. doi: 10.1016/j.powtec.2015.11.052.

[85] S. R. Williams and A. P. Philipse. Random packings of spheres and spherocylinders simulated by mechanical contraction. *Physical review. E, Statistical, nonlinear, and soft matter physics*, 67(5 Pt 1):051301, 2003. ISSN 1539-3755. doi: 10.1103/PhysRevE.67.051301.

[86] Han-Chin Wu. *Continuum mechanics and plasticity*, volume [3] of *CRC series–modern mechanics and mathematics*. Chapman & Hall, Boca Raton, Fla. and London, 2005. ISBN 1-58488-363-4.

[87] Clément Zémerli. *Continuum mechanical modeling of dry granular systems: From dilute flow to solid-like behavior: Techn. Univ., Diss.–Kaiserslautern, 2013*, volume 7 of *Forschungsbericht / Technische Universität Kaiserslautern, Lehrstuhl für Technische Mechanik*. Techn. Univ. Lehrstuhl für Techn. Mechanik, Kaiserslautern, 2013. ISBN 9783942695077.

This thesis deals with the topic of size segregation in granular materials. Mathematical models are developed, describing the granular flow and the segregation process. The granular flow equations consist of a set of Navier-Stokes-like equations as well as an equation for the granular temperature. With the help of the granular temperature equation, the model is able to cover dense and dilute regimes. To derive the segregation equation, special focus is lain on the segregation direction and the packing of binary particle systems. For solving the set of equations, a finite volume approach is chosen. The segregation equation explicitly depends on the volume fraction of the granular system. Since the granular flow model is compressible, the segregation equation requires special numerical treatment. Therefore, a modified Godunov scheme is formulated based on the solutions of the underlying Riemann problems. The method guarantees that the system stays in a physically valid state. The final model is extensively tested using different frameworks in two- and three-dimensional space. Particularly, the influence of the granular flow model on the segregation process is pointed out in detail.

ISBN 978-3-8396-1411-2

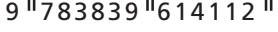

FRAUNHOFER VERLAG

Curriculum Vitae

deutsch:

07/2014-2018	**Doktorand**, Fraunhofer-Institut für Techno- und Wirtschaftsmathematik Kaiserslautern
04/2014	**Master-Abschluss**, Technische Universität Kaiserslautern
04/2012-04/2014	**Master-Studium**, Technomathematik, Technische Universität Kaiserslautern
05/2012	**Bachelor-Abschluss**, Technische Universität Kaiserslautern
10/2008-05/2012	**Bachelor-Studium**, Mathematik, Technische Universität Kaiserslautern
03/2008	**Abitur**, Goethe Gymnasium Bad Ems

english:

07/2014-2018	**Doctoral student**, Fraunhofer Institute for Industrial Mathematics Kaiserslautern
04/2014	**Master degree**, University Kaiserslautern
04/2012-04/2014	**Master studies**, Technomathematics, University Kaiserslautern
05/2012	**Bachelor degree**, University Kaiserslautern
10/2008-05/2012	**Bachelor studies**, Mathematics, University Kaiserslautern
03/2008	**Diploma secondary school**, Goethe Gymnasium Bad Ems